Contributions au développement d'absorbeurs à vibro-impacts : de la caractérisation à la conception d'absorbeurs multiples

Robin Chabrier

École doctorale N º 37 Sciences Pour l'Ingénieur et Microtechniques

Thèse de doctorat de l'Université Bourgogne Franche-Comté

préparée à

Université de Franche-Comté

par

Robin CHABRIER

Thèse soutenue à Besançon, le 14 novembre 2022

Contributions au développement d'absorbeurs à vibro-impacts : de la caractérisation à la conception d'absorbeurs multiples

(Contributions to the development of vibro-impact absorbers : from the characterization towards the design of multiple absorbers)

Directrice de thèse : **Émeline SADOULET-REBOUL** (UFC)
Co-directeur de thèse : **Gaël CHEVALLIER** (UFC)
Co-directeur de thèse : **Emmanuel FOLTÊTE** (Supmicrotech - ENSMM)

Jury

Malte Krack,	Professeur (Université de Stuttgart)	Rapporteur
Jean-Luc Dion,	Professeur (ISAE-SUPMECA)	Rapporteur
François Louf,	Maître de Conférences (ENS Paris-Saclay)	Examinateur
Cyril Touzé (président du jury),	Professeur (ENSTA Paris)	Examinateur
Stefania Lo Feudo,	Maître de Conférences (ISAE-SUPMECA)	Examinatrice

FEMTO-ST
Département de Mécanique Appliquée
24 rue de l'épitaphe, France

THÈSE

Remerciements

L'écriture de ce chapitre clôture véritablement l'aventure qu'a été cette thèse, mais aussi cette petite période de vie que j'ai passée à Besançon... Et beaucoup de noms me viennent à l'esprit dans les personnes que je souhaite citer ici. Alors tâchons d'être structuré (pas trop quand même), bien que je crois que je ne saurais être exhaustif !

Pour commencer, je tiens à remercier les membres du jury Malte Krack, Jean-Luc Dion, Cyril Touzé, François Louf et Stefania Lo Feudo, tout d'abord pour l'intérêt porté à ce travail. Ensuite, pour les relectures attentives du manuscrit, et enfin pour les échanges riches qui ont suivi la soutenance durant la phase de questions. Je tiens à faire une mention spéciale à François Louf, qui a indirectement été l'initiateur de cette aventure que je ne regrette pas d'avoir vécu... Merci d'avoir su m'orienter pendant cette année où je ne savais pas encore si je décidais de tenter l'expérience de la recherche.

Je voudrais ensuite m'attarder sur l'équipe encadrante, qui, on le sait bien, a une place toute particulière pour nous les (ex) doctorants : Émeline, Gaël, Manu. Je tiens sincèrement à vous remercier pour ce que nous avons pu partager à travers cette thèse, depuis ma première venue au DMA en mars 2019, jusqu'à encore aujourd'hui. Émeline, lors de ma première visite au DMA, je me souviens avoir passé deux heures en ta présence, et avoir rencontré dans le labo un certain nombre de personnes que j'ai pu côtoyer ensuite pendant mes années passées à Besançon. Tout a commencé à ce moment-là, car tu m'as permis de me projeter ici, à Besançon. Bien sûr, vous m'avez beaucoup apporté scientifiquement pendant la thèse et je dois reconnaître que vous avez formé un trio vraiment super : Émeline pour ta capacité incroyable à débloquer les situations sous COMSOL ou Matlab en quelques dizaines de minutes, mais aussi à organiser et structurer les réunions, Gaël et Manu pour vos regards aiguisés sur les résultats expérimentaux qui me donnaient au début l'impression que vous connaissiez mieux la manip que moi... Je crois que l'on se souviendra aussi des réunions qui paraissaient toujours trop courtes (en tout cas pour moi) malgré les trois heures passées ensemble ! Je me souviendrai aussi des idées toujours plus folles de Gaël, que tu m'avais toi-même conseillé de ne pas toutes suivre... Au-delà de la science, j'ai aussi beaucoup apprécié vos qualités humaines qui étaient pour moi au moins aussi importantes que le sujet de la thèse lui-même : l'accompagnement et la présence rassurante d'Émeline au démarrage de la thèse, l'enthousiasme inépuisable de Gaël à chaque nouveau résultat qui me semblait insignifiant, le calme et la sérénité imperturbable de Manu. Tout ceci a contribué à lever mes doutes, à me redonner de l'énergie et de la motivation lorsque cela manquait, et finalement nous a permis d'avancer même lorsque le chemin à prendre ne me semblait pas tout tracé. Ces qualités sont précieuses, gardez-les ! Nos chemins devraient continuer à se croiser, au moins lors de mes passages à Besançon...

Bien évidemment, je voudrais aussi remercier toutes les personnes du DMA qui m'ont aidé dans certaines étapes de cette thèse. Je pense en premier lieu à Vincent Tissot,

d'abord partenaire d'escalade ! puis ensuite expert pour la réalisation de mes montages nécessaires à toutes les parties expérimentales de cette thèse. Merci pour le temps passé avec moi pour ajuster les CAO, puis pour les retouches imprévues lorsque l'on réalise que tout ne se monte pas comme prévu... Ensuite Thomas Jeannin, pour ton aide précieuse durant ma première année sur la partie expérimentale et la réalisation d'images. En particulier, les expériences que tu as réalisées pour moi pendant le premier confinement m'ont permis de continuer avancer bien que je ne sois pas sur place. Je dois aussi beaucoup à Manu Bachy pour l'utilisation des différents équipements au pôle vib. Toujours là pour expliquer, montrer, dépanner. Tu m'as si souvent donné de ton temps pour m'aider avec nos équipements, merci ! Je dois également citer Éric Joseph pour les conseils prodigués à la volée, mais aussi pour le dépannage et prêt de matériel lorsque les outils, colle, et autres conditionneurs se révélaient difficile à trouver dans notre cher pôle vib. Merci aussi à Stani pour ton aide dans la gestion et l'utilisation des équipements. Enfin, j'adresse un grand merci à Johann pour le travail réalisé pendant ton stage qui a alimenté une bonne partie du chapitre 5 de ce manuscrit ! Travailler avec toi a été une expérience très enrichissante, continue ainsi en thèse ! Merci également à Pierre pour les essais réalisés ensemble sur la maquette d'avion. Je voudrais aussi remercier toutes les personnes du DMA mais également au-delà qui ont apporté un soutien précieux pour les aspects administratifs et financiers auxquels nous sommes parfois confrontés : Delphine, Isabelle, Christine, merci pour votre aide efficace lors des déplacements en conférence ou en formation. En dehors du DMA, je remercie Sandrine Chatrenet pour la gestion financière de ma thèse auprès de qui j'ai toujours obtenu les réponses dont j'avais besoin, ainsi qu'Alika Rossetti pour l'aide et les renseignements apportés lors des déplacements en conférence ou formation. À celles et ceux que je n'ai pas cité et que j'oublie ici, merci pour l'aide que vous avez pu m'apporter.

Bien sûr ces trois années ne se résument pas à de la production scientifique, et je tiens aussi à remercier toutes les personnes avec qui j'ai pu partager des moments qui ont contribué à rendre cette période unique. Je commence tout d'abord par le bureau 40H : Quentin, Quentin (alias QL), Martin, Camille et Stéphanie. Que de discussions dans ce bureau... Pas toujours pour nos aider dans notre efficacité, mais merci d'avoir fait que ce bureau soit vivant ! Quentin (Lefebvre), merci de nous avoir démontré tes compétences culinaires ! Je pense aussi à tous les autres doctorants, post-doc, stagiaires, permanents... que je ne pourrai pas tous citer. À celles et ceux qui ont soutenu avant moi et qui ont été inspirant.e.s : Margaux et Svenja. Merci Svenja pour ton soutien rassurant dans les dernières semaines de rédaction. Merci à Kaouthar, Shakiba, Jessé pour ce que nous avons fait ensemble pour les JJCABs ! Jessé, Francesco, Scott pour notre aventure ensemble aux États-Unis pendant l'IMAC. Camille et Kévin, merci pour les supers moments passés ensemble au CSMA ! Alexandre, Jason, pour votre bonne humeur et votre humour quotidien au DMA. À ceux qui ont déménagé et se sont rapprochés : Solène, Etienne... toujours le sourire ! Ludo pour les conversations existentielles sur l'enseignement ou l'utilisation de gitlab (je n'ai finalement pas encore réussi à m'y mettre, oups). Pauline et Thomas, pour m'avoir emmené au BUC dès mes premières semaines à Besançon !! et me permettre ainsi de découvrir le ski de rando, mais aussi d'aller jusqu'après Pontarlier en tandem... Merci aussi d'être inspirants, et de prouver que l'on peut faire différemment ! Merci à toutes et tous d'avoir fait que le DMA soit un lieu de vie agréable !

Enfin, je ne pourrais pas terminer ce chapitre sans mentionner les gens avec qui j'ai pu partager des moments tout aussi intense en dehors du labo, pendant les weekends,

les vacances... et qui ont rendu cette période inoubliable. Tout a commencé avec les expéditions ski de fond avec Alexis, Laure, André, Manu, Romero... Vous m'avez fait découvrir une région superbe. Puis ensuite avec Quentin, Alexis, Laure, Justine, Kilian, que d'aventures partagées ensemble ! Il faudrait des pages pour retranscrire, ne serait-ce que les plus marquantes. De l'escalade, des bivouacs à tout moment de l'année (même, voire surtout aux moins opportuns), puis petit à petit l'idée de faire de la grande voie, dans le Val d'Aoste par exemple, histoire de pouvoir ramasser des cailloux pour Kilian au passage... Et enfin Ailefroide. Au-delà du partage sportif, il y a avec vous une sérénité et une spontanéité rare. Peut-être êtes-vous la découverte la plus importante de ma thèse ? Merci pour tout. Et je sais que tout cela n'est pas fini. Thomas bien sûr ! slacker de talent, partenaire particulier d'escalade, et surtout générateur de motivation, d'enthousiasme, et de lien social ! Tout ceci fait de toi un ami exceptionnel. Je pense aussi aux amis qui n'étaient pas sur place. Mina, pour nos nombreux appels, souvent bons pour le moral ! Mais aussi pour les chouettes moments partagés à Besançon lorsque tu étais là. Et puis les anciens du vélo et d'ailleurs : Florian, Marion, Lionel, Epalus, Gautier, Adeline. Merci pour les organisations des sorties gravel sur les bords de la loire, bike packing en Ardèche et autre tour du lac qui m'ont redonné de l'énergie, et permis de me rappeler que la vie, ce sont ces aventures là aussi. Et les gens rencontrés aux Glénans pendant ces trois années où j'ai aussi commencé et achevé ma formation de moniteur, et qui m'auront appris et apporté tant de choses utiles aussi bien sur les îles qu'au labo, dans l'encadrement, et dans l'enseignement. Stéphane, Sébastien, Augustin, Thomas chef d'île, Pauline...

Vraiment enfin, je voudrais remercier celles et ceux qui, de manière peut-être moins directe ont aussi joué un rôle particulier. Antoine, pour ta participation à l'avant-dernière répétition qui me fut d'une grande aide sur le plan moral, ainsi que pour ta présence à la soutenance qui m'a beaucoup touché. Pauline et maman bien sûr, parce que vous avez toujours représenté l'environnement rassurant dans lequel il était possible de se réfugier. Maman, en mai 2019, alors que je devais prendre une décision pour la thèse, tu m'avais suggéré de me fier à l'impression positive que j'avais eu et m'avais incité à répondre favorablement à cette opportunité. Cette contribution, petite en apparence, m'a permis de vivre tout ce qui a suivi. Christian et Jocelyne, quelle surprise de vous voir pour la soutenance ! Merci d'avoir été là.

"Tous les enfants grimpent pour le plaisir de grimper. Pour le plaisir de découvrir, de voir plus loin et de plus haut."

Gaston Rébuffat

Contents

List of figures

List of Tables

Introduction

Every system and structure has its own dynamic behavior. This means that submitted to external forces, the structure may exhibit responses with very high or low amplitudes, depending on the frequency content and spatial distribution of the excitation. If the structural damping is sufficiently low, resonances phenomena can take place at the eigenfrequencies of the structure. This can lead to very high amplitude of vibration even for low excitation forces. This phenomenon might be desired like in the case of musical instruments where the vibrations are needed to produce a sound. On the contrary, vibrations in mechanical systems are generally undesired because they may lead to acoustic disturbances, and to repetitive strain that might accelerate the degradation and end with failure of the system. Nowadays, lightweight designs are required for consumption reduction, as well as economical and ecological purposes. The field of aerospace and the transportation domain in general are concerned, amongst others. Generally, this leads to build structures with bad dynamic properties. In other terms, resonances appear in the operating range of the concerned devices, and the less the structure is damped, the stronger the resonances are. Therefore, controlling and reducing the vibrations are crucial issues in the design process of a structure. Since many solutions exists to reach this objective, the first chapter presents the most common strategies available and currently used.

However, engineers and researchers are facing increasingly severe requirements. Indeed, the will to reduce the environmental impact while conserving high performance level imposes compact designs, low added mass, and to limit the use of polymer materials. In the same time, it is necessary to design safe and robust solutions, with large frequency range of effectiveness. In this context, non-linear absorbers have an interesting role to play because of their high performance potential compared to traditional linear strategies. In particular, this PhD thesis is dedicated to the study of vibro-impact absorbers.

Vibro-impact absorbers are a particular type of non-linear absorbers, taking advantage of the contact non-linearity. Practically, it consists in integrating one (or more) oscillating mass(es) to the main vibrating structure. The vibrations of the structure lead to impacts between the oscillating mass and the structure, and the physical phenomena involved are beneficial to the vibration reduction. Many numerical and theoretical results related to the non-linear and hard-to-understand dynamic behavior of such absorbers are available in the literature.

In this PhD thesis, the approach is complementary to the works already and currently done on vibro-impact absorbers. We adopted experimental approaches, in order to measure and characterize vibro-impact phenomenon. Moreover, we investigated the effect of VI absorbers on structures of progressive complexity. Since many results are established for single degree-of-freedom system, we started to use a vibro-impact absorber on a beam. Then, we studied a three-dimensional structure equipped with vibro-impact absorbers.

This work has been supported by the EUR EIPHI Project, France (contract ANR-17-EURE-0002) and Bourgogne Franche-Comté Region, Fr

Chapter 1

An introduction to vibro-impact based strategies

Contents

Preamble

This chapter is devoted to introduce the general objectives related to vibration mitigation. The vibro-impact phenomenon is presented, as well as its utilization in vibro-impact absorber for vibration mitigation purposes. The global context of the strategies available in the literature used for vibration reduction is presented, and the benefits of using nonlinear absorbers such as vibro-impact absorbers are introduced. At the end of this chapter, the organization of this manuscript is presented and the scientific objectives of this PhD thesis are listed.

1.1 Vibro-impacts as a non-desired phenomenon

Vibro-impact (VI) phenomenon usually refers to impacts triggered by vibrations. Originally, vibro-impacts are non-desired phenomena that systems with slack may undergo. For instance, vibro-impacts may be observed in geared sytems where torque fluctuations

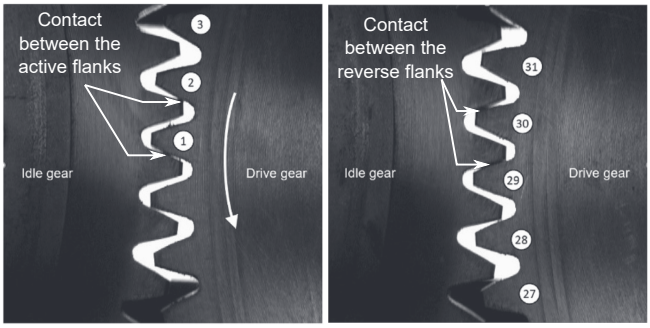

(a) Geared system with contact loss [108].

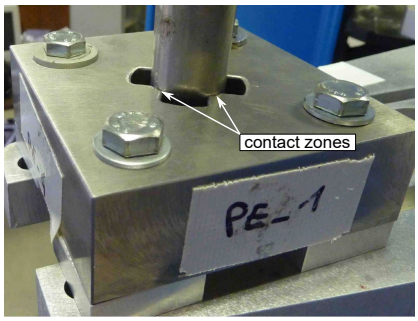

(b) Tube in the steam generator of a nuclear power plant [127].

Figure 1.1: Examples of two systems submitted to vibro-impacts.

lead to contact losses between gear teeth [57, 32, 15]. In nuclear power plants and more specifically in the steam generator, the fluid flowing in the tubes makes them vibrate. As these tubes are very close to the rest of the structure, vibro-impacts may occur [127, 89], transforming the dynamic behavior of the structure as non-linear and damaging the tubes in a problematic manner. Such examples are illustrated in figure 1.1. In civil engineering, close buildings submitted to earthquake excitations can also undergo repetitive impacts [90]. Moreover, backlash can be observed in systems like gearboxes [120] or assemblies [123], corresponding generally to contact loss between the different parts of the system. Under particular excitation conditions, such a phenomenon can lead to vibro-impacts. Besides, some methods are proposed to control and suppress the effect of backlash in mechanisms [94]. Similarly, cracked structures excited by an oscillating force undergo alternating phases of contact and contact loss [60], leading to non-linear behavior of the cracked structure.

The consequences are often unwelcome, since vibro-impacts may generate noise in gear boxes [108, 112]. Because they are a major source of discomfort, it is necessary to develop specific approaches to localize the source of the noise [119]. Vibro-impacts also modify the dynamic property of the main structure that becomes non-linear [12], and they may involve fatigue, surfaces damage in the contact zone, suggesting a reinforcement of the considered materials [69]. In other engineering fields, vibro-impacts occur in drilling systems, and the phenomena must be well understood in order to optimize the drilling performance [100]. The present chapter details the common vibration control strategies, and the one based on vibro-impact phenomenon. As a remark, the interested reader can find applications based on vibro-impact phenomenon that are out of the scope of this PhD thesis: for example, some medical devices rely on the non-linear behavior of small vibro-impact devices to generate a motion in the human body [144, 47], or more generally to obtain locomotion systems [93, 78].

1.2 A short review of vibration control strategies

1.2.1 Context and common solutions

Reducing the vibrations of all types of structures has occupied engineers and researchers for many years. Indeed, when a mechanical system is excited by an external load, it can vibrate at special frequencies corresponding generally to its eigenmodes, exhibiting

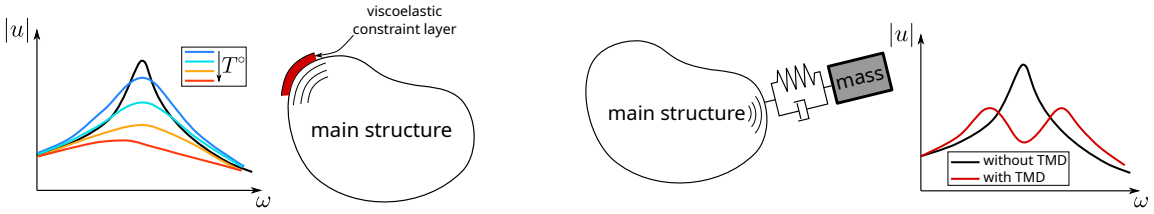

(a) Viscoelastic material.

(b) TMD.

Figure 1.2: Notional diagrams representing a structure equipped with a TMD or a viscoelastic constraint layer, and the corresponding frequency response.

sometimes large amplitudes. The vibrational response of the primary structure depends on many factors, such as the type and the amplitude of the external load, the intrinsic damping capacity of the structure... The lower the structural damping of the structure, the higher the vibration amplitude of its resonant peaks. Therefore, if the external load has a frequency content that matches the eigenfrequencies of the structure, the vibrations may become problematic. Vibrations are at the origin of acoustic disturbances like in automobile cabins [11] or in electrical machines [21], they can also prevent mechanical systems to operate properly, in particular if optical components are involved since such devices are very sensitive even to small vibrations [55, 70]. When structural components are concerned by vibrations, the repetitive stress can also lead to fatigue [131], and finally to dramatic failure of the structure. All these reasons justify that vibrations have to be tailored. The most common strategies currently adopted to tackle such issues are presented in the following of this section.

1.2.1.1 Passive strategies

Solutions enabling to reduce the vibrations and to absorb the vibrational energy without any need of external energy supply refer to passive strategies. For instance, elastomer components are often used for their high damping capacity and relatively low density [101]. However, their damping capacity may depend on the temperature as illustrated in figure 1.2a and robust design methods must be considered [56]. Tuned Mass Absorbers (TMD) are another well-known strategy that consists in absorbing the vibrational energy of the main structure in a linear attachment and dissipating it locally. Schematically, these devices correspond to a spring-mass element with a parallel damper. A schematic representation is provided in figure 1.2b. Therefore, they have a narrow frequency range of effectiveness which is centered on the natural frequency of the absorber and leads to the apparition of two side resonant peaks on both sides of the eigenfrequency of the absorber. Moreover, TMDs are known to be effective for a specific excitation frequency, but they are not very robust to eigenfrequencies variations, that can take place in bolted assemblies [30]. It is worthy to note that the damping component may be chosen in order to optimize the absorber and increase its effectiveness range [62]. Nevertheless, the practical realization of such devices may be challenging, especially if the precise control of the damping of the absorber is required [13]. Based on this last strategy, recent studies have focused on Non-linear Energy Sinks (NES) that are obtained replacing the linear stiffness by a cubic stiffness for instance, though other types of non-linearity can be employed. Cubic NES are usually obtained imposing a transverse displacement of a mass attached to linear springs, as illustrated in figure 1.3a. NES can surpass the performance of classical TMDs. Firstly,

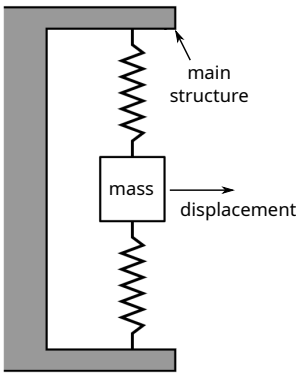

(a) Illustration of the realization of a cubic NES [43].

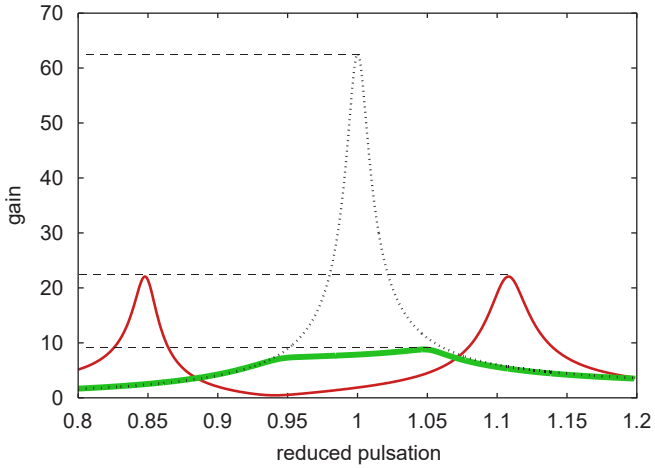

(b) Comparison of the performance of a cubic NES (green line) and a TMD (red line) on a single DOF system (dotted line), from Gourdon et al. [46].

Figure 1.3: Cubic NES.

they can achieve very high level of vibration reduction using a smaller mass for an equivalent damping. A comparison between a cubic NES and a classical TMD is provided in [99]. Secondly, they are less sensitive to a small change in the eigenfrequency of the main structure (due to ageing or damaging for example), thus the robustness is increased. Moreover, NES absorbers allow to mitigate a vibration mode efficiently without creating any parasite resonant peak like in the case of the TMD as illustrated in figure 1.3b. However, as such absorbers are non-linear, they are more complex to control, and their optimal design requires specific methods to simulate their behavior. Moreover, NES often need a minimal level of energy to be activated. Coming back to vibro-impacts, the phenomena is also used by researchers for vibration reduction application, leading to the design of what is commonly referred to as vibro-impact absorbers. VI absorbers can be qualified as NES, even if the way the energy is dissipated might be different from the case of a traditional cubic NES. This point will be discussed in the chapter 4. In the case of VI absorbers, the cubic non-linearity is replaced by a contact non-linearity.

1.2.1.2 Active and adaptive strategies

Such strategies need an external energy supply. A common technique is to use piezoelectric materials that supply a voltage when they are strained. Conversely, they are strained under electric voltage. Therefore, monitoring the voltage and supplying them an electrical signal is a common control strategy that has very high performances for vibration reduction with minimal added mass [104, 28]. In assemblies, friction dampers are used and the tightening load can be tuned to manage the optimal load [23]. Other strategies consist in adapting the structural property of the system using shape memory polymers and a heating source [24]. Indeed, the mechanical properties of polymer materials are temperature dependent, and they can reach outstanding performances in terms of loss factor if the polymer is at the glass transition. However, even if such approaches may be more efficient than passive strategies, they are more complex and, to some extent, less robust since vibration reduction cannot be performed in case of default of the system.

Before concluding this section, it should be noticed that other less common techniques exist and give rise to intense research. For instance, we can cite non-linear piezoelectric shunts [118], friction damper [122], centrifugal pendulum absorbers [84], or even Acoustic Black Holes (ABH) that help to dissipate the energy locally on the structure. Because on the effectiveness of ABH for sufficiently high frequencies, they can be combined to vibro-impact absorbers [68, 67, 66].

1.2.2 Impact based technologies

Among the passive strategies presented before, one can mention a sub-category that refers to impact-based technologies. In more traditional passive strategies, the energy is dissipated thanks to dissipative viscoelastic materials, like in the case of polymers, or thanks to a dissipative component. In the case of TMD and NES, a damper (linear or not) is used. Considering impact based technologies the energy is dissipated differently, relying on the impact phenomenon between the main vibrating structure and one (or more) secondary structure, often denominated as particle. In this section, we decided to separate two approaches: the one related to particle damping, and the other one related to vibro-impact absorbers. We will see that the two approaches can be distinct on a few aspects: in particular, the technology and the design, the physical phenomena involved, and the numerical methods adopted to deal with both devices are different.

1.2.2.1 Particle damping

Many research works dealing with vibro-impact related to damping and vibration suppression are focused on particle damping [82, 39]. Particle damping refers to technologies employing granular materials made of multiple particles enclosed in a same cavity attached to the vibrating structure. An illustration is provided in figure 1.4. Sometimes,

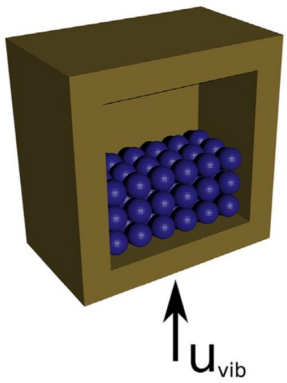

Figure 1.4: Illustration of a multiple particle dampers [39].

some studies dealing with particle damping using a single particle may be found. However, in the present case these solutions are sorted in the following section devoted to VI absorbers because they are closer to these systems in terms of design and working principle. Particle dampers have found application on structures like beams [5, 132], or on more realistic structures like gears [143], as illustrated in figure 1.5. More generally particle dampers can be widely used in industrial systems, such as cutting tools for vibration suppression, engine turbine, antenna structures, etc [82]. Particle dampers rely on impacts

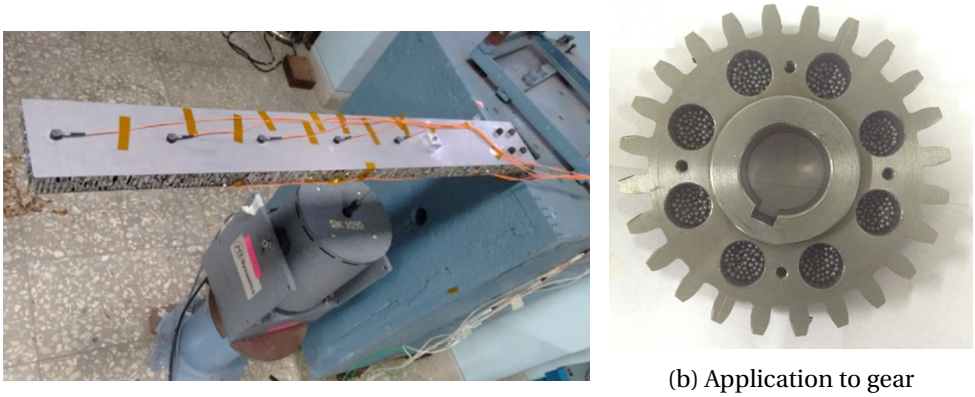

(a) Honeycomb beam filled with particles [5].

(b) Application to gear transmission [143].

Figure 1.5: Examples of applications for particles dampers.

and friction to dissipate the energy. Thus, the energy is assumed to be dissipated during particle-to-particle and particle-to-wall inelastic collisions, but also thanks to friction between the particles. When simulations of particle dampers are needed, the studies often rely on the Discrete Element Method (DEM) that is especially suited to solve dynamic problems involving granular materials [39]. Therefore, designing a particle damper generally aims at maximizing the energy dissipated during the impacts and the contact phases by means of friction, and inelastic impacts. Therefore, some design parameters can be identified like the mass ratio of the particles to the main system, the filling ratio, and the density of the particles [80]. The size of the particles is also sometimes investigated.

It is also possible to find other strategies, like liquid dampers that have replaced the granular materials by a liquid [110], or even the association of a particle damper and a liquid damper [29].

1.2.2.2 Vibro-impact absorbers

Here we decided to employ *vibro-impact absorber* as a general term to denote strategies of vibration mitigation based on vibro-impacts. Contrary to the previous section, we consider that a single particle is used in a cavity. Therefore, no granular materials are dealt with anymore. Other terms than *vibro-impact absorber* can be found in the literature, such as *impact damper*, *impact absorbers* or *Vibro-Impact Non-Linear Energy Sink (VI-NES)*. Most of the time, these different terminologies are related to different scientific points of view, even if the systems are practically the same in terms of design. The following aims at clarifying this last point.

As preliminary considerations, VI absorbers consist in triggering the vibro-impact phenomenon voluntarily in order to achieve a vibration reduction of a main vibrating structure. For this purpose, the most common approach is to place a free mass in a cavity attached to the structure. The cavity is defined by a certain gap value that defines the distance available for the ball. Obviously, the direction of displacement of the free mass must be as collinear as possible with the vibration direction of the main structure in order to trigger the impacts. Since the free oscillating mass has a finite space in the cavity, vibro-impacts occur at the ends of the cavity if the vibrations of the main structure become large enough. Usually, the small oscillating mass is a ball, and the cavity is a cylinder because such designs are easy to realize. A notional diagram of a VI absorber is provided in fig-

ure 1.6. At first sight, the main design parameter is the gap of the absorber, corresponding

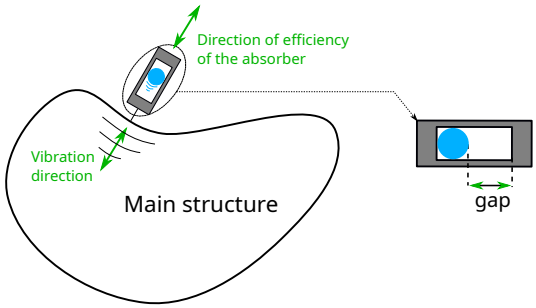

Figure 1.6: Notional diagram of a VI absorber attached to a main structure.

to the distance available for the ball inside the cavity, but the mass ratio plays also an important role in the performance of the absorber.

Impact damper The studies related to impact dampers deal with passive devices based on impacts between an auxiliary mass and the main vibrating structure. Impact dampers are often related to applied studies, that try to take advantage of impact dampers for vibration reduction purposes using practical approaches.

The structures considered are mostly simple systems like beams [14, 138, 113] or one-story building models [138, 31]. Whatever the case, the structures are studied in the vicinity of a specific mode, therefore they are systematically modelled as a single degree of freedom (S-DOF). As an exception, the authors have modelled a multi-DOF system in [86] in order to extend the results already available for S-DOF structures.

In the experimental studies, the authors mainly use harmonic excitations [35, 138, 146] and transient excitations [14, 138, 113]. The harmonic excitations can be a pointwise force applied by a shaker, or a base acceleration imposed to the structure via a shaking table, or less common methods like an electric imbalanced motor [138]. Transient excitations generally correspond to an initial displacement without velocity, before releasing the structure that can freely oscillate.

Many numerical studies are also available. Because of the contact conditions that sometimes lead to complex responses of the main structure, time integration is often used since it can provide very accurate solutions, despite the high computational cost [35, 14, 138, 146]. The Runge-Kutta scheme is often used for its accuracy property. The Moreau scheme is also often used [128, 37] for its property of energy conservation [65, 2]. However, special attention must be paid to the determination of impacts instants. For instance, events function are built-in methods available in many commercial software (such as Matlab) that realize zero-crossing detection, corresponding to impacts instant. can achieve this in Matlab when using the Ordinary Differential Equation solver. Another strategy is to determine the response of the system analytically between the impacts [86]. Moreover, in this same paper the authors have used random excitations to strive to assess the effectiveness of the impact damper in the case of a broadband seismic excitation.

Contrary to particle dampers, the dissipation phenomena are assumed to occur almost exclusively during the contact phases. Phenomena like plasticity or viscous damping of the impacted material are usually assumed. Several models are often used to describe the impact process and traduce both the elastic behavior of the contact, and the dissipation part.

In the context of this manuscript, only simple rheological models are presented. Nevertheless, we will see that more complex approaches exist, and that it is possible to build impact models representing richer phenomena if needed.

The first very simple model that can be used to describe the contact between the mass and the main structure is the Kelvin-Voigt model. It conveys the viscoelastic behavior of the contact material, and it can be represented by a linear spring and damper in parallel. Hence, in the case of a vibro-impact problem, the contact force is defined as:

$$\begin{cases} F = K.(\delta - \delta_0) + c.\dot{\delta} & \text{if} \quad \delta > \delta_0; \\ F = 0 & \text{if} \quad -\delta_0 \geq \delta \geq \delta_0; \\ F = K.(\delta + \delta_0) + c.\dot{\delta} & \text{if} \quad \delta < -\delta_0; \end{cases}$$

where δ is the relative displacement of the colliding solids, δ_0 is the distance before contact from the neutral position, and the dot indicates the first derivative with respect to time. The rheological model and the graphical representation of the contact force as function of relative displacement is provided in figure 1.7. This model can be easily

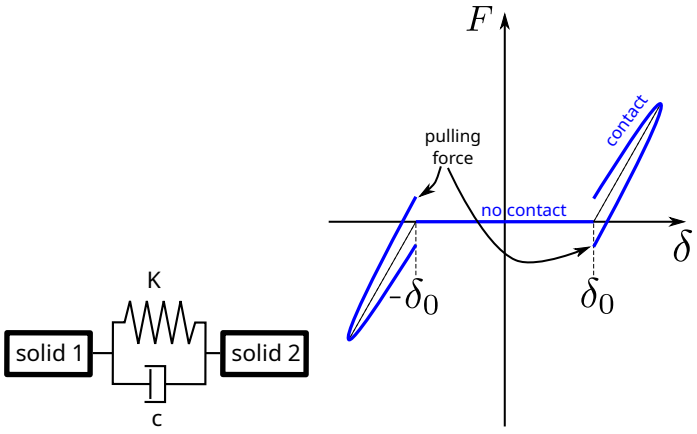

(a) Kelvin-Voigt rheological model.

(b) Force versus displacement for the Kelvin-Voigt model.

Figure 1.7: Kelvin-Voigt model.

implemented in a time simulation, and because of the linear relation between the force and the displacement, it is even possible to determine analytical solutions of the motions during the contact phase. However, one of the issue with the Kelvin-Voigt model to describe impact phenomenon is the damping force proposed by this model. Indeed, at the end of the contact phase, the damping term $c.\dot{\delta}$ creates a pulling force because of the negative velocity $\dot{\delta}$. However, this pulling force is not physically realistic since the contact opens in these circumstances, and no pulling force exists. As a remark, the size of the hysteresis loop displayed in the curve depicting the force versus the relative displacement depends on the relative velocity when the contact begins.

Although, the Kelvin-Voigt model is sometimes used as a contact model, it is more suited to describe the material behavior than the contact properties. Thus, the Hertz contact model is more suited to depict the contact force between two solids in contact. In

particular, the Hertz model takes into account that the contact surface increases with the contact force, what results in an increase of the contact stiffness. This non-linear behavior (though the model considers a linear elastic behavior for the materials) depends on the geometrical properties of the solids in contact. In the case of a sphere in contact with a plane, the contact stiffness depends on the relative displacement to the power $\frac{3}{2}$. Moreover, a non-linear damper can be used in parallel in order to represent the dissipation phenomena occurring during the contact, as illustrated in figure 1.8. Therefore, for a

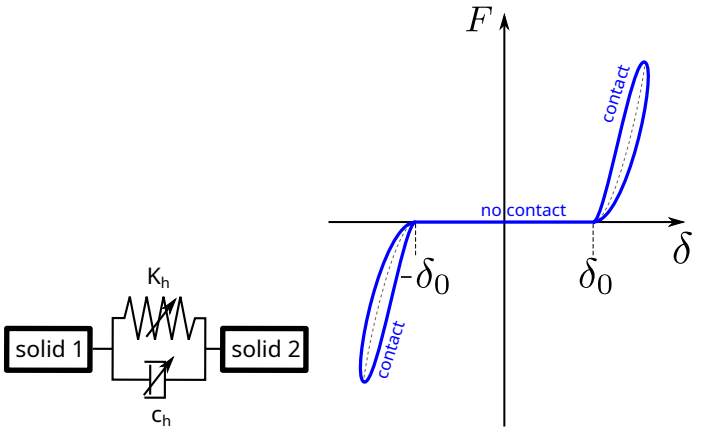

(a) Hertz-damped rheological model.

(b) Force versus displacement for the Hertz-damped model.

Figure 1.8: Hertz-damped model.

spherical contact, the contact force is defined as:

$$\begin{cases} F = K_h.(\delta-\delta_0)^{\frac{3}{2}} + c_h.\delta^{\frac{3}{2}}.\dot{\delta} & \text{if} \quad \delta > \delta_0; \\ F = -K_h.|\delta-\delta_0|^{\frac{3}{2}} + c_h.|\delta|^{\frac{3}{2}}.\dot{\delta} & \text{if} \quad \delta < -\delta_0; \end{cases}$$

where K_h depends on the radius R of the sphere, the Young's modulus and Poisson's ratio E_i and ν_i of the materials, so that $K_h = \frac{4.R^{1/2}}{3.(k_1+k_2)}$, and $k_i = \frac{1-\nu_i^2}{E_i}$ $(i \in \{1,2\})$. c_h is the damping coefficient. Using this expression for the damping term leads to avoid the previous problem met with the Kelvin-Voigt model. Like before, the size and the shape of the hysteresis loop depends on the initial contact velocity $\dot{\delta}$. This model can be easily implemented in a time simulation, though the non-linear stiffness prevents from deriving analytical motions during the contact phase, contrary to the Kelvin-Voigt model.

However, even if the two previous models are based on the physical properties of the colliding solids, the damping term remains difficult to determine, since several physical phenomena are likely to dissipate the energy during the impact. This aspect is investigated in chapter 2.

For this reason, a more practical approach consists in considering a Coefficient of Restitution (COR) $e \in [0,1]$ that directly relates the relative velocities before and after the contact instant t_c using the following equation:

$$V_2^+ - V_1^+ = -e.(V_2^- - V_1^-). \tag{1.1}$$

Using the equation of momentum conservation $m_1.V_1^- + m_2.V_2^- = m_1.V_1^+ + m_2.V_2^+$, the post-impact velocities can be calculated. The impact process is assumed to be instanta-

neous and is represented in figure 1.9. The COR conveys the energy loss during the impact

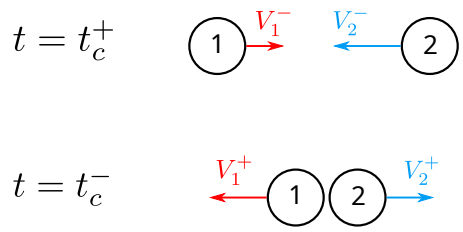

Figure 1.9: Illustration of the instantaneous impact process.

process, and it was demonstrated in [90] that it can be related to the damping coefficient of the Kelvin-Voigt model equating the energy loss of each model:

$$c = -2.\frac{\ln e}{\sqrt{\pi^2 + (\ln e)^2}}.\sqrt{\mathrm{K}.\frac{m_1.m_2}{m_1 + m_2}}; \tag{1.2}$$

where m_1 and m_2 are the masses of the two colliding solids. The same applies to the Hertz model, though some discrepancies are met when the COR approaches zero [148]:

$$c_h = \frac{3.\mathrm{K}_h.(1 - e^2)}{4.\dot{\delta}_0}; \tag{1.3}$$

where $\dot{\delta}_0$ is the initial relative velocity.

Using a Coefficient of Restitution is an extremely simple manner to describe impacts phenomena, since the contact phase itself is neglected. In first approximation, it seems to be a reasonable hypothesis since the contact duration is generally very short compared to the usual other mechanical phenomena considered in structural dynamics. For this reason, this approach is widely used in numerical simulations. However, being able to determine a realistic value for the COR can be a tough problem, as it depends on many parameters, such as the materials in contact [33], the relative velocities [109], etc... Indeed, many physical phenomena are likely to occur during the impacts and can affect the coefficient of restitution. The interested reader can refer to the following studies where the influence of several phenomena on the COR are investigated, such as the influence of plasticity and vibration of the impacted structure [116], or the influence of viscous damping and elastic waves [20]. Moreover, richer models are available in the literature to represent impacts phenomena. For instance, Boettcher et al. proposed more complex models considering the material behavior and the elastic waves following the impact [20]. In [79], the authors compare an instantaneous contact model with several finite duration contact models.

Vibro-Impact Non-Linear Energy Sink (VI-NES) Practically, the design of VI-NES is identical to impact dampers. However, the studies related to VI-NES are often more theoretical and focus on the non-linear dynamics of the vibro-impact system. This will be developed later in this paragraph. The non-linear part is realized using a mass free to oscillate in a cavity. Like impact dampers, VI-NES are used for vibration reduction purposes. As illustrated in figure 1.10, the studies dealing with VI-NES mostly consider S-DOF structures embedding a VI-NES. The same applies to experimental works that use a main structure made of spring-mass elements in order to reproduce the behavior of a S-DOF

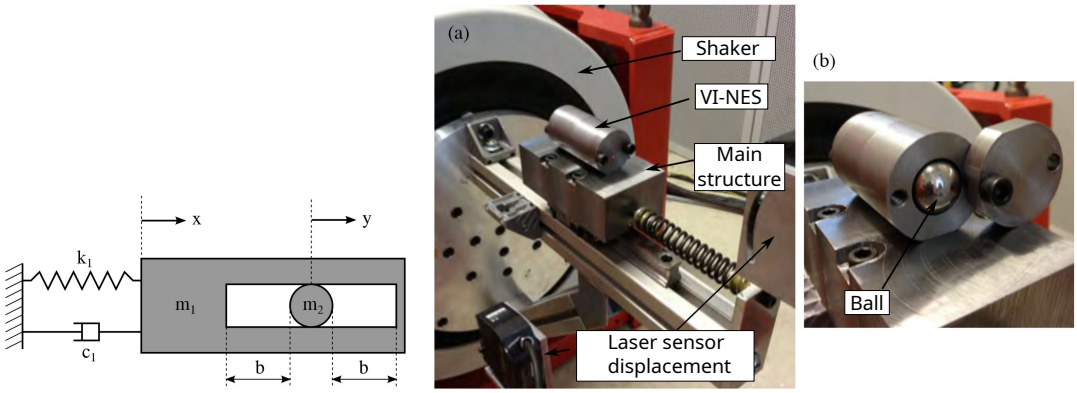

(a) Model of a S-DOF structure embedded with a VI-NES.

(b) Experimental set-up made of a spring-mass element structure endowed with the VI-NES.

Figure 1.10: Illustration of a VI-NES attached to a S-DOF structure, from Gourc et al. [43].

structure. Sometimes however, building models with finite number degrees of freedom are considered like in figure 1.11. Indeed, a promising application for VI-NES concerns the field of earthquake protection.

As explained earlier in this chapter, even if the design of VI-NES and impact dampers are very similar, the scientific objectives related to VI-NES are often more theoretical and focus on the non-linear response of the system. To start with, let us consider a S-DOF system with a mass m, a stiffness k, and a damping coefficient c excited by an external force F_{ext} endowed with a VI-NES. Its equation of motion is:

$$m.\ddot{x} + c.\dot{x} + k.x = F_{ext} + F_{VI}(x, \dot{x}); \tag{1.4}$$

where F_{VI} is the force applied by the VI-NES on the system. The equation of motion of the ball is:

$$m_b.\ddot{x}_b = -F_{VI}. \tag{1.5}$$

The force applied by the VI-NES on the system F_{VI} depends on the relative position and velocity of the ball in the cavity. While the contact conditions are not reached, $F_{VI} = 0$, otherwise $F_{VI} \neq 0$ and its exact value depends on the contact model chosen. Therefore, because of the contact conditions, the global behavior of the main system is non-linear and no easy solutions are known for the system with the VI-NES. Accordingly, many studies dealing with VI-NES pursue the objective to solve the non-linear dynamic problem obtained with the VI-NES, in order to predict the response of the system, to better understand its working principle, and at the end to be able to optimize it [63]. Besides, equation (1.4) becomes a matrix equation in the case of multi-DOF systems, and is also more challenging to solve. Some existing methods to solve such problems will be briefly discussed in the following. In particular, the works adopting theoretical approaches address the question of the stability of the solutions determined [117]. Indeed, only stable solutions can effectively take place in reality. Moreover, particular solutions are sometimes found, such as periodic solutions, quasiperiodic solutions, or even chaotic solutions [44]. Some of them are illustrated in figure 1.13. Actually, we will see later that these categories of solutions are related to the performance of the VI-NES. Therefore, they are of particular interest. In addition, the conditions to obtain such solutions and more precisely the Targeted Energy Transfer (TET) that corresponds to the optimal operating regime are studied

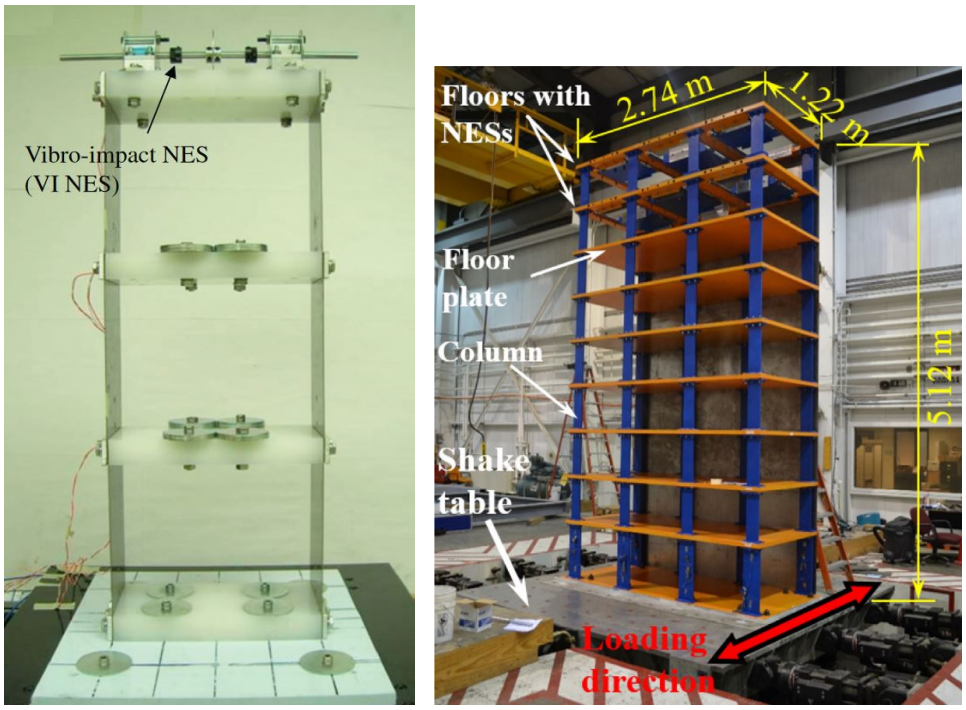

(a) Three-story model building [95]. (b) Nine-story model building [83].

Figure 1.11: Examples of VI-NES applied on models building.

[74, 96]. The more recent studies rely on the comprehensive works that was proposed in the past few years to tackle the problem of the optimal design of a VI-NES [74, 145, 6].

In order to determine the solutions of the dynamic system, several approaches are possible and the review [64] discussed the different possible methods in the section 2.4 of the article. Since the equation of the dynamic system is a non-linear ordinary differential equation, a common way to compute the solution of the equation is to proceed to time integration. The results are very accurate, and the method is relatively easy to implement since ordinary differential equation solver are available. Usually, the Runge-Kutta scheme is used, while others may be used and have their proper advantages and drawbacks[1]. However, the major drawback of this approach is its high computational cost. Consequently, if large parametric studies are required, the computation time might become prohibitive. Moreover, the numerical integration scheme as well as the time step should be chosen carefully in order to ensure convergence of the algorithm and accurate results. Indeed, vibro-impact problems have a non-smooth non-linearity that may be hard to deal with for the time integration program. Some discrepancies related to non-conservation of the energy of the system may also be observed in the case of an ill-defined time-step and integration scheme [103, 102]. The interested reader can also refer to the work of Acary et al. [2]. Others widely employed technique are the perturbation methods. They are a class of methods that help to find approximate solutions considering a simplification of the initial problem. One of them is the method of multiple scales that consists in introducing fast time scale and slow time scale variables for the time variable, and to consider that they are independent. For instance, this method is widely used in the following

[1] In Matlab for instance, the most common solvers are ODE45, ODE23, ODE23t. For more details, see https://www.mathworks.com/help/matlab/math/choose-an-ode-solver.html

studies in the case of S-DOF systems [44, 74, 145]. When periodic solutions are expected, the Harmonic Balance Method (HBM) is suited. It consists in assuming that the solution of the non-linear dynamic system is a sum of sine and cosine terms. The accuracy of the solution depends on the number of harmonics considered in the solution. Although the HBM can deal with strongly non-linear systems, it approximates only the steady-state responses [64]. Even though VI-NES do not always exhibit periodic responses, some papers rely on the HBM to predict the response of their system [128]. Very recently, special Harmonic Balance Methods are presented in [133] using Lagrangian multipliers for vibro-impact systems.

VI-NES have also been studied experimentally. The experiments are mainly dedicated to validate the existence of specific regimes predicted numerically [44], to validate particular analytical approaches aiming to predict complicated response of the VI-NES [72], or to demonstrate the existence of an optimal response already predicted numerically [74]. In these studies, harmonic and transient excitations corresponding to initial displacement of the system are considered. On the other hand, building models are considered [136, 83, 95] that are often related to earthquake protection application. Actually, the structures considered are multi-DOF systems, generally 2-DOF [136] or 3-DOF [95], but sometimes more [83]. Because of the underlying applications, the tests aim at assessing the effectiveness of the VI-NES for broad-band excitations corresponding to real seismic excitations, and more specifically to assess the robustness of VI-NES. In very recent studies, interesting energy-based approaches are adopted to quantify the role of the dissipation phenomena likely to occur in VI-NES [7, 49].

1.3 Technological benefits of vibro-impact based strategies

As presented before, many strategies are already available to tailor the vibrations that take place in everyday life structures. Although VI absorbers have interesting properties, they are still not widely used in industrial cases.

To begin with, since VI absorbers are passive devices, they have all the advantages related to such strategies, namely the robustness and safety. Moreover, VI absorbers are expected to have a constant performance even under temperature changes since the contact properties generally do not vary with temperature. Thus, it makes such strategies suited for harsh environments and aerospace applications. Furthermore, we will see that VI absorbers allow to mitigate the low frequency modes of the structure, which is sometimes difficult to achieve with traditional strategies. This point will be developed later in this manuscript. In the case of transient excitations, they perform vibration reduction on a fast time scale [63] compared to other traditional strategies. In addition, in the context of the current ecological issues, viscoelastic materials will probably be less used in the futur because of their carbon footprint. Since the realization of VI absorbers *a priori* does not require polymer materials, they could offer promising alternatives to usual technologies. In the same idea, their design seems to remain reasonably simple from the technological point of view, even if few realizations have taken shape for the moment. Thus, further experimental work needs to be done on this aspect. On the contrary, the practical realization of a cubic stiffness (widely used in the context of NES) is sometimes challenging, especially when very limited space is available to integrate the device on the main structure [45]. At last, the vibro-impact phenomenon is strongly non-linear. Therefore, the VI absorbers are also expected to have the benefits of NES, like a small added

mass compared to the main structure, and a low sensitivity to detuning. Nevertheless, non-linear phenomena are more complex to understand, simulate, and control. In order to take advantage of the vibro-impact phenomena for vibration mitigation applications, comprehensive works must be done to model, predict and experiment the behavior of vibro-impact based strategies.

1.4 Focus on the application of vibro-impact absorbers

The previous studies have listed some application fields, such as the limitation of the displacements of buildings submitted to earthquake excitations or for civil engineering structures likely to oscillate on their vibration modes [92]. Another promising application is the chatter control of the cutting tool during a turning process where interesting experimental realizations have already been proposed [45]. Indeed, since VI-absorbers need a minimal energy level to be activated, the instable vibration phenomena encountered in machining guarantees the activation of the device. Moreover, VI absorbers can generate undesired noise due to the repetitive impacts, what is not a major drawback in machining applications. Besides, because of the potential insensitivity of VI absorbers to environmental conditions, such strategies could be suited for applications where these conditions are likely to vary. For example, the integration of oscillating balls in a brake pad that undergoes high temperature changes is proposed in [58] for brake squeal attenuation. Rare other realizations concern industrial structures such as blades and vanes for damping purposes [50]. These two examples are illustrated in figure 1.12. More generally, the technological simplicity and the little space required for VI absorbers make them promising solutions for applications with high restrictive constraints, such as in the transportation sector in general.

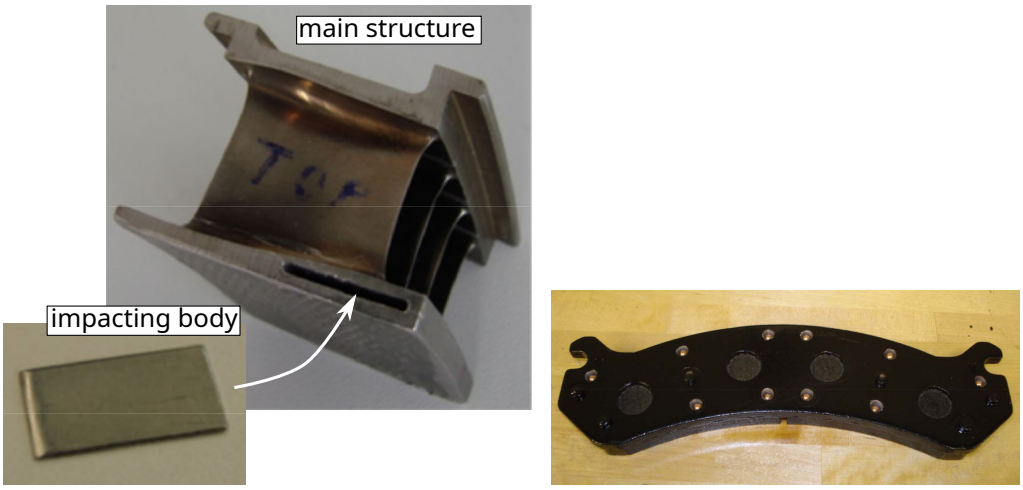

(a) Frictional impact damper integrated in a blade [50].

(b) VI dampers integrated in a brake pad for brake squeal attenuation [58].

Figure 1.12: Examples of realizations using VI and impact absorbers.

1.5 Earlier results and scientific opportunities on vibro-impact absorbers

The objective of this section is to provide a brief state of the art concerning VI absorbers, mentioning the major results already known in order to justify the approaches adopted in this PhD thesis. For the sake of clarity, this section is kept relatively short and the bibliography on the different topics will be more detailed in the corresponding chapters of this manuscript.

To start with, some of the authors interested in employing vibro-impacts for vibration reduction have addressed the question of the optimization of a VI absorber [74, 105, 145, 49]. The case of harmonic excitations has been the most covered. In this case, the existence of two main specific regimes have been raised. They definition is based on the number of impacts per period: the regime with two impacts per period of the excitation, and the Strongly Modulated Regime (SMR) when less than two impacts per period occur. This regime is observed in [41] in 2007, and it is called *Stronlgy Modulated Regime* or *SMR* for the first time in [121] in 2008. SMR refers to a regime where the amplitude of oscillation of the main structure alternates regularly between high and low amplitude. In other terms, the maximum and minimum amplitudes are significantly different from the mean amplitude. On the contrary, in the regime with two impacts per period, the response of the main structure is almost periodic, the amplitude does not vary over time. These two regimes are illustrated in figure 1.13. Understanding the occurrence of these regimes is a critical aspect in the perspective of an optimization process of a VI absorber, since the optimal point leading to the best vibration reduction is at the limit between these two regimes [74], where the optimal and irreversible Targeted Energy Transfer takes place. These two families of regimes can be extended, and the interested reader will find further developments in [73]. Up to now, these results have essentially been reported numerically, and experimentally in the case of S-DOF structures for harmonic and transient excitations. Besides, numerical studies dealing with continuous structures like beams have drawn the same conclusions [128], even if no experimental validation has

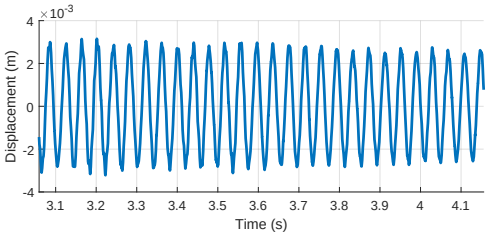

(a) Displacement of the main structure during the regime with two impacts per period.

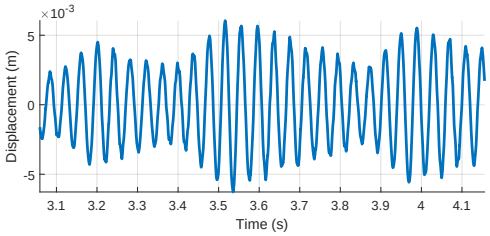

(b) Displacement of the main structure during the SMR.

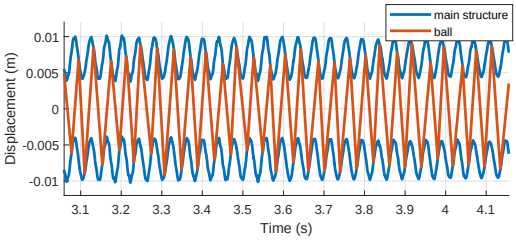

(c) Displacement of the ball within the main structure during the regime with two impacts per period.

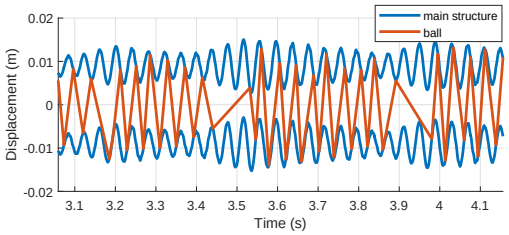

(d) Displacement of the ball within the main structure during the SMR.

Figure 1.13: Illustration of the regime with two impacts per period and the SMR based on simulation results.

been proposed yet. Consequently, more complex structures should be studied in order to generalize the previous results, and to derive optimization rules for VI absorbers.

Furthermore, at least two assumptions are presented in the literature to explain how vibro-impacts help to dissipate the vibrational energy. On the one hand, an assumption is that dissipation occurs during the contact phases, and the energy is dissipated throughout the successive impacts. According to [145], energy dissipation and Targeted Energy Transfers can only be achieved in the case of dissipative impacts. Therefore, such observations raise the question of the experimental characterization of vibro-impact phenomenon. On the other hand, because of the non-linear behavior of vibro-impacts, other studies claim that a multi-modal structure undergoing vibro-impacts is submitted to modal energy exchanges. These energy transfers turn out to be beneficial to the vibrational energy dissipation that occur even in the case of perfectly elastic and non-dissipative impacts [128, 48], what is inconsistent with the previous observation. Therefore, the role of the two previous assumptions should be inquired both numerically and experimentally. Moreover, such energy transfers are not likely to occur in S-DOF systems. Since almost no experimental studies tackle the case of continuous and multimodal structures, further work must be done in that way in order to study the physical phenomena at stake in vibro-impacts in parallel of numerical investigations.

To summarize, some results on the optimal design of VI absorbers are available, but they essentially concern simple structures. Furthermore, there is still a lack of experimental validation for more complex systems. Besides, two main physical phenomena seems to play an important role in vibro-impact devices: the energy dissipation during impacts, and modal energy transfers. Accordingly, further experimental and numerical work should be done to better understand both phenomena, and the role they play in the performance of VI absorbers.

1.6 Objectives and structure of the PhD

1.6.1 Scientific objectives of the PhD

Based on the earlier works dealing with vibro-impact based strategies for vibration mitigation application, the objectives for further investigations have emerged. Therefore, the objectives pursued in this PhD thesis are described below.

1st Objective: measure and characterize vibro-impact phenomenon A major field that still needs to be explored concerns experimental investigations dealing with vibro-impact. Since the physical phenomena at stakes are not clearly identified yet, comprehensive works must be done in this direction. More specifically, in vibro-impact systems classical instrumentation cannot be used on the flying mass in general. Therefore being able to characterize the contact properties and the vibro-impact phenomenon is still a challenge. Though, it remains a critical point to well understand the physics of vibro-impact and to be able to build representative models of the phenomenon.

Accordingly, the first objective of this PhD is to propose a method to measure the displacement of the ball in a vibro-impact system and to characterize the vibro-impact phenomenon.

2nd Objective: inquire the effect of a VI absorber on a multimodal structure Moreover, previous experimental studies are mostly focused on S-DOF structures, or sometimes on multi-DOF structures. Even if this helped to obtain interesting results related to the behavior of a simple structure embedded with a VI absorber, more realistic structures should be considered in order to come closer to industrial structures that may exhibit a more complex behavior. In particular, the literature mentioned that multimodal structures have an important role to play, because of the energy transfers that are observed in the presence of vibro-impacts. Such modal energy exchanges cannot occur in a S-DOF structure.

Hence, the second objective of this PhD is to experiment VI absorbers on continuous and multimodal structures to inquire the results already established in the case of simpler structures. Two sub-objectives are involved. The first one consists in the design and realization of an effective VI absorber that can be easily integrated to the structure. The second one concerns the effectiveness of the VI absorber in the case where the main structure is submitted not only to harmonic excitations, but also to broadband excitations.

3rd Objective: take advantage of multiple VI absorbers to improve VI absorber performance Then, we will see throughout this manuscript that even if we obtained very promising results demonstrating the ability of a VI absorber to tackle vibration issues, using a single VI absorber can lead to some limitations.

Consequently, the third objective concerns the use of multiple VI absorbers on a three-dimensional structure in order to improve the robustness and the effectiveness of the VI absorbers. Like previously, it involves a sub-objective related to the design and the realization of smaller VI absorbers.

4th Objective: assess the importance of the modal energy transfers on the effectiveness of the absorber At last, the literature is sometimes ambiguous concerning the physical

phenomena at stake during vibro-impacts. Indeed, it is well-known that vibro-impacts dissipate energy, while no consensus is reached on the way the energy is dissipated: both dissipative impacts and modal energy exchanges seem to play an important role. Accordingly, the fourth objective is to assess the importance of the modal energy transfers highlighted in the literature on the effectiveness of the absorber.

1.6.2 Content and structure of the manuscript

The research work presented in this PhD thesis deals with the development of vibro-impact based strategies for vibration reduction purposes. The objectives listed above are addressed in this work throughout the following chapter.

In chapter 2, a new methodology for motion reconstruction of a vibro-impact system is presented. For this purpose, a Digital Image Correlation process is performed associated to full-field measurements realized by a high speed camera. Based on this non-contact technique, we reconstruct the continuous displacements of both the ball and the main structure from the discrete displacements. Doing so, the Coefficient of Restitution and the friction forces acting on the ball during the free flight phases are determined.

The results of this chapter are published in *Mechanical Systems and Signal Processing, Volume 156* entitled *Full-field measurements with Digital Image Correlation for vibro-impact characterisation*, and were presented in the international ISMA conference in 2020 [26].

Chapter 3 concerns experimental investigations of a cantilever beam endowed with a VI absorber. We designed a VI absorber with tunable gap, allowing to perform parametric studies. The influence of both the gap and the excitation amplitude are explored, and interesting vibration reduction is achieved. Moreover, the two specific regimes (two impacts per period and SMR) described above are found, and their role related to the performance of the absorber is confirmed. These results concern both the first and the second mode of the beam. Then, the response of the beam and the VI absorber are also studied under white noise excitations, demonstrating the effectiveness of the absorber and providing new results for non-harmonic excitations. Moreover, the limitations of using a single VI absorber are highlighted.

The results of this chapter are published in *Mechanical Systems and Signal Processing, Volume 180* entitled *Experimental investigations of a vibro-impact absorber attached to a continuous structure*, and presented in the international IMAC conference in 2022.

Chapter 4 addresses the question of the energy balance of a beam with a VI absorber embedded through a numerical approach. More specifically, the dynamics of the beam is projected onto a modal basis, and the energy transfers within the modal space are quantitatively assessed. To achieve this, a model of an Euler-Bernoulli beam is proposed and solved semi-analytically, allowing to derive exact energy balances. Therefore, the energy taken from the excited mode and the energy received by each other mode is computed. In order to deal with the widest range of situations, the cases of an excitation centered on the first, second and third mode are considered. In particular, the energy received by the lower modes is studied, since it could be detrimental to the vibration reduction.

At last, chapter 5 is devoted to the application of VI absorbers to a three-dimensional structure. For this study, a model plane is considered. First and foremost, a numerical method is proposed in order to simulate the response of a three-dimensional structure submitted to vibro-impacts. The finite element model of the structure is built, then the matrices of the dynamic system are extracted in order to add the vibro-impact force directly in the equation of motion of the system. Then, the response is calculated using time integration. Secondly, the response of the model plane equipped with one VI absorbers is investigated experimentally. Although interesting performance is achieved, we strive to highlight the limitations met using a single VI absorber. Therefore, multiple VI absorbers with tunable gap are designed and realized, with the drive to change the localization of the VI absorbers handily. The benefits drawn from this approach are presented. In particular, a procedure to achieve multimodal effectiveness is proposed.

Some of the results of this chapter were presented during the national CSMA conference in 2022 [25].

Chapter 2

Full-field measurements with Digital Image Correlation for vibro-impact characterization

Contents

Preamble

In the first chapter, we have evidenced that several models are available to describe impact phenomenon. However, determining the correct parameters of these models for a device undergoing vibro-impacts may be challenging. Indeed, traditional measuring devices such as accelerometers or vibrometers cannot be used on the oscillating ball. Therefore, this chapter is dedicated to present a non-contact technique based on a high-speed

camera and a Digital Image Correlation (DIC) process allowing to reconstruct the displacement of both the ball and the structure in order to characterize vibro-impact phenomenon.

2.1 Introduction

The effectiveness of VI absorbers in mitigating the vibrations relies on the interactions between the oscillating mass and the main structure that occur during the impacts. Mostly, two assumptions emerge to explain energy dissipation: contact effects such as plastic deformation during the repeated impacts [115] or viscous damping during the contact phase [20] on the one hand, and dynamic effects leading to a high frequency energy transfer and to a faster vibration mitigation [128] on the other hand. In the last case, the vibrational energy of the main structure is redistributed within the modal space from low to high modes that possess higher energy dissipation efficiency.

To better understand the physics of VI phenomenon, it is interesting to adopt an experimental approach. However, several difficulties must be overcome. Impact phenomenon is non-linear, and occurs on a very short time scale, making its study particularly challenging. Moreover, VI absorbers are often difficult to equip with measuring instruments, especially for the free oscillating masses. Using accelerometers on a non-linear structure may also modify the dynamics of the structure in a complex manner [140]. Therefore, non-contact techniques could offer an interesting alternative. Among these techniques, DIC has many interests for VI study to measure the displacements that cannot be measured with an accelerometer nor a laser vibrometer. Indeed, a low level of noise is generated using this method (accuracy is below pixel size) and combined with a high-speed camera, it becomes possible to capture the dynamic behavior of a VI system. In solid mechanics, DIC and full-field measurement techniques have paved the way to new approaches to measure displacement, velocity or strain field and have a growing interest thanks to the advent of high-speed cameras that allow to get pictures even for dynamic system with short typical variation time. Many applications are found for dynamic testing in combination with high-speed or ultra-high-speed cameras [107]. This enables the visualization of transient deformation [130], the development of local deformation [17, 124], or phase transformation during dynamic test on shape memory alloys [114]. Moreover, measuring 3-D displacement field becomes possible if two cameras are used [107].

The purpose of this chapter is to take advantage of these methods to reconstruct the motions of both the main structure and the oscillating mass, and to compare different contact modelling strategies.

Full-field measurement techniques have already been set up in the context of granular materials to measure the coefficient of restitution of impact between particles, and between wall and particles, combined with different methods. In the following articles, authors have built a special apparatus to film the collision between particles or between a particle and a wall with a high-speed camera. In [54], [141] and [34], the authors can calculate the COR from the height of the rebounds or free flights duration of the particle. These quantities are directly derived from the images obtained from the high speed cameras. In [137], the COR is calculated with the averaged velocities obtained by the displacement over the duration between successive images. Other authors like [51] and [52] have used an energetic definition of the COR and need both translational and rotational

velocities of the particle. In the first case, the authors have used the Image Pro Plus software to track the particle and calculate the velocities. In the second case, the locations and velocities of the particle are determined using a particle tracking velocimetry method. In all these cases, calculations are made to obtain the velocities necessary to obtain the COR: they are obtained from the measure of the height of rebound, from the duration between impacts, or from the simple ratio of displacement and duration between images. But the entire motion of the particle is not considered, and this can result in a lack of accuracy if only considering the experimental data just before and after impact. The total motion of the particle provides accurate information to estimate displacements and velocities, especially in the case of noisy measurements. This statement is the basis of the method that is presented in this chapter.

In the field of vibro-impact, full-field measurement with a high speed camera has been used in [108] to visualize VI regimes between gears. According to the authors, the video post-processing allows to measure the instantaneous position of the gears from the shape recognition. Recently, a simple method using limited experimental information to reconstruct the motions of the oscillating mass of a VI absorber and measure the COR has been presented in [75]. The authors used a laser sensor and an accelerometer to measure the position of the main structure and its acceleration respectively. From this, the velocity of the main structure can be derived, and the impact time is given by the discontinuities on the acceleration signal. Knowing the position of the oscillating mass at impact, its motion can be reconstructed assuming a friction coefficient between the oscillating mass and the main structure. Nevertheless, the motion of the oscillating mass is not directly measured as no visualization of the ball is possible. Thus, no information about the friction coefficient can be provided from this experimental set-up. Moreover, the uncertainty on the friction coefficient leads to uncertainty on the velocity estimation, necessary to calculate the COR. At last, the authors noticed a different coefficient of restitution on the left and right sides of their VI absorber prototype, which is an interesting but unexplained phenomenon. The same observation is reported here.

In this chapter, a dedicated set-up has been designed composed of a ball oscillating in a cavity, reproducing the behavior of a vibro-impact absorber. A method is proposed to reconstruct the motion of the oscillating mass and the main structure using DIC with a single high-speed camera. This method is used to reach the two following objectives. Firstly, evaluate the performance of DIC for experimental VI characterization, and secondly, use measurements as input in two modelling strategies based on the coefficient of restitution and on a Hertzian contact.

The tracking of the displacement of the main structure and the oscillating mass is realized. Models are assumed for the displacement of both the ball and the structure, and their parameters are identified from curve fitting. The advantage of this is that the velocities can be easily and accurately obtained by analytical derivation without amplifying the noise. Then, these results allow to characterize the VI absorber and are used as inputs to run simulations of the COR model and Hertz damped contact model.

This chapter is organized as follows. Section 2.2 describes the experimental set-up designed for this study, presents the DIC technique and the post-processing of measurements. Section 2.3 presents the modelling of the VI problem, and the identification of some of its parameters. Section 2.4 presents the numerical results. In section 2.5, uncertainties on the COR are discussed.

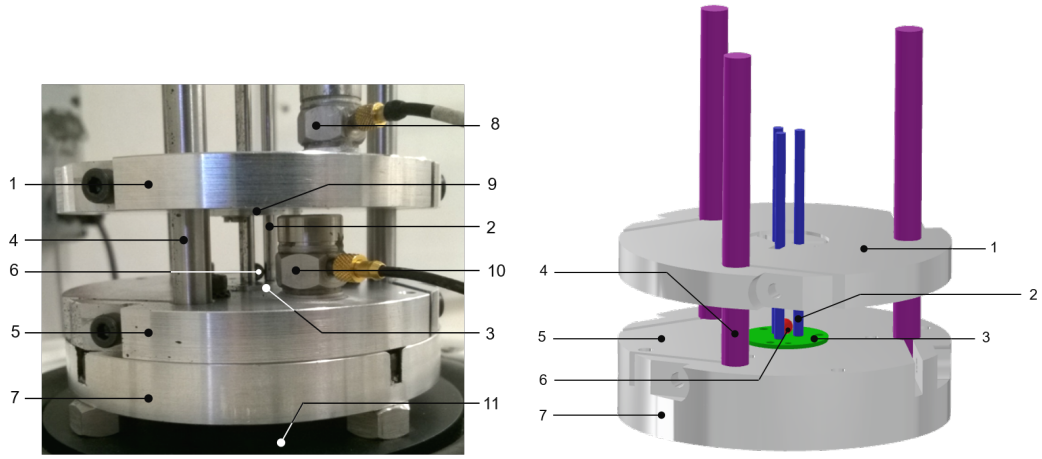

(a) Photo of the experimental set-up.

(b) CAD view.

Figure 2.1: Experimental set-up. 1. Upper plate; 2. Guiding rod; 3. Lower disk shaped part; 4. Holding rod; 5. Lower plate; 6. Ball; 7. Adapter plate; 8. Upper accelerometer; 9. Upper disk shaped part; 10. Lower accelerometer; 11. Shaker.

2.2 DIC for VI measurement

2.2.1 Design of a set-up and instrumentation

For this study, an experimental set-up consisting of a ball enclosed between two plates has been designed (figure 2.1). More details on the materials and dimensions are given in appendix A.

The main structure is made of two plates separated by an adjustable distance and maintained by three holding rods. The structure is rigid enough to ensure that the first natural frequencies cannot be excited in the frequency range of the tests [22 Hz - 30 Hz]. For this purpose, the set-up was designed using numerical modal analysis. The ball is guided to ensure vertical motion by three guiding rods, so that it is possible to visualize the entire motion of the ball during its oscillation. The main structure has a sine wave motion imposed by a Dataphysics shaker (1000 N maximum sine force peak). An adapter plate has also been used to fasten the set-up on the shaker.

Two accelerometers are stuck on each plate to monitor the acceleration of the plates and analyze the impact signals. A high speed camera with a 1000 fps frame rate is used during the test to visualize the oscillation of the ball between the two impact plates. Some photos extracted from the videos are represented in figure 2.2, where it is possible to see the ball going up, colliding the upper plate and going down.

2.2.2 Description of the experiments

Different parameters were varied during the experiments, namely the frequency of the excitation and the displacement magnitude of the shaker. These different parameters are summarized in table 2.1. Each test was run once and successively. One test lasts approximately 1,5 seconds, producing 1500 frames to analyze. The frequency and the acceleration of the shaker were chosen in order to obtain VI regimes with two impacts per cycle, one on the upper plate and one on the lower plate.

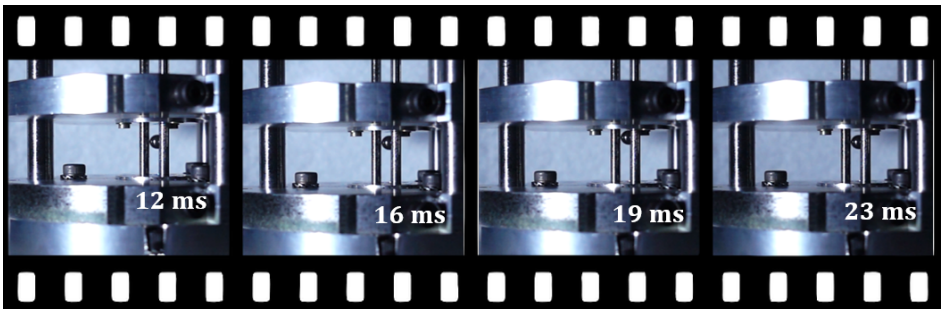

Figure 2.2: Images extracted from the video recorded with the high-speed camera.

Test number	f_{exc}	Displacement magnitude
Test 1	$22\,Hz$	$27\,mm$
Test 2	$22\,Hz$	$35\,mm$
Test 3	$22\,Hz$	$21\,mm$
Test 4	$30\,Hz$	$27\,mm$

Table 2.1: Parameters for the tests.

2.2.3 Digital Image Correlation and motion reconstruction

In order to reconstruct the motion of the main structure and the motion of the oscillating ball, a Digital Image Correlation (DIC) technique is used to follow the motions of both the ball and the structure. Two zones containing a mesh of points are defined corresponding to the ball and to the main structure (see figure 2.3). A 30 pixels wide centered on each point of the mesh is defined. After the displacement, the subset is localized in the new picture thanks to a cross-correlation calculation. The principle of the cross-correlation to determine the displacement of a subset in an image is as follows. Let's consider two subsets: the reference subset, or subset 1, and the current subset, or subset 2. In the present case, each subset contains 30×30 pixels and each pixel is represented by a gray level intensity. Let's call $I_1(x,y)$ the function that gives the gray level intensity of the pixel of coordinates (x,y) belonging to the reference subset (x and y represent a number of pixels), and $I_2(x,y)$ the same function for the current subset. The Zero-mean Normalized Cross Correlation function used in Matlab is defined as [16]:

$$\gamma(d_x,d_y) = \frac{\sum_{i,j}[I_1(x+i,y+j)-\bar{I}_1][I_2(x+d_x+i,y+d_y+j)-\bar{I}_2]}{\sqrt{\sum_{i,j}[I_1(x+i,y+j)-\bar{I}_1]^2}\sqrt{\sum_{i,j}[I_2(x+d_x+i,y+d_y+j)-\bar{I}_2]^2}}; \tag{2.1}$$

where i,j scan all the pixels of the subset, $\bar{I}_1$ and $\bar{I}_2$ are the average intensity of the pixels in the considered subset (1 or 2), d_x and d_y represent the displacements to determine: they must correspond to the maximum of the cross-correlation function. This criterion is nonsensitive to intensity variations between the reference and the current subset, as it is normalized with averaged intensity. Therefore, the displacements of each point of the mesh is obtained (see figure 2.4). In the present case, as no deformation is expected, the displacement of the ball and of the main structure are calculated as the average displacement of the points of each mesh. Knowing the length of the cavity, it is possible to deduce the displacement of the upper and lower plate, and to position them relatively to the ball displacement. Such results are presented in figure 2.5.

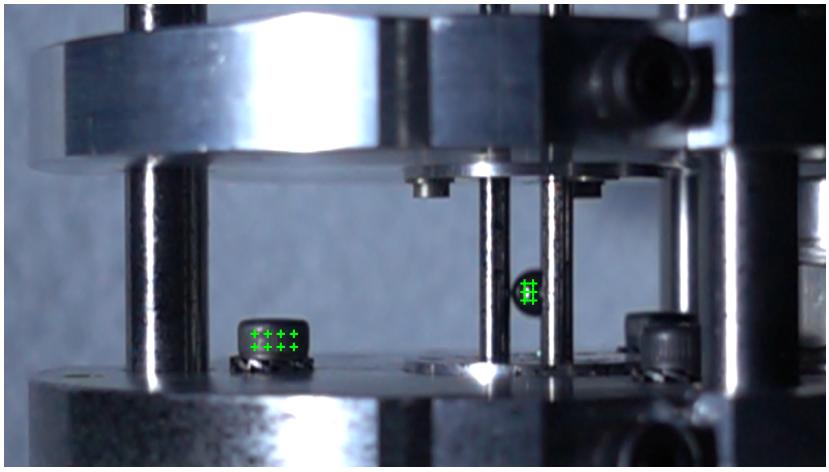

Figure 2.3: Mesh of points used for the DIC.

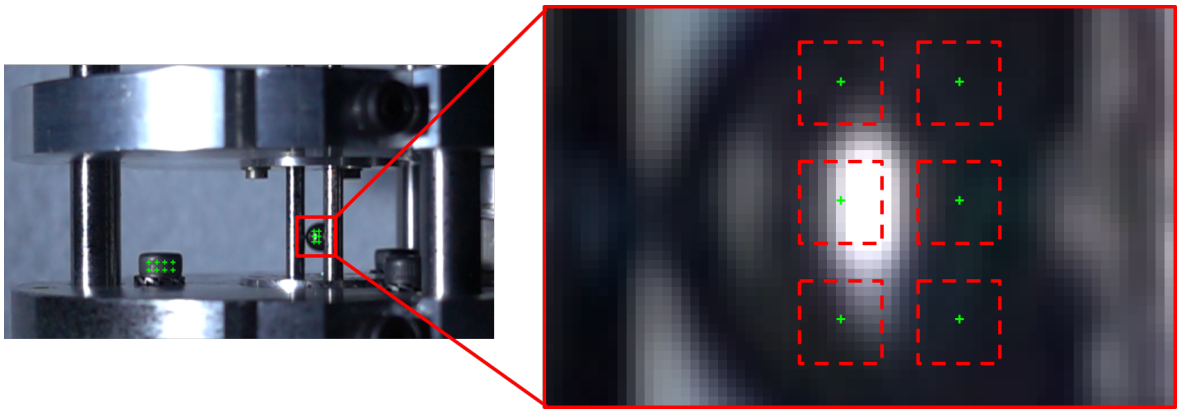

(a) Meshes for DIC: general view.

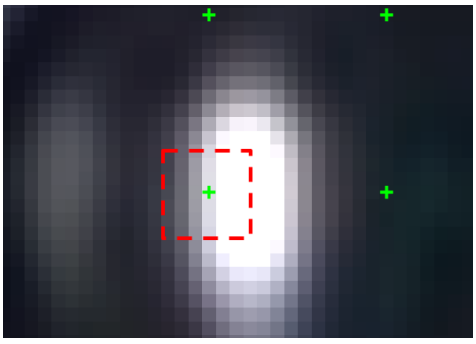

(b) Reference configuration.

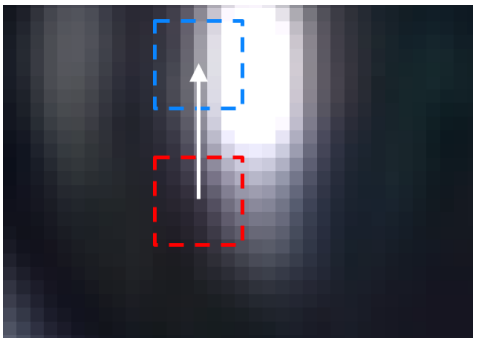

(c) Configuration after displacement.

Figure 2.4: Principle of DIC. (a) and (b) red squares: subsets. (c) Red square: reference subset. Blue square: matched subset after displacement. White arrow: displacement vector.

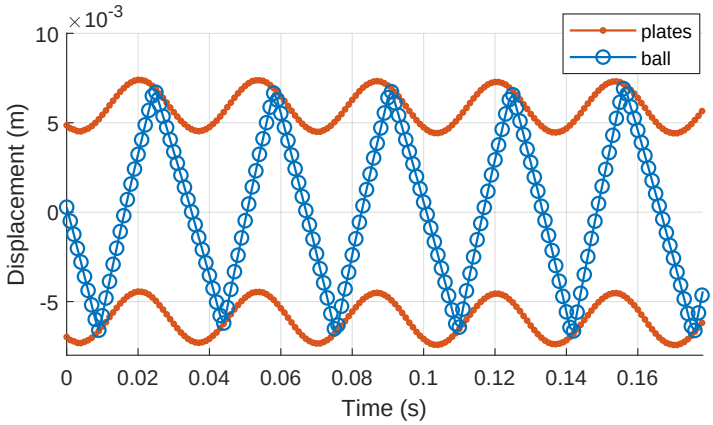

Figure 2.5: Experimental displacements obtained from DIC.

2.2.4 Signals from accelerometers: post-processing

Two accelerometers were stuck on each plate, (see figure 2.1a) during the dynamic tests. They were used to monitor the acceleration of the main structure on the one hand, and to study the post-impact vibrations in the frequency domain on the other hand.

Typical acceleration signals recorded by the accelerometers are shown in figure 2.6a. The sampling frequency is 50 kHz. One can clearly distinguish the low frequency sine wave acceleration corresponding to the excitation of the shaker, and the repeating pattern of high frequency vibrations due to the impacts of the ball on the structure. In order to analyze the frequency content of the impact signals, it is necessary to focus especially on the high frequency content of the acceleration signals. Therefore, the following method is applied. To begin with, signals are filtered using a high-pass filter with a 100 Hz cut-off frequency to remove the low frequency excitation (see figure 2.6b). The frequency of the excitation is no more than 30 Hz. Next, each transient vibration due to impact is isolated considering a signal length equal to a half-period of the excitation signal. The Fourier transform of each impact is calculated using a Fast Fourier Transform method, and the results in the frequency domain are averaged using all the impacts recorded on both the upper and lower plates. At the end, figure 2.7 represents $\frac{1}{N}.\sum_{k=1}^{N}\hat{\gamma}_k(\omega)$, where $\hat{\gamma}_k(\omega)$ is the Fourier transform related to the signal from the k-th impact. The frequencies in the Fourier spectrum in figure 2.7 may correspond to the natural frequencies of the structure. This can be explained considering energy transfer between the ball and the main structure. In [128], the authors have shown numerically that when using a VI absorber at a beam end excited on its first mode, the activation of the VI absorber leads to excitation of higher vibrational modes of the beam. This non-linear behavior can be interpreted as a high frequency energy transfer: the energy initially localized on the first mode of the beam is transferred to higher modes because of impacts. A similar phenomenon is probably observed here, even if it was not confirmed by further analyses: an experimental modal analysis was difficult to perform because of the impact location that is impossible to reach with a classical hammer, and modes identification using a numerical modal analysis turned out to be difficult because several modes are located in a same frequency range. Nevertheless, the Fourier transform obtained in figure 2.7 demonstrates the excitation of the structure due to the vibro-impacts.

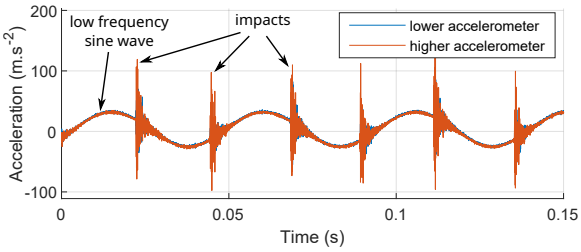

(a) Acceleration signals before filtering.

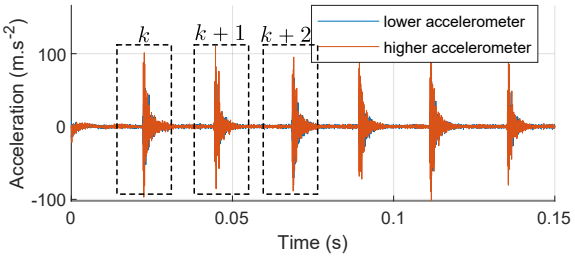

(b) Acceleration signals filtered.

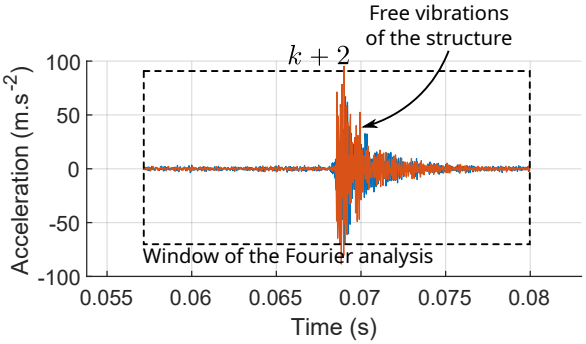

(c) One impact signal isolated.

Figure 2.6: Post-processing of acceleration signals.

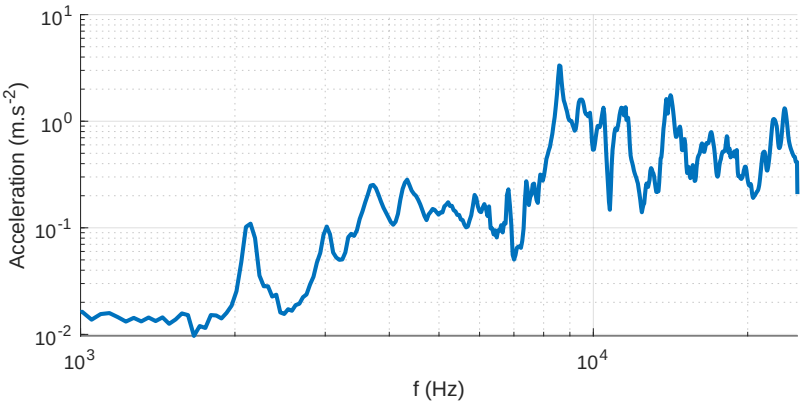

Figure 2.7: Average Fourier transform of all the impact signals : $\frac{1}{N}.\sum_{k=1}^{N}\hat{\gamma}_k(\omega)$.

2.3 Vibro-impact modeling and parameter identification

2.3.1 Modeling and parametrization

A scheme of the experimental set-up studied in the previous section is represented in figure 2.8. In [117] the authors have analyzed the influence of gravity on stability conditions for the same device as the one studied here. Even if stability conditions are out of the scope of this paper, the equations of motions are the same as in the present case.

$Y_s(t)$ and $Y_b(t)$ denote the position of the main structure (i.e the cavity) and the ball, respectively. The total distance travelled by the ball in the cavity is $2.b$. As the excitation signal of the shaker is a sine wave motion, the displacement of the main structure is supposed to be given by equation (2.2):

$$Y_s(t) = A.\sin(\omega.t + \varphi) + B; \tag{2.2}$$

where A is the amplitude, ω is the pulsation, φ is the phase term and B is the offset, what seems to be in accordance with the experimental displacements of the plates shown in figure 2.5.

The motion of the ball can be separated into two phases: the free flight phase and the contact phase. Looking closely at figure 2.5, the displacement of the ball is not perfectly linear during the free flight phases. It makes sense as the ball is submitted to gravity because of its vertical motion. Therefore, its displacement is assumed to be quadratic with respect to time and given by equation (2.3)

$$Y_b^i = a_i.t^2 + b_i.t + c_i; \qquad t \in [t_i; t_{i+1}]; \tag{2.3}$$

for the i-th free flight phase.

With such a model, constant forces acting on a ball are represented such as weight and friction, and the of motion governing the displacement of the ball is:

$$m_b.\ddot{y} = -m_b.g + F_{friction}; \tag{2.4}$$

where m_b is the mass of the ball, g is the acceleration of gravity, and $F_{friction}$ represents the friction force that may apply on the ball when sliding in the cavity. Here, inertia of the ball is neglected and it is assumed to be a point mass.

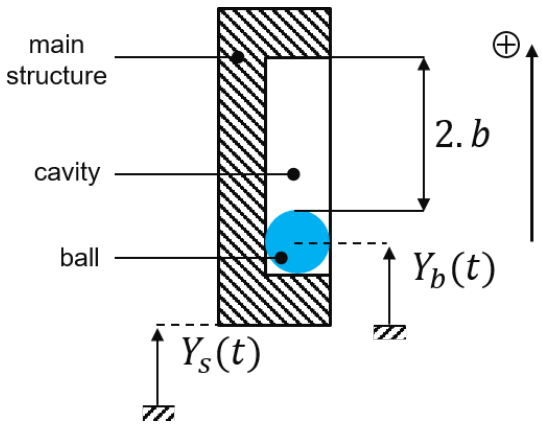

Figure 2.8: Illustration of the VI absorber.

2.3.2 Contact modelling strategies

Two contact models are used here: the first one is based on the COR, and the second one is a Hertz-damped contact model. In the first approach, the contact phase is assumed infinitely short, and the physical phenomena that occur during impact are wrapped in a coefficient of restitution e defined in equation (2.5) that traduces the energy loss during the impact: $e = 1$ represents perfectly elastic impacts (no energy is dissipated during the impact), while $e = 0$ represents perfectly inelastic impacts (there is no restitution of energy after the impact, the solids remain in contact). Therefore, each time an impact occurs, the relative speed before and after impact are related by the following equation:

$$\dot{Y}_b^+ - \dot{Y}_s^+ = -e.(\dot{Y}_b^- - \dot{Y}_s^-); \tag{2.5}$$

Practically, the problem is reduced to free flight phases (see equation (2.4)), with an initial condition for $\dot{Y}_b$ given by equation (2.5).

In the second approach, the contact phase is governed by the Hertz damped contact model. So the contact force applied on the ball depends on the interpenetration δ defined as

$$\delta = Y_b - Y_s - b \qquad \text{if} \qquad Y_b - Y_s \geq b; \tag{2.6}$$

$$\delta = Y_b - Y_s + b \qquad \text{if} \qquad Y_b - Y_s \leq -b. \tag{2.7}$$

In the case of a sphere in contact with a plate, the contact stiffness K considered here is the one given by the Hertz model and defined as

$$K = \frac{4.R^{1/2}}{3.\pi.(k_b + k_s)}; \tag{2.8}$$

where the subscripts b and s denote the ball and the structure, respectively, and $k_i = \frac{1-\nu_i^2}{\pi.E_i}$ ($i \in \{b, s\}$). The contact force of the Hertz damped model is

$$F_{contact} = -K.\delta^{3/2} - c.\dot{\delta}; \tag{2.9}$$

in accordance with the sign convention of figure 2.8, and δ is defined by equation (2.6) and equation (2.7). In equation (2.9), c is the damping coefficient. As it will be explained later, c can be chosen to represent the same energy loss than the one represented by the COR e.

This time, the contact duration is not neglected and the equation of motion that governs the motion of the ball during the contact phase is

$$m_b.\ddot{Y}_b = -m_b.g + F_{friction} + F_{contact}. \tag{2.10}$$

The entire motion of the ball can be simulated using an ODE solver to integrate the equation of motion given by equation (2.4) for the COR model, or equation (2.10) in the case of the Hertz damped contact model.

As the COR model traduces the energy loss by the system during the impact, the Hertz damped model must be able to represent the same dissipation. In the Hertz damped contact model, the dissipation is due to the damping coefficient c. Indeed, this contact damping creates an opposing force to the ball displacement that contributes to slow down

the ball and implies an irreversible kinetic energy loss. In [91], Nagurka et al. provide an approximation that relates the damping coefficient and the COR so that the COR model and a Hertz damped contact model lead to the same dissipation:

$$c = -\frac{2.\sqrt{\mathrm{K}_{lin}.m}.\ln e}{\sqrt{\pi^2 + (\ln e)^2}}; \tag{2.11}$$

where K_{lin} denotes the linearized contact stiffness for an average interpenetration δ_a defined as

$$\mathrm{K}_{lin} = \frac{3}{2}.\mathrm{K}.\delta_a^{1/2}. \tag{2.12}$$

2.3.3 Parameter estimation

In the previous section, discrete-time displacements of the ball and the structure are obtained thanks to the DIC method. In order to obtain velocities, many approaches are possible. In the context of DIC, some authors have used finite differences to estimate velocities and accelerations knowing the displacement field [61], but this method is noise sensitive and leads to inaccuracy in the process of velocity estimation. In order to reduce the uncertainties or to improve the spatial resolution of the results, others have used a method to regularize the displacement, taking into account a set of images instead of using only two pictures corresponding to the reference and deformed configuration [18]. The method used in this paper is to identify the parameters of displacement equations (equation (2.2) and equation (2.3)) from curve fitting using the experimental displacement points obtained from DIC method. As a result, A, B, ω and φ for the structure, and a_i, b_i and c_i for the ball are obtained minimizing the least-square functions:

$$\mathrm{A},\mathrm{B},\omega,\varphi = \arg\min_{\mathrm{A},\mathrm{B},\omega,\varphi} \sum_{k=1}^{\mathrm{N}} [\mathrm{Y}_s(t_k) - \mathrm{Y}_s^{exp}(t_k)]^2; \tag{2.13}$$

$$a_i, b_i, c_i = \arg\min_{a_i,b_i,c_i} \sum_{k=1}^{\mathrm{N}} [\mathrm{Y}_b^i(t_k) - \mathrm{Y}_b^{exp}(t_k)]^2; \tag{2.14}$$

where N is the length of time vector, Y_s^{exp} and Y_b^{exp} are the experimental displacements of the structure and the ball. The fitting displacements are represented in figure 2.9.

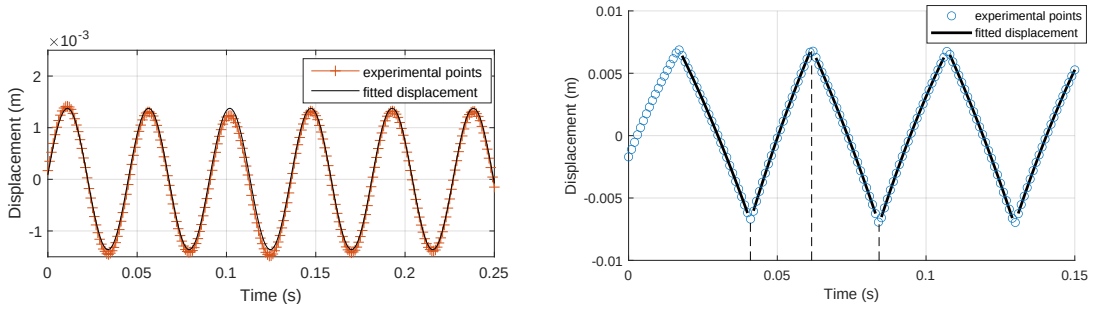

(a) Structure displacement.

(b) Ball displacement.

Figure 2.9: Fitting displacements for the main structure and the ball.

It is now possible to calculate the velocity of the main structure and ball differentiating equation (2.2) and equation (2.3).

Thus, displacements and velocities equations can be used to estimate the kinematics quantities relative to the main structure and ball at every moment, and the whole motion is reconstructed.

With the discrete-time displacements, impact times remain unknown as contact phases are very short and happen between two images. In figure 2.9b, one can see that impacts occur at the intersection of each free flight trajectory (see figure 2.9b), so impact time t_i between freeflight $i-1$ and freeflight i can be deduced with equation (2.15).

$$(a_i - a_{i-1}).t_i^2 + (b_i - b_{i-1}).t_i + c_i - c_{i-1} = 0. \tag{2.15}$$

It is now possible to calculate the velocities when the impact occurs to estimate the COR, defined as:

$$e_i = \frac{\dot{Y}_b^i(t_i) - \dot{Y}_s(t_i)}{\dot{Y}_b^{i-1}(t_i) - \dot{Y}_s(t_i)}. \tag{2.16}$$

2.4 Results of VI characterization

In this section, the results of the characterization of the VI absorber designed for this study are presented and fall into two parts. The first one is the measurement of the COR, and the second one is the measurement of the friction forces acting on the ball during its free flight phases. The measurements presented can be considered as reliable, as the question of the accuracy and uncertainties of the measurements is addressed in section 2.5.

2.4.1 Coefficient Of Restitution

The COR is calculated for each impact using equation (2.16). An example of the values measured for the fourth test is presented in figure 2.10. Table 2.2 summarizes the mean value of the COR on the lower and upper plate and their standard deviations for each test.

As one can see, the COR is different whether the impact occurs on the upper plate or on the lower plate. This unexpected phenomenon has already been reported in [75]. Therefore the two following sections are devoted to propose some explanations for this result.

	e_b	e_t	σ_b	σ_t
Test 1	0,76	0,65	$3,37.10^{-2}$	$4,69.10^{-2}$
Test 2	0,74	0,59	$4,9.10^{-2}$	$3,47.10^{-2}$
Test 3	0,72	0,60	$5,29.10^{-2}$	$5,06.10^{-2}$
Test 4	0,73	0,50	$4,89.10^{-2}$	$3,38.10^{-2}$

Table 2.2: Summary of average COR values and standard deviations (b: bottom. t: top).

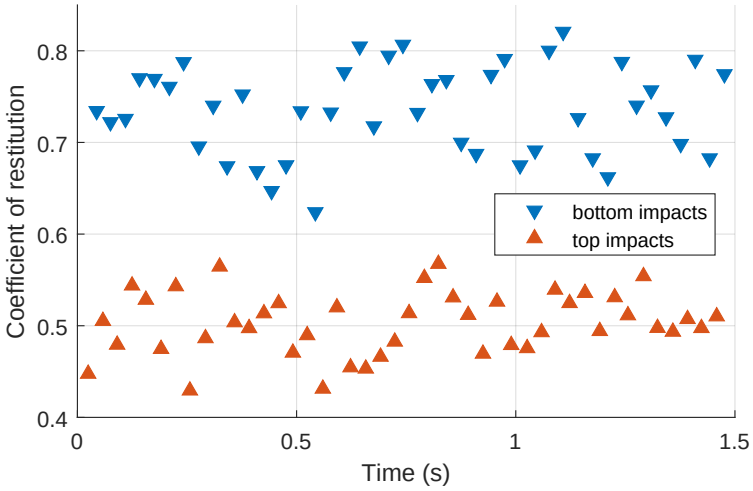

Figure 2.10: Example of experimental results of the COR (4-th test).

2.4.1.1 Role of the gravity

Further experiments have been made to try to determine if gravity could influence the COR and provide an explanation of the differences of COR observed between the upper plate and the lower plate. Therefore, the same testing conditions as in test 4 (see table 2.1) were reproduced for three direction of the set-up, namely vertical, tilted (45 degrees from vertical), and horizontal. The results are presented in figure 2.11. The average values of the COR for the top and bottom impacts are given in the figure. The COR values are not significantly changed by the direction of the set-up, and the top and bottom values are still different whatever the direction. As a consequence gravity does not seem to be the predominating parameter determining the value of the COR.

In the next section, the influence of the tightening torque of the contact parts is investigated.

2.4.1.2 Role of the tightening torque

In the experimental set-up, the contact parts n°3 and 9 that can be seen in figure 2.1 are screwed to the rest of the structure. During the experimentation realized to obtain the results of this chapter, we noticed that the COR values changed after disassembling and reassembling the experimental set-up. Accordingly, the role of the tightening torque applied on the screws of the contact parts is investigated in this section. For this purpose, the tightening torque of only one side is varied, while the second one is kept constant and equal to 30 cN.m. Then the following procedure is applied. The torque is set for both side of the experimental set-up, and a test is run. Each test last one second, enabling to record 1449 pictures. During one test, approximately 60 impacts occur. Then, the experimental set-up is disassembled and reassembled before setting the new torque for the side concerned. It is worthy to note that this disassembling and reassembling process is not applied to the side where the torque is kept constant for practical reasons. Indeed, it would necessitate to entirely remove the experimental set-up from the shaker. As a consequence, the influence of the tightening torque is only studied on one side of the experimental set-up. Once all the torque values are tested, all this process is repeated three times in order to assess the repeatability of the tests.

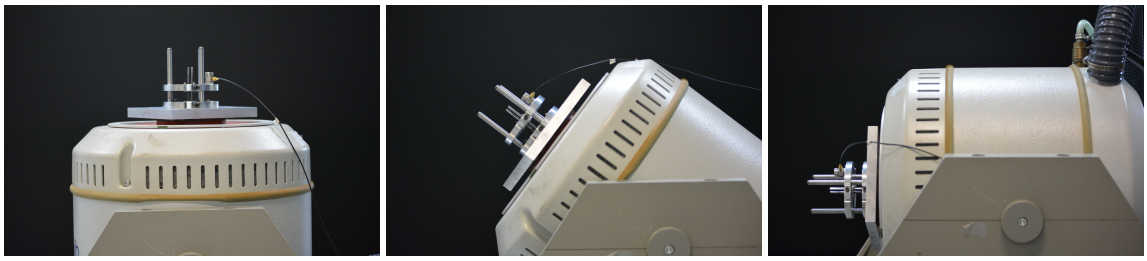

(a) vertical. (b) tilted (45°). (c) horizontal.

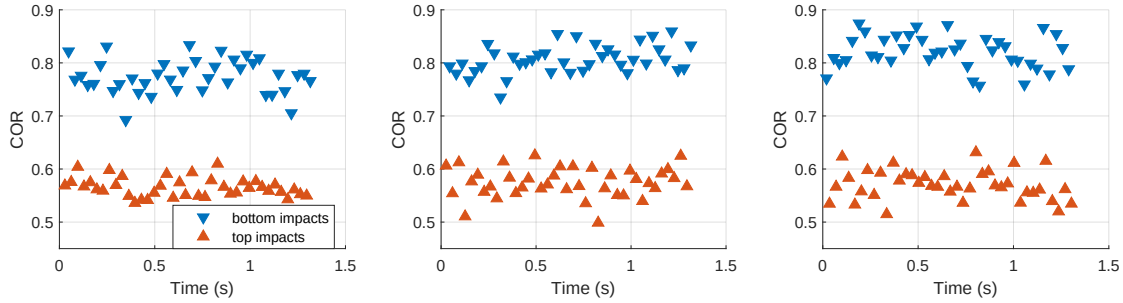

(d) vertical: $e_b = 0,77; e_t = 0,57$. (e) tilted (45°): $e_b = 0,81; e_t = 0,57$. (f) horizontal: $e_b = 0,82; e_t = 0,57$.

Figure 2.11: Influence of gravity on the coefficient of restitution: pictures of the set-up and COR values.

The average COR obtained for each of the three tests and each tightening torque are depicted in figure 2.12a, and the standard deviations are represented in figure 2.12b. The role of the tightening torque on the COR is clearly demonstrated. Indeed, on the right side where the torque is varied, the COR increases with the tightening torque, starting at 0,5 corresponding to 10 cN.m and finishing at 0,65 corresponding to 30 cN.m. On the contrary, the COR does not vary significantly (between 0,75 and 0,77) on the left side since the torque is kept constant. Looking closely to figure 2.12, some remarks and interpretations can be provided. Firstly, considering the COR in figure 2.12a, the repeatability of the three tests is not very good. However, less dispersion is noticed on the side without disassembly than on the other side. This suggests that disassembling and reassembling the experimental set-up is related to this result. For instance, it can be due to uncertainties when setting the torque. Secondly, the figure 2.12b suggests that the standard deviation is larger on the left side than on the right side, but it does not depend on the tightening torque. It is possible to separate the values of the left side from the right side anyway. In order to try to understand why the COR measured is not the same at each impact, it could be interesting to look at the contact surface shown in figure 2.13. It is well visible that the contact zone is deformed by the repetitive impacts of the ball. Consequently, the rebound of the ball is probably modified (and therefore the COR is also modified) depending on the exact area where the contact occurs.

Other authors have established a link between the COR and vibrational energy, considering spring-mass elements [111]. Therefore, a certain part of the initial kinetic energy of the ball is lost because converted into vibrational energy of the main structure and leads to a COR smaller than unity. In particular, this phenomenon is well shown in [115] where longitudinal impacts of a ball on rods are studied. The link between the COR and the vibrational energy of the rod after impact is clearly demonstrated. In the field of sport and especially tennis and golf, studies have been made to understand which design pa-

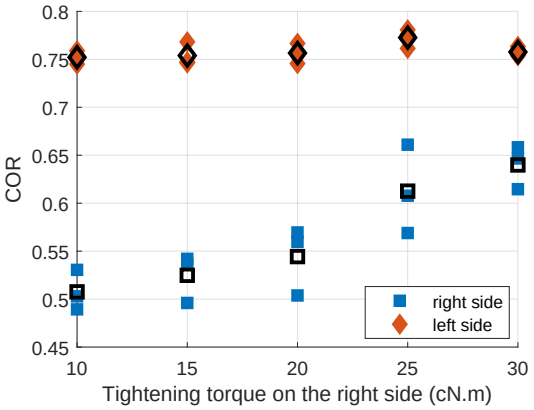

(a) COR versus torque. Black markers: mean of the tests realized for each torque value.

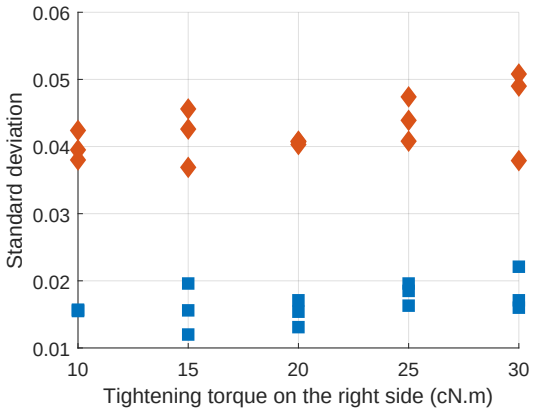

(b) Standard deviation of the COR.

Figure 2.12: COR and standard deviations versus the tightening torque.

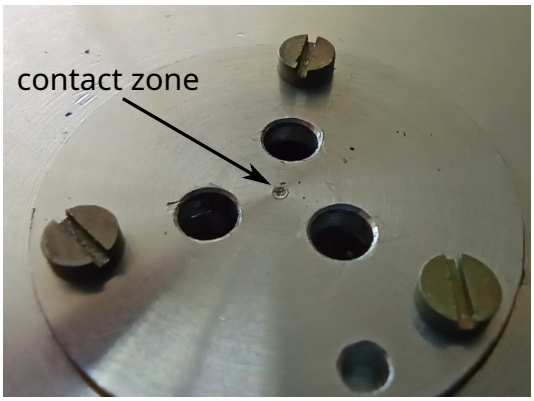

Figure 2.13: Contact part with a zoom on the contact zone.

rameters influence the COR [97, 1, 142, 109, 71, 59]. As presented earlier, two main trends emerge. In the first one, the variation of the COR is studied depending on the materials encountered by the ball or string tension in tennis rackets [71, 1, 109]. In the other approach, the authors try to link the COR with the dynamic properties of the structures that collide. For instance, the authors in [71, 59] have studied the effect of impact location on the COR. In [59], it is shown that the COR is higher when the ball hits the racket close to its vibration node for the first bending mode. In [142], a link between the natural frequencies of the solids that collide and the COR is established.

These results and the previous work briefly presented here confirm the existence of dynamic phenomena during impact that modify the COR and thus the energy dissipation. It also shows that further work still needs to be done to well understand the physics of impact phenomenon that occurs in VI absorbers. In the experiments presented in this chapter various phenomena can occur, in addition to the one previously mentioned. As the set-up is an assembly of several parts, its dynamic behavior in response to an impact is difficult to predict. Further work should be done to precisely understand the predominating physical phenomena that influence the COR, even if the tightening torque seems to play the most important role in the present case. However, they are beyond the objectives of this work.

2.4.2 Friction forces

The identification of the parameters a_i provides information on the forces acting on the ball during its free flight phase. Indeed, the dynamic law states that the product of the mass of the ball by its acceleration is equal to the forces acting on it. The acceleration of the ball can be derived from equation (2.3) and is given by $2.a_i$. In the case where no friction forces act on the ball, its acceleration must be equal to the acceleration of gravity $-g$. However, it was found that the acceleration of the ball was slightly different from $-g$, what can be explained by the existence of a friction force $\mathrm{F}^i_{friction}$ that acts on the ball during the $i-th$ free flight phase. Therefore, numerical values were obtained from the difference between the acceleration of the ball and acceleration of gravity:

$$\mathrm{F}^i_{friction} = m_b.(2.a_i + g). \tag{2.17}$$

These forces are represented in figure 2.14. It is relevant to notice that these forces are effectively opposed to the motion of the ball, except for the 29^{th} ascent free flight where the value is not consistent.

2.4.3 Simulation of the VI model

The results presented in the two previous sections allow to characterize the contact phases with the COR for each impact, and the free flight phases with the friction forces for each free flight. These results, for each contact phase and free flight phase, can be used in the models presented in section 2.3 and they can be simulated. In figure 2.15, one can see that using the experimental values of the COR and of the friction forces leads to the same behavior of the VI absorber in simulation than in the experience. The same result is found for the Hertz damped model. The deviation D between experimental and

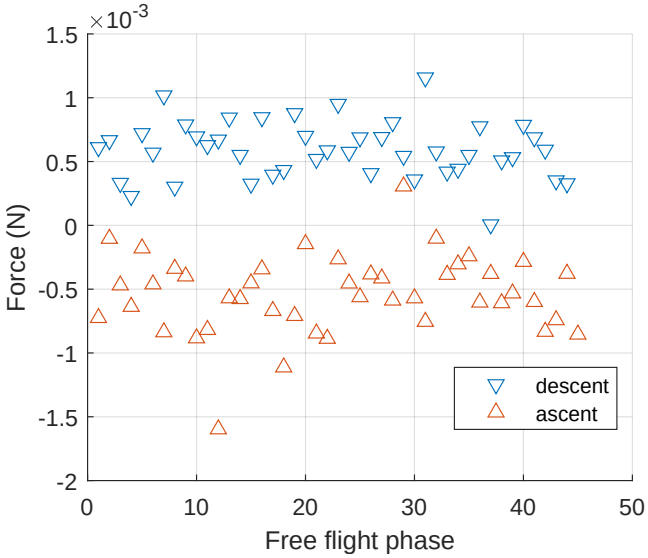

Figure 2.14: Example of friction forces (4-th test).

	Test 1	**Test 2**	**Test 3**	**Test 4**
COR model	2,78 %	2,51 %	2,44 %	3,5 %
Hertz damped model	3,15 %	3,34 %	3,43 %	3,71 %

Table 2.3: Error between experience and simulation for the COR model and Hertz model.

simulation displacements for the ball is quantified using equation (2.18):

$$D = \sqrt{\frac{\int_{t_i}^{t_f} (Y_b^{simu} - Y_b^{expe})^2 . dt}{\int_{t_i}^{t_f} (Y_b^{expe})^2 . dt}}; \tag{2.18}$$

where t_i and t_f denote initial instant and final instant of the experience, respectively. The deviations calculated for the different tests and for both models are presented in table 2.3. As a consequence, it can be concluded that the motion reconstruction method presented in this paper is able to perform accurate measurements of the position of both the ball and the main structure in the configuration chosen for the tests.

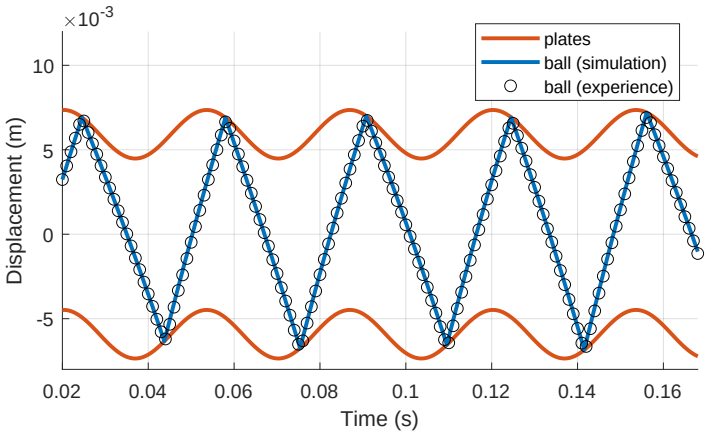

Figure 2.15: Comparison of experimental and simulated displacement using the COR model.

2.5 Discussion: statistical analysis of experimental data and uncertainties

As presented in section 2.4 the COR values are scattered around an average value (depending on the plate where the impact occurs). The COR values are analyzed from a statistical point of view. To determine if the values follow a special distribution, histograms are plotted in figure 2.17. μ and σ denote the average value and the standard deviation respectively. As normal distribution seems to fit the experimental data, quantile-quantile diagrams are plotted in figure 2.18. High correlation coefficients suggest that the COR values follow a normal distribution. Similar results were found for the other tests. Average values for the 4 tests with standard deviation error bars ($\pm\sigma$) are presented in figure 2.16. Comparatively, the COR values presented in [75] seem to be scattered similarly, and the standard deviations given in [52] are consistent with the one presented in this paper.

Further work should be done to explain the origin of the scattering of the measurements. In [53], the authors have made a movie of a motionless specimen (a disk in compression between Hopkinson bars) to quantify the uncertainty on the gray level between pictures because of noised pictures. The same methodology is applied here to determine the noise displacement involved by noise on the pictures. Such a displacement is represented in figure 2.19. One can see that the displacement can be divided into a high frequency content and a low frequency content. The first part can be attributed to the noise on pictures, that leads to accuracy loss in the correlation process. The second part is very likely to be due to unwanted motion of the camera while recording the pictures. As the total displacement is approximately 100 times smaller than the motion amplitude of the ball (and 50 times for the structure), it is reasonably low to assume that its effects on the displacement reconstruction and COR estimation are negligible. Moreover, here is the main advantage of the reconstruction method proposed in this paper. Using a model associated to a curve fitting process, the noise existing on the measurements has a negligible influence on the displacement and velocity estimation, whereas using classical finite differences to determine the velocity is well-known to be very noise sensitive, what leads to a bad estimation of the velocity. Other sources of uncertainty in the COR estimation can be identified, such as the non horizontality of the camera or the rotation of the ball. As an angle of the camera to the horizontal does not modify the measure of the COR because the relative velocities of equation (2.5) in each side of the equation are multiplied by the

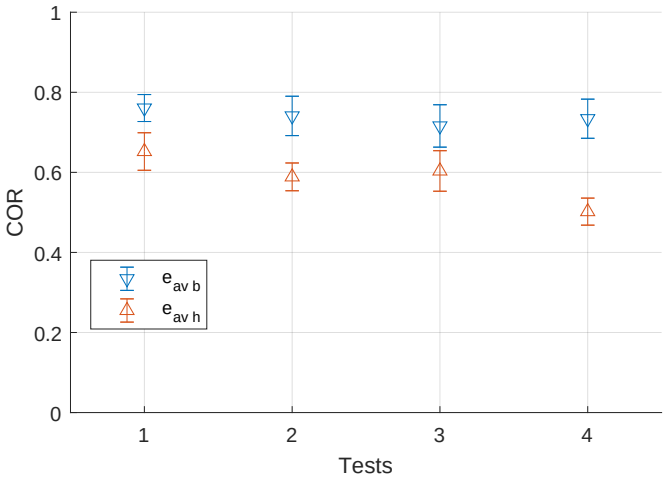

Figure 2.16: Summary of average COR values with error bars (±σ).

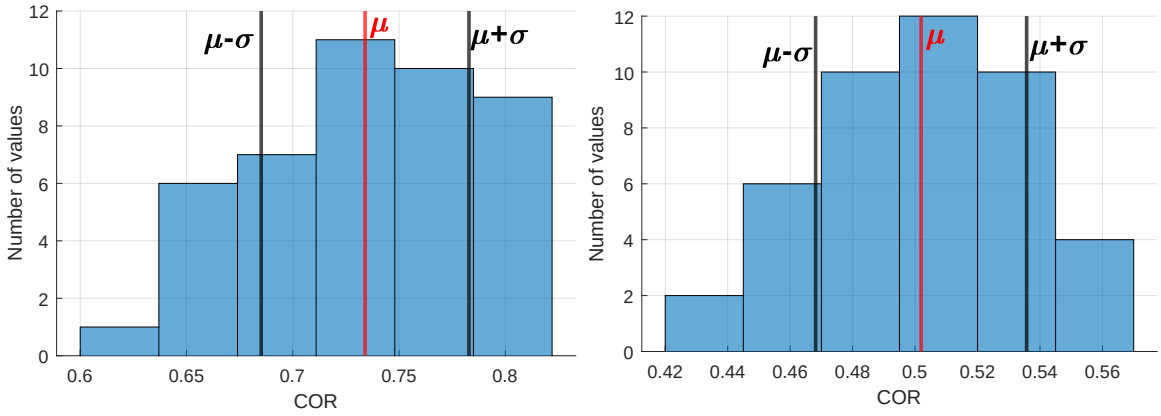

(a) Lower plate.

(b) Upper plate.

Figure 2.17: Histogram of COR values (4-th test).

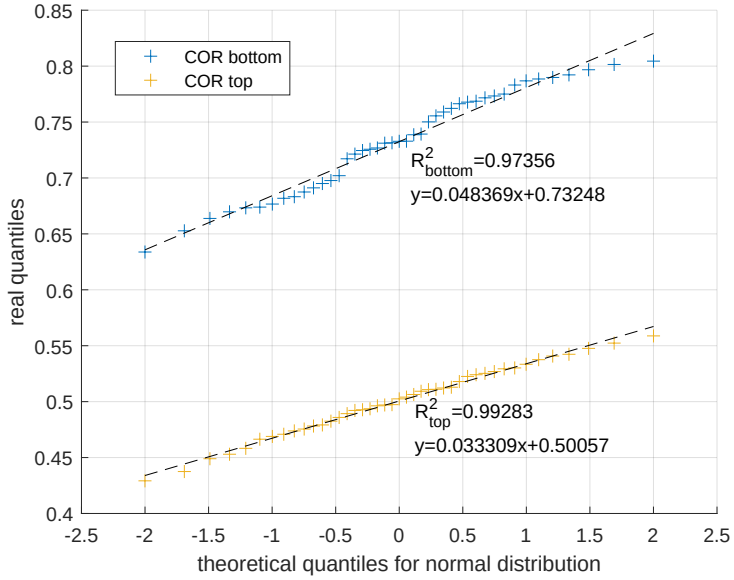

Figure 2.18: Quantile-quantile diagram for normal distribution (4-th test).

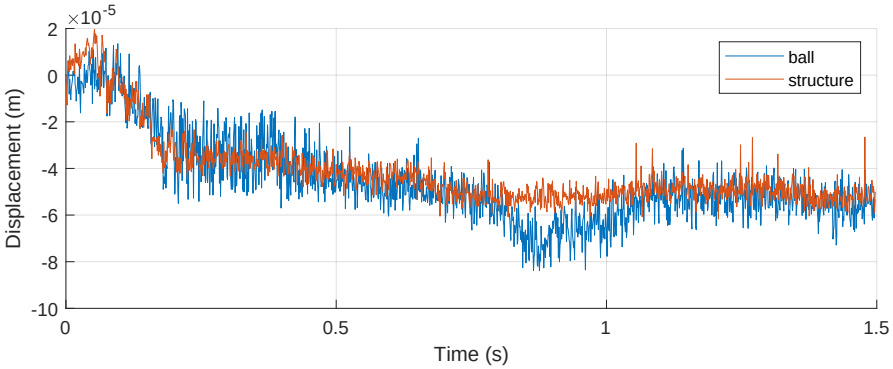

Figure 2.19: Noise displacements measured during motionless test.

same coefficient (depending on the angle), this cannot be responsible for the scattering of the COR values. Concerning the rotation of the ball, it is demonstrated in [52] that the six degrees of freedom of the ball must be considered to determine repeatable values of the COR (i.e with a small standard deviation) for a bouncing ball on a plane. In the present case, only the vertical translation is possible, but rotations around the three axis are a priori possible, but not considered here to calculate the COR. Moreover, such rotations of the ball may be induced by the friction forces identified previously, in the case where they correspond to friction on the guiding rods. Nevertheless, the ceramic ball is too smooth and shiny to visualize its rotation. Some attempts with paint marks on the ball in order to observe its rotation turned out to be unsuccessful, since the ball was stuck due to paint...

No special work has been done to find the origin of the friction forces identified in this paper. But two assumptions can be made. These forces can be due to friction on the guiding rods when the ball is in contact with them. Another source of friction can be the aerodynamic drag of the ball. Further work could be done to try to estimate the proportion of each category of force, and to understand how to design a set-up to control the effect of their intensity. Such results could be linked with [128] in which the effect of friction on the absorber effectiveness is analyzed.

2.6 Conclusions

In this study, an experimental set-up has been designed to take advantage of Digital Image Correlation and full-field measurement using a high-speed camera in order to reconstruct the motions of the main structure and the free oscillating mass of a vibro-impact system. This method overcomes the difficulties encountered to measure the displacement of the oscillating mass with conventional sensors. Once the discrete-time displacements are obtained from Digital Image Correlation, continuous displacements are derived identifying models parameters using curve fitting on the experimental points. Velocities can be deduced with the analytical derivative of displacements without amplifying the noise, and the coefficient of restitution can be calculated. With this method, impact instants can be accurately determined even if they occur between two images recorded by the camera. Moreover, friction forces are evaluated during the free flight phase of the oscillating mass. The method turns out to be accurate in the different configurations tested, as the agreement with two simulated models is very good. Experimental characterization of a vibro-impact absorber can now be realized, and allows to determine the coefficient of

restitution and friction forces that can be used in a model. The dynamic response of the structure highlights that a high-frequency energy transfer exists because of vibro-impact phenomenon, which could be one of the source of dissipation during impact, leading to a coefficient of restitution smaller than unity. It was demonstrated that gravity has no significant influence on the coefficient of restitution, whereas the tightening torque of the contact parts plays a significant role. Further work must be done in order to explain more precisely the scattering of the COR measurements.

Chapter 3

Experimental investigations of a vibro-impact absorber attached to a continuous structure

Contents

Preamble

The previous chapter presented a non-contact technique for vibro-impact characterization, enabling to measure the Coefficient Of Restitution and the friction forces acting on the ball during the free flight phases. However, the structure embedding the ball can be considered as rigid regarding the excitation frequencies, so that its dynamic behavior can be neglected. Accordingly, flexible structures should be considered in order to study the non-linear behavior of the system formed by the structure and the ball. For this purpose, this chapter deals with an experimental study of a beam endowed with a vibro-impact absorber in order to assess its performance.

3.1 Introduction

Vibro-impact absorbers can be applied in various situations where structural vibrations should be reduced. In [83], the authors have used a single-sided vibro-impact Non-Linear Energy Sink (NES) combined with traditional NES with non-linear restoring force to suppress the low-frequency and high amplitude vibrations of a nine-story model building structure. Nakamura et al. have also used an impact damper on a structure submitted to walking and seismic excitations [92]. In [50], an absorber is designed for two industrial structures, a blade and a vane, while Kappagantu et al. [58] tried to benefit from the temperature independence of their vibro-impact absorber to attenuate break squeal. Gourc et al. [45] managed to reduce the vibration of the tool during turning process thanks to a vibro-impact absorber. The non-linearity of vibro-impact phenomenon is also utilized for energy harvesting, as in [65, 147, 36].

The literature dealing with vibro-impact can be divided in two categories, the first one concerning numerical studies, and the second one dealing with experimental works. Focusing on the first one, several numerical studies are available in the literature that aim to better understand how vibro-impact can reduce the vibrations. Most of the time, harmonic excitations are considered. In these conditions, the existence of two regimes of motion of the free mass are studied: the Strongly Modulated Regime (SMR) and the regime with two impacts per period of the main structure [44]. Indeed, the conditions of existence of these regimes are particularly relevant to study, since they are related to the capacity of the absorber to effectively reduce the vibrations of the main structure. The optimal operating point to obtain the best effectiveness (i.e the lowest amplitude of vibration) of the absorber corresponds to the limit between these two regimes [74, 105]. In these same papers, simple structures with a single degree of freedom (S-DOF) are considered. To explain the ability of the vibro-impact phenomenon to mitigate the vibrations, some researchers have studied vibro-impact absorber adopting an energetic point of view. When considering a S-DOF structure (or equivalently a uni-modal structure), the energy is assumed to be dissipated during the successive impacts [44] and is calculated in [8]. This energy dissipation is very often quantified using a Coefficient Of Restitution (COR) when modelling the vibro-impact phenomenon, that can be defined in various manners, using a kinetic, kinematic or energetic definition [116].

Still looking at numerical studies, continuous structures are studied such as beams or plates [37, 128, 42, 19, 102], and very promising results are obtained in [37] and [42] to reduce the vibrations of a cantilever beam. The existence of the regimes SMR [128, 37] and two impacts per period [128] are also found, and the role of SMR in vibration mitigation

is confirmed. Nevertheless, on these continuous and therefore multi-modal structures, the physical phenomena at stakes may be different, and as a consequence, the way the vibrational energy is dissipated is also different. Indeed, Theurich et al. [128] have quantitatively showed that the vibro-impacts on a vibrating beam lead to excite higher modes, corresponding to the modes that are not harmonically excited by the external force. This results in two beneficial phenomena. Firstly, the higher the mode, the lower its amplitude of vibration. As the energy of the first low frequency mode is redistributed within the modal space, the global amplitude of vibration of the structure is reduced. Secondly, the energy on the higher modes dissipates faster, as they realize more oscillations in the same amount of time than low frequency modes. As a consequence, the non-linearity introduced by the vibro-impacts helps to dissipate the vibrational energy on a shorter time scale using only the intrinsic damping capacity of the structure. An energetic study on a 9-DOF structure is also available in [49]. In [128, 50], the numerical results of the authors demonstrate that the reduction of the amplitude of vibration is possible even in the case of conservative impacts, confirming that dissipation during impacts cannot be the only phenomenon contributing to vibration mitigation.

One can now consider the second categories of studies dealing with experimental approaches. Some of them confirm the numerical results listed above. Most of the time, the experiments concern systems made of spring-mass elements intentionally designed to behave as S-DOF system or, in the more complex cases, structures with a finite number of degrees of freedom, and the flying mass is a metallic ball. In [74, 105], it is experimentally confirmed that the transition point between SMR and the regime with two impacts per period corresponds to the configuration leading to the best vibration reduction. The tunable parameter is the size of the gap available for the flying mass to oscillate. Changing its size leads to a specific regime or another, while the amplitude of the excitation is constant. Besides, these systems need to be characterized, especially in terms of contact properties, in order to develop representative models and to better understand the working principle of vibro-impact absorbers. Li et al. [75] have recently proposed a method to reconstruct the motions of the oscillating ball with limited experimental information. They are able to estimate the COR of their experimental set-up. The work proposed in the previous chapter and published in [27] pursues the same objective, but this time the motions of the ball and the structure are reconstructed from a series of pictures using a high speed camera and a Digital Image Correlation technique. In both studies, the value of the COR shows some variations that the authors are not able to explain, what confirms that some work still remains to be done to understand which parameter influences the contact properties in vibro-impact applications.

Very few experimental studies dealing with continuous or more complex structures are available. In [135], the authors made some experiments on a cantilever beam equipped with a vibro-impact absorber at its tip. The results presented bring to light that the impacts lead the other modes to respond, and not only the excited mode, but no details are given on the design of the cavity. In the context of particle damping using granular materials, some pictures of the cavity attached to a beam containing the particles can be seen in [132], even if the design details are still not delivered. Other authors have designed a cavity with different lengths when changing the cap to reduce the vibration of a wheel structure [139]. In [5], the authors have made a different design choice, as they have filled a honeycomb beam with particles. The particles are integrated to the structure and not attached to it as seen before.

The purpose of this work is to experimentally investigate the performances of a vibro-impact absorber attached at the tip end of a continuous cantilever beam structure and to inquire the theoretical findings of the literature. To this end, a specific modular device has been designed allowing a tunable gap as required to find an optimal configuration through the design-of-experiments method. Full-field measurements allow to measure precisely the motion of the ball in order to better understand its role in the establishment of specific vibrational regimes. The chapter is organized as follows. The experimental set-up including the VI absorber as well as the measuring tools are introduced in section 2. The section 3 presents the vibration reduction obtained under harmonic excitations for the first mode on the one hand, and for the second mode on the other hand. The vibration reduction of the first and second mode for white noise excitation is provided in section 4.

The temporal responses of both the beam and the ball are analyzed in section 5 in relation with the vibration mitigation performance of the absorber. To do so, a clustering method is adopted using the number of impacts per period as feature. An analysis of the phenomena at stakes is conducted in section 6. The chapter ends with conclusions in section 7.

3.2 Design of the VI absorber for a cantilever beam

3.2.1 The experimental set-up: global overview

In the present work, the attention is focused on an aluminum cantilever beam submitted to base excitation. As shown in figure 3.1, the clamping system of the beam is directly attached to the shaker. An accelerometer is stuck on the base of the beam to measure the base acceleration. The exact shape and dimensions of the beam are given in appendix B.3. The vibro-impact absorber designed in this study is attached at the beam end. More details concerning the design are given later in this paper (see section 3.2.3). The experimental set-up is oriented so that gravity does not influence neither the bending vibrations of the beam nor the motion of the ball.

3.2.2 Measuring devices

The base acceleration is measured using an accelerometer and controlled during the test under harmonic excitation. To reach this goal, the acceleration signal is monitored in real time using National Instrument acquisition card NI 9234 and corrected thanks to a dedicated Matlab program. The corrected signal is sent to the shaker via a NI 9263 excitation card. More details on the algorithm used to realize the control of acceleration are given in [125].

The vibrational response of the beam is measured using a vibrometer pointing the beam end. A high speed camera with four spots light is placed in front of the VI absorber. Thanks to this, the motion of the ball in the cavity is recorded with 3003 frames per second. The global arrangement of all the measuring devices is shown in figure 3.1.

3.2.3 Design of the VI absorber

The VI absorber has been conceived to be attached to the beam end, and not integrated within the structure itself as done in [5]. There are many reasons for this. To begin with,

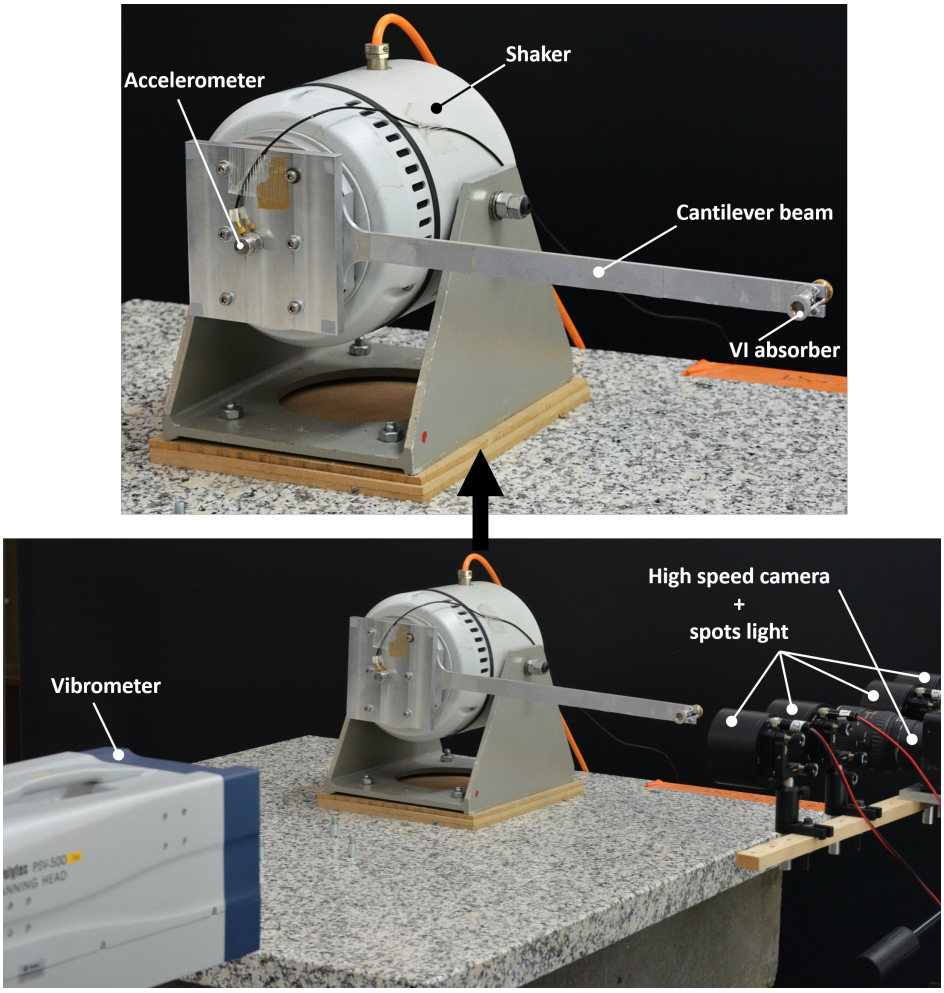

Figure 3.1: Overview of the experimental set-up.

the beam was designed to obtain its first eigenfrequency around approximately 15 Hz. Once the material is chosen, the dimensions determine directly the eigenfrequencies of the beam. In the present case, the height of the beam was too small to integrate the ball within the beam. Moreover, one of the objective was to visualize the motion of the ball, and this is easier to realize with an external cavity. Then, the authors wanted to design a VI absorber with a tunable gap that can be added to a main structure in order to enhance its damping properties. To reach these last objectives, it was easier to design a VI absorber independently of the main structure, and to imagine the mounting on the beam at the end of the design process. Another interesting point is that the VI absorber remains symmetrical along the middle plane of the beam what limits the risks of obtaining different phenomena [75, 27] whether the ball collides the beam on the upper side or on the lower side.

Therefore, the VI absorber proposed here is made of four elements (see figure 3.2):

1. One cavity;
2. One ball;
3. Two adjusting screws;
4. Two counter nuts.

The ball corresponds to the flying mass travelling inside the cavity. The impacts occur on the stud of the adjusting screws. The latter are used to adjust the gap between studs, what results in a longer or shorter distance to travel for the ball before colliding the beam. The counter nuts allow to lock the screws in their current position and to avoid them to loosen. The adjustment range enables to lock the ball in the cavity, or to leave a large space for the ball in the limit of length of the screws (see for example figure 3.2b). At the end, the cavity is bolted on the beam at three points.

The mass of the ball is equal to 2,7 g, the VI absorber added at the beam end weights 31,3 g and the mass of the free part of the beam (considering the volume and the density of the material) is 88,4 g. Therefore, the mass of the ball represents 2,26 % of the moving mass. More details on the materials, the masses and the dimensions are given at the end of this paper in appendix B.3.

3.2.4 DIC for motion reconstruction

In order to reconstruct the motion of the oscillating ball, a Digital Image Correlation (DIC) technique is used to follow the motion of the ball. The process is identical as the one presented in chapter 2, where the methodology is described in section 2.2.3. An example of the motion of the ball and of the beam end reconstructed using the DIC technique is shown in figure 3.3. Particular attention can be paid to the fact that the motion of the beam is rather measured with the vibrometer than with the camera. Indeed, the vibrometer enables a sampling frequency of 250 kHz whereas the camera records the pictures at the rate of 3003 frames per second. As the beam is expected to vibrate at relatively high frequencies due to the excitation of its eigenmodes following the impacts, the vibrometer is more appropriate. On the contrary, the motion of the ball can be well described with the camera, and no other way to measure its displacement is available. Moreover, as the vibrometer is able to measure a velocity, the following methodology was applied to obtain

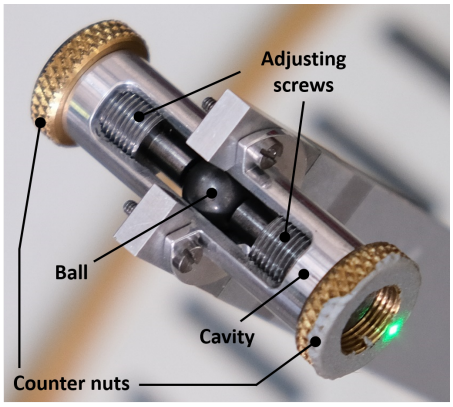

(a) Zoom on the VI absorber.

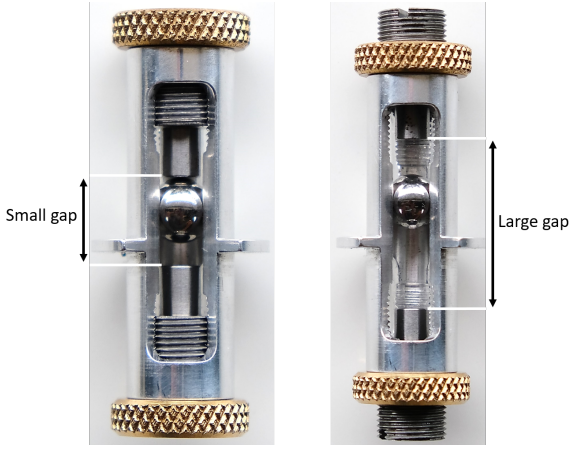

(b) Different adjustments for the gap.

(c) Exploded view.

Figure 3.2: View of the VI absorber.

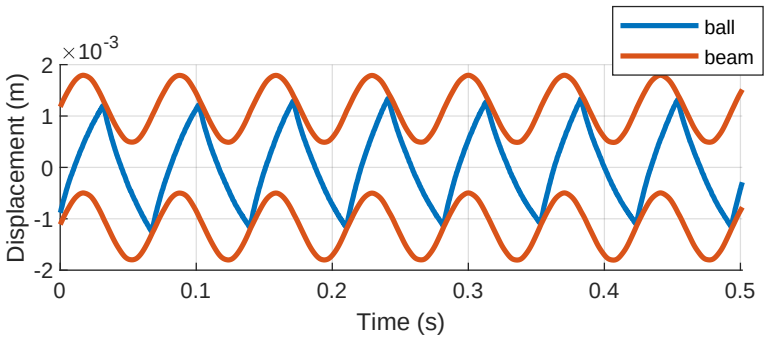

Figure 3.3: Displacement of the ball (blue) and the ends of the cavity (orange) using DIC technique and laser vibrometry.

the displacement. The signal was integrated using the trapezoidal rule. As the non-zero offset of the signal leads to a constant slope in the integrated signal, a linear regression was realized and the corresponding equation was subtracted to the integrated signal to remove the slope.

3.2.5 Calculation of amplitudes and FRFs

During the tests under harmonic excitation, the temporal signal from the accelerometer and from the vibrometer are recorded via the National Instruments device with a sampling frequency of 51200 Hz. In order to obtain the average amplitude of vibration at the beam end at a certain excitation frequency, the envelope of the signal was calculated using the modulus of the analytic signal that is calculated with the Hilbert transform [38].

Indeed, let's denote by $\mathrm{HT}[x(t)]$ the Hilbert transform of the signal $x(t)$. Therefore, the analytic signal is defined as:

$$y(t) = x(t) + i.\mathrm{HT}[x(t)]; \tag{3.1}$$

where i is the unitary imaginary number. The envelope $\mathrm{E}(t)$ of the signal $x(t)$ is calculated in equation (3.2):

$$\mathrm{E}(t) = |y(t)|. \tag{3.2}$$

An example of the extraction of the envelope of the signal using equation (3.1) and equation (3.2) is presented in figure 3.4. The average value of the envelope allows to determine the average value of the velocity at the beam end for a certain amplitude of acceleration and excitation frequency.

The signal obtained from the accelerometer stuck at the base of the beam is not purely harmonic because of the impacts. As a consequence, the acceleration amplitude is calculated using the component of the Fourier Transform of the acceleration at the frequency of excitation ω_{exc} as presented in figure 3.5. It is worthy to note that the value of the excitation frequency and the duration of the acquisition are chosen in order to obtain an entire number of periods. It ensures a proper estimation of the amplitude of the signal at the excitation frequency in the frequency domain.

As explained later in this chapter, tests with stepped sine excitation are realized around the first and second eigenfrequency of the beam. Knowing the amplitude of the

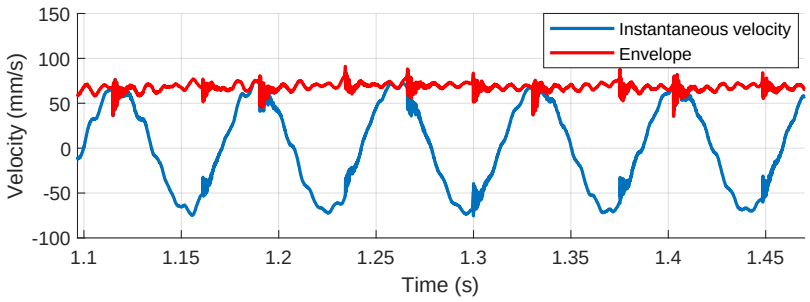

Figure 3.4: Extraction of the envelope of the beam response.

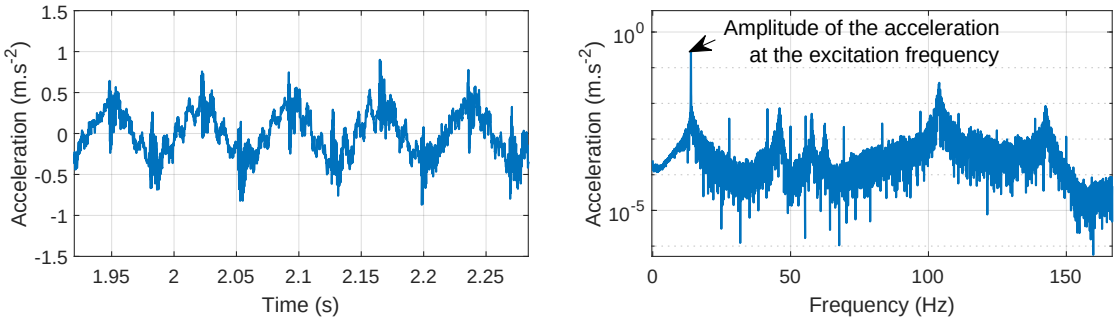

Figure 3.5: Determination of the acceleration amplitude at the base of the beam using the Fourier Transform. Left: time domain signal; Right: frequency domain signal.

response of the beam and the amplitude of the acceleration imposed at the base for each excitation frequency, the amplitude of the FRF can be calculated dividing the first amplitude by the last one. To obtain the acceleration - acceleration FRF, the acceleration response of the beam is calculated multiplying the average value of the envelope (see equation (3.1), equation (3.2) and figure 3.4) by ω_{exc}.

The phase of the FRF is determined calculating the angle between the complex numbers given by the Fourier transform of the response of the beam and the reference signal (base acceleration) at the excitation frequency. Here again, an angle of $\pi/2$ is added to obtain the acceleration - acceleration FRF.

3.3 Harmonic excitation: vibration mitigation of the first and second mode

In this section, the beam is excited around its first eigenfrequency by a harmonic excitation. The objective is to validate the ability of the absorber to effectively reduce the vibrations of the beam. Some relations between the gap value and the optimal operating point are established.

3.3.1 Vibration mitigation of the first mode

The first flexural modes of the beam were identified and the eigenfrequencies are gathered in the table 3.1. At this point, it is worth noting that when exciting the first mode, the tests are run on a shaker with a 200 N rated peak force. A stronger shaker with a 2500

N°	1	2	3	4	5	6	7
Frequency (Hz)	14,23	103,31	142,75	341,00	631,64	977,70	1433,57

Table 3.1: First eigenfrequencies measured on the 200 N shaker.

N rated peak force was used when exciting the second mode. More details are given in section 3.3.2.

3.3.1.1 Gap influence: parametric study

The influence of the gap is analyzed under harmonic excitation with constant acceleration amplitude using the design-of-experiments method. The amplitude of the excitation was fixed to 0,03 g. This value enabled sufficiently large displacements to analyze the motions with the camera, but small enough to stay in the linearity range of the beam. The first eigenfrequency of the beam with a gap equal to zero (the ball plays the role of an added mass) is equal to 13,87 Hz. The tests are realized using stepped sine excitation, the frequency range was centered around this value going from 13,21 Hz to 14,87 Hz with 26 values regularly spaced.

Six values of gap were tested, starting from 1,53 mm up to 3,77 mm. The amplitude and phase FRFs are given in figure 3.6. One can see that when the gap is small, the vibration reduction is not very effective. Basically, the ball behaves like an added mass that shifts the first eigenfrequency from 14,23 Hz to 13,87 Hz. When the gap goes larger, it is possible to get a more effective vibration reduction for the frequency range tested and the peak in the FRF becomes flat. This is the case when the gap is equal to 2,67 mm where the vibration reduction is optimal. The vibration reduction can be quantified comparing the maximum of the amplitude of the FRF when the ball is locked $A_{VI\ locked}$ with the maximum of the amplitude for a certain gap value A_{VI}. The level of reduction in decibels is equal to $20.log_{10}\frac{A_{VI\ locked}}{A_{VI}}$. If the gap keeps increasing, the amplitude of the FRF starts growing again. These results demonstrate that under harmonic and constant excitation amplitude, there is an optimal gap leading to a maximum vibration reduction.

The phase of the FRFs plotted in figure 3.6b shows a good correlation with the amplitude of the FRFs in figure 3.6a. Indeed, when the vibration reduction is the most effective, it corresponds to a decreasing of the phase on the largest frequency range (see the curve for gap = 2,67 mm), what is consistent with the fact that the damping obtained thanks to the vibro-impacts is the greatest.

Besides, one can wonder what role plays the acceleration amplitude on the performance of the absorber.

3.3.1.2 Scalability property

Theurich and al. [128], relying on the equations of their model, pointed out that there exists a scalability property that allows to establish a relation between the gap, the excitation amplitude and the response of the beam. Their statement is as follows. If one knows the response $y(t)$ of the VI beam for a gap g_0 and an excitation $e(t)$, therefore the response of the system with a gap equal to $\alpha.g_0$ and an excitation $\alpha.e(t)$ is $\alpha.y(t)$, where $\alpha \in \mathbb{R}$. This property is illustrated in figure 3.7.

A consequence of this property is that the FRF should remain unchanged if both the gap and the excitation amplitude are multiplied by the same coefficient α. This statement

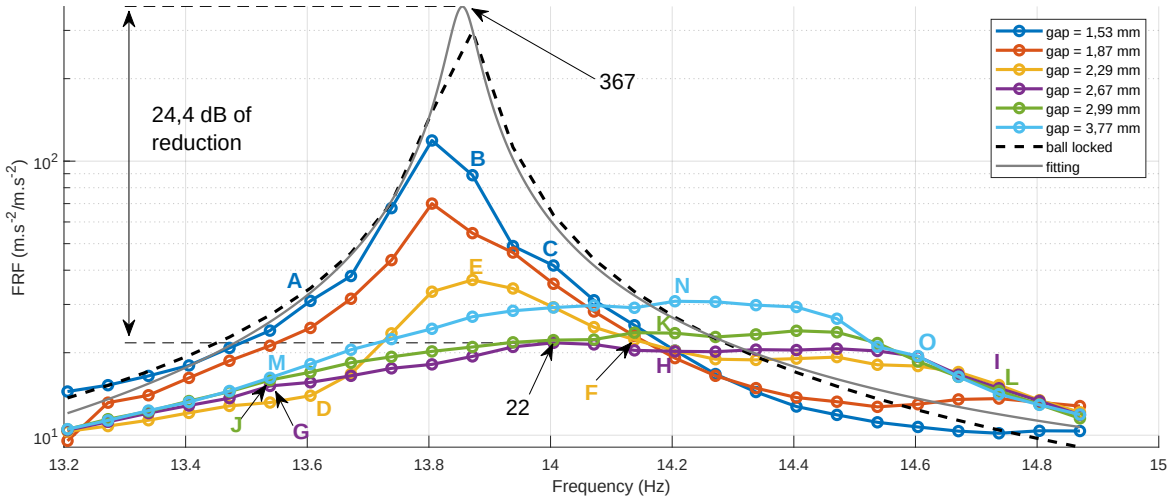

(a) Amplitude of the FRFs. The letters A - O corresponds to points that will be analyzed in section 3.5.

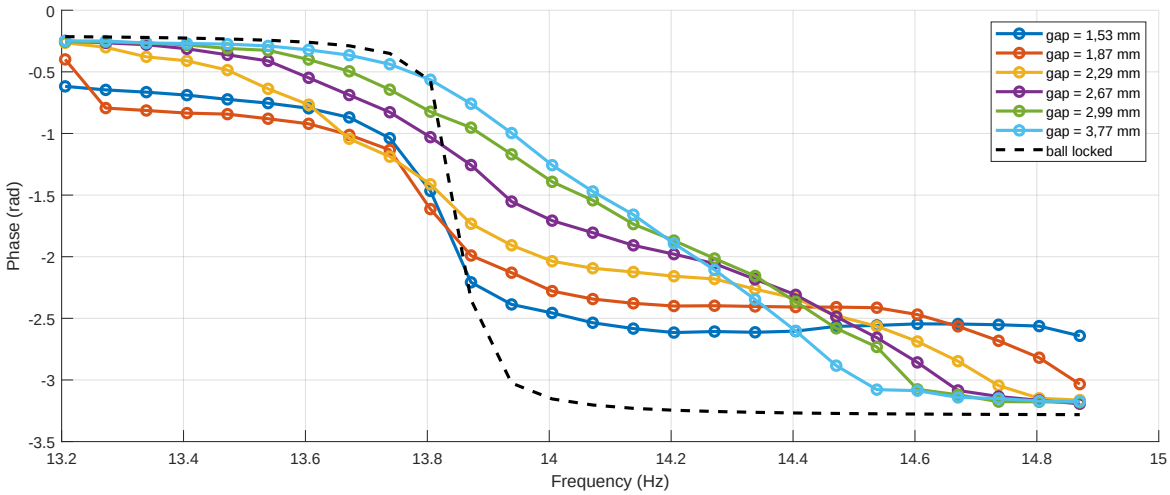

(b) Phase of the FRFs.

Figure 3.6: FRFs of the parametric study on the gap.

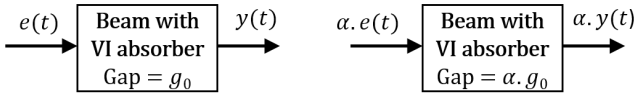

Figure 3.7: Illustration of the scalability property that relates the gap, the excitation amplitude and the response.

Gap g_1 (mm)	Excitation e_1 (g)	Ratio R = e_1/g_1 (g/mm)	Gap g_2 (mm)	Excitation e_2 (g) = R × g_2
1,53	3.10^{-2}	$1,96.10^{-2}$	2	$3,92.10^{-2}$
1,87	3.10^{-2}	$1,61.10^{-2}$	2	$3,21.10^{-2}$
2,29	3.10^{-2}	$1,31.10^{-2}$	2	$2,62.10^{-2}$
2,67	3.10^{-2}	$1,12.10^{-2}$	2	$2,25.10^{-2}$
2,99	3.10^{-2}	$1,00.10^{-2}$	2	$2,01.10^{-2}$
3,77	3.10^{-2}	$7,96.10^{-3}$	2	$1,59.10^{-2}$

Table 3.2: Gap and excitation parameters to illustrate the scalability property.

is verified experimentally in this section. Assuming that the property is true, the gap was fixed at 2 mm and the corresponding excitation amplitude was calculated in order to obtain the same FRFs as in figure 3.6. To do this, the ratio R = $\frac{Excitation}{Gap}$ between the gap and the excitation amplitude was conserved in the following tests (see table 3.2).

The FRFs obtained are superimposed to the ones obtained before in figure 3.8. In order to quantify the difference between the results and the theory if the scalability property was verified, the ratios between the FRFs obtained under an excitation of 0,03 g and the FRFs obtained for a gap of 2 mm are calculated for the configurations presented in table 3.2 for each frequency. A ratio of 1 is expected, the experimental ratios calculated are plotted in figure 3.9 and the mean values are also presented in the legend.

One can see that the scalability property seems to be reasonably verified for this experimental set-up and for the conditions tested. Indeed, the FRFs are almost superimposed in figure 3.8a, and the ratios between these same FRFs are close to unity (figure 3.9). Moreover, the same trends are observed: in terms of vibration reduction, the performance increases when the acceleration amplitude is reduced (which is equivalent to increase the gap value) up to the optimal operating point. The latter is associated to a gap of 2 mm and an acceleration amplitude of $2,25.10^{-2}$ g. After this optimal operating point, decreasing the amplitude leads to deteriorate the performance of the absorber. The slight differences with the theory predicted by the scalability property can have various origins. In particular the uncertainties when tuning the gap, or because of the presence of friction that can affect the domain of validity of the property. The examination of the precise conditions of validity of the property are beyond the scope of this paper and will be investigated in another study. In the following of this work, this scalability property will be considered as valid.

3.3.1.3 Role of the mass of the ball

In the previous experiments, the ball used represents 2,26 % of the total moving mass (free part of the beam and VI absorber). The results suggest a reduction of the amplitude of vibration up to 24 dB. Other experiments are realized with smaller balls. Their mass and the proportion of the total moving mass are given in table 3.3. In these experiments, we took advantage of the scalability property to run the tests varying the amplitude of the excitation instead of varying the gap, what is easier to realize as it does not need any intervention by the user on the absorber and avoids running the same test with different gaps several times. The gap was set at 2 mm.

The FRF obtained can be visualized in figure 3.10, where the optimal response cor-

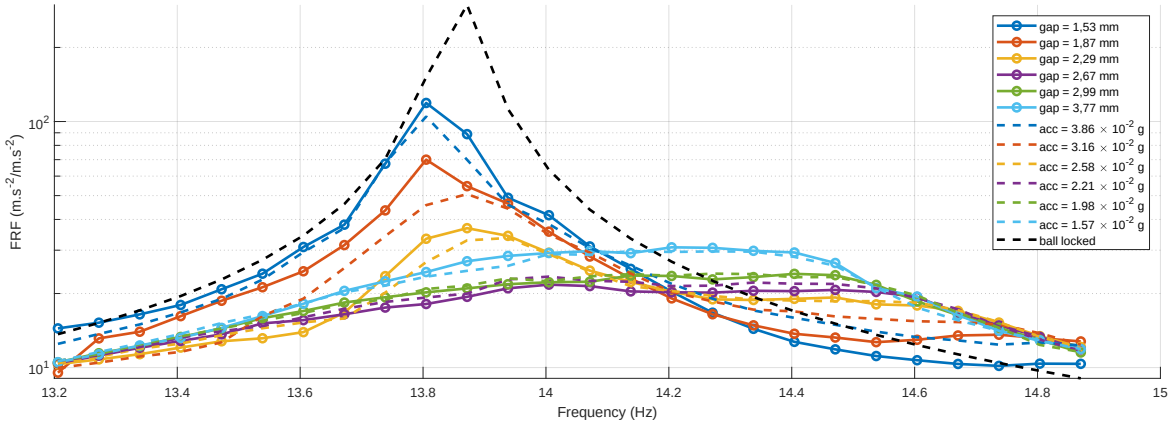

(a) Amplitude of the FRFs.

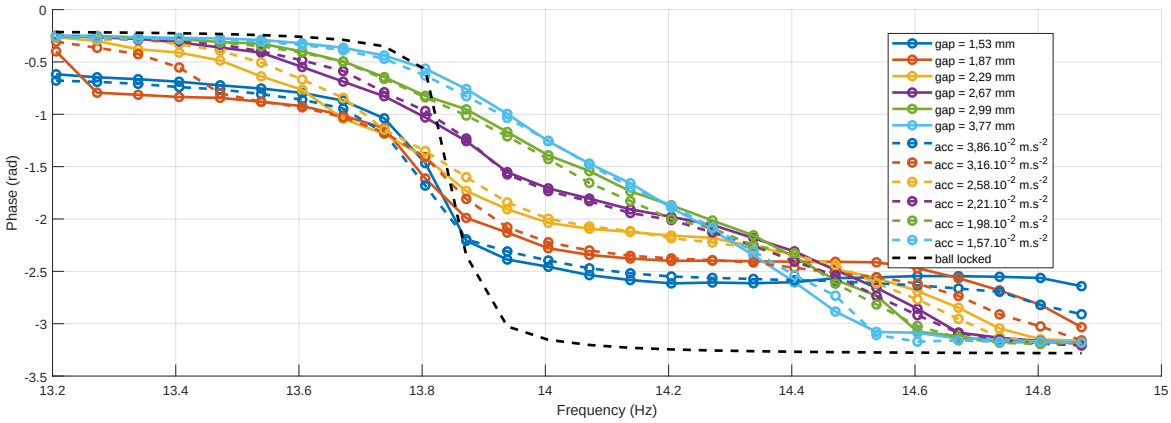

(b) Phase of the FRFs.

Figure 3.8: FRFs obtained varying the acceleration amplitude instead of the gap and demonstrating the scalability property.

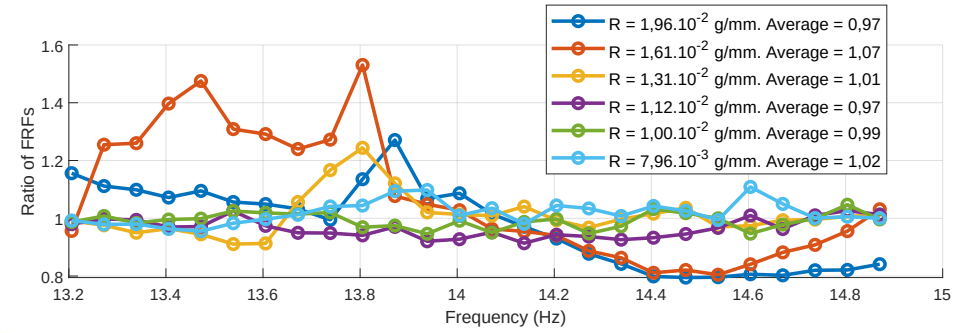

Figure 3.9: Examination of the validity of the scalability property calculating the ratios of the amplitude of the FRFs for the configuration presented in table 3.2.

Mass of the ball (g)	0,86	1,49	2,04	2,71
Proportion of the total moving mass	0,72 %	1,24 %	1,71 %	2,26 %

Table 3.3: Mass of the balls and proportions of the total moving mass.

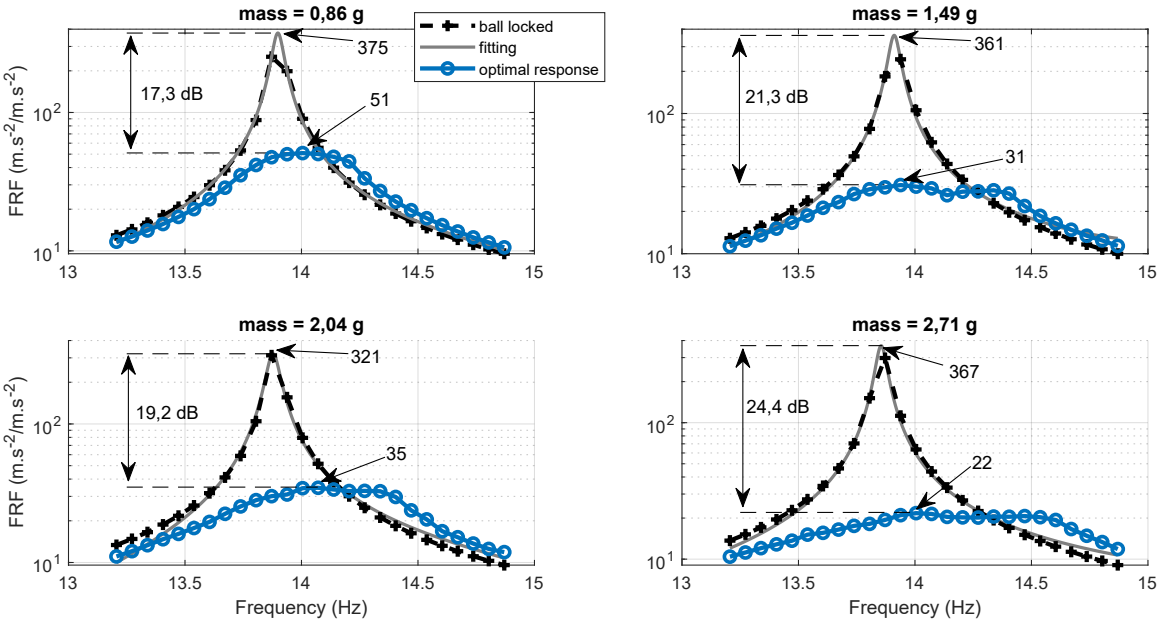

Figure 3.10: FRF and vibration reduction for each ball.

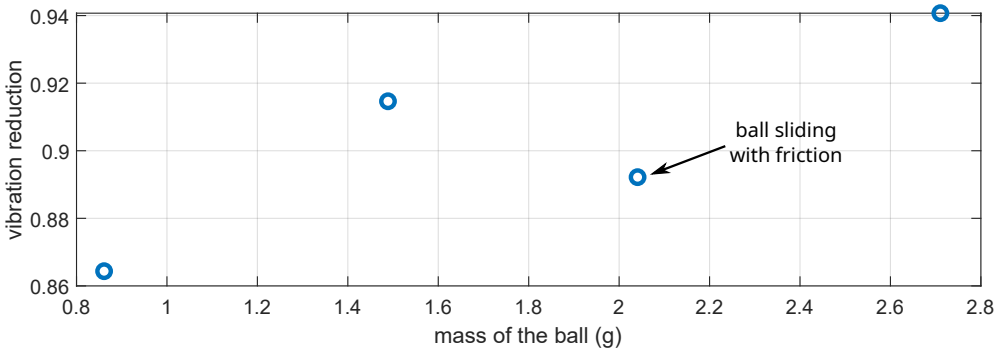

Figure 3.11: Vibration reduction depending of the mass of the ball.

responds to the FRF leading to the maximum vibration reduction. The overall vibration reduction depending on the mass is represented in figure 3.11. In this last figure, the vibration reduction is calculated as $(A_{BL}^{max} - A_{VI}^{max})/A_{BL}^{max}$, where A_{BL}^{max} represents the maximum amplitude of the FRF when the ball is locked taken on the fitting curve, and A_{VI}^{max} represents the maximum amplitude of the FRF with the vibro-impact absorber activated. As a remark, considering the response with the ball locked (and not without ball) for the reference amplitude allows to compare responses of the structure with the same embedded mass, what would be the case on a real structure equipped with a vibro-impact absorber. One of the consequence is that the maximum amplitude of the response is around the same frequency, making the responses easy to compare.

One could expect that the heavier the ball, the better the vibration reduction. It is illustrated if the third ball (2,04 g) is set aside. For this ball, the reduction is slightly too low comparing to the tendency of the other balls. It was observed that the ball was sliding in the cavity with more friction than the others. As a consequence, this vibro-impact absorber may have a behavior slightly different from the others in terms of vibration reduction. However it is hard to say which of the four absorbers behaves significantly differently than the expected average behavior. Therefore, these results confirm that a larger mass helps to reduce the vibrations with more effectiveness but no precise rule can be obtained concerning the dependency of the reduction to the mass of the ball.

3.3.2 Vibration mitigation of the second mode

In order to run the experiments of this section, the experimental set-up was mounted on a stronger shaker with a 2500 N rated peak force. The latter was more suited to the excitation of the second mode as it can supply a higher force, and it is stiffer. Indeed, the 200 N shaker used for the previous experiments was reaching its limits when increasing the excitation frequency, as the set-up resulted in a too heavy eccentric mass in these conditions. The consequence is that the new eigenfrequencies of the beam are quite different in this new configuration, as suggested comparing table 3.1 and table 3.4. These differences arise because the new shaker is stiffer, and hardly affected by the eccentric mass contrary to the 200 N shaker. Nevertheless, the methodology employed is still valid.

In these experiments, we took advantage of the scalability property to run the tests varying the amplitude of the excitation instead of varying the gap, as it is easier to realize as it does not need any intervention by the user on the absorber and avoids running the same test with different gaps several times. The FRFs obtained are presented in figure 3.12.

The same trends are observed when the excitation frequency is centered around the second mode. An optimal acceleration amplitude (or equivalently a gap) can be found to reduce the vibrations of the second mode with the best effectiveness. In comparison with the first mode, the vibration reduction is smaller (around 10 dB for the second mode instead of 24 dB for the first mode). The reason of this might be the location of the vibro-impact absorber in relation with the location of the vibration node of the beam. For the

N°	1	2	3	4	5
Frequency (Hz)	15,27	120,3	338,6	636,6	987,6

Table 3.4: First eigenfrequencies of the beam on the 2500 N shaker.

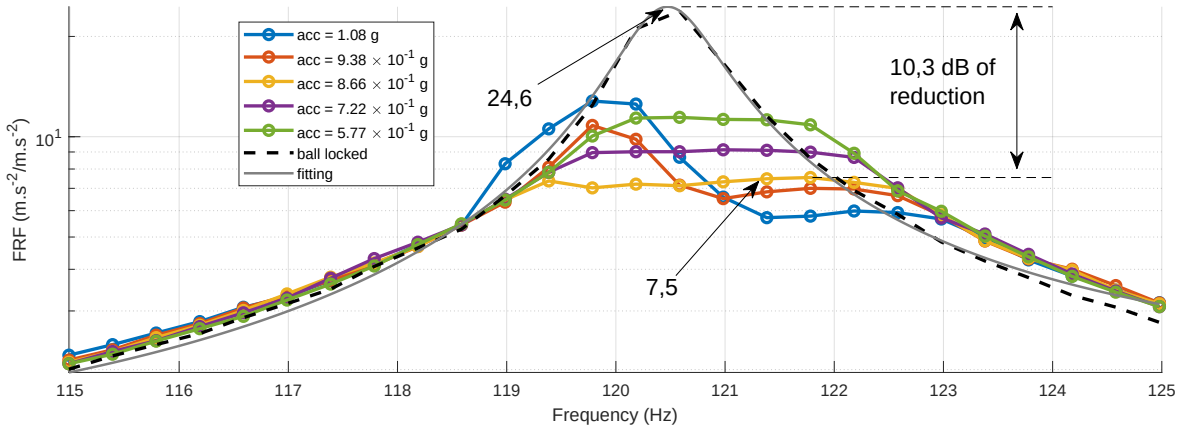

(a) Amplitude of the FRFs.

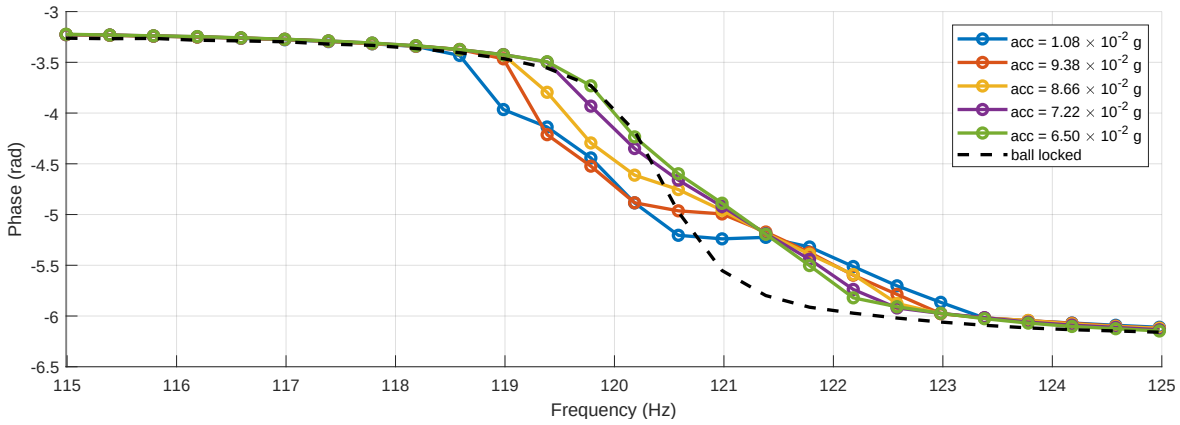

(b) Phase of the FRFs.

Figure 3.12: FRFs of the parametric study on the acceleration amplitude for the 2nd mode.

first mode, there is only one node and it is located at the base of the beam, which is the opposite side of the vibro-impact absorber. One can assume that it corresponds to the most effective configuration, as the absorber is located where the vibrational energy of the beam is maximal. In the case of the second mode, there exists another vibration node close to the beam end, what may lead to a suboptimal configuration from the point of view of the absorber location. Another explanation may concern the energy transfer towards the higher modes. When exciting the second mode of the beam, the possibility of energy transfer is probably smaller than when exciting the first mode. As a consequence, the effectiveness of the absorber is reduced. At last, the friction may play an important role in the behavior of the ball as the relative velocity is significantly higher when exciting the second mode than exciting the first one.

The results of this part demonstrate that VI absorbers can be used to mitigate the vibrations even of the second or higher modes of a structure. The main limitation is the length of the gap. Indeed, the higher the mode, the lower its amplitude of vibration and therefore the lower the gap. If the optimal value is too small, it may become difficult to tune it properly.

In the next part, the performance of the absorber under random excitation is investigated. Then, in section 3.5, the responses of the beam in the time domain for the tests of the current section are analyzed and the two well-known regimes (namely SMR and 2 impacts per period) are identified. Their role in the effectiveness of the absorber is also brought to light.

3.4 Vibration mitigation for white noise excitation

In order to assess the capacity of the vibro-impact absorber to mitigate the vibrations for non-harmonic excitation, its performance was evaluated for white noise excitation in the frequency range 10 Hz - 2000 Hz. The FRFs were calculated using Hanning window for both the vibrometer response and the signal from the accelerometer. The FRFs are the result of the average of 100 measurements. Contrary to the harmonic excitation tests, the base acceleration amplitude was not controlled. The gap was set to 1 mm and the amplitude of the excitation signal was varied.

The amplitudes of the FRFs for the first mode are depicted in figure 3.13a. The best configuration corresponds to a gap value of 1 mm and $7,5.10^{-3}$ m.s^{-2} for the amplitude of the excitation signal. It results in a reduction of the amplitude of 16 dB. The same trends are observed than for the tests under harmonic excitations. Namely, for a high excitation amplitude, the vibration reduction is not quite effective, and a smaller excitation amplitude leads also to a bad reduction with a frequency peak close to the initial frequency resonance of the beam. The optimal excitation amplitude is between these two configurations. Even if SMR and the regime with two impacts per cycle do not exist any more under random excitations, the videos confirm that the optimal configuration leads to more recurring and efficient impacts than in the suboptimal cases. For a too large amplitude of excitation, the ball undergoes multiple impacts, colliding several times the same side of the cavity, whereas very few impacts occur when the excitation is too small, resulting in the non-activation of the VI absorber.

Concerning the second mode of the beam, the FRFs presented in figure 3.13b did not show any significant reduction of the amplitude. This low effectiveness on the second mode can be explained because the gap is too large to activate the impacts efficiently

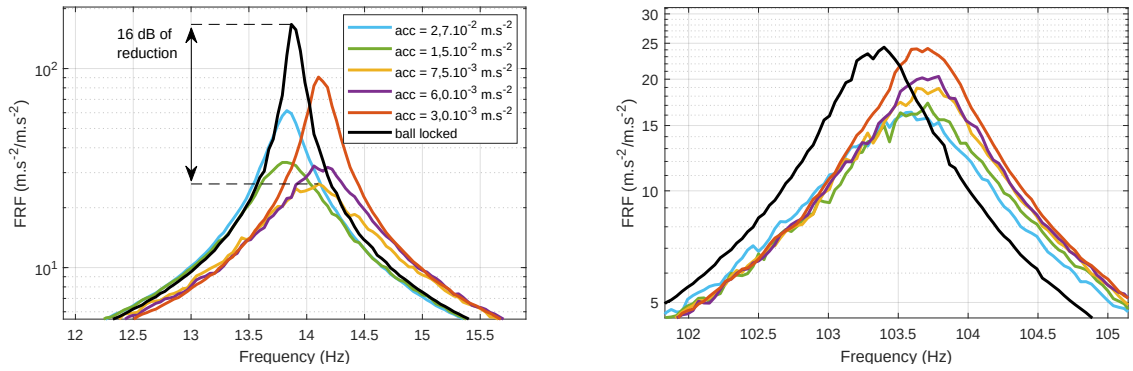

(a) Mode 1. (b) Mode 2.

Figure 3.13: Amplitude of the FRF for white noise excitation and gap = 1 mm.

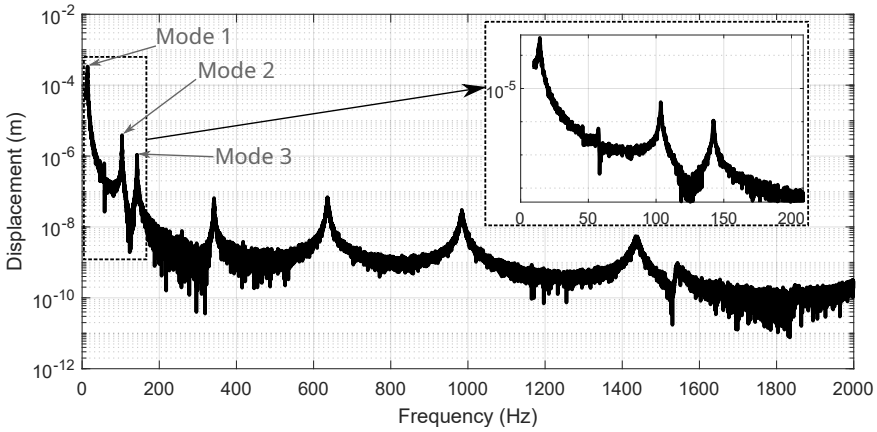

Figure 3.14: Spectrum of the beam displacement with the ball locked.

in this part of the frequency range. Indeed, the amplitude of displacements for the second resonant peak is significantly lower than for the first resonant peak as shown in figure 3.14. Moreover, the figure 3.13b shows that, the higher the amplitude of the excitation, the lower the peak of the FRF. This suggests that it would be necessary to increase significantly the excitation (or equivalently to reduce gap) in order to reach a maximum of the vibration reduction for the second mode.

These random excitation tests demonstrate that even for non-harmonic excitations, there exists an optimal configuration. However, the best configuration is found for one mode, but is not suited for the other modes since their amplitudes of vibration are very different. This observation is consistent with the results obtained under harmonic excitations. Therefore, no multi-mode mitigation can be performed with a single VI absorber on the beam, and a perspective would be to use several absorbers with very different gap values to deal with several modes simultaneously. Doing this, the absorbers with larger and smaller gaps would be effective for the lower and higher frequency modes, respectively.

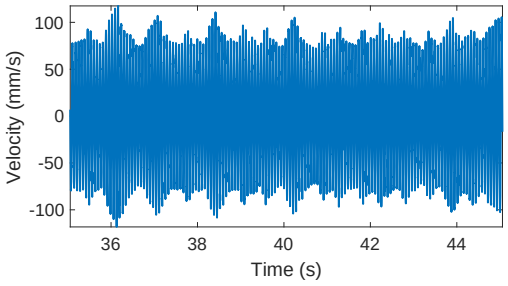

(a) Response of the beam undergoing SMR;

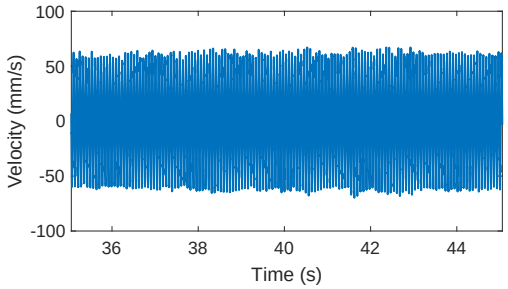

(b) Response of the beam undergoing 2 impacts per cycle.

Figure 3.15: Observation of the two regimes: SMR and two impacts per cycle.

3.5 Regimes and optimal operating point

3.5.1 Two regimes: SMR and 2 impacts per cycle

When structures possess an essential non-linearity as in the case of Non-Linear Energy Sink (NES), they exhibit specific operating regimes in the temporal domain. In the case of structures equipped with a VI absorber, the SMR and the regime with two impacts per cycle are of interest as they are related to the optimal operating point of the VI absorber [105].

The SMR is characterized by strong and visible changes of the envelope amplitude of the response of the main structure (see figure 3.15a). In this regime, phases with continuous impacts alternate with phases without impacts. As a consequence, less than two impacts per cycle are observed in average.

In the regime with two impacts per cycle, the impacts are continuously sustained and occur two times during an excitation period (see figure 3.15b). The envelope amplitude does not show significant changes and the response is almost periodic.

3.5.2 Optimal performance

The relation between the optimal performance of the absorber and the existence of the two regimes described above has been highlighted in [105, 74] numerically and experimentally. However, these studies deal with structures intentionally designed to behave as a S-DOF system. Such results have never been reported concerning multi-modal structures adopting an experimental approach. In the following paragraphs, the response of the beam is analysed in the time domain for different points designated from A to O on the FRFs (figure 3.6a). All the videos used to obtain the results of this section are provided as supplementary material of the article related to this chapter : *Experimental investigations of a vibro-impact absorber attached to a continuous structure*.

3.5.3 Counting the impacts

As the number of impacts per period is identified in the literature as an interesting feature to discriminate the different regimes, a method is developed to count the impacts given the temporal responses of the beam. For this purpose, the velocity of the beam is filtered using a highpass filter with a 500 Hz cut-off frequency, and its envelope is computed us-

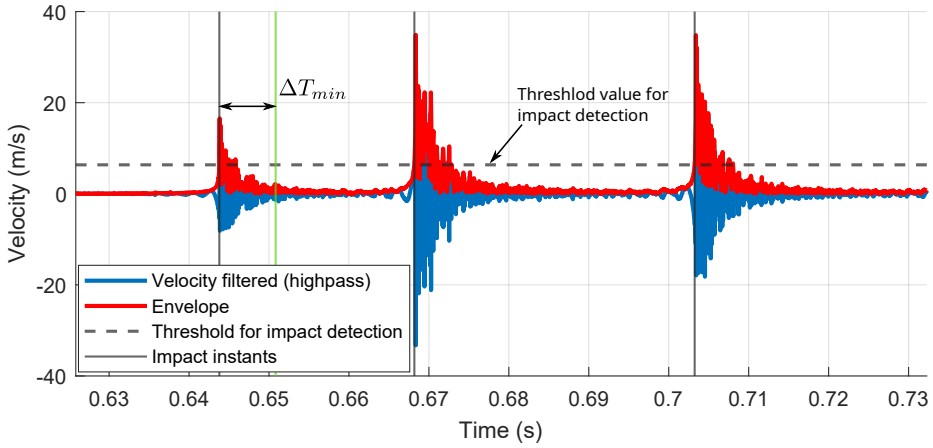

Figure 3.16: Illustration of the method developed for the impact detection.

ing the Hilbert transform. Then, two parameters must be set. Firstly, a threshold value is defined above which an impact is detected. Secondly, a minimum duration ΔT_{min} between impacts is assumed in order to avoid the detection of multiple impacts when only one occur. The method is illustrated in figure 3.16.

3.5.4 Clustering the regimes

Relying on the previous method, the number of impacts per period is counted for each temporal responses. The corresponding results are depicted in figure 3.17. The figure suggests gather the results in clusters using the number of impacts per period of the excitation as feature. Thus, three clusters are identified. In the first one, multiple impacts per period are observed. In the second one, two impacts per period occur, while in the third one, less than two impacts per period take place, corresponding mostly to the SMR. The temporal responses are given in appendix B.1 for more details.

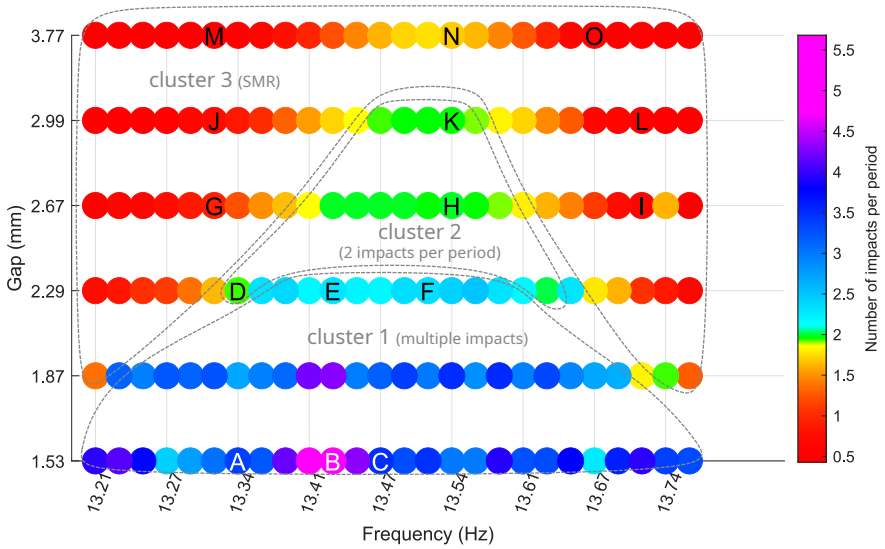

Figure 3.17: Number of impacts per period for each temporal responses.

The distribution of these clusters in the graph gap - frequency can be explained in

the following manner. Concerning the cluster one, the gap is very small making the ball bounce several times in the cavity. This is illustrated by the responses at point A, B, C, E and F. On the contrary, when the gap is increased, the course of the ball is longer and a quasiperiodic motion can be established. The oscillations of the ball are quite well synchronized with the oscillations of the beam, so that around two impacts per period are observed for points D, H and K. One should notice that the responses around point K for a gap equal to 2,99 mm are at the limit between the cluster two and the cluster three, as a desynchronization can be observed on the temporal response at point K (figure B.4), even if the regime with two impacts per cycle mostly happens. A similar remark can be done for points E and F which are between the two first clusters (figure B.2). At last, when the gap becomes too large compared to the amplitude of the beam the SMR is observed, that corresponds to the red areas where less than two impacts per period occur. This is the case when the gap is excessively increased, such as for responses corresponding to gap = 3,77 mm (points M, N and O), but also when the frequency of excitation is far from the resonance (points G, J, L, and I). The behavior of both the ball and the beam during the SMR can be described this way. Assuming that there are no impacts at the beginning of the analysis because the beam is at rest, the amplitude is increasing until the first vibro-impact occurs. At this moment the impacts are sustained for a while, and they contribute to reduce the amplitude of the beam. When the amplitude becomes too small, the impacts stop, the amplitude of the beam increases again and the process is repeated continuously. This can be well visualized looking at the temporal responses at point N in figure B.5.

In terms of vibration reduction, the regime with two impacts per period is the most effective as seen in figure 3.6a, and especially when the impacts occur at the maxima of velocity of the beam (point H). Indeed, more energy is involved in the impacts, and they contribute effectively to reduce the vibrations. When the regime with two impacts per period is observed but the impacts are not well synchronized on the maxima of velocity of the beam (this can be seen on the temporal response of point E for instance, even if it belongs to the first cluster), the vibration reduction is good but it is not as high as possible. In the optimal response reached for a gap equal to 2,67 mm, the two regimes SMR and two impacts per cycle are observed in the whole frequency range. This suggests that the gap value leading to the optimal response is at the limit between the appearance of the SMR and the regime with two impacts per period. On the contrary, if the gap is too small, multiple and low kinetic energy impacts occur. As explained before, the ball behaves mostly as an added mass and the vibration mitigation is not effective (points A, B, and C).

3.5.5 Conclusions

In conclusion of this analysis, the results lead to the following statements. (i) The gap value must be chosen in relation with the amplitude of the main structure, and the frequency of vibration has no direct influence on the choice of the gap (its influence on the amplitude is indirect since the frequency is close to the resonance frequency). (ii) If the gap is too small, the regime with two impacts per cycle is observed but the intensity of the impacts is low as they do not occur at the maxima of the velocity and the vibration reduction is not very effective. In this case, the impacts occur before the maximum velocity of the beam. If the gap is too large, the synchronization of the impacts on the beam is not sustainable and the SMR takes place, leading to a suboptimal vibration reduction.

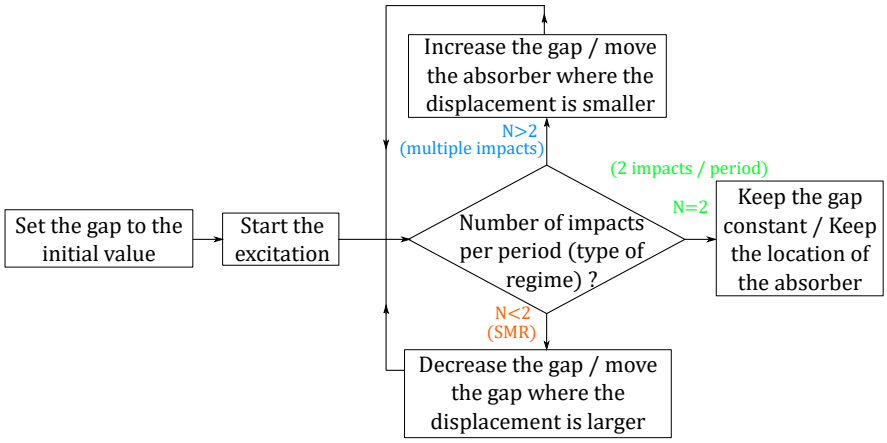

Figure 3.18: Flowchart for the optimal design of the absorber.

Just before the impacts stop, they occur after the maximum velocity of the beam. The optimal operating point is at the transition between those two regimes. (iii) Thanks to the scalability property, it is possible to extrapolate the argumentation to the acceleration amplitude while the gap is maintained constant. Increasing the gap is equivalent to reducing the acceleration and vice versa. A design flowchart is proposed in figure 3.18 in the case of harmonic excitation in order to help to choose the design parameters. More specifically, we can consider that the design parameters are the gap and the location of the VI absorber. Indeed, the excitation amplitude cannot be chosen in general. Therefore, we propose to modify either the gap or to move the VI absorber on the structure in order obtain the appropriate vibration amplitude.

The same conclusions are drawn when the second mode is excited. The corresponding results and analysis are in appendix B.2.

3.6 Physical phenomena at stake

3.6.1 Excitation of the higher modes

Previous studies [128] have presented numerical results highlighting the energy transfer that occurs towards the non-excited modes of a structure submitted to vibro-impacts. Here, it is not possible to quantify the energy transfer that takes place between the modes of the beam, but analyzing the Fourier transform of the temporal response of the beam for certain values of gaps and frequencies confirms the non-linear response of the beam and the excitation of the higher modes. As a remark, an interesting and recent study combining numerical and experimental results of a sphere impacting a beam are presented in [40], where the modal energy quantities of the beam are evaluated both experimentally and numerically. Figure 3.19 represents the Fourier transform of the temporal beam response at point H in figure 3.6a, the black vertical lines represent the eigenfrequencies of the beam. The curve plotted is the result of an average calculus. The temporal signal is divided in 40 parts of 10 periods long. The Fourier transform of each part is calculated, and the average corresponds to the curve in figure 3.19. The higher modes of the beam are clearly responding due to the vibro-impacts. It is also possible to visualize some harmonics of the excitation, as there are some peaks located at frequencies corresponding to multiples of 14,21 Hz indicated by arrows in the figure.

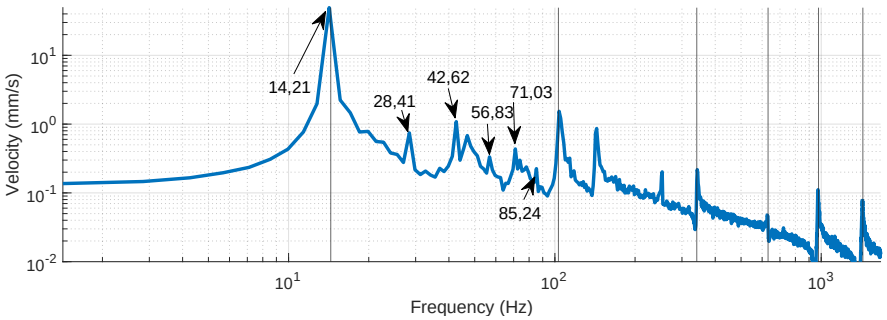

Figure 3.19: Fourier Transform of the temporal beam response at point H (gap = 2,67 mm and f = 14,2 Hz).

Here, one may want to compare the spectrum of the beam response for different gap configurations, and more precisely the amplitude of the peak for higher modes. However, when the gap value is changed, the vibration regime is also modified as well as the intensity of the impacts. As a consequence, it is not possible to compare directly the amplitudes in the spectrum without any information about the impact force applied by the ball. Measuring this force and the mechanical energy of the beam would be an interesting approach, but is still an experimental challenge to take up.

3.6.2 Energy stored and dissipated by the ball

As explained earlier in this paper, the way vibro-impacts help to dissipate the vibrational energy still needs to be clarified. In some cases, the energy is assumed to be dissipated during inelastic impacts (i.e a certain amount of the kinetic energy of the two bodies colliding is lost during the impact). In other cases, and more particularly in the case of multi-modal structures, the energy is supposed to be redistributed within the modal space thanks to the vibro-impacts and dissipated faster than when the energy is only contained in a low frequency mode.

Another point is that the ball itself stores a small part of the vibrational energy in the form of translational or rotational kinetic energy (the rotation is quite visible on the videos). Before the first vibro-impact, the ball is at rest and its kinetic energy is zero. When the first impact occurs, a certain amount of energy goes from the beam to the ball that starts moving. After a few impacts, this transient motion ends and the ball oscillates more regularly (it can be said that the beam has reached a steady state, but this notion is not suited to the case of a VI beam as the response is never exactly periodic). A certain amount of the vibrational energy of the beam goes to the ball to maintain its oscillating motion, otherwise it would stop because of friction that slows the ball during its free flight phases. Indeed, the kinetic energy of the ball is decreasing between impacts in figure 3.20. This means that a small amount of the energy is dissipated through friction in the cavity. Another amount of the energy initially localized on the first mode is redistributed to the higher modes of the beam when the impacts occur.

The energy of the ball is plotted for different gap configurations in figure 3.20. Particular attention should be paid to the ordinate scale that is the same for all graphs at the top of the figure in order to compare the amplitudes between the gap configurations. One can see that the lowest level of kinetic energy of the ball is reached when the gap is 2,67 mm, what corresponds to the optimal case in terms of vibration reduction of the first mode

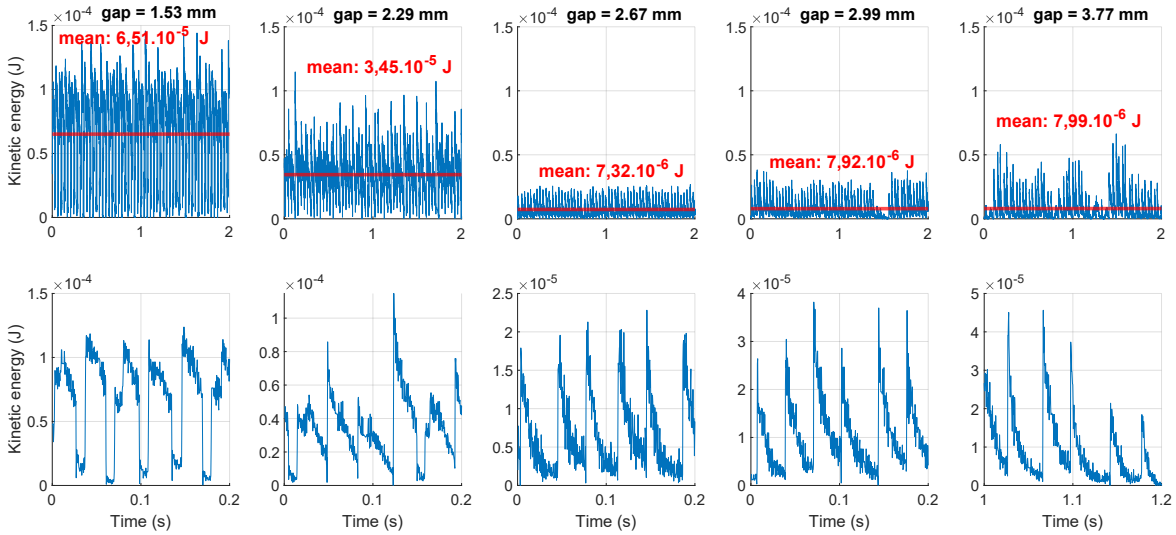

Figure 3.20: Kinetic energy of the ball in time domain for different gap values. Top: Entire signal. Bottom: zoom on a few periods.

(regime with two impacts per period). Even if it can be surprising at first sight, it makes sense as the lowest amplitude of the beam leads to smaller velocities of the ball. For the gap of 3,77 mm corresponding to the regime SMR, the phases with no impacts are quite visible as they correspond to the smallest amplitudes of the kinetic energy of the ball.

As a conclusion, these results demonstrate that if the ball stores a small amount of the vibrational energy of the beam, it is not the main way to reduce the vibrations as the more effective configuration (gap = 2,67 mm) leads to the smallest energy of the ball. The theory that the energy is transferred to the higher modes of the beam is therefore compatible with the previous observations.

3.7 Conclusions

In this work, the effectiveness of a vibro-impact absorber with tunable gap attached to the tip of a beam is demonstrated experimentally. The beam is harmonically excited at its base, and both the response of the beam end and the motion of the ball are measured, using respectively a laser vibrometer and a high-speed camera associated with a Digital Image Correlation technique. Such experimental study dealing with vibro-impact absorber on a multi-modal and continuous structure has never been reported in the literature before.

A parametric study highlights the existence of an optimal gap that reduces efficiently the vibration amplitude of one mode of the beam under constant excitation amplitude. Equivalently, there exists an optimal excitation amplitude if the gap is maintained constant, and this can be translated into a scalability property. At last, an optimal configuration was found for the first and for the second mode of the beam under harmonic excitation. Under white noise excitation, an optimal vibration mitigation was found for the first mode but multi-mode mitigation was not possible to achieve with a single VI absorber.

In order to better understand the working principle of the vibro-impact absorber, the temporal responses of the beam and the motion of the ball are analyzed for different con-

figurations. The responses of the beam can be gathered in three clusters. In the first one, the gap is too small compared to the amplitude of the beam, so that multiple and weak impacts occur leading to a poor vibration reduction. In the second cluster, the gap is well tuned and a quasiperiodic motion takes place with two impacts per period. This regime is optimal in terms of vibration reduction. The last cluster corresponds to the case where the amplitude of the beam is not high enough to activate the impacts continuously. Therefore, less than two impacts per period are observed and the Strongly Modulated Regime is visible, leading to a suboptimal vibration reduction.

Furthermore, analyzing the spectrum of the response of the beam undergoing the optimal regime shows that the higher modes of the beam are excited as well as the harmonics of the excitation. This demonstrates the energy transfer and the non-linear behavior of the vibro-impacted beam. The study of the energy of the ball highlights its role in the energy transfer during vibro-impact.

On the whole, these promising results open up new perspectives for vibro-impact absorbers, especially concerning their technological development and their optimal design.

Chapter 4

Understanding vibro-impacts through a numerical energy-based approach

Contents

Preamble

In the previous chapters, we have derived the coefficient of restitution in the case of a specific experimental set-up using full-field measurements. In this respect, the coefficient of restitution informs about the energy dissipated during the impacts. Furthermore, we have also demonstrated experimentally the performance of a vibro-impact absorber attached to a beam in chapter 3. In this last case however, tackling the physical phenomena at stake in order to explain experimentally and quantitatively how the energy is dissipated is still a challenge. Accordingly, this question can be addressed numerically as energy quantities can be more easily computed than experimentally measured. Thus, the objective of this chapter is to analyze the energy balance of a beam submitted to vibro-impact to better explain the working principle of vibro-impact absorbers.

4.1 Introduction

In the papers dealing with vibro-impact absorbers, many of them consider systems represented by a single degree of freedom (S-DOF) [79, 76, 3, 45, 74]. In these cases, the energy is assumed to be dissipated during the impacts. To describe this process, two modeling approaches are proposed. In the first one, the impacts are considered instantaneous, and the energy dissipated is related to a coefficient of restitution [116]. The energy dissipated during the impacts is evaluated in [76, 77, 74]. Even if using a coefficient of restitution is very convenient from a numerical point of view, it can lead to undesirable approximations [79] and the choice of a realistic value for the coefficient of restitution can turn out to be a hard problem [27]. The second approach consists in resolving the dynamics during the contact phase. To do so, contact models are used such as the Hertz contact model for instance [79, 90, 42, 116], though other models can be used. Usually, a damper is considered and it models the energy dissipation. Moreover, the damping coefficient is often related to a coefficient of restitution in order to obtain an equivalent energy dissipation [90, 79, 27, 116].

However, S-DOF systems may not represent the dynamic behavior of more realistic structures where other physical phenomena can occur. Indeed, a few papers consider multi-modal structures and have evidenced that the vibro-impacts lead to redistribute the vibrational energy within the modal space [136, 8, 83, 95] even if this redistribution is not quantitatively determined. In other works, the energy transfers are evaluated for 2-DOF structures [106, 48], for multi-DOF structures [7, 49], or for a beam structure [128, 37, 129]. Transient excitations are mainly considered, whereas in the case of harmonic excitations, the frequency is close to the first resonance only.

In the previous cases, the equations of motion are seldom solved in the frequency domain using the Harmonic Balance Method, though the hypothesis of periodic response can be questioned. Mostly, the differential equations are solved in the time domain using numerical integration. Thus, the energy balance can be derived. But the accuracy of the calculations is related to the integration scheme and to the size of the time step, that may be hard to choose in the case of vibro-impact problems.

The approach adopted in this chapter is to focus on the energy transfers within the modal space for a beam endowed with a vibro-impact absorber, considering conservative impacts. For this purpose, the impacts are described using a coefficient of restitution equal to one, and the equations of motion are solved analytically between impacts. This method allows deriving energy balance with negligible error. Then, the energy transfers in the case of a harmonic excitation centered on the first, second, and third mode are considered demonstrating the effectiveness of the vibro-impact absorber in each case. Additionally, the way the energy is dissipated is explained and quantitatively assessed. At least, the results obtained for the first three modes are compared.

4.2 Dynamics of a beam with vibro-impacts

4.2.1 Model, parametrisation, and equations of motion

4.2.1.1 Model and parametrisation

The problem considered in this chapter is a cantilever beam submitted to a bending load. A vibro-impact absorber is attached to the beam, consisting in a ball able to travel vertically in a cavity. The displacement of the ball is limited by two stops linked to the beam.

The beam is oriented by the $\vec{x}$ axis, while the $\vec{y}$ axis corresponds to the bending direction. A notional diagram is provided in figure 4.1.

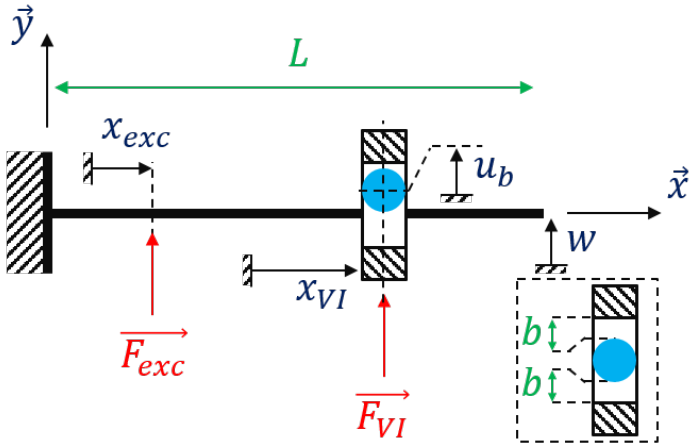

Figure 4.1: Clamped-free beam with an attached vibro-impact absorber.

The following list defines the parameters of the problem:

- $w(x,t)$ is the transverse displacement of the beam;
- $u_b(t)$ is the displacement of the ball;
- x_{exc} is the position of the external excitation force;
- x_{VI} is the position of the vibro-impact absorber on the beam;
- L is the length of the beam;
- b is the half-gap of the cavity (the ball can oscillate over a distance equals to $2.b$);
- m_b is the mass of the ball;
- ρ is the density of the material of the beam;
- E is the Young's modulus of the material of the beam;
- I is the second moment of area of the beam;
- A is the area of the cross-section of the beam;
- $\overrightarrow{\mathrm{F}_{exc}}$ is the external exciting force;

- $\overrightarrow{\mathrm{F_{VI}}}$ is the contact force of the ball on the beam during impacts.

All the simulations presented are done for the numerical values given in table 4.1. Therefore the mass ratio is equal to $1,8\%$, calculated as $\frac{m_b}{\rho.A.L}$.

m_b (kg)	E (Pa)	ρ (kg.m^{-3})	I (m^4)	A (m^2)	L (m)	x_{exc} (m)	x_{VI} (m)	F_{exc} (N)
$3,9.10^{-3}$	7.10^{10}	2700	$4,17.10^{-10}$	2.10^{-4}	0,4	0,08	0,4	10

Table 4.1: Numerical values of the parameters.

4.2.1.2 Equations of motion

Here, the beam is modeled using linear Euler-Bernoulli theory, so that only bending motions are considered and rotational inertia of the cross-sections are neglected. In this context, the equation governing the dynamic of the beam is:

$$E.I.\frac{\partial^4 w}{\partial x^4} + \rho.A.\frac{\partial^2 w}{\partial t^2} = \delta(x - x_{exc}).F_{ext}(t) + \delta(x - x_{VI}).F_{VI}(u_b, w); \tag{4.1}$$

while the second Newton's law applied to the ball gives:

$$m_b.\ddot{u}_b = -F_{VI}(u_b, w). \tag{4.2}$$

4.2.1.3 Definition of the excitation force and the contact force

For the purpose of this numerical study, we consider a harmonic external forcing. Therefore, $\overrightarrow{F_{exc}} = F_{exc}(t).\vec{y}$ is defined as:

$$F_{exc}(t) = F_{exc}.\sin(\omega.t). \tag{4.3}$$

The contact force of the ball on the beam is defined as:

$$\overrightarrow{F_{VI}} = F_{VI}(u_b, w).\vec{y}; \tag{4.4}$$

and:

$$\begin{cases} F_{VI}(u_b, w) = 0 & \text{if} \quad |u_b(t) - w(x_{VI}, t)| < b; \\ F_{VI}(u_b, w) > 0 & \text{if} \quad u_b(t) - w(x_{VI}, t) \geq b; \\ F_{VI}(u_b, w) < 0 & \text{if} \quad u_b(t) - w(x_{VI}, t) \leq -b. \end{cases}$$

The exact expression of $F_{VI}(u_b, w)$ will be detailed later in this chapter.

4.2.2 Modal decomposition and problem reformulation

4.2.2.1 Determination of the modal basis

The dynamic behavior of the beam is governed by equation (4.1), where the displacement $w(x,t)$ must be determined. We first look for the free response of the system, so that F_{exc} and $F_{VI}(u_b, w)$ are null.

A common technique is to use the method of separation of variables. We look for a solution $w(x,t)$ which is the product of a spatial-dependent function φ and a time-dependent function q:

$$w(x,t) = \varphi(x).q(t). \tag{4.5}$$

Using the notations $\frac{\partial^2 q}{\partial t^2} = \ddot{q}$ and $\frac{\partial^k \varphi}{\partial x^k} = \varphi^{(k)}$ to express the derivatives, injecting equation (4.5) in equation (4.1), and assuming that $q \neq 0$ and $\varphi \neq 0$ we obtain:

$$\rho.A.\ddot{q}.\varphi + E.I.q.\varphi^{(4)} = 0 \quad \Leftrightarrow \quad \frac{\ddot{q}}{q} = -\frac{E.I}{\rho.A}.\frac{\varphi^{(4)}}{\varphi}. \tag{4.6}$$

The left-hand side is a time-dependent function, while the right-hand side is a spatial-dependant function. As a consequence, both sides of the equation are constant with respect to time and space. Let's set:

$$\frac{\ddot{q}}{q} = \lambda; \tag{4.7}$$

and:

$$\frac{\varphi^{(4)}}{\varphi} = k^4; \tag{4.8}$$

where k is the wave number and is:

$$k^4 = -\frac{\rho.A}{E.I}.\lambda. \tag{4.9}$$

Since we are interested in oscillating solutions, we consider the case where $\lambda > 0$, and we set:

$$\lambda = -\omega^2. \tag{4.10}$$

The solution of equation (4.8) is given in equation (4.11):

$$\varphi(x) = c.\cos(k.x) + d.\sin(k.x) + e.\cosh(k.x) + h.\sinh(k.x); \tag{4.11}$$

where c, d, e and h are fixed by the boundary conditions of the beam. These clamped-free conditions must be verified at all time, and they are formulated in appendix C.1. The equation system obtained leads to the final equation (4.12) that governs the wave number of the bending clamped-free beam.

$$\cos(k.L).\cosh(k.L) = -1. \tag{4.12}$$

There exists an infinite number of solutions k_i ($i \in \mathbb{N}^*$) that can be determined numerically. From equation (4.9) and equation (4.10), we are also able to derive the eigenfrequencies of the beam, or the eigenvalues of the problem, associated to the mode shapes using equation (4.11), or the eigenvectors of the problem. The association of an eigenvalue and eigenvector is an eigenmode, and they form a basis for the solutions.

Finally, the equation system in appendix C.1 allows to determine only three of the four constants c, d, e and h. Thus, it is necessary to fix one of the constants, what corresponds to normalize the mode shapes φ_i. Renaming the constant to determine α_i, it is therefore possible to derive the following expression for the mode shapes:

$$\varphi_i(x) = \frac{1}{\alpha_i}.[\sin(k_i.x) - \sinh(k_i.x) + \beta_i.(\cos(k_i.x) - \cosh(k_i.x))]; \tag{4.13}$$

where α_i depends on the normalisation. It is common to choose α_i in order to obtain unitary modal masses as explained below, which is $\int_0^L \rho.A.\varphi_i^2(x).dx = 1$.

And:

$$\beta_i = \frac{\cos(k_i.L) + \cosh(k_i.L)}{\sin(k_i.L) - \sinh(k_i.L)}. \tag{4.14}$$

4.2.2.2 Determination of the modal equation with external forcing

In this part, the external forcing is considered as non-zero. Using the modal basis determined previously, the response of the beam is projected onto the modal basis, so that:

$$w(x,t) = \sum_{i=1}^{+\infty} \varphi_i(x).q_i(t); \tag{4.15}$$

where φ_i and q_i are the mode shape and the modal coordinate of the i-th mode, respectively. As it is not possible to work with a basis of solutions that has an infinite dimension, a modal truncation is adopted. It consists in considering only the N first modes, assuming that neglecting the higher modes leads to negligible error in the dynamic behavior of the system. The displacement becomes:

$$w(x,t) = \sum_{i=1}^{N} \varphi_i(x).q_i(t). \tag{4.16}$$

Furthermore, the eigenmodes satisfy the orthogonality properties in the meaning of dot product. We have:

$$\begin{cases} \int_0^L \rho.A.\varphi_i(x).\varphi_j(x).dx = 0 & \text{if} \quad i \neq j; \\ \int_0^L \rho.A.\varphi_i(x).\varphi_j(x).dx = m_i & \text{if} \quad i = j; \end{cases}$$

and:

$$\begin{cases} \int_0^L E.I.\varphi_i(x).\varphi_j^{(4)}(x).dx = 0 & \text{if} \quad i \neq j; \\ \int_0^L E.I.\varphi_i(x).\varphi_j^{(4)}(x).dx = k_i & \text{if} \quad i = j; \end{cases}$$

where m_i and k_i are called the modal mass and the modal stiffness, respectively. Usually, the normalization of the modal shapes is chosen in order to obtain unitary modal mass, which is $m_i = 1$. Reinjecting equation (4.16) in equation (4.1), we can get rid of the sum using the dot product with respect to mass premultiplying by $\varphi_i(x)$ and integrating along the x-axis. At this point we can directly add a damping term in the modal equation using the modal damping coefficient c_i. This is an easy way to take in account the dissipation of the material without using a complex model of dissipation. Thus, equation (4.17) is obtained and the unknown q_i can be determined solving this modal equation:

$$m_i.\ddot{q}_i + c_i.\dot{q}_i + k_i.q_i = \varphi_i(x_{exc}).\mathrm{F}_{exc}(t) + \varphi_i(x_{\mathrm{VI}}).\mathrm{F}_{\mathrm{VI}}(u_b, w) \qquad i \in [\![1\ ;\ \mathrm{N}]\!]. \tag{4.17}$$

Or, using a matrix formalism:

$$[\mathrm{M}].\{\ddot{q}\} + [\mathrm{C}].\{\dot{q}\} + [\mathrm{K}].\{q\} = \mathrm{F}_{exc}.\{\varphi(x_{exc})\} + \mathrm{F}_{\mathrm{VI}}.\{\varphi(x_{\mathrm{VI}})\}; \tag{4.18}$$

where [M], [C], [K] denote the modal mass, damping and stiffness matrices. If unitary modal masses are used, then $[\mathrm{M}] = [\mathbb{1}]$. For general considerations, the mass matrix term [M] will be kept.

4.2.3 Analytical solutions during free flight phases

We start to study the response of the system between impacts. This situation corresponds to $\mathrm{F}_{\mathrm{VI}}(u_b, w) = 0$ and the equation (4.17) and equation (4.2) become:

$$m_i.\ddot{q}_i + c_i.\dot{q}_i + k_i.q_i = \varphi_i(x_{exc}).\mathrm{F}_{exc}(t); \tag{4.19}$$

and:

$$m_b.\ddot{u}_b = 0. \tag{4.20}$$

The solution of equation (4.20) is:

$$u_b(t) = \mathrm{A}.t + \mathrm{B}; \tag{4.21}$$

where A and B must be determined thanks to the initial conditions.
Let's define the following quantities for the i-th mode:

- $\omega_i = \sqrt{\frac{k_i}{m_i}}$ the eigenpulsation;
- $\xi_i = \frac{c_i}{2.\sqrt{m_i.k_i}}$ the modal damping ratio;
- $\Omega_i = \omega_i.\sqrt{1-\xi_i^2}$ the pseudo-pulsation.

The well-known solution of a second order ordinary differential equation (4.19) with a harmonic second member is the sum of the homogeneous solution $q_i^h(t)$ and of a particular solution $q_i^p(t)$ where:

$$q_i^h(t) = e^{-\omega_i.\xi_i.t}.[a_i.\cos(\Omega_i.t) + b_i.\sin(\Omega_i.t)]; \tag{4.22}$$

and:

$$q_i^p(t) = d_i.\sin(\omega.t) + e_i.\cos(\omega.t). \tag{4.23}$$

The constants a_i and b_i must be determined using the initial conditions, while the constants d_i and e_i must satisfy equation (4.19) in the stationary response when the homogeneous solution given in equation (4.22) has vanished. In appendix C.2, the determination of the constants are described, and a remark related to the implementation of equation (4.22) in a computer program is proposed.

4.2.4 Determination of the solutions at impact instants

4.2.4.1 On the determination of impacts instants

Up to now, we were able to determine the solutions for $w(x,t)$ and $u_b(t)$ analytically without approximations. However, we will see that no analytical solution exists to determine the exact impact instant.

The contact conditions corresponding to an impact of the ball on the beam are:

$$\begin{cases} u_b(t) - w(x_{\text{VI}}, t) = b & \text{for contact on top;} \\ u_b(t) - w(x_{\text{VI}}, t) = -b & \text{for contact at the bottom.} \end{cases} \tag{4.24}$$

Given the form of $u_b(t)$ and $w(x,t)$ in equation (4.21) and equation (4.16), the only way to compute the contact instant t_c is to solve the contact conditions 4.24 numerically. To reach this objective, the same methodology presented in [9] is used. Practically, it consists in a dichotomy: for each time step, the contact conditions are monitored. When one of them is reached at time step t_i, we come back to the previous time step t_{i-1} and divide it by ten ($\Delta t = \Delta t/10$). The process is repeated until the time step has reached a threshold value, which is chosen small enough to consider that contact instant is accurately determined on the one hand, and that the calculation is fast enough on the other hand.

Let's consider that the displacements are computed for discrete time steps t_i. The initial width of the time step is $\Delta t = t_{i+1} - t_i$. We also define two vectors D_{top} and D_{bot} whose components are a measure of the distance between the ball and the top and bottom of the cavity for the first ten time steps:

$$\mathrm{D}_{top} = \begin{pmatrix} u_b(t_1) - w(x_{\text{VI}}, t_1) - b \\ \vdots \\ u_b(t_{10}) - w(x_{\text{VI}}, t_{10}) - b \end{pmatrix} \quad \text{and} \quad \mathrm{D}_{bot} = \begin{pmatrix} u_b(t_1) - w(x_{\text{VI}}, t_1) + b \\ \vdots \\ u_b(t_{10}) - w(x_{\text{VI}}, t_{10}) + b \end{pmatrix}.$$

Let's call $\mathrm{D}_{top}(t_i)$ the component of D_{top} in which the time step is equal to t_i (the same applies to D_{bot}). We are looking for a change of sign in each component of D_{top} and D_{bot} that would mean that one of the contact conditions is reached. More specifically the components of D_{top} are always strictly negative without contact, while the components of D_{bot} are always strictly positive. Therefore, a contact at the top gives $\mathrm{D}_{top}(t_i) \geq 0$, and a contact at the bottom leads to $\mathrm{D}_{bot}(t_i) \leq 0$. While no contact is detected, the next ten time steps are considered. The general expressions of the vectors D_{top} and D_{bot} starting at t_i are:

$$\mathrm{D}_{top} = \begin{pmatrix} u_b(t_i) - w(x_{\mathrm{VI}}, t_i) - b \\ \vdots \\ u_b(t_{i+k}) - w(x_{\mathrm{VI}}, t_{i+k}) - b \\ \vdots \\ u_b(t_{i+10}) - w(x_{\mathrm{VI}}, t_{i+10}) - b \end{pmatrix} \quad \text{and} \quad \mathrm{D}_{bot} = \begin{pmatrix} u_b(t_i) - w(x_{\mathrm{VI}}, t_i) + b \\ \vdots \\ u_b(t_{i+k}) - w(x_{\mathrm{VI}}, t_{i+k}) + b \\ \vdots \\ u_b(t_{i+10}) - w(x_{\mathrm{VI}}, t_{i+10}) + b \end{pmatrix}.$$

When a change of sign is detected between the time steps t_{i+k} and t_{i+k+1} ($k \in [\![0;9]\!]$), the following method is applied:

- we come back to the time step t_{i+k};
- the width of the time step is divided by ten: $\Delta t = \Delta t/10$, so that we have ten new time steps between t_{i+k} and t_{i+k+1};
- we compute the vectors D_{top} and D_{bot} starting now at t_{i+k}.

Again, we can now look for the change of sign and repeat this process iteratively while $\Delta t > \Delta t_{thr}$ where Δt_{thr} is a threshold value that determines the accuracy of the approximation of the contact instant. The figure 4.2 illustrates the reduction of the step size before the impact instant, and the flowchart in figure 4.3 describes the process.

When this condition is reached, we know that the contact instant t_c verifies the following inequality:

$$t_{i+k} < t_c < t_{i+k+1}; \tag{4.25}$$

and we make the approximation: $t_c \approx t_{i+k}$ with an error smaller or equal to Δt_{thr}.

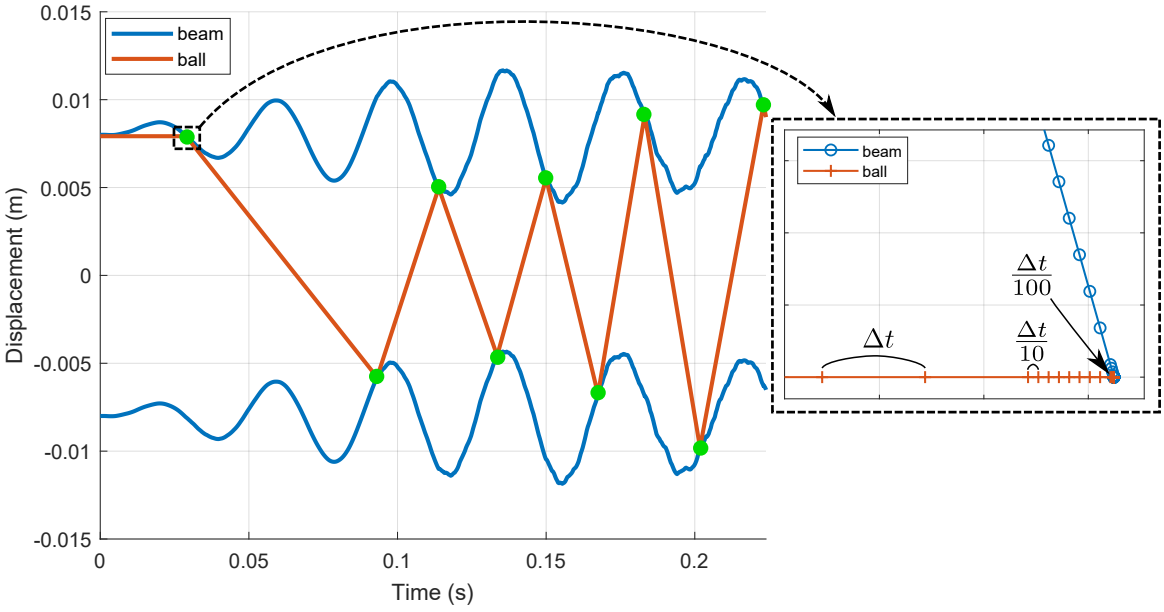

Figure 4.2: Illustration of the iterative process implemented in order to approximate the impact instant. The green dots denote the impact of the ball with the beam.

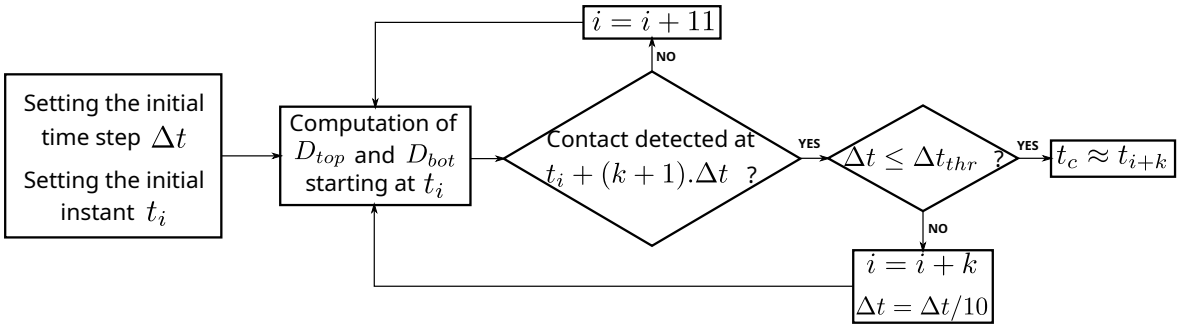

Figure 4.3: Flowchart describing the impact detection process.

4.2.4.2 Post-impact solutions

When the impact occurs, several strategies can be used to describe what happens during the contact and to obtain the state of the system immediately after the impact. Here, the choice is made to use a coefficient of restitution to describe the impact behavior. Many reasons have motivated this choice. First, the contact duration is reasonably short compared to the typical duration of oscillation of the first mode of the beam. As a consequence, the coefficient of restitution is suited as it allows to obtain the state of the system immediately after the impact without computing the behavior of the system during the contact phases. Moreover, an alternative could be to use a Hertz model to describe the contact between the ball and the beam, but unfortunately in this case no analytical solutions exist. This strategy is therefore eliminated as the objective is to use only analytical solutions in order to derive exact energy balance. Furthermore, one of the objective is to study the modal energy transfer induced by the vibro-impacts and to investigate the ability of this strategy to reduce the vibrations even in the case of non-dissipative impacts. This can be easily realized setting the coefficient of restitution to one.

The coefficient of restitution may be defined in various manners. Usually, a kinematic, kinetic, or energetic coefficient of restitution is used. The previous definitions are provided in [116]. Here, we choose to use the kinematic definition considering the COR as the ratio of the relative velocities below and after the impact:

$$e = \frac{\dot{u}_b(t_c^+) - \dot{w}(x_{\mathrm{VI}}, t_c^+)}{\dot{u}_b(t_c^-) - \dot{w}(x_{\mathrm{VI}}, t_c^-)}. \tag{4.26}$$

In equation (4.26), t_c denotes the impact instant, and t_c^+ and t_c^- are the instant immediately after and before the impact respectively. The objective is to use e to determine the unknowns after an impact for $t = t_c^+$, which are $u_b(t_c^+)$, $\dot{u}_b(t_c^+)$, $q_i(t_c^+)$, $\dot{q}_i(t_c^+)$ knowing the state of the system for $t = t_c^-$. For this purpose, we will integrate the modal equation (4.17) during the impact [37]. This can be written using a matrix formalism:

$$[\mathrm{M}].\{\ddot{q}\} + [\mathrm{C}].\{\dot{q}\} + [\mathrm{K}].\{q\} = \mathrm{F}_{exc}.\{\varphi(x_{exc})\} + \mathrm{F}_{\mathrm{VI}}.\{\varphi(x_{\mathrm{VI}})\}.$$

Integrating between $t = t^-$ and $t = t^+$ and multiplying by $[\mathrm{M}]^{-1}$ leads to:

$$\{\dot{q}^+\} - \{\dot{q}^-\} = [\mathrm{M}]^{-1}.\{\varphi(x_{\mathrm{VI}})\}.\int_{t_c^-}^{t_c^+}.\mathrm{F}_{\mathrm{VI}}(u_b, w).dt. \tag{4.27}$$

Indeed, as the modal coordinates $\{q(t)\}$ and $\mathrm{F}_{exc}(t)$ are continuous functions of time, it implies that $\int_{t_c^-}^{t_c^+}\{q(t)\}.dt = 0$, $\int_{t_c^-}^{t_c^+}\{\dot{q}(t)\}.dt = \{q^+\} - \{q^-\}) = 0$, and

$\int_{t_c^-}^{t_c^+} \mathrm{F}_{exc}(t).dt = 0$. Therefore, $[\mathrm{M}]^{-1}.[\mathrm{K}].\int_{t_c^-}^{t_c^+} \{q(t)\}.dt = 0$, $[\mathrm{M}]^{-1}.[\mathrm{C}].(\{q^+\} - \{q^-\}) = 0$ and $[\mathrm{M}]^{-1}.\int_{t_c^-}^{t_c^+} \mathrm{F}_{exc}(t).dt = 0$.

Moreover, the impulse P applied by the ball on the beam is defined as $\mathrm{P} = \int_{t_c^-}^{t_c^+} \mathrm{F}_{\mathrm{VI}}(u_b, w).dt$, and the second Newton's law gives that:

$$\mathrm{P} = -m_b.(\dot{u}_b^+ - \dot{u}_b^-); \tag{4.28}$$

Injecting equation (4.28) in equation (4.27) and multiplying by $\{\varphi(x_{\mathrm{VI}})^{\mathrm{T}}\}$, we obtain:

$$\dot{w}^+ - \dot{w}^- = -m_b.(\dot{u}_b^+ - \dot{u}_b^-).\{\varphi(x_{\mathrm{VI}})^{\mathrm{T}}\}.[\mathrm{M}]^{-1}.\{\varphi(x_{\mathrm{VI}})\}; \tag{4.29}$$

We can now replace $\dot{w}^+$ in equation (4.26) in order to express $\dot{u}_b^+$ only as a function of quantities evaluated at t_c^-:

$$\dot{u}_b^+ = \frac{\dot{w}^-.(1+e) + \dot{u}_b^-.(m_b.\{\varphi(x_{\mathrm{VI}})\}^{\mathrm{T}}.[\mathrm{M}]^{-1}.\{\varphi(x_{\mathrm{VI}})\} - e)}{m_b.\{\varphi(x_{\mathrm{VI}})\}^{\mathrm{T}}.[\mathrm{M}]^{-1}.\{\varphi(x_{\mathrm{VI}})\} + 1}. \tag{4.30}$$

Equation (4.30) can be used in equation (4.27) to obtain the modal coordinates after the impact:

$$\{\dot{q}^+\} = \{\dot{q}^-\} - m_b.(\dot{u}_b^+ - \dot{u}_b^-)[\mathrm{M}]^{-1}.\{\varphi(x_{\mathrm{VI}})\}. \tag{4.31}$$

At the end, the derivatives of the modal coordinates and the velocity of the ball after the impact are fully determined thanks to equation (4.30) and equation (4.31). The displacement of the ball and modal displacements are unchanged during an impact, such that $u_b^+ = u_b^-$ and $\{q^+\} = \{q^-\}$. Thus, the time response of the beam submitted to vibro-impact can be determined analytically, where negligible approximations are necessary to solve the contact instant.

4.3 Energy-based approach

The behavior of the beam under harmonic excitations is studied. The excitation frequencies are chosen in the vicinity of the first three modes of the beam. The displacements and velocities are evaluated at the end of the beam. For all the results obtained in this section, the parameters of the model are defined as follows:

- the number of modes in the modal basis is arbitrarily set to eight [2];
- the initial time step is equal to $2.\pi/(20.\omega_8)$, so that twenty time steps are used to describe the fastest oscillation of the beam;
- the threshold value Δt_{thr} for the impact detection is set to 1.10^{-13} s;
- the coefficient of restitution e is set to one.

More specifically, we decided to set $e = 1$ in order to assess numerically the effectiveness of a vibro-impact absorber in the case of non-dissipative impacts. The other phenomena leading to energy dissipation will be investigated and described in this section.

[2] The same study is realized with 6 modes in appendix C.6.

As a remark, considering more than eight modes in the modal basis leads to prohibitive simulation cost. Meanwhile, it allows to represent the multimodal behavior of the beam with a sufficient accuracy to keep eight modes in the basis.

4.3.1 Specific regimes and vibration attenuation

In this section, we will present the typical responses of the beam with the VI absorber using the model presented in the previous section. At the beginning of each response, both the beam and the ball are at rest: $\{\dot{q}(t=0)\} = \{0\}$ and $\dot{u}_b(t=0) = 0$. The displacement of the ball is null, whereas the position of the ball is $0,99 \times b$ (close to the contact condition) in order to ensure the occurrence of the vibro-impacts.

4.3.1.1 Determination of the mean amplitude

In order to be able to plot the response of the beam in the frequency domain, it is necessary to determine the amplitude of the response of the beam for each excitation frequency. For this purpose, the method applied is to detect the maxima for each period of excitation and to calculate the average of these maxima to obtain the mean amplitude of the beam. In order to get rid of a possible transient regime at the beginning of the response, the maxima are detected after a duration $\tau = \frac{\log(1000)}{\xi_1.\omega_1}$ that corresponds to the duration necessary to reduce of a factor 1000 the transient regime of the first mode which is the slowest mode to mitigate. One hundred of maxima are used to calculate the average as illustrated in figure 4.4.

It is worthy to note that, in chapter 3, the mean amplitude was calculated from the envelope of the signal computed using the Hilbert transform and not the maxima during each period of excitation. As it was verified that the two methods give the same mean amplitude, and that the results presented in this section were obtained prior to the experimental results of the chapter 3, the method has been left unchanged.

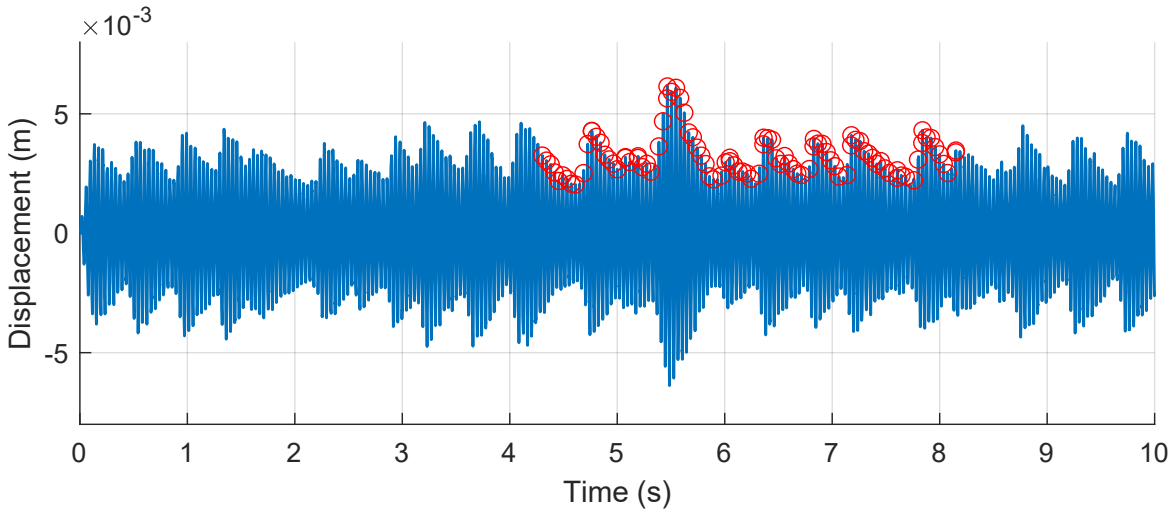

Figure 4.4: Response of the beam in the time domain. The red circles denote the maxima for each period of excitation.

4.3.1.2 Optimal gap and time responses

We realized a parametric study on the gap, varying the gap in the range 1 mm - 15 mm with increments of 1 mm. The mean amplitude of the beam is calculated for each frequency and for the different gap values based on the temporal response. It allows to identify an optimal value of the gap that leads to the best vibration reduction. The results are provided in figure 4.5 where the optimal response is obtained for a gap within the range 7-8 mm. For the smaller gaps, the frequency response is close to the response with the ball locked, since almost no attenuation is observed and the resonant peak is slightly shifted due to the added mass. An optimum is found if the gap is increased, though this is not monotonic. Indeed, increasing the gap beyond this optimal value has a detrimental effect on the vibration reduction. By comparison, the attenuation obtained with a Tuned Mass Damper is provided in appendix C.5. Furthermore, it seems relevant to notice that the vibration reduction is very sensitive to gap changes when the latter is smaller than the optimal value, whereas the reduction is less sensitive to the gap changes when it is larger than the optimal value. This suggests that the vibro-impact absorber is more robust to gap changes in the last case, that corresponds to the SMR. In order to illustrate this result, the amplitude of the beam and the attenuation obtained with the VI absorber are depicted in figure 4.6, depending on the gap value.

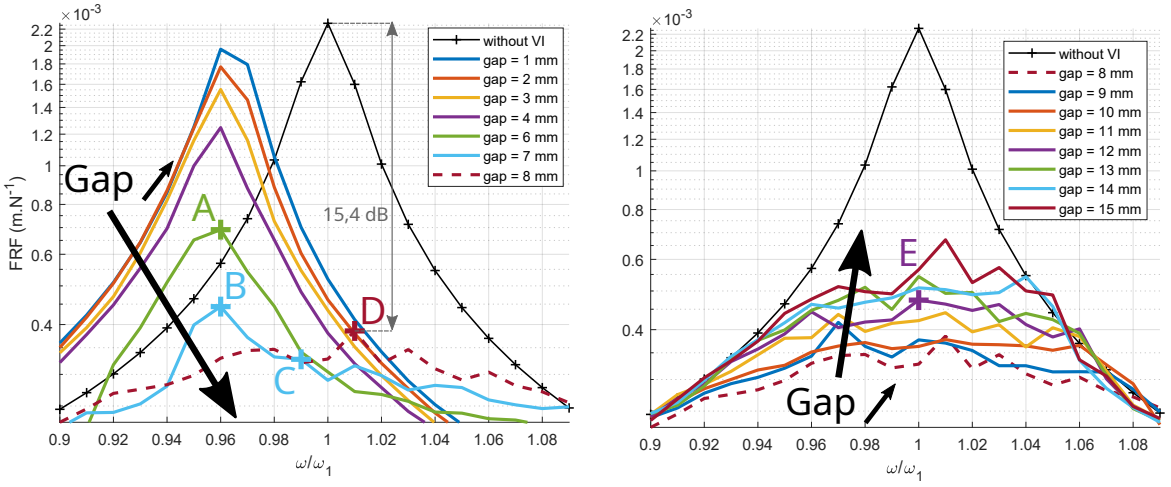

Figure 4.5: Response of the beam in the frequency domain for several gap values. Left: the amplitude is decreasing up to an optimum while the gap is increased. Right: the amplitude is increasing while the gap is increased again.

Five points (A-E) are specified. For some of them, the response of the beam and the displacement of the ball in the cavity are also depicted in figure 4.7.

As already seen experimentally, the response leading to the minimum amplitude vibration is at the limit of the SMR (this regime can be observed for point D and E in figure 4.7) and the regime with two impacts per period (point C in figure 4.7). It is interesting to see that in the response at point C, the regime with two impacts per period is mainly observed, but the SMR briefly emerges after 5 seconds, illustrating well that the separation between the two regimes occurs around a gap equals to 7 mm.

In the following of the section, the objective is to understand how the energy is dissipated thanks to the vibro-impacts. To do so, the energy transfers that occur for the points A, B, D and E are analyzed.

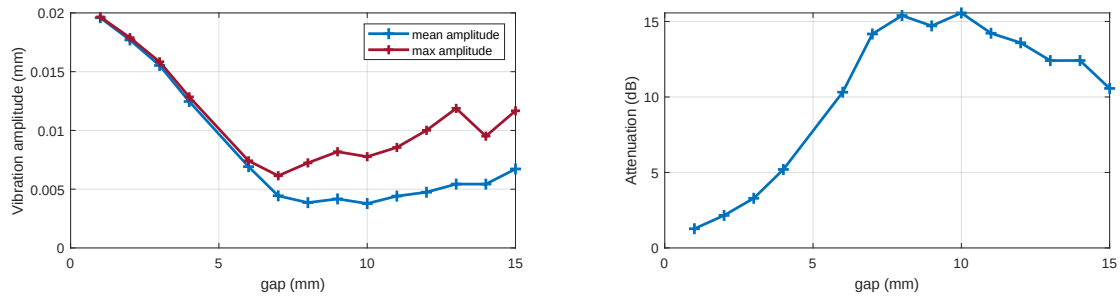

(a) Vibration amplitude depending on the gap.

(b) Attenuation depending on the gap.

Figure 4.6: Illustration of the robustness to gap variations.

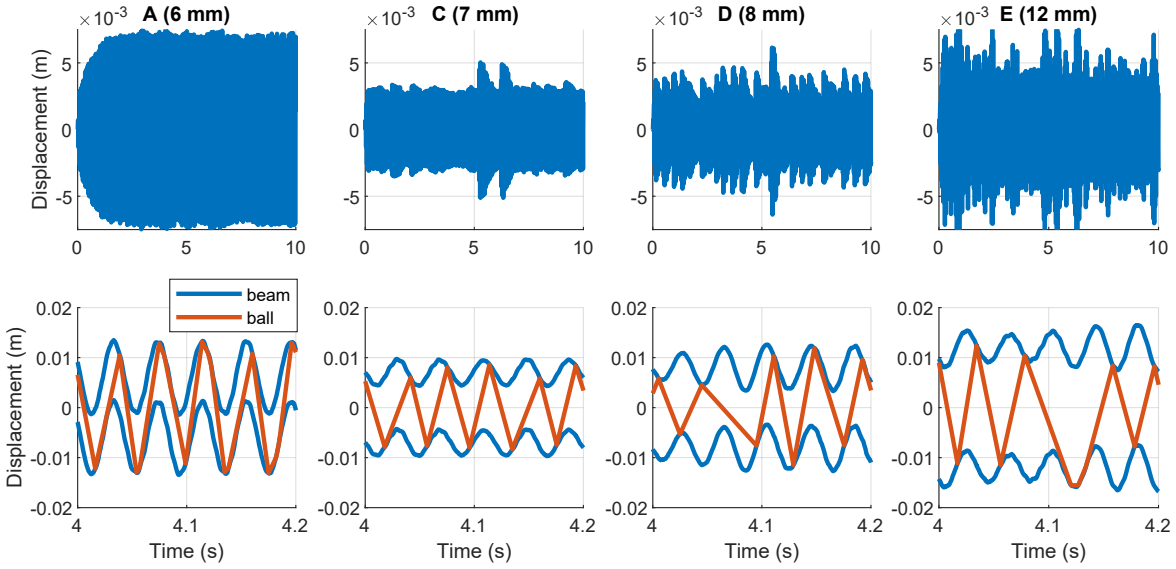

Figure 4.7: Time responses for the four points A,B,C and D (see figure 4.5). First line: displacement of the end of the beam. Second line: displacement of the ball in the cavity attached at the end of the beam.

4.3.2 Preliminary definitions

4.3.2.1 Definitions of the terms of the energy balance

For the purpose of the energy-based approach proposed in this chapter, it is necessary to define the energetic quantities that will be studied. We consider the system {beam + ball} submitted to the external excitation F_{exc}. For the i-th mode of the beam, we have:

- The kinetic energy $E^i_{kin} = \frac{1}{2}.m_i.\dot{q}_i^2$;
- The potential energy $E^i_{pot} = \frac{1}{2}.k_i.q_i^2$;
- The mechanical energy $E^i_{mec} = E^i_{kin} + E^i_{pot}$;
- The dissipated energy $E^i_{diss} = \int_0^t c_i.\dot{q}_i^2.dt$;
- The energy of the excitation $E^i_{exc} = \int_0^t F_{exc}(t).\varphi_i(x_{exc}).\dot{q}_i(t).dt$;
- The kinetic energy of the ball $E_{ball} = \frac{1}{2}.m_b.\dot{u}_b^2$.

In order to compute the previous terms without approximations, the dissipated energy E^i_{diss} and the energy of the excitation E^i_{exc} which are expressed with an integral are calculated analytically instead of using numerical integration. To reach this goal, a few technical difficulties must be overcome and are detailed in appendix C.4.

4.3.2.2 Instantaneous and average energy balance

Prior to looking at the energy transfers occurring during the vibro-impacts, it is necessary to focus on the energy balances of the system. Let's consider a vibro-impact. The change in the mechanical energy of the system during an impact for the i-th mode can be expressed as $\Delta E^i_{mec} = E^i_{mec}{}^+ - E^i_{mec}{}^-$. Similarly, the change in the kinetic energy of the ball is $\Delta E_{ball} = E^+_{ball} - E^-_{ball}$. Therefore, the instantaneous energy balance during a vibro-impact is:

$$\sum_{i=1}^{N} \Delta E^i_{mec} + \Delta E_{ball} = 0. \tag{4.32}$$

The equation (4.32) can be visualized graphically in figure 4.8 for the point A. The green curve demonstrates that the energy balance is well verified and that the error made solving the model and the different terms of the energy balance is negligible. Indeed, in the right part of the figure that represents the value of the left-handed member of equation (4.32), we can see that the values remains below 4.10^{-16} (whereas they are expected to be zero), which may be neglected compared to the individual terms of the energy balance.

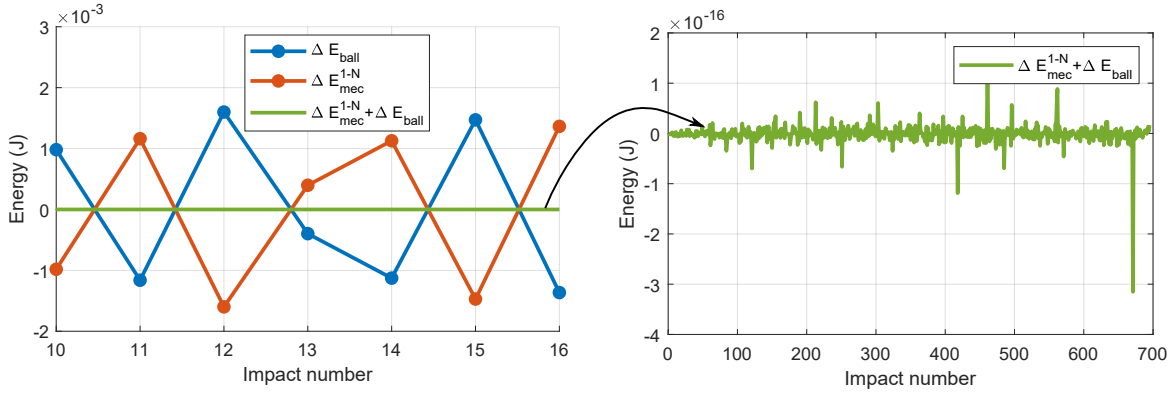

Figure 4.8: Energy balance at each impact for the point A. Left: zoom for a few impacts. Right: focus on the green curve that is close to zero.

On the other hand, one may consider the global energy balance of the system over a certain amount of time, which is expressed as:

$$\sum_{i=1}^{N} E^i_{kin} + \sum_{i=1}^{N} E^i_{pot} + \sum_{i=1}^{N} E^i_{diss} + E_{ball} = \sum_{i=1}^{N} E^i_{exc}. \tag{4.33}$$

The validity of equation (4.33) can also be verified graphically in figure 4.9 for the point A. Once again, the values remain below 5.10^{-14}, that is negligible compared to the values of the terms of equation (4.33) displayed in figure 4.10. For longer simulations, it should be necessary to verify if the divergence observed in figure 4.9 remains below an acceptable threshold...

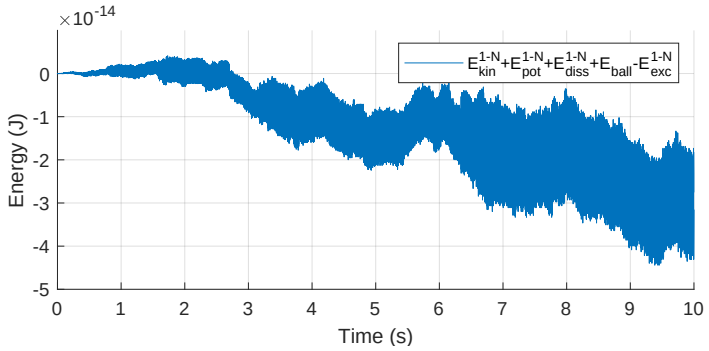

Figure 4.9: Global energy balance over the entire period of resolution for the point A.

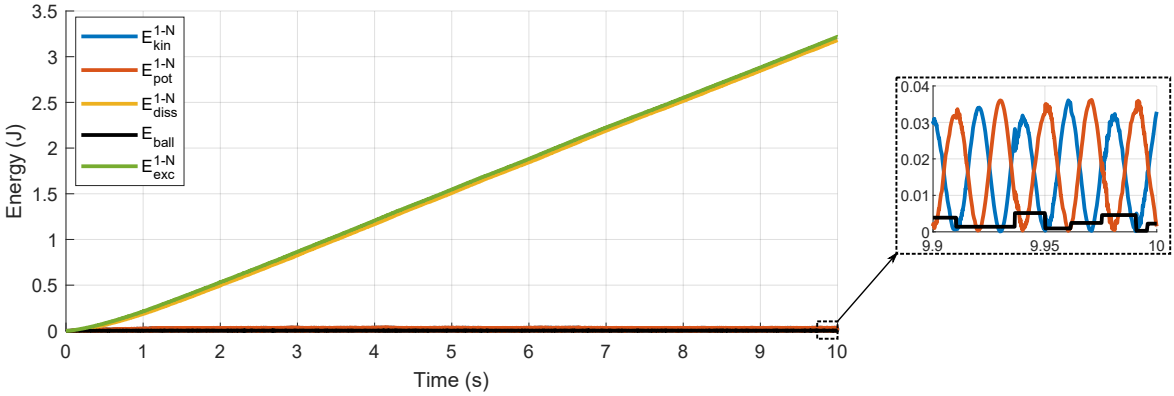

Figure 4.10: Value of each term of the global energy balance 4.33.

As the energy balances presented in this section are reasonably verified, we are now definitely able to study the energy transfers that occur in the system {beam + ball} in the presence of vibro-impacts.

4.3.3 Harmonic excitation on the first mode

In this section, the energy transfers occurring at points A, B, D and E of figure 4.5 are assessed. First and foremost, the energy transfers are analyzed for the configuration of point A. Then, the energy transfers for the four points are compared.

4.3.3.1 Energy transfers for a single frequency (point A)

Since the objective is to study how the mechanical energy of both the beam and the ball is distributed among the modes and how it is dissipated, let's begin by observing the energy transfers at each impact and for each mode. To do so, the variation of the mechanical energy ΔE^i_{mec} for the i-th mode is represented in the figure 4.11. One can notice that $\Delta E^i_{mec} > 0$ means that the mode i has received energy during the vibro-impact, whereas $\Delta E^i_{mec} < 0$ means that it has lost energy.

Therefore, we can observe that the first mode looses energy during the majority of the vibro-impacts, while the modes 2 to 8 receive energy, though the variations are smaller than the one observed for the first mode. Moreover, as the variation is not the same at each vibro-impact, the figure 4.12 depicts the average variation of the mechanical energy ΔE^i_{mec} for the i-th mode normalized by the energy of the entire system {beam + ball } at

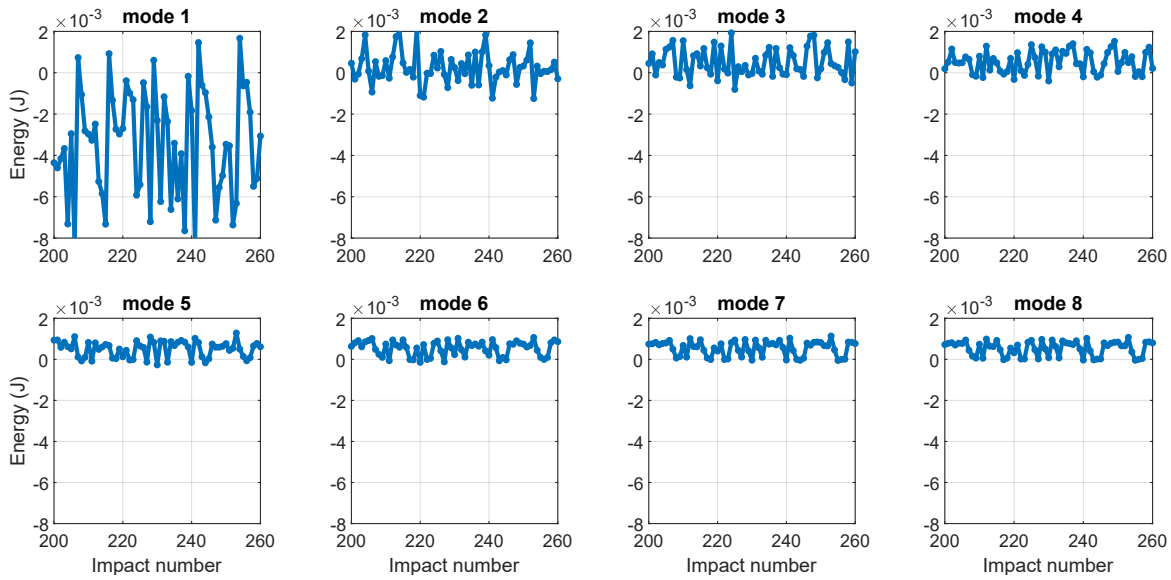

Figure 4.11: Variation of mechanical energy of each mode at each impact.

the moment of the impact $E_{syst} = \sum_{i=1}^{N} E_{mec}^{i} + E_{ball}$, so that the figure 4.12 represents the quantity $\frac{\Delta E_{mec}^{i}}{E_{syst}}$ for each mode. These results confirm the previous conclusions, as the first mode looses almost 10% of the total energy in average. Regarding the higher modes, they receive around 1,5% of the total energy in average.

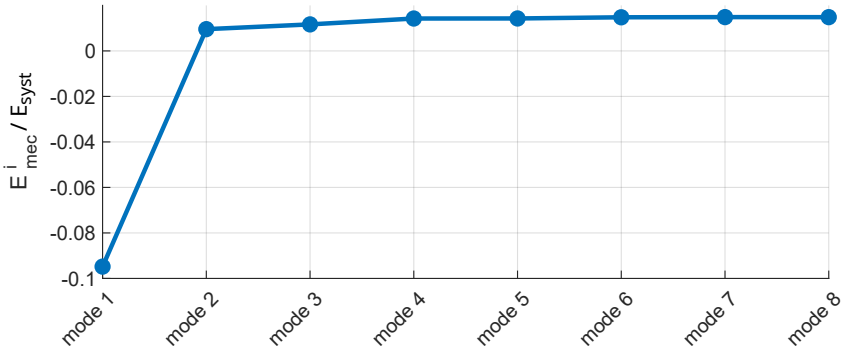

Figure 4.12: Average variation of energy during the impacts.

Between the impacts, the mechanical energy on each mode is dissipated. And the higher the mode, the faster the energy is dissipated. Indeed, referring to appendix C.4, $E_{diss}^{i}(t)$ contains terms proportional to $e^{-2.\omega_i.\xi_i.t}$ and $e^{-\omega_i.\xi_i.t}$. In figure 4.13, it can be seen that for the modes 2 to 4, the mechanical energy received during a vibro-impact is not entirely dissipated before the next vibro-impact. On the contrary, for the modes 5 to 8, the mechanical energy decreases to almost zero between vibro-impacts. On average on the whole response of the beam, we can compute the energy dissipated by each mode. The ratio between the energy dissipated by each mode and the total energy dissipated $E_{diss}^{tot} = \sum_{i=1}^{N} E_{diss}^{i}$ is represented in figure 4.14, so that it represents the quantity $\frac{E_{diss}^{i}}{E_{diss}^{tot}}$ for each mode. One can see that the first mode contributes up to 29 % of the total dissipation, while the last modes are closer to 11 %.

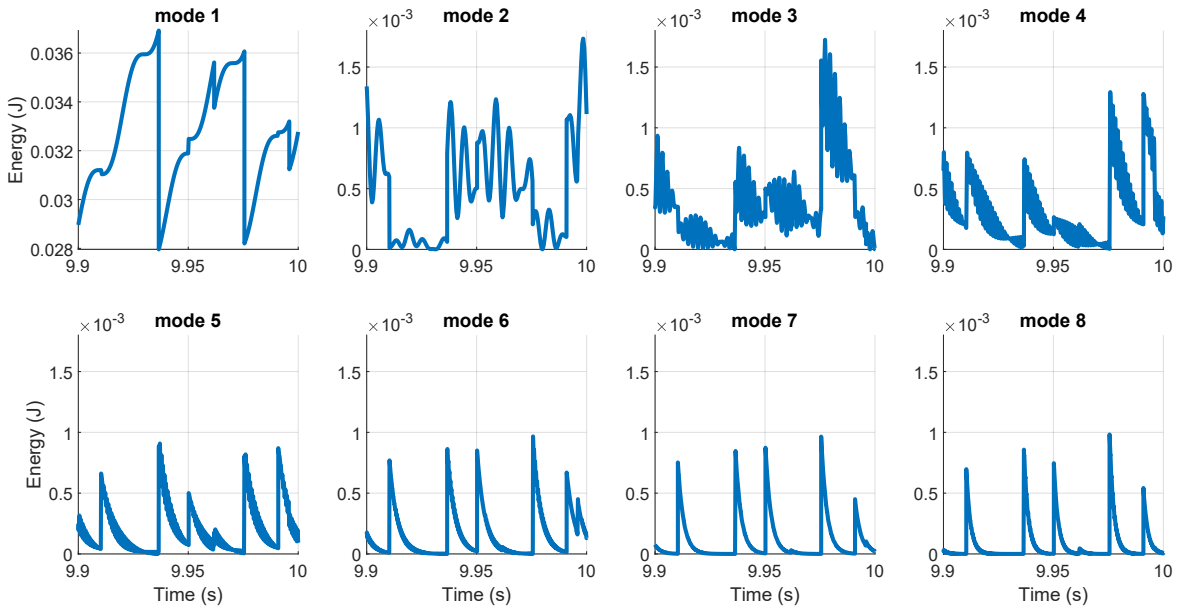

Figure 4.13: Mechanical energy for each mode versus time.

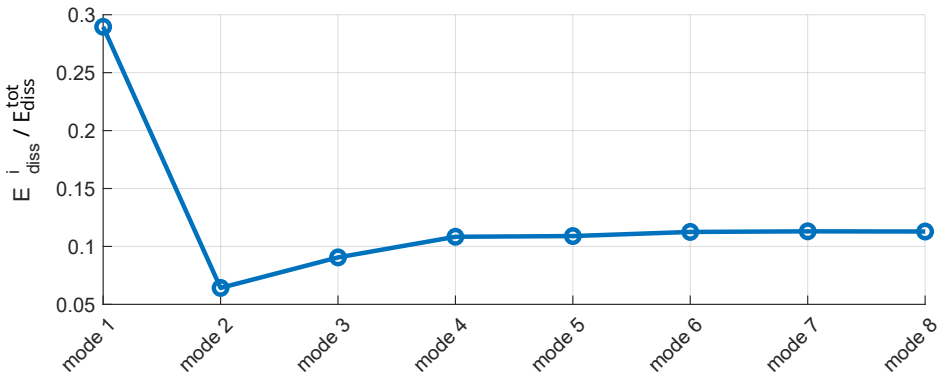

Figure 4.14: Energy dissipated by each mode over the whole duration.

4.3.3.2 Comparison of the four points A, B, D and E

In this section, the energy transfers at the suboptimal points A, B, E and at the optimal point D are compared. In figure 4.15, the energy received by each mode is represented. It is quite visible that at the optimal point D, more energy is subtracted from the first mode and is redistributed to the higher modes. On the contrary, at point A for instance, fewer energy is taken from the first mode while the higher modes are less excited. The result is that most of the energy is concentrated in the first mode, that has the largest amplitude of vibration. This energy transfer towards the higher modes leads some authors to combine a VI absorber with an acoustic black hole that can absorb the vibrations for sufficiently high frequencies [68, 67, 66].

As the first mode receives less energy at the optimal point D, its contribution to the dissipation of the vibrational energy is lower. Simultaneously, the higher modes dissipate a larger amount of energy. These observations are illustrated in figure 4.16. As the higher modes realize more oscillations in the same amount of time than the lower modes, their energy is dissipated faster than in the case of the lower modes, which is another beneficial phenomenon that helps to reduce the amplitude of vibration.

On the whole, the results presented in this section demonstrate that the effectiveness of the vibro-impact absorber can be explained in terms of energy transfers that are related to the gap value. Let's start with the smallest and largest gap values that lead to observe in figure 4.7 the regime with multiple impacts (or more rarely the regime with two impacts per cycle) and the Strongly Modulated Regime, respectively. In these cases, the results in figure 4.15 show that the energy transfer from the first excited mode to the higher modes is small, resulting in a poor effectiveness of the absorber as the vibrational energy is not dissipated efficiently by the higher modes. On the contrary, when the gap is well tuned so that the regime with two impacts per cycle is mainly observed, the energy transfer from the first excited mode to the higher modes is maximized. The figure 4.16 shows that the vibrational energy is efficiently dissipated by the higher modes, resulting in the highest vibration reduction.

Then, the following sections address the problem of an excitation on the second and the third mode.

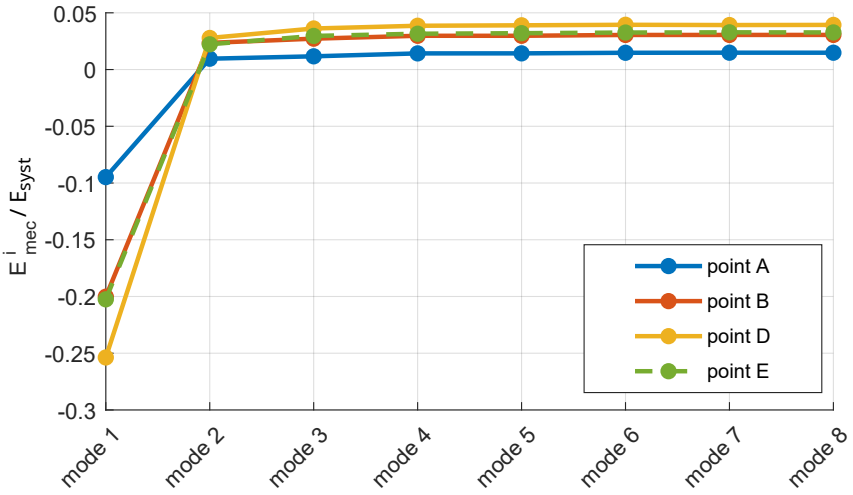

Figure 4.15: Comparison of the energy received for four gap values corresponding to the points A, B, D and E.

4.3.4 Harmonic excitation on the second and third mode

In the previous section, it was demonstrated that the maximal effectiveness of the VI absorber corresponds to the maximum energy transfer from the first excited mode towards the higher modes.

However, assuming that the excited mode is not the first mode, but the second or the third one, it is particularly relevant to study the distribution of the energy between the modes due to the impacts. Since the lower modes have a poor damping capacity, and their amplitude is often larger than the higher modes, such an energy transfer towards these lower modes could be detrimental to the effectiveness of the absorber.

The figure 4.17 and figure 4.18 shows the FRFs obtained varying the gap for an excitation in the vicinity of the second and third mode, respectively. It should be mentioned that the gap values are adjusted in order to visualize a maximum in the vibration reduction performance of the absorber. The corresponding values are probably impossible to obtain experimentally, but the conclusions drawn in the section remain valid. In each

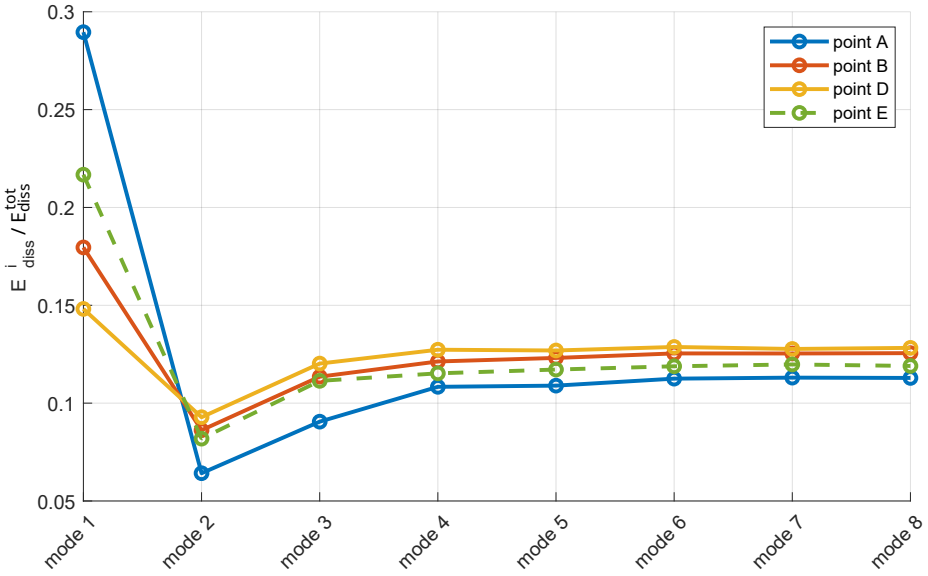

Figure 4.16: Comparison of the energy dissipated for four gap values corresponding to the points A, B, D and E.

case, the energy distribution is analyzed for four points A, B, C and D of the FRFs. As previously, the average energy transferred to the modes in proportion of the mechanical energy available in the system throughout the impacts is studied on the one hand, and the energy dissipated by each mode in proportion of the total energy dissipated is examined on the other hand. These quantities are depicted in figure 4.19, 4.20, 4.21 and 4.22.

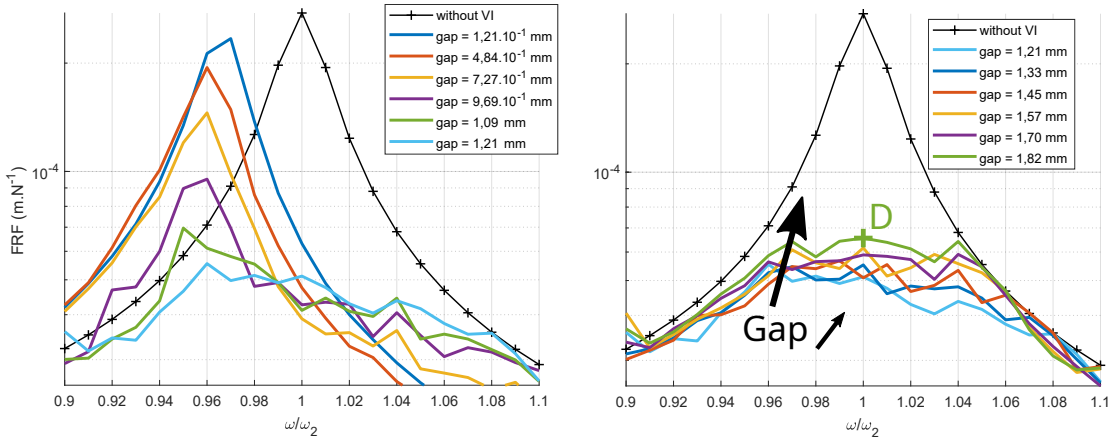

Figure 4.17: FRFs of the beam excited on the second mode for several gap values.

Focusing on the optimal point C for mode 2 and 3, we still observe that the energy transfer is maximized from the excited mode towards the higher modes, corresponding to the highest amount of energy dissipated by the higher modes, and the lowest for the excited mode. Consequently, the previous conclusions seem to remain valid. Moreover, it is worthy to note that a negligible amount of energy is transferred to the lower modes (-0,3 % to the first mode in figure 4.19, -0,02 % to the first mode and 0,2 % to the second mode in figure 4.20), what is beneficial to the effectiveness of the absorber to mitigate the vibrations of not only the first mode. Another interesting point is the energy transfers ob-

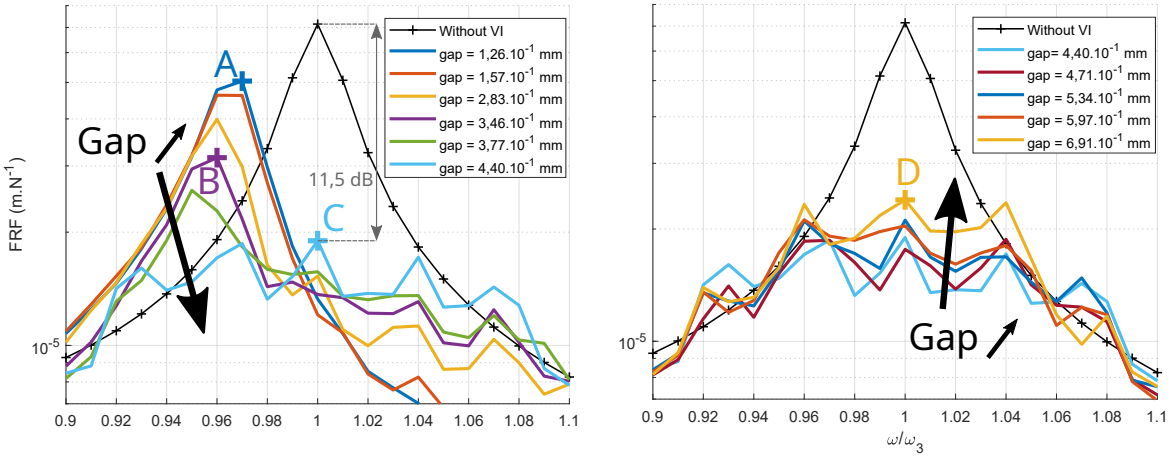

Figure 4.18: FRFs of the beam excited on the third mode for several gap values.

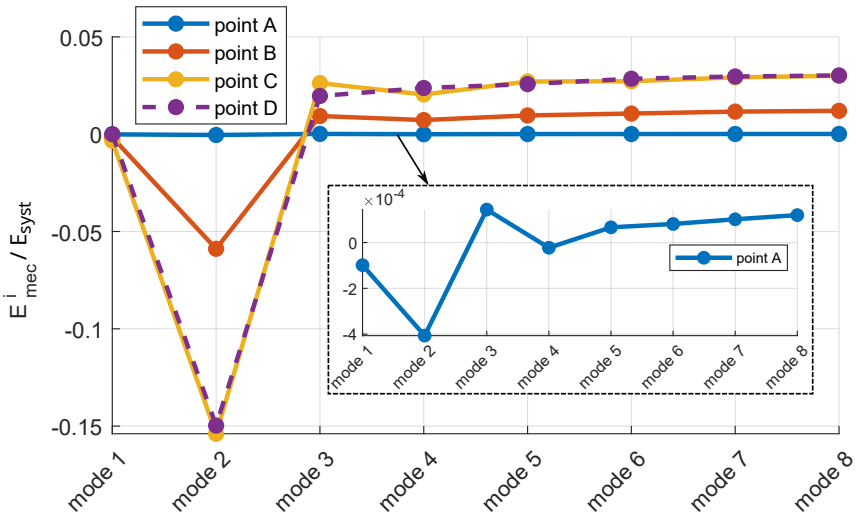

Figure 4.19: Energy received by mode for an excitation on the second mode.

served at point A in figure 4.19 and figure 4.20. The graphs reveal that the energy transfers are very small: below 0,04 % in figure 4.19 and 0,4 % in figure 4.20. The reason of this is very probably that as the gap is very small, the multiple impacts involve small kinetic energy, and thus small energy transfers, illustrating well that some regimes are less efficient than others in terms of energy transfers.

Nevertheless, comparing the case of an excitation in the vicinity of the first and second mode, the energy transferred to the higher modes is lower in the second case than in the first one (for the optimal case and for the eightth mode, 3% versus 3,9%). The same observation can be made looking at the energy transfers for an excitation in the vicinity of the third (2,6% for the eightth mode). This suggests that the higher the mode to mitigate, the worse the effectiveness of the absorber. Besides, this is illustrated in figure 4.5, 4.17 and 4.18 since the vibration reductions obtained are respectively 15,4 dB; 13,9 dB and 11,5 dB. However, this last remark should be read carefully. Since the model used is based on a finite modal base truncated to eight modes, it is necessarily simplifies the phenomena. Therefore, comparing the energy transfers in these different cases can lead to misinterpretations that may not correspond to reality as long as higher modes might be

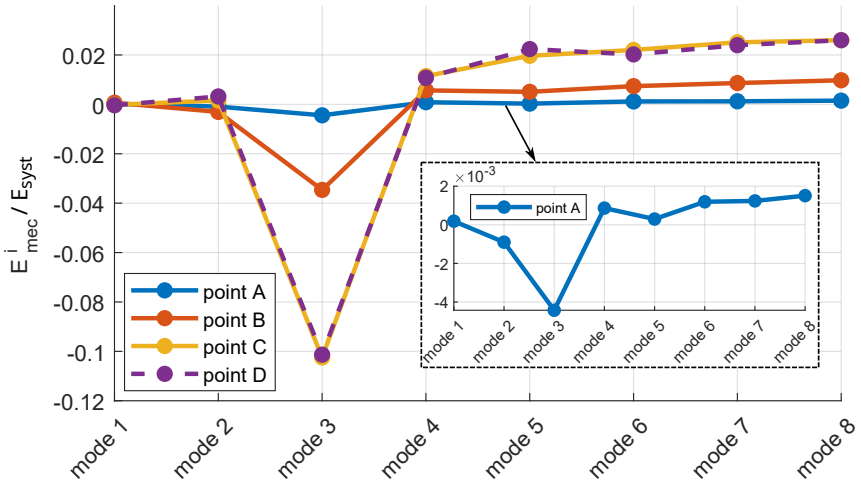

Figure 4.20: Energy received by mode for an excitation on the third mode.

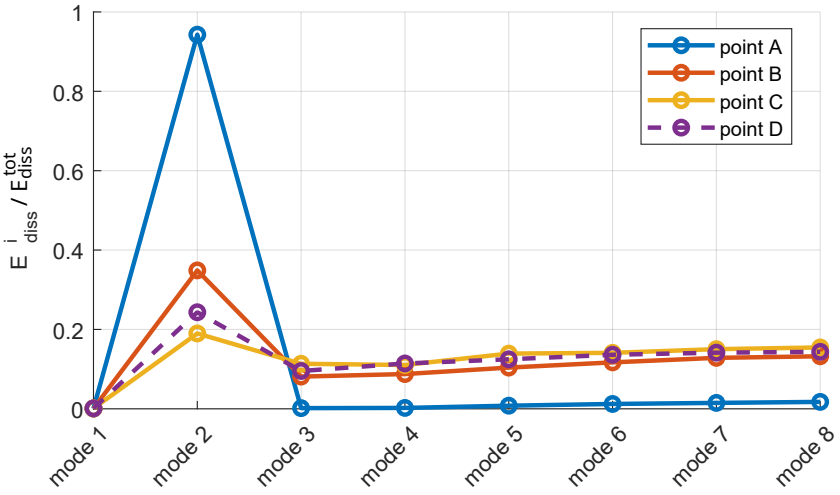

Figure 4.21: Energy dissipated by mode for an excitation on the second mode.

considered in the modal basis to represent rigorously the behavior of the beam submitted to vibro-impacts.

The same results based on a model with only six modes instead of eight are provided in appendix C.6, and they lead to the same conclusions. Therefore, the number of modes in the modal basis does not seem to change the present conclusions. Here, we decided not to increase the number of modes because of the high computational cost.

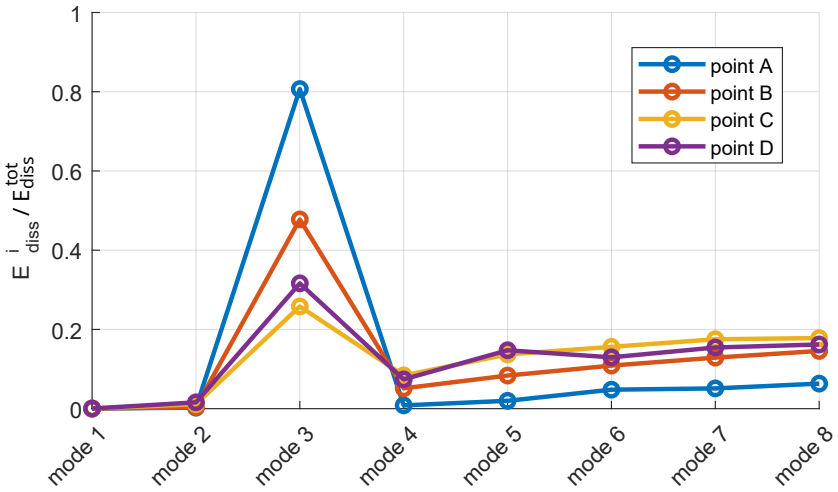

Figure 4.22: Energy dissipated by mode for an excitation on the third mode.

4.4 Robustness to eigenfrequencies variations

Contrary to TMD that have a narrow frequency range of effectiveness, VI absorber are expected to be more robust to frequency variations. More specifically, it is assumed that if the main structure present eigenfrequencies changes, it should not modify significantly the performance of the absorber. Eigenfrequencies variations can be due to aging or sensitivity to environmental conditions in the case of natural materials like wood or composite made of natural fibers, or due to damage that can modify the stiffness properties of the main structure, during an earthquake for instance. In order to quantify this potential interesting property of VI absorbers, the performance of the VI absorber is assessed for two gap value. The first one is set to 8 mm, and corresponds to the optimal value found previously. The second one is set to 10mm, larger than the optimal gap. Indeed, we found in figure 4.6 that a slightly larger gap than the optimal value enables to obtain a better robustness to gap variations. Therefore, it seems relevant to examine if the robustness still stands for frequency variations. Meanwhile, the eigenfrequencies of the beam are changed. For this purpose, the square of the modal stiffnesses k_i of each mode are varied at the same time in the range $[-20\%;+20\%]$ with increments of $2,5\%$, so that the new eigenfrequencies are varied in the same range, and they are called ω_i^* ($\omega_i^* = -20\% \times \omega_1$; $-17,5\% \times \omega_1$; $-15\% \times \omega_1$; ... ; $10\% \times \omega_1$). With the VI absorber embedded, the maximum of the new vibration amplitude $u^{\mathrm{VI}}_{xx\%}$ of the beam (with an eigenfrequency shift of $xx\%$) is analyzed, and it can be compared to the maximum amplitude of the beam $u^{\mathrm{VI}}_{0\%}$ with the initial eigenfrequencies, or to the maximum amplitude of the beam $u_{0\%}$ with the initial eigenfrequencies without VI absorber, or at last to the maximum amplitude $u_{xx\%}$ with the same eigenfrequency shift of $xx\%$. The figure 4.23 depicts a few frequency responses of the beam depending on the variations of the eigenfrequencies and illustrates the previous quantities $u^{\mathrm{VI}}_{xx\%}$; $u^{\mathrm{VI}}_{0\%}$; $u_{0\%}$; $u_{xx\%}$. In figure 4.24, the subset 4.24a depicts the ratio $\max(u^{\mathrm{VI}}_{xx\%})/\max(u^{\mathrm{VI}}_{0\%})$. Accordingly, if the ratio is greater than 1, the response of the beam with the modified eigenfrequencies is higher than the response with the initial eigenfrequencies. On the contrary, a ratio smaller than 1 indicates a lower response with the modified eigenfrequencies than without. In figure 4.24b, the attenuation $20.\log[\max(u^{\mathrm{VI}}_{xx\%})/\max(u_{0\%})]$ is depicted, allowing to compare the attenuation obtained

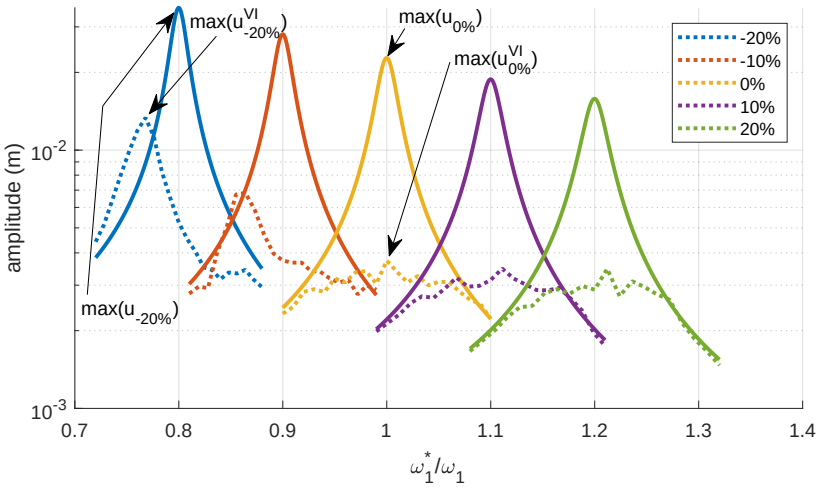

Figure 4.23: Frequency responses varying the eigenfrequencies, the gap is set to 8 mm. Dotted lines: responses with VI absorber. Solid lines: responses without VI absorber.

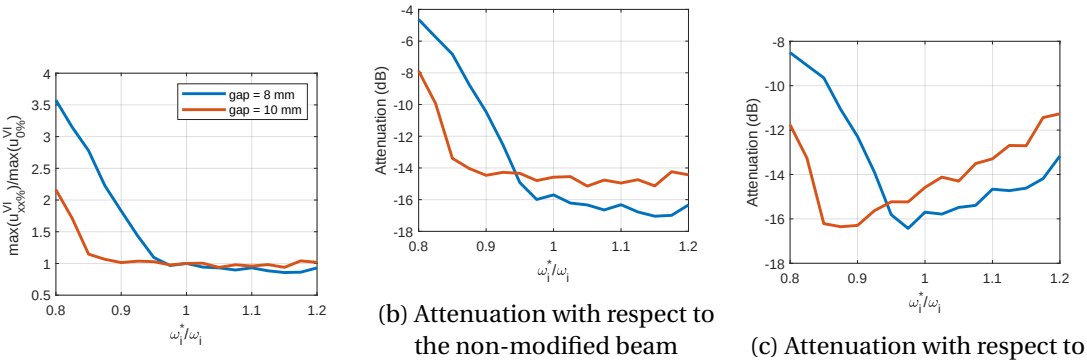

(a) Ratio of the amplitudes.

(b) Attenuation with respect to the non-modified beam amplitude.

(c) Attenuation with respect to the modified beam amplitude.

Figure 4.24: Robustness of the VI absorber to eigenfrequencies variations.

in presence of eigenfrequencies variations with the initial attenuation. At last, the figure 4.24c illustrates the attenuation $20.\log[\max(u^{\mathrm{VI}}_{xx\%})/\max(u_{xx\%})]$ in order to quantify the attenuation with respect to the amplitude of the modified beam (eigenfrequencies shifted) without absorber.

As a consequence, these results suggest that a very interesting robustness to eigenfrequencies variations is achieved using a VI absorber. For instance, looking at figure 4.24a almost no variations of the amplitude level are observed between -5% up to $+20\%$ for the gap of 8 mm, demonstrating the robustness of the VI absorber. The same conclusion is drawn from figure 4.24b, where one can see that the initial level of attenuation of 15,7 dB is guaranteed in the same range. Interestingly, the range of the robustness is extended when the gap is set to 10 mm, allowing an almost constant amplitude between -15% up to $+20\%$. However, the attenuation level is slightly deteriorated from at least 16 dB to 14dB, since the gap is greater than its optimal value. This improvement of robustness could be expected regarding the figure 4.6. Indeed, under constant excitation amplitude, a gap larger than its optimal value leads to observe the SMR. During this regime, the attenuation is less sensitive to gap variations. On the contrary, in the regime with two (or more) impacts per period obtained for gaps smaller than the optimal value, the atten-

uation is quite sensitive to gap variations. Moreover, the scalability property illustrated in chapter 3 shows that the gap and the vibration amplitude of the beam are related by a scalability property and play analogous roles regarding the attenuation. Since varying the eigenfrequencies of the structure modify the amplitude of its resonant peaks (see figure 4.23), the robustness during the SMR regime observed in figure 4.6 still applies in the present case. At last, the last subset 4.24c demonstrates that changing the eigenfrequencies of the structure changes the optimal gap. Indeed, one can see that the gap of 10 mm becomes optimal for $\omega_i^* = 0.9 \times \omega_i$. Moreover, it is worthy to note that setting the gap to 10 mm allows keeping the vibration attenuation below 11 dB, while setting the gap to 8 mm only allows remaining below 8 dB. Therefore, depending on the requirements of the application, it could be relevant to set the gap to its optimal value in order to obtain the best vibration reduction level, or more suited to choose a greater gap value to ensure the robustness of the VI absorber, in particular to frequencies and amplitude variations of the main structure.

4.5 Conclusions

In this chapter, the vibration mitigation achieved using a vibro-impact absorber attached to a beam submitted to a harmonic excitation is explained through an energy-based approach. A model of an Euler-Bernoulli beam with a VI absorber attached at its end is solved using a semi-analytical method. As long as no solver is used, this method enables to derive exact energy balances leading to negligible errors.

The first result is that the vibration reduction of the excited mode of the beam is performed in spite of the impacts are perfectly elastic and non-dissipative. Thus, even if energy dissipation occurs in reality during the vibro-impacts, this is not the only phenomenon at stake that helps to reduce the vibrations.

Besides, the energy transfers due to the vibro-impacts are analyzed. More specifically, two quantities are examined. The first one is the average energy transferred to the modes in proportion of the mechanical energy available in the system throughout the impacts. The second one is the energy dissipated by each mode in proportion of the total energy dissipated. In the case of an excitation on the first mode, the results obtained highlight an energy transfer from the first excited mode towards the higher modes of the beam. Moreover, considering the modes four to eight, the energy is uniformly distributed between them. Two beneficial phenomena are identified. Firstly, the higher modes have a lower amplitude of vibration. Thus, the less energy is contained on the lower modes, the smaller the amplitude of vibrations. Secondly, as they realize more oscillations in the same amount of time than the lower modes, the energy dissipation occurs faster and the vibrational energy is dissipated more efficiently.

Finally, the case of an excitation on the second and on the third mode is considered in order to achieve two objectives. The first one is to assess the ability of the absorber to mitigate the vibrations of higher modes, and the second one is to analyze the energy transfers towards the lower modes as it could be detrimental to the effectiveness of the absorber. The study reveals that an interesting vibration attenuation is performed for the second and the third mode. Moreover, the energy transfers towards the lower modes are negligible.

In conclusion, the effectiveness of the vibro-impact absorber is confirmed for harmonic excitations on the first three modes, and the effectiveness is physically explained

examining the energy transfers between the modes.

At last, the robustness of the VI absorber is assessed in the case of eigenfrequencies variations of the beam. We found that the absorber is quite robust since almost no variations of the amplitude are observed while the eigenfrequencies are changed. Interestingly, the robustness can be further increased setting a greater gap than the optimal value.

Chapter 5

Application to a three-dimensional flexible structure

Contents

Preamble

The previous chapters have considered a beam equipped with a vibro-impact absorber. Indeed, these structures are well-known, facilitating the interpretation of the role of the vibro-impact absorber on the behavior of the main vibrating structure. The effectiveness of a vibro-impact absorber was assessed experimentally in chapter 3, and explained numerically in chapter 4. In order to go towards the application of vibro-impact absorbers

to industrial cases, more realistic structures should be considered. Moreover, using a single VI-absorber has demonstrated some limitations, such as the ability to mitigate a single mode at a time with two different optimal settings. The objectives of this chapter are twofold. Firstly, a model plane is considered as a more realistic structure, and it is equipped with a vibro-impact absorber. Both numerical and experimental approaches are proposed. Secondly, the model plane is equipped with multiple VI absorbers in order to enhance the effectiveness of the vibration reduction achieved on the plane, especially concerning the multimodal attenuation.

5.1 Introduction

The literature and the previous chapters have highlighted the potential and the promising effectiveness of vibro-impact absorbers with respect to their technological simplicity. A crucial point to understand the physical phenomena at stakes in vibro-impact is the multi-modal behavior of the main structure because of the modal interactions that occur in the presence of vibro-impacts. However, the studies are still far from dealing with real industrial structures. Very often, single-DOF or multi-DOF structures are considered [83], while other cases focus on beams [128, 4, 42]. Therefore, single-DOF structures inevitably oversimplify vibro-impact phenomena since energy transfers between modes cannot exist, and structures like beams are more likely to represent the physical phenomena at stakes. Yet, they remain quite simple. Consequently, the behavior of more complex structures equipped with vibro-impact absorbers need to be investigated. Moreover, the questions of modeling, simulating and predicting the response of a three-dimensional structure endowed with vibro-impact absorbers still need to be addressed in the perspective of the design of absorbers to tackle industrial problems. In addition, experimental approaches on such structures still need to be adopted.

Besides, two main drawbacks related to vibro-impact absorbers have been raised in the literature. Firstly, a single vibro-impact absorber is often used to tackle a single mode of a multi-modal structure [42]. Indeed, as the displacements obtained at the resonances are smaller for higher modes than for lower modes, the gap of the absorber cannot be properly tuned for several modes that have very different amplitudes. In addition, since vibro-impact absorbers are non-linear devices, they necessitate a certain level of energy to be activated. As a consequence, the effectiveness of such an absorber may be limited to a certain range of excitation level. For these two reasons, a promising strategy is to use multiple absorbers, and this results in several benefits. In the case of vibro-impact absorbers, it allows to reduce the size of the oscillating mass, and therefore the noise and the stress when the contacts occur [85]. But employing multiple absorbers can also increase the robustness and the range of effectiveness of linear [10, 13] or non-linear [105] absorbers. In the last case for instance, the vibration reduction of a single-DOF structure is increased using two VI-NES that activate at different levels of excitation. Other works have taken advantage of this principle to improve the effectiveness of multiple non-linear absorbers [22]. Furthermore, the use of multiple absorbers may have other benefits, especially concerning the multimodal effectiveness. In the case of linear absorbers, using multiple absorbers tuned at different frequencies may lead to achieve vibration reduction on several modes simultaneously and for broadband vibration absorption [134, 98]. A design methodology is provided in [37] in the case of a beam equipped with two VI absorbers that aim to reduce the vibrations of the two first modes. Nevertheless, these works exclusively

deal with single-DOF, multi-DOF structure, or beams, and no more than two absorbers are used simultaneously in the case of vibro-impacts absorbers. Yet again, using multiple absorbers on more realistic three-dimensional structure should be investigated.

The conclusions of the previous studies are synthesized here. Few studies dealing with the application of vibro-impact absorbers on three-dimensional structures are available, whether experimentally or numerically. In particular, being able to simulate the vibration reduction of a three-dimensional structure obtained thanks to a vibro-impact absorber is rarely discussed. At last, the strategy of using multiple absorbers has already been investigated in the case of linear absorbers, NES, and VI NES in very recent studies. Nevertheless, further work remains to be done before being able to propose a design methodology. Moreover, none of them have adopted an experimental approach, and the application concerns mostly simple structures like beams or multi-DOF structures. In this chapter, a numerical approach based on the finite element model of a three-dimensional structure is proposed in order to simulate the dynamic behavior of a model plane in the presence of a vibro-impact absorber. It is worthy to note that simultaneously to this study, another work was proposed in [87] in order to realize long-term simulations of vibro-impacts problems based on a finite element model. The authors argued that their approach help to reduce significantly the computational efforts. The method proposed is validated experimentally in another paper [88]. In our work, the structure that we studied is a model plane. Based on the numerical results, some rules are presented regarding the design process of a VI absorber leading to the optimal vibration reduction. In order to confirm the trends observed in the simulation results, experiences are realized, demonstrating the ability of the VI absorbers to reduce the vibration level of the model plane, but also highlighting the limitations of using a single VI absorber. Then, multiple absorbers are designed, and they are spatially distributed on the wings of the plane. The benefits of using multiple absorbers, as well as the influence of both their position and gap on the level of vibration mitigation is presented.

5.2 Dynamic of a three-dimensional structure submitted to vibro-impacts

5.2.1 Finite element model and matrix formalism

In order to assess the vibration mitigation effectiveness of a vibro-impact based strategy on a three-dimensional structure, a model plane is considered in this chapter. It is equipped with a vibro-impact absorber at each end of the wings. The vibro-impact absorber is designed in a very similar manner than in chapter 3, though its dimensions and the size of the ball are modified. The CAD views are available in figure 5.1.

The geometry file is then imported in COMSOL in order to build the finite element model of the plane equipped with the absorbers. Therefore, the equation to solve is given in equation (5.1):

$$[\mathrm{M}].\{\ddot{u}\} + [\mathrm{C}].\{\dot{u}\} + [\mathrm{K}].\{u\} = \{\mathrm{F}\}; \tag{5.1}$$

where $\{\mathrm{F}\} = \{\mathrm{F}_{exc}\} + \{\mathrm{F}_{\mathrm{VI}}\}$. Assuming that the finite element model contains N_{node} nodes, then the number of degrees of freedom is $\mathrm{N}_{dof} = 3 \times \mathrm{N}_{node}$ since the translations in the three directions are possible. Therefore the dimension of [M], [C] and [K] is

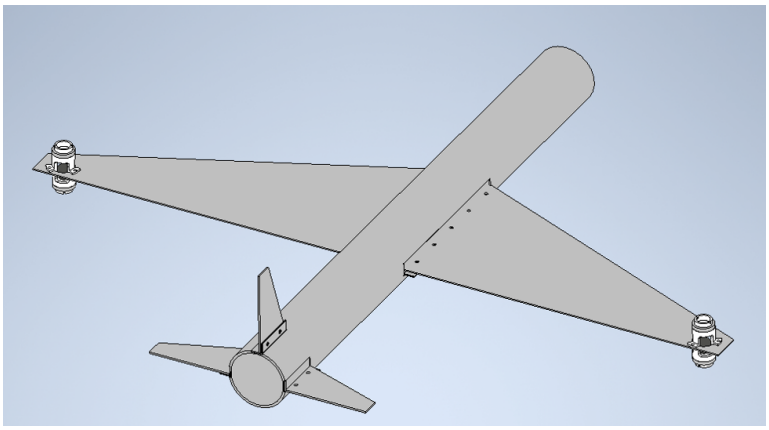

(a) CAD view of the model plane.

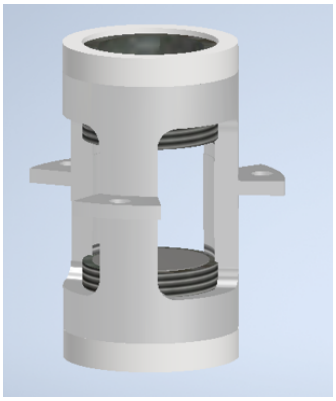

(b) CAD view of the VI absorber.

Figure 5.1: CAD view.

$N_{dof} \times N_{dof}$. Moreover, $\{u\}$ is the vector of the nodal displacements, $\{F_{exc}\}$ is the force of the excitation, and $\{F_{VI}\}$ is the force of the vibro-impact absorber on the plane. Assuming punctual forces, $\{F_{exc}\}$ and $\{F_{VI}\}$ have only one non-null component (respectively called F_{exc} and F_{VI}), they correspond to the degrees of freedom where the forces apply. For all the previous vectors, their dimension is $N_{dof} \times 1$.

The materials properties of the different parts of the plane illustrated in figure 5.2 are given in table 5.1. The angle bars are used to connect the wings and the ailerons to the fuselage. The interfaces have no equivalent in the real system. They are used to tune the stiffness of the connections in the model updating process, not presented here.

The damping model used in COMSOL is based on a loss factor η, so that the damping matrix becomes :

$$[C] = \frac{\eta.[K]}{\omega}. \tag{5.2}$$

5.2.2 Modal decomposition

Considering equation (5.1), the size of the matrix system to solve is $N_{dof} \times N_{dof}$. In order to reduce the size of this system, a modal decomposition is adopted. The same approach as used in chapter 4 is adopted here. Therefore, we decide to consider the N_{mode} first modes of the structure ($N_{mode} \leq N_{dof}$), and the displacement field $\{u\}$ is supposed to be a product of a spatial dependant function $[\phi]$ and a time dependant function $\{q\}$:

$$\{u\} = [\phi].\{q\}; \tag{5.3}$$

where $[\phi]$ ($N_{dof} \times N_{mode}$) is the matrix of the mode shapes $\{\phi_k\}$ ($N_{dof} \times 1$):

$$[\phi] = \left[\{\phi_1\}, \{\phi_2\}, \ldots, \{\phi_{N_{mode}}\}\right]; \tag{5.4}$$

and $\{q\}$ ($N_{mode} \times 1$) is the vector of the generalized coordinates $q_k(t)$:

Parameter	**Value**
Wings and ailerons (steel)	
Young's modulus E	196.10^9 Pa
Density ρ	7721 kg.m^{-3}
Loss factor η	0,005
Fuselage (aluminum)	
Young's modulus E	70.10^9 Pa
Density ρ	2775 kg.m^{-3}
Loss factor η	0,01
Angle bars (aluminum)	
Young's modulus E	70.10^9 Pa
Density ρ	2694 kg.m^{-3}
Loss factor η	0,01
Interface wings / angle bars	
Young's modulus E	$13,36.10^6$ Pa
Density ρ	2694 kg.m^{-3}
Loss factor η	0,01
Interface ailerons / angle bars	
Young's modulus E	$16,09.10^6$ Pa
Density ρ	2694 kg.m^{-3}
Loss factor η	0,01
VI absorber (aluminum)	
Young's modulus E	70.10^9 Pa
Density ρ	2700 kg.m^{-3}
Loss factor η	0,01

Table 5.1: Material properties used in the model of the plane.

$$\{q\} = \begin{Bmatrix} q_1(t) \\ \vdots \\ q_k(t) \\ \vdots \\ q_{\mathrm{N}_{mode}}(t) \end{Bmatrix}. \tag{5.5}$$

The eigenpulsations are given by the the N_{mode} first solutions of equation (5.6):

$$\det([\mathrm{K}] - \omega^2.[\mathrm{M}]) = 0. \tag{5.6}$$

Then, the mode shape $\{\phi_i\}$ of the i-th mode can be calculated solving:

$$(-\omega_i^2.[\mathrm{M}] + [\mathrm{K}]).\{\phi_i\} = \{0\};$$

and it is necessary to fix the components of $[\phi]$ in order to obtain unitary modal masses, what is $[\phi]^{\mathrm{T}}.[\mathrm{M}].[\phi] = [\mathrm{I}]$.

At the end, we obtain:

$$[\mathrm{M}_r].\{\ddot{q}\} + [\mathrm{C}_r].\{\dot{q}\} + [\mathrm{K}_r].\{q\} = [\phi]^{\mathrm{T}}.\{\mathrm{F}\}; \tag{5.7}$$

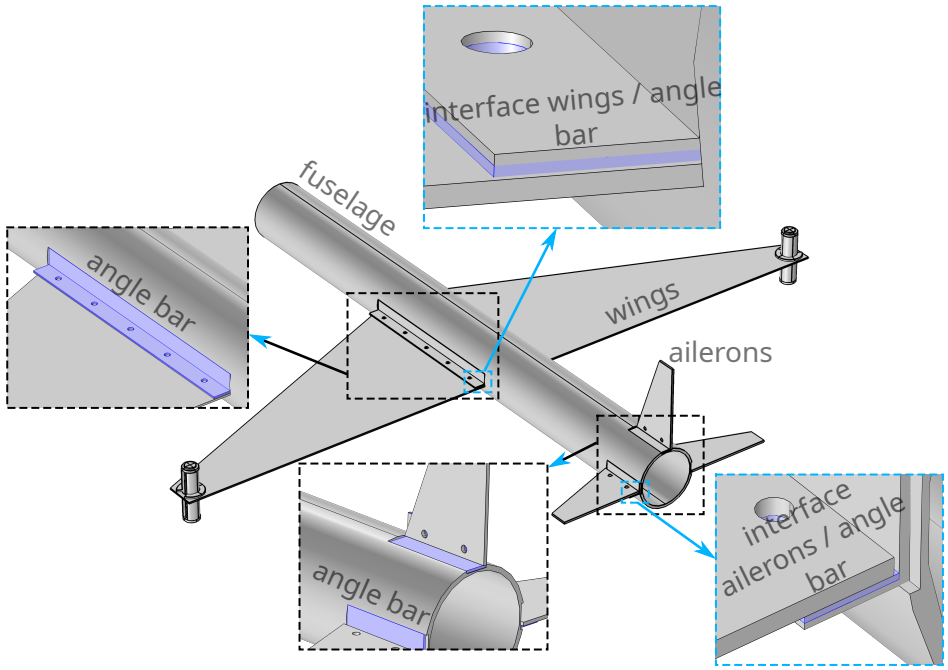

Figure 5.2: Illustration of the parts and materials of the plane.

where $[M_r] = [\phi]^T.[M].[\phi] = [I]$, $[K_r] = [\phi]^T.[K].[\phi] = \text{diag}(k_i)$, $[C_r] = [\phi]^T.[C].[\phi] = \text{diag}(c_i)$ (since Basile's hypothesis is verified) are the reduced matrices, projected onto the modal basis. Using COMSOL with Matlab, it is possible to use the reduced mass, damping and stiffness matrices $[M_r]$, $[C_r]$ and $[K_r]$ of the finite element model in Matlab.

Then, equation (5.7) can be transformed in a first order equation, which is a necessary step to proceed to numerical integration, using:

$$\{Z\} = \begin{Bmatrix} \{q\} \\ \{\dot{q}\} \end{Bmatrix}. \tag{5.8}$$

This leads to:

$$\{\dot{Z}\} = \begin{bmatrix} [0] & [I] \\ -[K_r] & -[C_r] \end{bmatrix}.\{Z\} - [\phi]^T \begin{bmatrix} \{0\} \\ \{F\} \end{bmatrix} = [A].\{Z\} + \{B\}. \tag{5.9}$$

The equation governing the displacement of the ball is $m_b.\ddot{u}_b = -F_{VI}$. In order to include this equation in the first order differential matrix system 5.9, we can set $\{U_b\} = \begin{Bmatrix} \dot{u}_b \\ \ddot{u}_b \end{Bmatrix}$ and derive that:

$$\{\dot{U}_b\} = \begin{bmatrix} 0 & 1 \\ 0 & 0 \end{bmatrix}.\{U_b\} - \frac{1}{m_b}.\begin{Bmatrix} 0 \\ F_{VI} \end{Bmatrix} = [A_b].\{U_b\} + \{B_b\}. \tag{5.10}$$

Therefore, equation (5.10) can be included in equation (5.9). For this purpose, we set $\{Y\} = \begin{Bmatrix} \{Z\} \\ \{U_b\} \end{Bmatrix}$ in order to obtain:

$$\{\dot{Y}\} = \begin{bmatrix} [A] & [0] \\ [0] & [A_b] \end{bmatrix}.\{Y\} + \begin{Bmatrix} \{B\} \\ \{B_b\} \end{Bmatrix} = [A^*].\{Y\} + [B^*]. \tag{5.11}$$

At the end, equation (5.11) traduces the dynamics of the structure and the ball during both the free-flight and contact phases. The contact force is defined in the following paragraph.

5.2.3 Contact phases

The contact of the ball with the wing plane occurs if the following conditions are satisfied:

$$\begin{cases} u_b(t) - u_{kt}(t) \geq 0 & \text{for contact on top;} \\ u_b(t) - u_{kb}(t) \leq 0 & \text{for contact at the bottom;} \end{cases} \tag{5.12}$$

where kt and kb denote the number of the degrees of freedom of the plane corresponding to the top and the bottom of the cavity where the contact applies. Then, the interpenetration δ between the ball and the structure can be defined as:

$$\begin{aligned} \delta &= u_b(t) - u_{kt}(t) \quad \text{for contact on top;} \\ \delta &= u_b(t) - u_{kb}(t) \quad \text{for contact at the bottom.} \end{aligned} \tag{5.13}$$

Here, we choose to define the contact force F_{VI} applied by the ball on the structure using the Hertz model:

$$\begin{cases} F_{VI} = K_h.\delta^{3/2} & \text{if the contact occurs on top;} \\ F_{VI} = -K_h.(-\delta)^{3/2} & \text{if the contact occurs at the bottom;} \\ F_{VI} = 0 & \text{if the contact conditions are not satisfied;} \end{cases} \tag{5.14}$$

where K_h is the contact stiffness. It depends on the materials and geometries of the solids in contact, and is given by the Hertz model described in chapter 1.

At the end, the matrix system 5.11 can be solved numerically using the Matlab solver ODE23t [3] based on a trapezoidal rule.

5.2.4 Simulation and design of the vibro-impact absorber

5.2.4.1 Configuration of the plane for the simulations

In the simulations, only one VI absorber was activated, the other one was left empty. The measurement and excitation points are the same, and they are located at the end of the wing, next to the VI absorber. The figure 5.3 illustrates this arrangement.

The plane is in free-free boundary conditions. The ten first modes are considered in the modal basis. The added mass due the cavity of one VI absorber and the ball represents 2,41 % of the total mass of the plane.

5.2.4.2 Relation between the gap and the force of excitation

We have defined an indicator I to assess the vibration reduction obtained in a given frequency range thanks to the VI absorber. In the frequency range studied, the maximum of the response of the structure with the vibro-impact absorber is compared to the maximum of the response without the absorber. The figure 5.4 illustrates the two compared responses, and the indicator is defined as follows:

[3] https://www.mathworks.com/help/matlab/math/choose-an-ode-solver.html

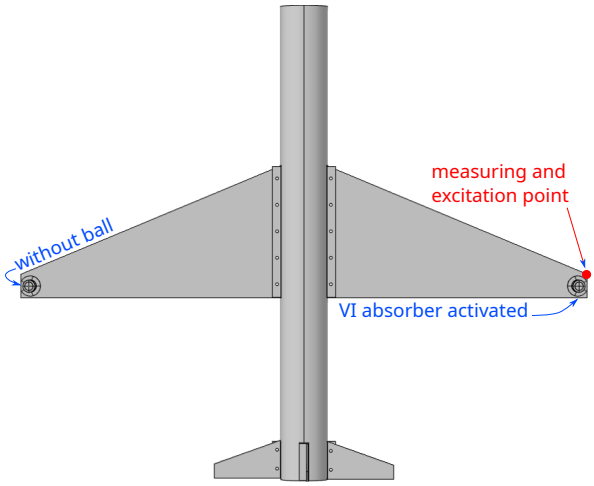

Figure 5.3: Illustration of the configuration of the plane in the simulations.

$$I = \frac{\max(R_{VI})}{\max(R_{ref})}. \tag{5.15}$$

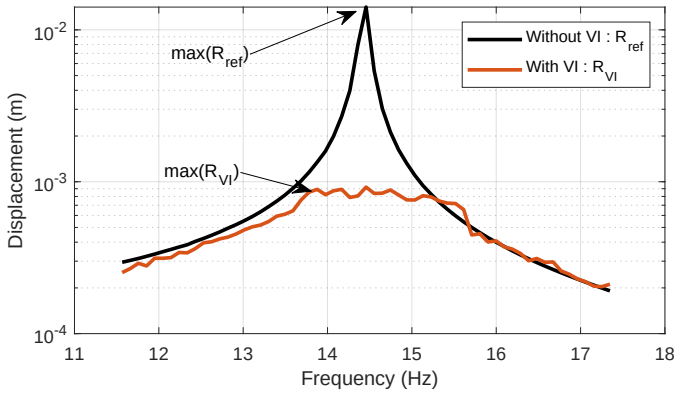

Figure 5.4: Illustration of the calculation of the indicator defined in equation (5.15).

From the indicator presented in equation (5.15), it is possible to derive the vibration attenuation A in decibels:

$$A = 20.\log_{10}(I). \tag{5.16}$$

The attenuation defined in equation (5.16) is calculated for the first mode of the plane, the excitation force is maintained constant at 0,05 N and the gap is varied. For each gap value, the attenuation obtained is reported in figure 5.5.

The results confirm what was previously observed. Under constant excitation amplitude, there exists an optimal gap value that leads to the best vibration reduction. It is worthy to note that the attenuation is less sensitive to the gap value when the gap is larger than the optimal value. On the contrary, for gap values smaller than the optimum, the attenuation can vary roughly even for tiny variations of the gap. This result is particularly relevant to notice in the context of a robust design of the absorber, although this question is not investigated. Then, several other simulations are performed, so that the

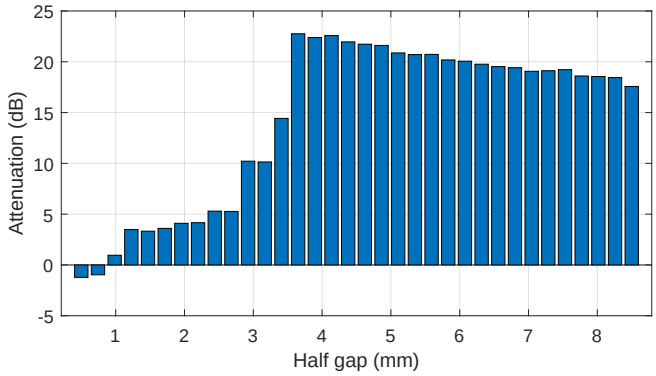

Figure 5.5: Attenuation of the first mode of the plane depending on the gap value for a constant excitation force.

attenuation is assessed for various gap values and amplitudes of the excitation force. The figure 5.6 depicts the results.

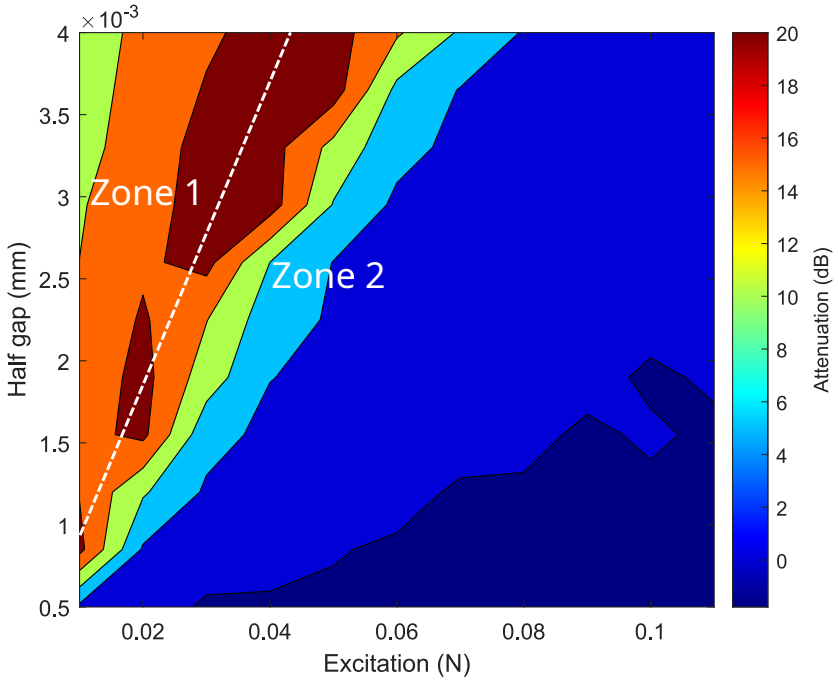

Figure 5.6: Map representing the attenuation obtained on the first mode depending on the gap and the amplitude of the excitation.

The blue areas correspond to a weak vibration attenuation, while the red areas correspond to the best vibration reduction. Up to now, we were used to maintain either the excitation force constant and to vary the gap, or to fix the gap and to vary the excitation in order to find an optimal value. Here, it is interesting to see that the excitation force plays a similar role than the gap in the vibration reduction. Indeed, considering a constant gap value, it is possible to find an excitation force that leads to the best vibration reduction. This result is reminiscent of the scalability property described and illustrated experimentally in the chapter 3 in section 3.3.1.2. In this chapter, it was found that if the ratio excitation / gap is maintained constant, the attenuation remains also at the same

value. This linear behavior can be visualized in figure 5.6, as the frontiers between the color zones are almost linear. Practically, it means that tracking the optimal point of the absorber can be performed satisfying the linear relation 5.17 where b is the gap, F_{exc} is the excitation force, and α is a positive coefficient that must be determined.

$$b = \alpha.F_{exc}. \tag{5.17}$$

At last, the same remark concerning the robustness can be done. The figure 5.6 can be divided in two zones, separated by the dotted gray line. In zone 1, the gap b is greater than its optimal value, and the excitation force F_{exc} is lower than its optimal value. In this zone the attenuation is slightly sensitive to variations of b and F_{exc}. Conversely, in zone 2 the attenuation is much more sensitive to variations of these two parameters. As the excitation is not a design parameter, the gap should be chosen advantageously depending on the excitation force in order to ensure a sufficient robustness of the tuning.

5.2.4.3 Multi-modal attenuation

The question of the attenuation of several modes simultaneously using a single VI absorber was raised in the previous chapters of this manuscript and in some papers [42]. It was shown that using a single vibro-impact absorber can reduce the vibrations of a single mode at a time, but the effectiveness on several modes simultaneously is essentially impossible to achieve. Indeed, the difference of vibration amplitude of the modes are incompatible with the level of activation of the vibro-impact absorber. For instance, if the gap is well tuned in order to trigger the vibro-impacts when the structure oscillates in the vicinity of its first mode, this gap value is too large to trigger the impacts when the structure is excited on higher modes since their amplitude of vibration is lower, unless the excitation force is increased. In the present case, a simulation of the response of the model plane on a wide frequency range (5-200 Hz) was performed. The force was set to 0,05 N and the gap was tuned at 3,65 mm, corresponding to the optimal value found in figure 5.5. The response in displacement of the plane is depicted in figure 5.7

The level of activation of the vibro-impact absorber is well visible: above 10^{-3} m, the impacts are triggered and the response is well attenuated compared to the response without absorber. Thus, the effectiveness on the first mode is quite interesting. Concerning the second mode, a moderate vibration reduction is achieved since the resonance peak is slightly above 10^{-3} m without the absorber. However, one can expect a larger vibration reduction if the gap was reduced appropriately. At last, the effectiveness on the third mode and higher is null because the resonance peak remains below the threshold of activation of the absorber. Consequently, no impacts occur, the ball remains at rest and the response of the structure is linear.

In the following section, the experimental behavior of the model plane equipped with a vibro-impact absorber is investigated.

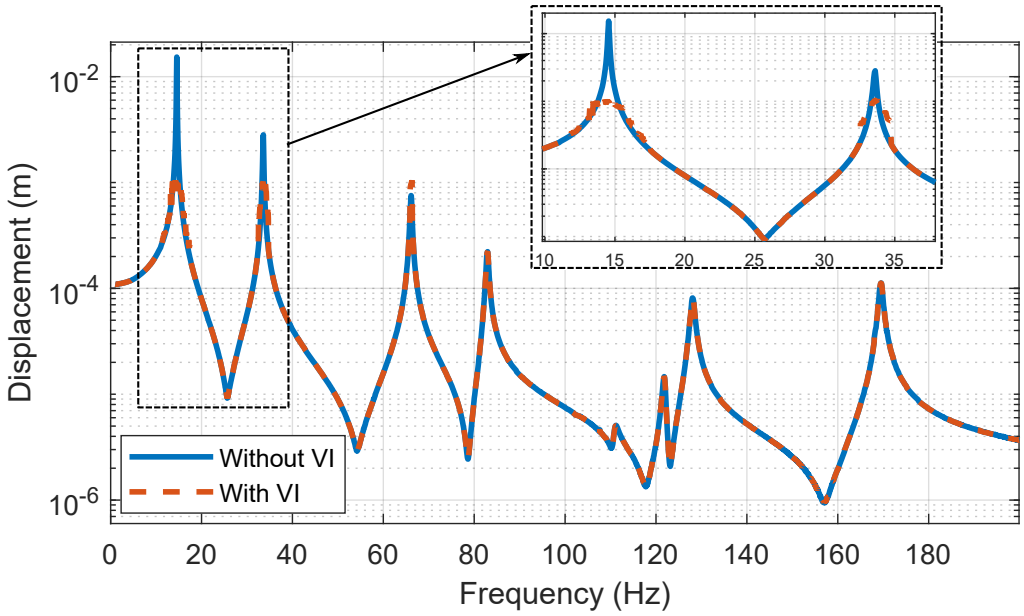

Figure 5.7: Response of the plane of the whole frequency range. $F_{exc} = 0,05N$; $b = 3,65mm$.

5.3 Experimental study of a model plane with one vibro-impact absorber

5.3.1 Description of the experiments

Based on the design shown in figure 5.1b, two VI absorbers were manufactured and attached at the end of the wings. However, only one absorber is activated at a time in the following experiences, otherwise it is specified. A shaker with a stinger is used to apply the excitation force on the plane. The response of the plane is measured at the left end of the wing thanks to a laser vibrometer. The figure 5.8 illustrates the arrangement of the equipments.

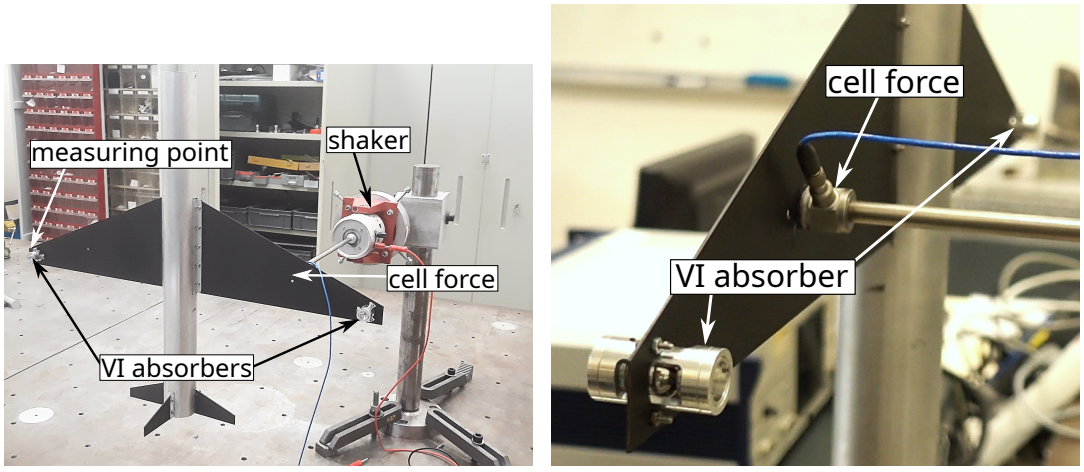

(a) (b)

Figure 5.8: Overview of the experimental set-up.

5.3.2 Harmonic excitation of the first mode

In this section, the plane is excited by a harmonic force which frequency is in the vicinity of its first mode. The control of the excitation force is realized using the same method than in chapter 3. The details are given in [125]. The gap of the VI absorber situated next to the observation point is equal to 2,4 mm. On the opposite side of the wing, the other VI absorber is locked, so that its gap is equal to zero. In these tests, the gap is fixed and the excitation force is varied. The methodology adopted to calculate the FRF of the plane from the time response is based on the Hilbert transform, as done previously in chapter 3 in section 3.2.5.

The figure 5.9 shows the FRFs obtained for each excitation force. Even if the values chosen for the excitation force do not allow to find an optimal configuration (the attenuation keep increasing when the excitation force decreases), the behavior observed is the same as found in the simulations before: high excitations lead to responses close to the response with the ball locked, while decreasing the excitation improves the attenuation. Furthermore, we can suppose that keep decreasing the force beyond the optimal excitation force should lead to obtain a response close to the response without ball.

In the following paragraph, the response of the plane to broadband excitations is studied and the effectiveness of the absorbers is examined.

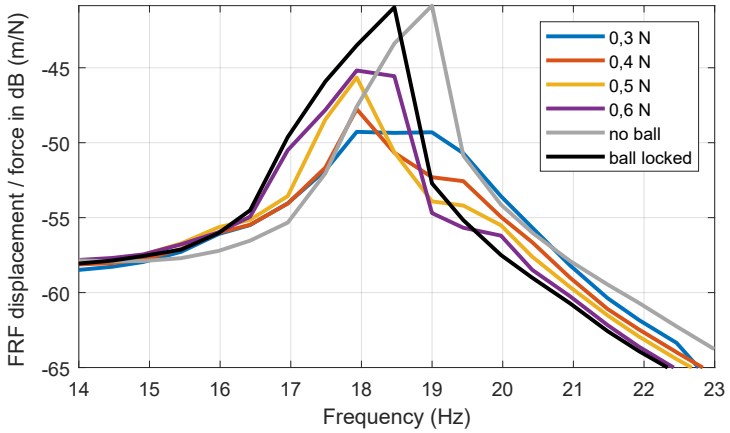

Figure 5.9: FRFs of the plane for several excitation force amplitudes.

5.3.3 White noise excitation

The vibration reduction obtained for white noise excitation is also investigated. We will see that interesting attenuations can be obtained on the first four modes of the plane, and we will end with the limitations of using a single VI absorber (or two with the same gap).

The excitation is a white noise signal in the frequency range [10;50] Hz. Three gap values and four excitation force amplitudes are tested: 0,1 mm ; 0,2 mm and 0,3 mm for the gaps, and $1\times F_{exc}$; $1,4\times F_{exc}$; $1,8\times F_{exc}$ and $2,3\times F_{exc}$ where F_{exc} is the reference level of the excitation force. It is worthy to note that the excitation is not controlled during these tests, only the voltage of the force signal is changed in order to change the excitation force. Then, the Root Mean Square value of the force is calculated for each voltage.

The FRFs obtained are compared in figure 5.10. Concerning the third mode, one should notice that the results are not presented because they are not usable. Indeed, the

curves are very noisy and impossible to distinguish from each other. A likely reason for this is that the excitation point is very close to the node of the third mode, leading to non-usable results for this mode. As usual, the same effects of the gap and of the excitation are observed. It is relevant to see that interesting vibration reductions are obtained for all the modes studied, depending on the gap and the force value. More details concerning the attenuation are depicted in figure 5.11. Hence, up to 7 dB are obtained for the first mode (gap = 0,1 mm and $1 \times F_{exc}$), 11 dB for the second mode (gap = 0,2 mm and $1,8 \times F_{exc}$), and more than 12 dB for the fourth mode (gap = 0,2 and $2,3 \times F_{exc}$). With two VI absorbers (one at each end of the wings) tuned with the same gap, the vibration reduction is even better: up to 19 dB, see figure 5.12.

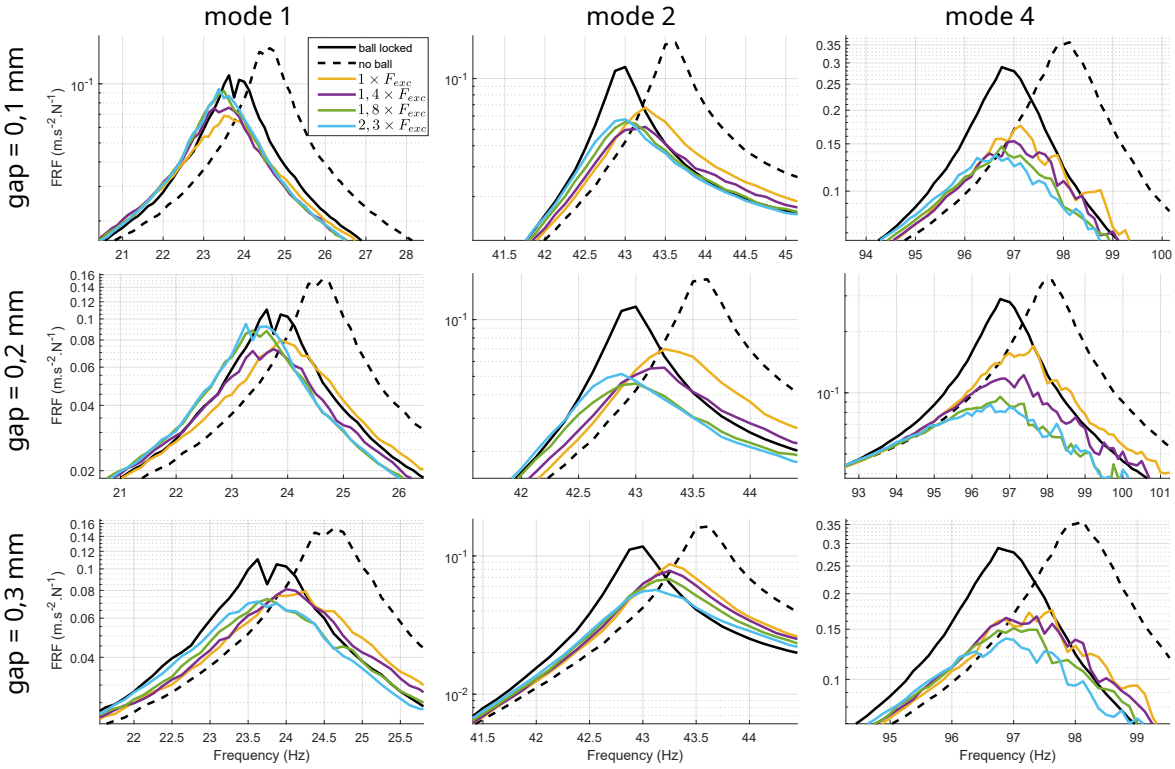

Figure 5.10: Zoom on the FRFs of each mode for white noise excitation.

Looking at the attenuation presented in figure 5.11 and figure 5.12, many relevant remarks must be done. To start with, the scalability property discussed earlier in this manuscript is visible here again. Indeed, when an optimal vibration reduction is found corresponding to the pair gap and F_{exc}, this optimum is moved to higher excitation force if the gap is increased, as illustrated on the second mode in figure 5.11. Then, considering the modes 1, 2 and 4, the optima are not simultaneous: when the value pair F_{exc} and gap is optimal for one mode, it is necessary not for the other modes (for instance, see figure 5.11 at gap = 0,2 mm). Therefore, increasing (respectively decreasing) the force has a beneficial (respectively detrimental) effect on the attenuation of one mode, while it has a detrimental (respectively beneficial) effect on the attenuation of another mode (see for example mode two and four at gap = 0,1 mm in figure 5.11). This is even clearer in figure 5.12 for the modes one and two on the one hand, and for the mode 4 on the other hand. This illustrates very well that multimodal attenuation cannot be achieved using a single VI absorber (or even two VI absorber since they have the same gap).

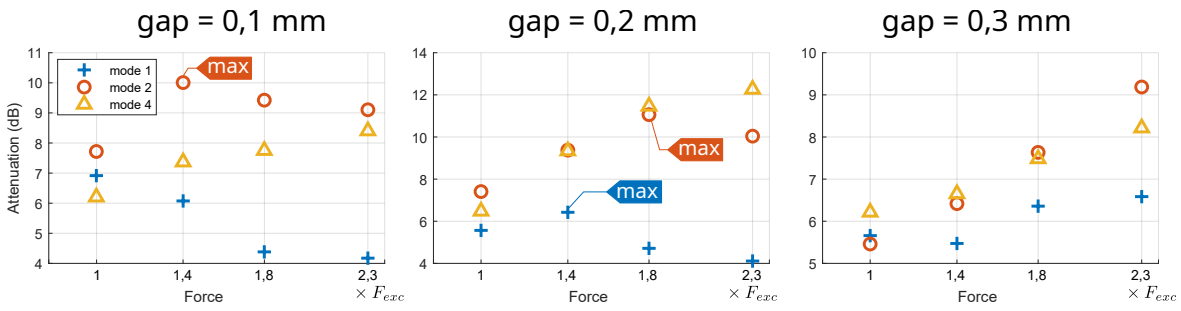

Figure 5.11: Vibration reduction obtained in figure 5.10 depending on the gap and the excitation force.

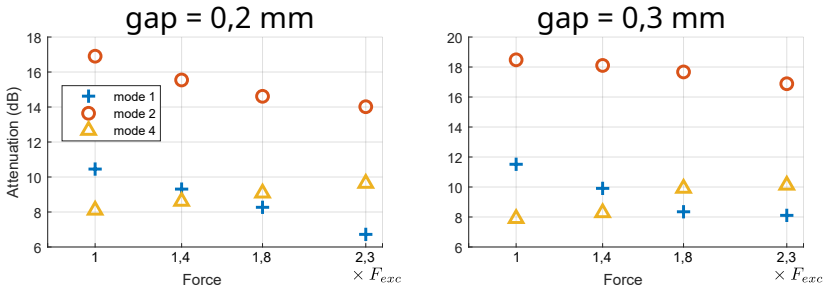

Figure 5.12: Vibration reduction obtained with two VI absorbers activated with the same gap at the wings ends.

Accordingly, the next section focuses on the realisation of multiple VI absorbers spatially distributed on the wing plane. The objective is to surpass the limitations observed in the previous cases where a single VI absorber is used.

5.4 Realization and experimentation of multiple VI absorbers spatially distributed on a three-dimensional structure

This section deals with the experimental results of the vibration behavior of the plane equipped with multiple VI absorbers, in order to address the question of multimodal attenuation. The reader should be warned that the plane used in this section has a slightly different design than the one used in the previous section. For practical reasons, the connections between the wings and the fuselage are realized differently. Therefore, their dynamic behavior are barely different. However, this is not a major issue since the results of this section are not directly compared to the previous section.

5.4.1 Description of the experimental set-up

The design of the VI absorbers is based on the CAD work done previously. The cavity is realized from a PMMA tube. The screw and the counter nut are manufactured, and

they close the top of the cavity. Thanks to the screw the gap can be set in the range 0 mm - 2 mm. A magnet is stuck at the bottom of the cavity in order to attach and move the VI absorbers very easily at the surface of the wings to study various locations of the absorbers. In order to try to obtain the same contact properties on each side of the cavity, thin steel disks are stuck on the magnet and on the screw. At the same time, it avoids any damages to the magnet and the screw that may not resist very well to repeated impacts. Photos of one VI absorber are presented in figure 5.13, and the masses of one VI absorber compared to the mass of the plane are given in table 5.2. Therefore, one VI absorber with its ball represents 0,32 % of the mass of the plane, and 0,69 % of the mass of the wing.

Figure 5.13: One VI absorber.

Plane	Wing	One VI absorber	One ball
875 g	408 g	1,8 g	1g

Table 5.2: Mass of the structure and of the VI absorber.

The plane is suspended by thin rigid wires in order to approach free-free boundary conditions (see figure 5.14). The plane is excited by a white noise signal using a shaker and the excitation force is measured using a cell force. The amplitude of the excitation force is not controlled. Nevertheless, the gain of the amplifier is set at the same level for each test, as is the voltage of the excitation signal. The fluctuations of the amplitude of the excitation force and the repeatability of the response of the plane are evaluated in appendix D.4. As illustrated in figure 5.15, the VI absorbers are behind the wings in order to leave the opposite surface free in order to perform the measurements of the observation points (depicted in figure 5.14) thanks to the vibrometer. In the following of this chapter, all the FRFs presented correspond to the average of the modulus of the FRF obtained at each measuring point.

5.4.2 Influence of the gap on the effectiveness in the frequency range

A first parametric study is realized in order to estimate the gap values that are susceptible to lead to an effective vibration reduction. For this purpose, three VI absorbers are positioned at the end of the wings as great displacements are expected at this location. Their gap are varied (they all have the same value), and the vibration attenuation obtained for each mode is evaluated like previously using equation (5.16). The FRFs obtained for all the gap values are depicted in figure 5.16. The figure is divided in ten frequency ranges. For each of them, a zoom on the FRFs can be visualized in figure 5.17, and the attenuation is assessed in figure 5.18.

As a remark, the mode at 82 Hz will not be considered in this study, because the excitation point is very close to a node. Therefore, the corresponding mode is hardly excited and the results obtained in this frequency range are not usable.

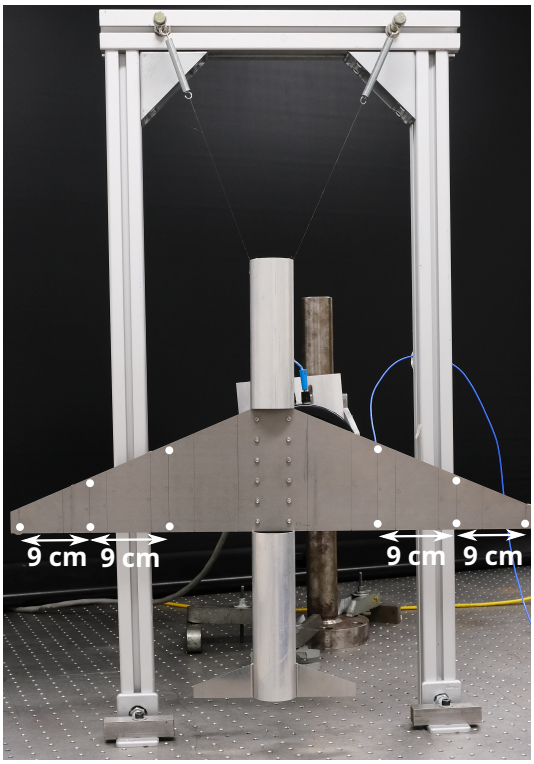

Figure 5.14: View of the plane in free-free conditions. The white dots correspond to the observation points measured by the vibrometer.

Looking at the results of figure 5.17 and figure 5.18, a general trend is observed: for the lowest frequency modes, the largest gaps lead to the best effectiveness. On the contrary, the smaller gaps are more efficient considering the higher frequency modes. It corroborates the conclusions drawn in the previous chapters. One can notice that the peaks have slightly moved to the left compared to the FRF without ball. This is due to the added mass of the VI absorbers. Moreover, these added masses may slightly change the mode shapes of the plane. Therefore, the FRFs without balls and with the balls locked are not superimposed (see appendix D.1). Here, the attenuation calculated does not take in account this change in the mode shapes. For the sake of simplicity, this phenomenon is not considered, and the attenuation is calculated using the FRF without ball as reference.

These preliminary results permit to verify that the range of gap available effectively allows significant attenuation. Moreover, they give an overview of the optimal gap values corresponding to each frequency range. Nevertheless, the influence of the location of the absorbers should be investigated as well. Accordingly, such tests are presented in the next paragraph.

5.4.3 Multi-modal attenuation

As we have previously seen that one gap value is mainly effective in a narrow frequency range, we will combine multiple absorbers tuned with different gaps in order to obtain a multimodal vibration reduction. To reach this objective, four locations are identified corresponding to the anti-nodes of specific modes. Thus, large displacements are expected at these locations. For each location, the gap is varied in order to find the best value leading to the best vibration reduction.

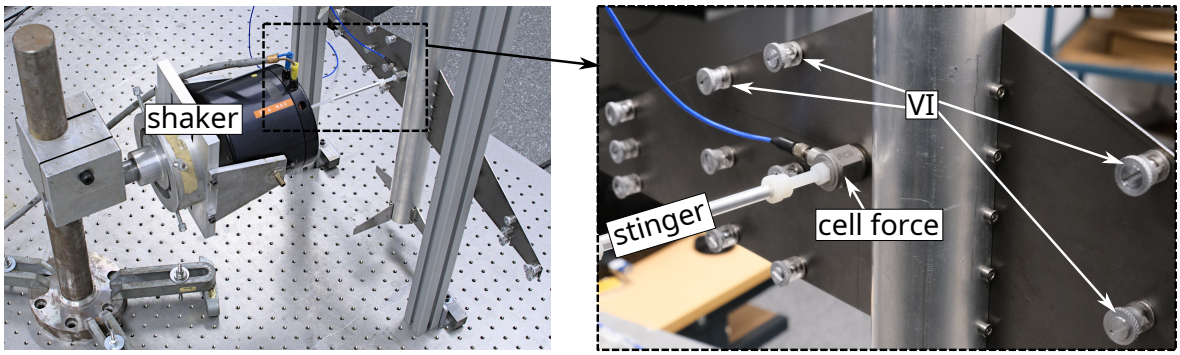

Figure 5.15: View of the shaker and the cell force.

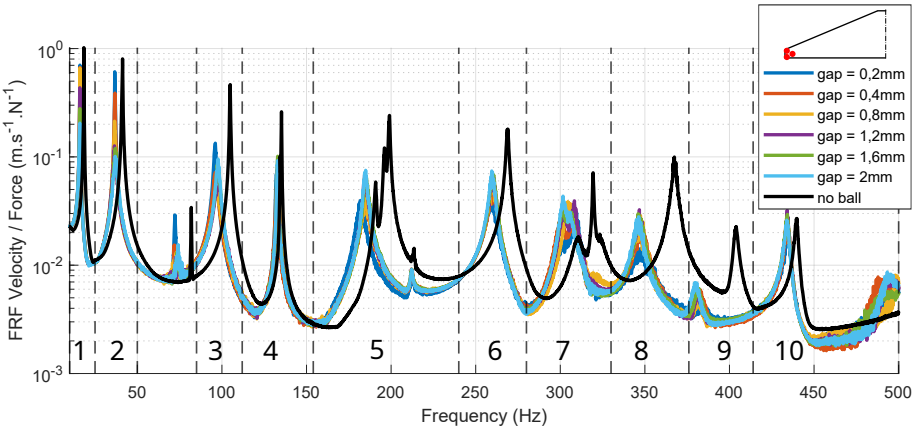

Figure 5.16: FRFs obtained with three VI absorbers at the end of the wings. The attenuation is calculated in the ten frequency ranges denoted in this figure.

5.4.3.1 Determination of the locations and gaps of the VI absorbers

The four locations tested are presented in figure 5.19. For each location, the gap is varied in order to determine its optimal value. Then, the attenuation is evaluated for all the gap values and for each frequency range. At the end we are able to determine the frequency range of effectiveness of the four locations, and the corresponding gap that enables the maximum vibration reduction. These attenuations are available in figure 5.21. The damping performance obtained in each frequency range will be discussed in the light of the modal shapes given in figure 5.20. Both experimental and numerical modal shapes are presented for a better visualization. However, the model did not predict correctly the mode shape for the two modes at 199 Hz and 215 Hz. Accordingly, they are removed from the figure. One can see that the two modes in the range [112 ; 154] Hz and [280 ; 330] Hz are very affected by the location 2 and 4, while the location 3 reaches its best effectiveness in the range [112 ; 154] Hz. The reason for this is that the modes at 135 Hz - 136 Hz and 316 - 320 Hz correspond to the torsional modes, and location 2 and 4 correspond to the anti-nodes of the second torsional mode (316 and 320 Hz) where large displacements are taking place. By contrast, the location 3 corresponds to a node of this same mode, while it corresponds to the anti-node of the first torsional mode (135 Hz). This is why such a great effectiveness can be achieved on this mode. Specifically, the FRF displacement / force gives responses ten times higher at the points in the middle of the wings compared to the points at the end of the wing for the first torsional mode. Similarly, the response is

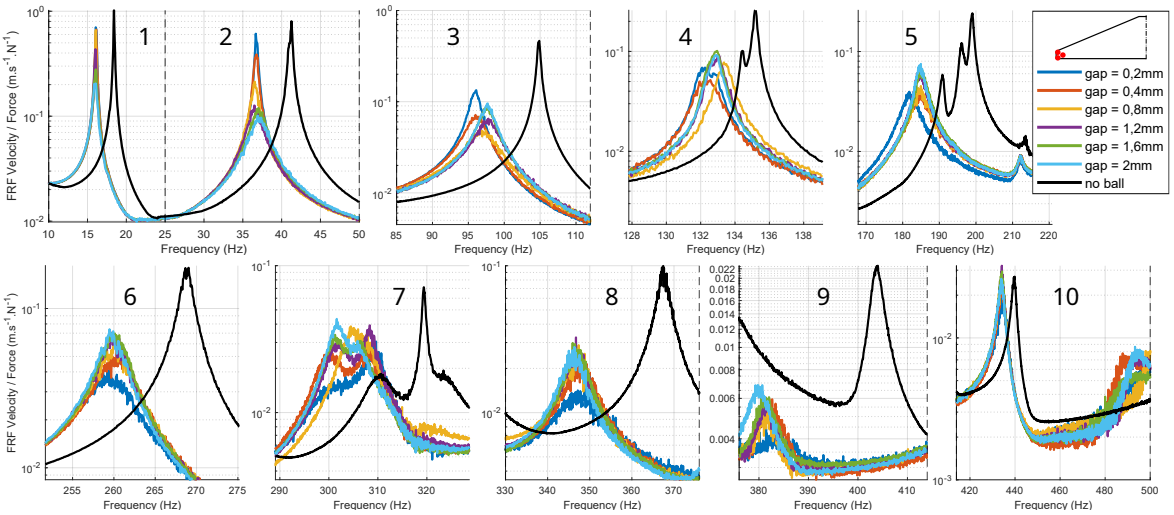

Figure 5.17: Zoom of the figure 5.16 on each frequency range.

5 times higher concerning the second torsional mode. On the contrary, location 1 does not exhibit much effectiveness for the two torsional modes, but interesting attenuation is achieved for almost all the others. Indeed, the end of the wings are submitted to large displacements in the case of the flexural modes (modes 1, 2, 3, 4, 7, 8, 9, 10, 13, 14 in figure 5.20), but not for the torsional modes. More details on the amplitude of the displacements are given in appendix D.2.

Moreover, the location 2 was supposed to be efficient on the mode at 270 Hz as it corresponds to an anti-node of this mode. However, the figure 5.21 shows that the attenuation reaches only 9 dB, what is less than expected. Looking carefully to the mode shape at 270 Hz in figure 5.20, we can see that this mode presents large displacements on the ailerons (the experimental mode shape shows this better than the numerical mode shape). Consequently, this mode is harder to mitigate since no VI absorbers are located on the ailerons. Despite this, placing the VI absorbers at the end of the wings where displacements are larger enables to achieve a better effectiveness of 14 dB.

At last, the effectiveness achieved on the two first modes (18 Hz and 41 Hz) could probably be increased using larger gaps, but the maximum gap is reached in this case.

In order to assess the multimodal effectiveness of multiple absorbers, we focused on the attenuation circled with red line that correspond to the targeted attenuation on the corresponding frequency range. Thus, it determines the gap to choose. Then, the four location are used simultaneously with the objective to improve the effectiveness for several frequency ranges simultaneously. Therefore, the following approach is adopted:

- The gap of the VI absorbers of location 1 are set to 2 mm in order to mitigate the two first modes;
- The gap of the VI absorbers of location 2 are set to 0,2 mm in order to mitigate the torsional modes in the frequency range [112 ; 154] Hz and [280 ; 330] Hz;
- The gap of the VI absorbers of location 3 are set to 0,4 mm in order to mitigate the mode in the frequency range [85 ; 112] Hz (a great effectiveness is also expected in [112 ; 154] Hz);

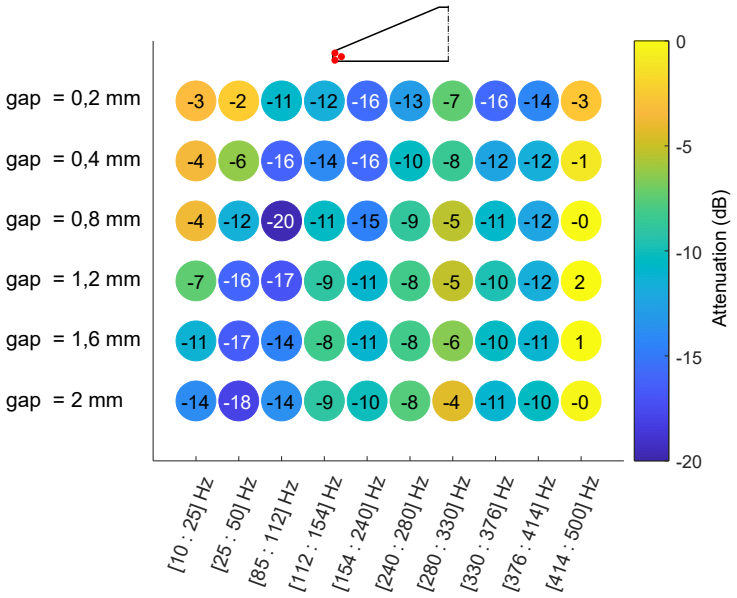

Figure 5.18: Vibration reduction obtained using three VI absorbers at the end of the wings in each frequency range.

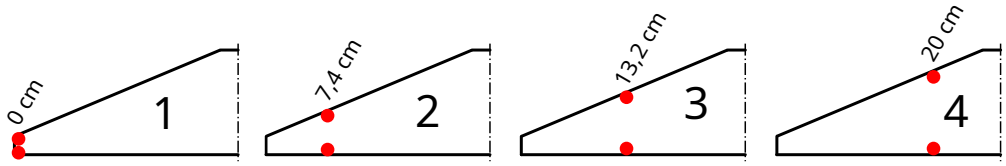

Figure 5.19: The four locations tested.

- The gap of the VI absorbers of location 4 are set to 0,2 mm in order to mitigate the modes in the frequency range [112 ; 154] Hz and [280 ; 330] Hz

5.4.3.2 Combination of multiple VI absorbers

The comparison of the FRFs obtained separately in each of the four locations of the absorbers and for the four locations simultaneously are presented in figure 5.22. The corresponding attenuations are given in figure 5.23.

It is interesting to see that the vibration reduction obtained in the case where all the VI absorbers are used simultaneously is equal or greater than in the case of each location 1, 2, 3 or 4 taken individually. Therefore, even in the case of the frequency range where no particular effectiveness was expected, a significant attenuation is achieved. Thus, the modes around 200 Hz are reduced up to 20 dB, the mode at 270 Hz is reduced of 14 dB. Even the modes at 371 Hz and 406 Hz are reduced of 18 dB and 15 dB respectively. However, none of the location tested are efficient in the frequency ranges [414 ; 500] Hz.

As a consequence, we have performed multimodal vibration reduction using multiple VI absorbers that are appropriately located on the structure, and choosing the gap value that leads to the best effectiveness. Moreover, the difference of the amplitudes of displacement of the lower and the higher modes of the plane is less than in the case of the beam that was studied in chapter chapter 3. For instance, the ratio of the amplitudes of displacements of the first and the fourth mode of the plane is approximately 18, while

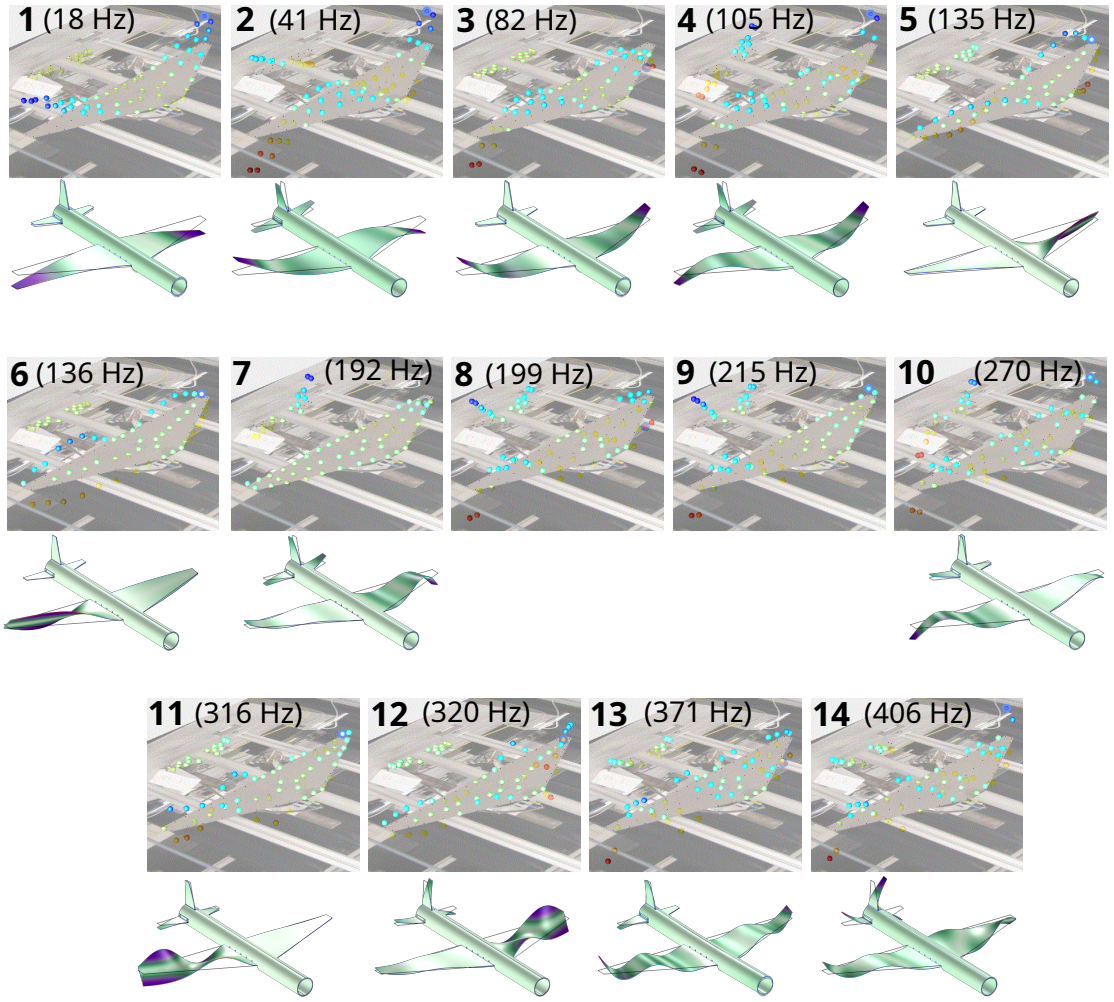

Figure 5.20: Mode shapes of the plane.

it is more than 5000 in the case of the beam ! The FRF displacement / force is given in appendix D.3 for more details. Such a result facilitates the effectiveness of the absorbers on several modes simultaneously, and this is probably the reason why vibration reduction could be performed even in frequency ranges where it was not particularly expected.

Lastly, one should be aware that adding masses to the structure slightly changes the frequency and the mode shapes, and it is not considered here.

5.4.4 Vibration reduction of the low-frequency modes

In the domain of vibration reduction, a difficulty is to perform vibration suppression of the first low frequency modes of the structure without deteriorating the static rigidity. Indeed, a common solution is to use polymer materials because they have very high damping properties in certain conditions of temperature. However, these interesting damping properties are often related to bad static rigidity of the material, what is a major problem for the structural resistance [24]. The previous chapters have shown that great vibration reduction was performed on the first mode of a beam using a VI absorber. Nevertheless, the static rigidity should be verified. This is done on the plane equipped with multiple VI absorbers. The figure 5.24 show the FRF displacement / force averaged on all the ob-

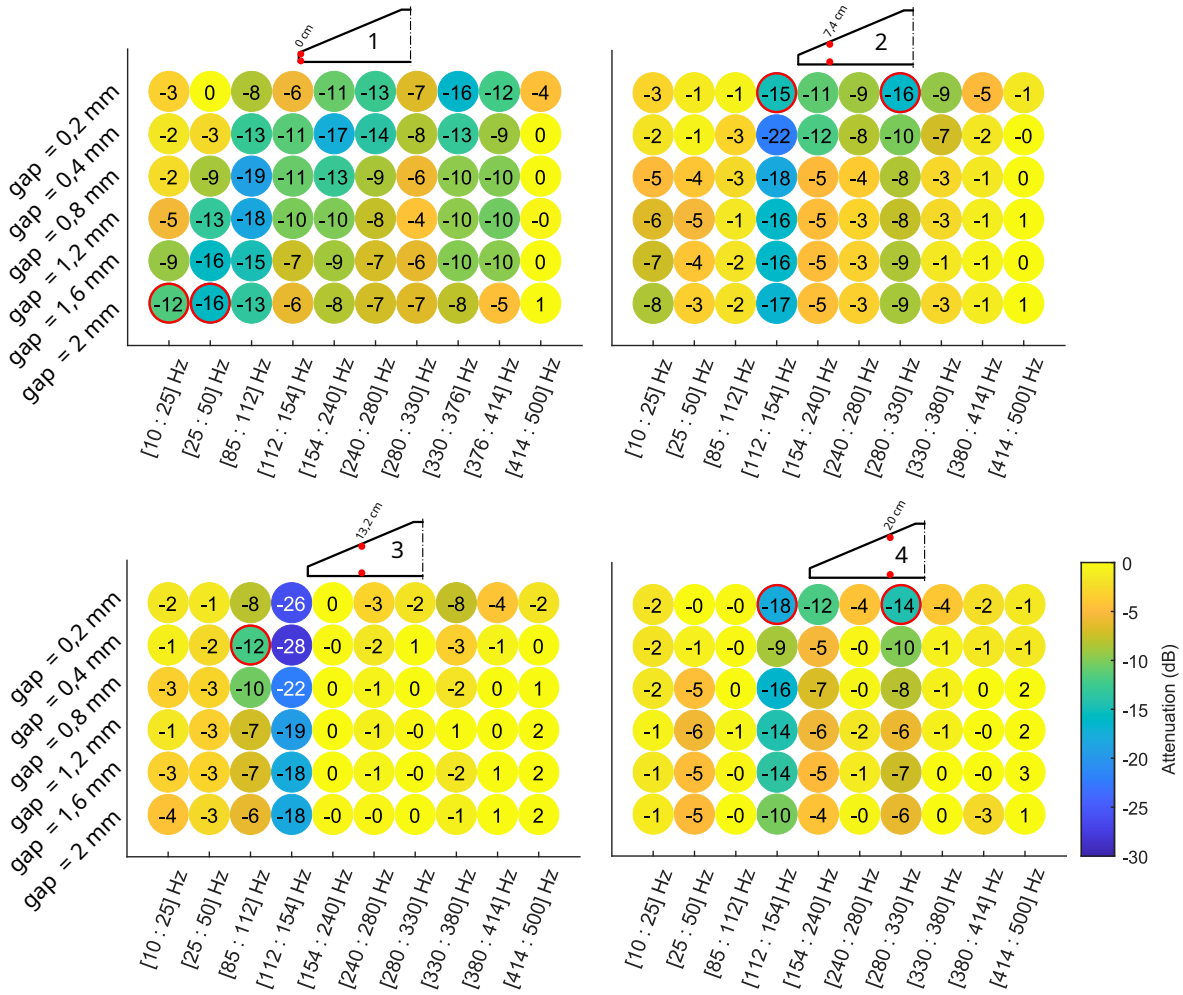

Figure 5.21: Determination of the frequency range of effectiveness for each location of the VI absorbers. The red circles correspond to the targeted attenuation and determine the gap value.

servation points on the plane. At the lowest frequencies (10 Hz in the present case) it represents the flexibility of the plane. Therefore, the static rigidity is obtained considering the inverse of the flexibility, and it means that the flexibility must be as low as in the case where no VI absorbers are attached to the plane. As the two curves merge for the lowest frequency, we can conclude that the attachment of the three VI absorbers at the ends of the wings does not deteriorate the static rigidity of the plane. Meanwhile, the two first low frequency modes of the plane are interestingly damped by the adding of the VI absorbers. Thus, VI based strategies are good candidates to perform both low frequency vibration reduction while guaranteeing that the structural properties of the structure are not significantly affected. Moreover, a greater attenuation could be expected for the first modes in the present case if the gap is increased. However, the maximum value was already reached.

5.4.5 Response to narrowband excitations

In the literature, many papers aiming to explain the mechanisms leading to energy dissipation in vibro-impacts state that energy transfers occur between modes [128, 49, 7]. More specifically, the vibro-impacts excite the higher modes of the considered structure.

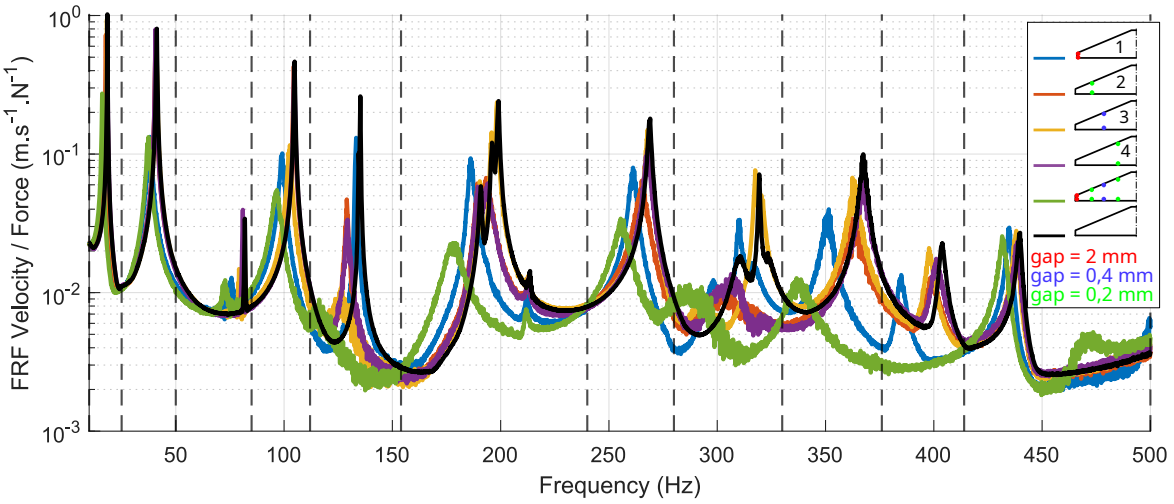

Figure 5.22: Comparison of the FRFs obtained for different locations and gaps of the VI absorbers.

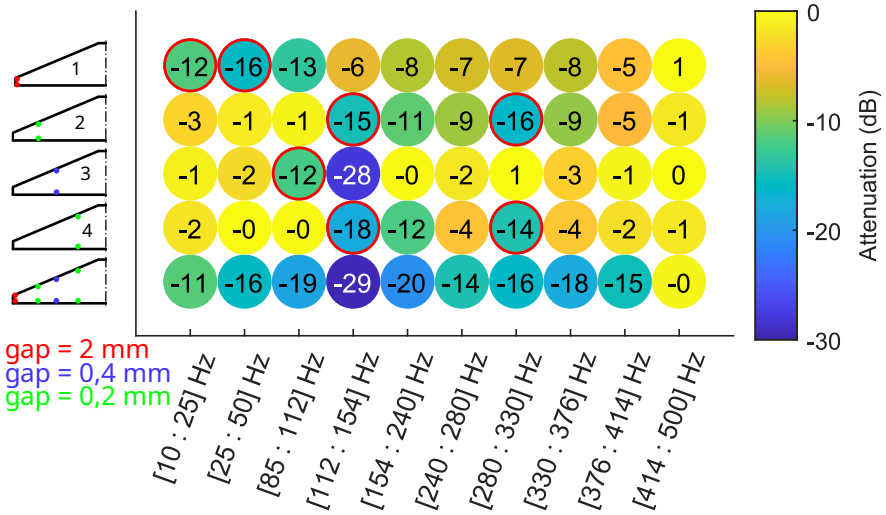

Figure 5.23: Attenuation obtained for different locations and gaps of the VI absorbers. The red circles are the targeted attenuation.

This statement has been verified numerically in chapter 4 of this manuscript, where a model of a beam submitted to vibro-impact is solved using a semi-analytical method.

The present section is devoted to study the response of the model plane submitted to narrowband white noise excitations, and to analyze the vibrational response of the structure to vibro-impacts out of the range of excitation. For this purpose, a narrow frequency range is selected for the excitation signal, and the response of the plane is analyzed up to 5000 Hz. The arrangement of the vibro-impact absorbers correspond to the one presented in figure 5.18, where three VI absorbers are set at the both ends of the wings.

5.4.5.1 Excitation of the two first modes: 10 - 70 Hz

The first case investigated consists in exciting the plane on its two first flexural modes, at 18 Hz and 41 Hz. Therefore, the white noise excitation is in the range 10 - 70 Hz. The excitation amplitude is maintained constant, and the gap is varied. The figure 5.25 shows

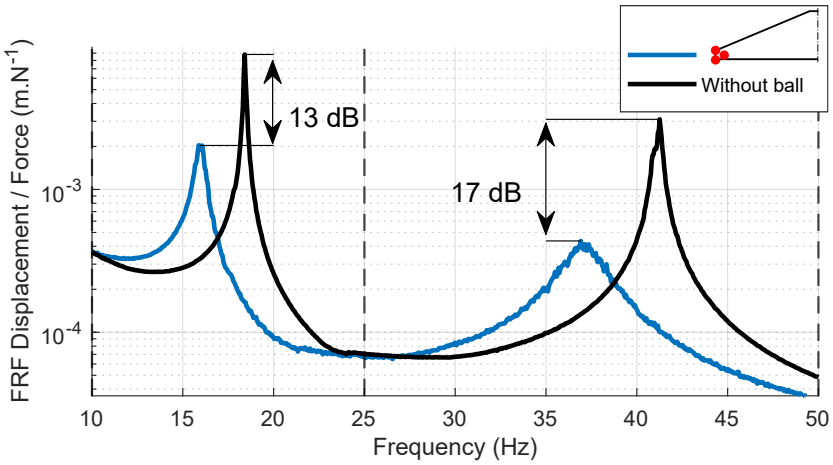

Figure 5.24: FRF in displacement illustrating the damping of the two first modes ensuring the static rigidity (gap = 2 mm).

that the gap of 2 mm leads to the best vibration reduction, especially for the second mode. The subfigure b) represents the quadratic velocity of the plane, averaged on the measuring points on the frequency range 70 - 5000 Hz. The choice was made to use the quadratic velocity instead of the velocity because it is proportional to the kinetic energy of the structure and has an interesting physical meaning. At this point, the subfigure b) allows to distinguish the responses with the VI absorbers from the responses without balls, as the first ones are largely higher than the last ones. Then, the subfigure c) shows the integral of the quadratic response over the frequency range 70 - 5000 Hz, so that it allows to compare the accumulation of the energy in the structure over the frequency range. It is worthy to note that the highest curves correspond to the gap values leading to the best vibration reduction. Interestingly the curves related to the responses without balls and with the balls locked are approximately one thousand times lower. As a consequence, it confirms that vibro-impacts lead to an energy transfer from the lower modes of the structure towards the higher modes. Moreover, the closer to the optimal response, the higher the energy transfer.

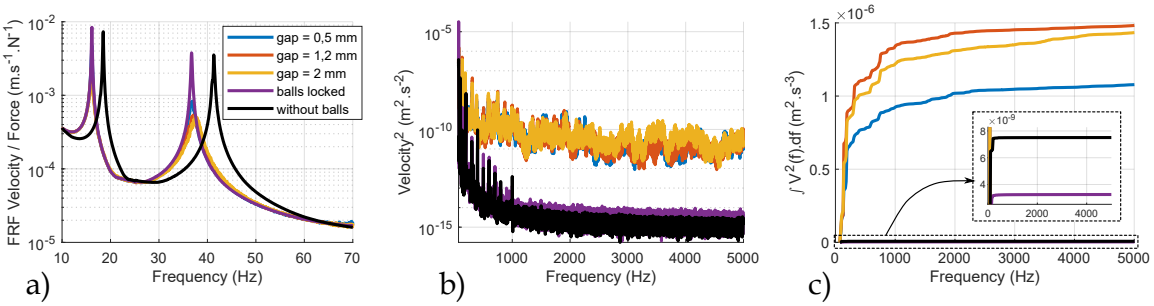

Figure 5.25: Analysis of the excitation in the range 10 - 70 Hz. a) FRF. b) quadratic velocity out of the excitation range. c) integral of the quadratic velocity out of the excitation range.

5.4.5.2 Excitation of the fourth mode: 85 - 123 Hz

In this second case, the excitation is in the vicinity of the fourth mode, so that we are able to study the response of the structure for frequencies both lower and higher than the ex-

citation frequencies. This time, the optimal gap is equal to 0,5 mm. In figure 5.26, the upper plots b) and c) focus on frequencies higher than the excitation range, while the lower plots d) and e) focus on frequencies lower than the excitation range. Looking first at the subfigures b) and c), the same conclusions than above can be drawn: the responses without balls and with the balls locked lead to negligible levels of vibration in this frequency range, while the optimal response is the one that accumulates the most energy over this frequency range. However, the conclusions are different regarding the plots d) and e). Indeed, the subfigure d) representing the quadratic velocity shows that the higher values are related to the worst response in terms of vibration reduction (gap equal to 2 mm and 1,2 mm). Furthermore, the subfigure e) confirms this observation, since the most energy is accumulated in the range 10 - 85 Hz for the gap equal to 2 mm. On the contrary, the curve associated to the optimal gap (equal to 0,5 mm) is quite below. This would suggest that, once the optimal gap is found, the vibro-impacts result in an energy transfer in the upper part of the frequency range larger compared to suboptimal cases, but not in the lower part of the frequency range. As explained in chapter 4, this phenomenon is beneficial to the vibration reduction, and the energy-based approach adopted in this same chapter comes to the same conclusions. Consequently, VI absorbers seem to be able to damp not only the first mode of a structure, but also the higher ones without significant detrimental effects.

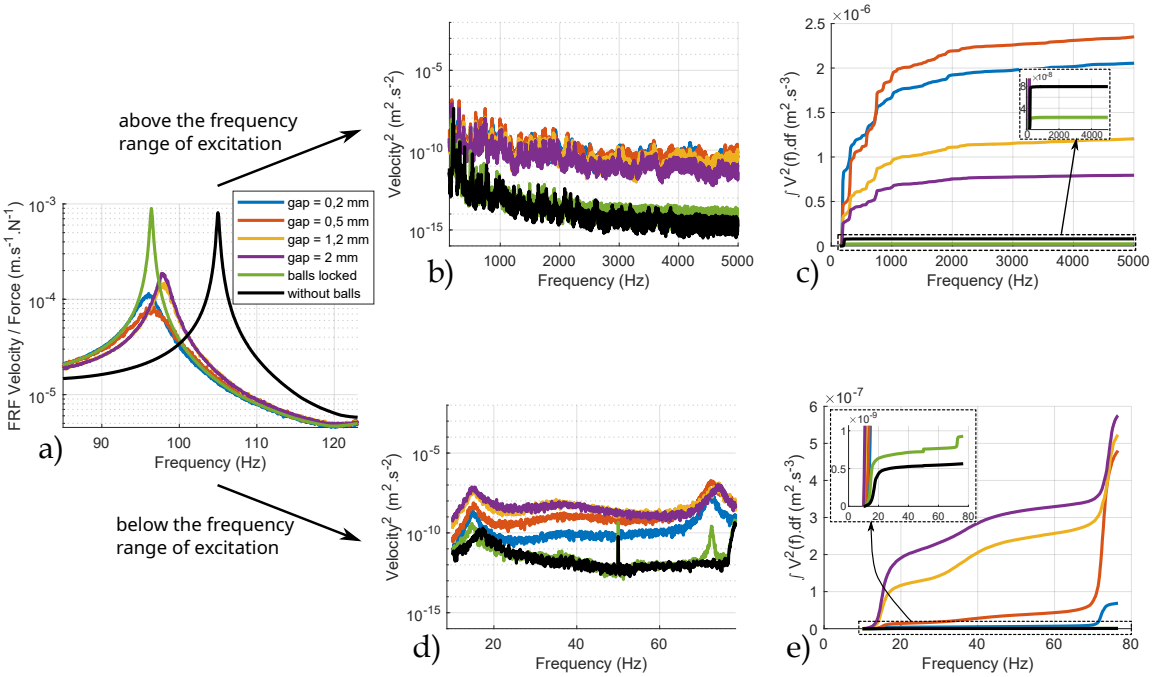

Figure 5.26: Analysis of the excitation in the range 85 - 123 Hz. a) FRF. b) quadratic velocity above the excitation range. c) integral of the quadratic velocity above of the excitation range. d) quadratic velocity below the excitation range. e) integral of the quadratic velocity below of the excitation range.

5.5 Conclusions

The study of the behavior of a multi-modal structure equipped with vibro-impact absorbers turned out to be a crucial point to represent the physical phenomena at stakes

on real structures. Accordingly, this chapter examines numerically and experimentally the behavior of a model plane endowed with a single vibro-impact absorber. In a second time, we realized experiments in order to investigate the benefits of employing multiple VI absorbers to overcome the limitations encountered with a single VI absorber.

First, a modeling and numerical work is proposed to simulate the time response of a three-dimensional structure equipped with a vibro-impact absorber. The approach adopted is based on a finite element model of the structure. Once the matrices of the system are known, the vibro-impact force is added to the equations and the system is solved using numerical integration. The simulations exhibit very clearly a relation between the gap and the excitation amplitude of the main structure. This can be turned into the following design rule: the optimal vibration reduction can be reached for several gaps and excitation forces, and the relation between these two parameters is linear. This finding should help to determine the optimal gap of the absorber, depending on the excitation conditions. Moreover, the influence of these two parameters are confirmed experimentally. In addition, the effectiveness of a VI absorber for white noise excitation is investigated. The results show distinctly that a single VI absorber can tackle one mode at a time, leading to attenuation up to 13 dB. However, no optimal configuration exists to address the problem of multimodal attenuation.

To this end, the model plane tested in this chapter is then equipped with smaller multiple VI absorbers. Preliminary tests confirm that smaller gaps are more suited to tackle higher modes, while larger gaps have a better effectiveness on the first modes of the plane. In order to deal with multimodal attenuation, the influence of the location of the absorbers on the frequency range of effectiveness is firstly examined. Furthermore, the level of performance obtained in each frequency range is explained based on the mode shapes. In the light of these results, four locations are combined and allow to perform an effective multimodal vibration reduction. Even if the attenuation obtained is more complex than simply the sum of the attenuation of each individual location, it is worthy to note that we achieved at least the same vibration attenuation than the one obtained for each individual location. And sometimes even better. Then, it was verified that such absorbers enable to perform low frequency vibration reduction without significantly modifying the structural properties of the plane, and in particular, the static rigidity, whereas it is usually difficult to achieve with polymer materials. At last, narrowband excitations are considered and the behavior of the plane is studied out the range of excitation in order to assess the nonlinearity effects due to vibro-impacts. The results corroborate the conclusions drawn in chapter 4, since the structure seems to undergo larger energy transfer towards the higher modes than towards the lower modes, confirming that no major detrimental effects occur in the presence of vibro-impact absorbers.

Conclusions and perspectives

The work presented is this PhD thesis is focused on the design of vibro-impact absorbers in the context of vibration mitigation. New experimental approaches are adopted, and provide novel and promising results concerning the performance and the design of vibro-impact absorbers. In particular, a full-field measurement method is proposed for vibro-impact systems. Then, structures of progressive complexity are equipped with vibro-impact absorbers, namely a beam and a three-dimensional structure corresponding to a model plane. Numerical approaches are adopted to complete and validate the experimental results.

The first contribution of this work concerns the development of a full-field measurement technique allowing to measure and characterize the vibro-impact phenomenon. The technique developed is based on a Digital Image Correlation process and a series of pictures recorded using a high speed camera. The motions of both the main structure and the ball are reconstructed, overcoming the difficulties encountered to measure the displacement of the oscillating mass with conventional sensors. Then, continuous displacements are obtained using curve fitting as a model identification process. Hence, it is possible to derive the velocities using analytical derivatives without noise amplification. At the end, the coefficient of restitution and the friction forces acting on the ball during the free flight phases are obtained. Up to now, these quantities remained unmeasurable, demonstrating the high benefit of such field measurement for vibro-impact applications. These results correspond to the chapter 2 and are published in *Mechanical Systems and Signal Processing, Volume 156* entitled *Full-field measurements with Digital Image Correlation for vibro-impact characterisation*.

The second contribution concerns the application of vibro-impact absorbers on multi-modal structures, since many theoretical results of the literature are obtained for single degree-of-freedom systems. Accordingly, two structures are equipped with a single vibro-impact absorber and are tested experimentally. The first one is a cantilever beam submitted to base excitation, and the second one is a model plane, playing the role of a more realistic structure. For both of them, a vibro-impact absorber with tunable gap has been designed and manufactured. Harmonic and random excitations are considered. In the case of harmonic excitations, parametric studies on the gap confirm that, like for single degree-of-freedom systems, the optimal gap is at the limit between the regime with two impacts per period of the excitation and the Strongly Modulated Regime. An optimal gap can also be found for random excitations, even if the previous regimes do not exist anymore. Interestingly, we also have clearly demonstrated that a single vibro-impact absorber can tackle one mode at a time, but that multimodal attenuation cannot be achieved. The corresponding results can be found in both chapter 3 concerning the beam, and chapter 5 for the model plane. Moreover, the results obtained on the beam in chapter 3 are also published in *Mechanical Systems and Signal Processing, Volume 180*

entitled *Experimental investigations of a vibro-impact absorber attached to a continuous structure*.

Consequently, the third contribution is related to the design of multiple vibro-impact absorbers in order to improve the vibration mitigation performance, and more specifically to obtain a multimodal attenuation. Therefore, the influence of two parameters is investigated, namely the gap and the location of the vibro-impact absorbers. The results show that smaller gaps are more likely to tackle higher modes, whereas larger gaps are more suited for lower modes. Regarding the location of the absorbers, it should be chosen on the antinodes of the mode(s) that must be mitigated. Combining several gaps and locations of the absorbers, it is possible to achieve multimodal attenuation. Moreover, we verified that it was possible to reduce the vibration amplitude of the lower modes of vibration without deteriorating the static rigidity of the structure. The corresponding studies are described in chapter 5.

Finally, the last contribution concerns the evaluation of the modal energy transfers in a structure equipped with a vibro-impact absorber, and their role in the effectiveness of the absorber. For this purpose, a model of an Euler-Bernoulli beam with a VI absorber attached at its end is solved using a semi-analytical method, allowing to derive exact energy balances. Firstly, we observed that vibration reduction is performed in spite of the impacts are perfectly elastic and non-dissipative. Considering a harmonic excitation of the first mode of the beam, the results show that mechanical energy is transferred from the first excited mode to the higher modes that contribute to the energy dissipation in a more effective manner. Moreover, this energy transfer is greater when the gap is set at its optimal value, which corresponds the best vibration reduction. The same conclusions are drawn for an excitation in the vicinity of the second and the third mode of the beam. In addition, we observed that negligible energy transfers occur from the excited mode toward the lower modes. This is worthy to note, since such phenomenon would be detrimental to the performance of the absorber. This results corresponds to chapter 4. Besides, in chapter 5, the response of the plane out of the frequency band of excitation is analyzed, and leads to similar conclusions.

Of course, further work are envisioned in the perspective of the design of vibro-impact absorbers for real industrial applications. To start with, it is necessary to identify the conditions that enable the best performances of the vibro-impact absorber. If the influence of the gap is now well understood and affects directly the level of vibration reduction, the question of the robustness is not fully addressed yet. Preliminary numerical results are proposed at the end of chapter 4 and highlight the robustness of the vibro-impact absorber to eigenfrequencies variations. This result must be validated experimentally, and random excitations should be considered in addition to harmonic excitations. With the same objective, the robustness to variations of the excitation amplitude must be studied.

Still focusing on the development of industrial applications, it seems crucial to be able to build predictive models that make engineers able to design absorbers that meet the performances required, using fast and low-cost numerical approaches. For this purpose, model updating related to the vibro-impact process needs to be realized. Yet, almost no work dealing with this problematic is proposed. The full-field measurement method proposed in chapter 2 may be a starting point allowing to obtain reliable experimental data. Accordingly, even if no model updating process was realized during this work, all the necessary elements are available, namely the models and the experimental data.

Then, very recent studies have shown the existence of damage in the contact zones of the vibro-impact absorber, due to the repetitive impacts of the ball. Therefore, the contact properties are modified. Before going towards industrial applications, it is absolutely necessary to investigate the influence of the damaging of the contact zone on the behavior and performance of the absorber. Moreover, the evolution of these damages over time must be analyzed in order to understand their influence on the service life of a vibro-impact absorber. To do so, adopting an experimental approach is probably a relevant strategy.

Furthermore, the vibro-impact absorbers developed in the present work lead to important noise during the experiment. For the moment, this drawback is not considered as irrevocably detrimental. Indeed, the presence of noise is acceptable considering applications such as machining, or the takeoff and landing phase of a plane. Nevertheless, the development of more silent devices should be considered in the future, using smaller absorbers or based on the encapsulation of the device for instance.

At last, the mechanical design of vibro-impact absorbers must be improved. In particular, the design efforts that have been realized in this PhD thesis to design and manufacture modular devices have to be continued. It seems relevant to go towards the miniaturization of the vibro-impact absorbers in order to reduce their mass and size, and meet the industrial challenges that we are facing.

Bibliography

[1] A. Vallatta, F. Casolo, M. Caffi. On The Coefficient Of Restitution Of Tennis Rackets. In *ISBS - Conference Proceedings Archive*, 1993.

[2] V. Acary. Energy conservation and dissipation properties of time-integration methods for nonsmooth elastodynamics with contact: Energy conservation and dissipation properties for nonsmooth elastodynamics with contact. *ZAMM - Journal of Applied Mathematics and Mechanics / Zeitschrift für Angewandte Mathematik und Mechanik*, 96(5):585–603, May 2016.

[3] A. Afsharfard. Suppressing forced vibrations of structures using smart vibro-impact systems. *Nonlinear Dynamics*, 83(3):1643–1652, Feb. 2016.

[4] A. Afsharfard. Application of nonlinear magnetic vibro-impact vibration suppressor and energy harvester. *Mechanical Systems and Signal Processing*, 98:371–381, Jan. 2018.

[5] N. Ahmad, R. Ranganath, and A. Ghosal. Modeling and experimental study of a honeycomb beam filled with damping particles. *Journal of Sound and Vibration*, 391:20–34, Mar. 2017.

[6] M. A. AL-Shudeifat and A. S. Saeed. Comparison of a modified vibro-impact nonlinear energy sink with other kinds of NESs. *Meccanica*, 56(4):735–752, Apr. 2021.

[7] M. A. AL-Shudeifat, A. F. Vakakis, and L. A. Bergman. Shock Mitigation by Means of Low- to High-Frequency Nonlinear Targeted Energy Transfers in a Large-Scale Structure. *Journal of Computational and Nonlinear Dynamics*, 11(2):021006, Mar. 2016.

[8] M. A. AL-Shudeifat, N. Wierschem, D. D. Quinn, A. F. Vakakis, L. A. Bergman, and B. F. Spencer. Numerical and experimental investigation of a highly effective single-sided vibro-impact non-linear energy sink for shock mitigation. *International Journal of Non-Linear Mechanics*, 52:96–109, June 2013.

[9] T. Amado. *Modélisation d'un système dynamique à jeu du groupe moto-propulseur*. PhD thesis, Ecole centrale de Lyon, Ecully, Jan. 2006.

[10] M. M. Americano da Costa, D. A. Castello, C. Magluta, and N. Roitman. On the optimal design and robustness of spatially distributed tuned mass dampers. *Mechanical Systems and Signal Processing*, 150:107289, Mar. 2021.

[11] L. Y. L. Ang, Y. K. Koh, and H. P. Lee. Acoustic Metamaterials: A Potential for Cabin Noise Control in Automobiles and Armored Vehicles. *International Journal of Applied Mechanics*, 08(05):1650072, July 2016.

[12] V. Astashev and V. Krupenin. About some scientific principles of vibro-impact machine design. In *17th International Scientific Conference Engineering for Rural Development*, May 2018.

[13] E. Bachy, K. Jaboviste, E. Sadoulet-Reboul, N. Peyret, G. Chevallier, C. Arnould, and E. Collard. Investigations on the performance and the robustness of a metabsorber designed for structural vibration mitigation. *Mechanical Systems and Signal Processing*, 170:108830, May 2022.

[14] C. Bapat and S. Sankar. Single unit impact damper in free and forced vibration. *Journal of Sound and Vibration*, 99(1):85–94, Mar. 1985.

[15] M. Barthod, B. Hayne, J.-L. Tébec, and J.-C. Pin. Experimental study of gear rattle excited by a multi-harmonic excitation. *Applied Acoustics*, 68(9):1003–1025, Sept. 2007.

[16] G. Besnard. *Caractérisation et quantification de surfaces par stéréocorrélation pour des essais mécaniques du quasi statique à la dynamique ultra-rapide*. PhD thesis, Ecole Normale Supérieure de Cachan, Cachan, 2010.

[17] G. Besnard, F. Hild, J.-M. Lagrange, P. Martinuzzi, and S. Roux. Analysis of necking in high speed experiments by stereocorrelation. *International Journal of Impact Engineering*, 49:179–191, Nov. 2012.

[18] G. Besnard, H. Leclerc, F. Hild, S. Roux, and N. Swiergiel. Analysis of image series through global digital image correlation. *The Journal of Strain Analysis for Engineering Design*, 47(4):214–228, May 2012.

[19] A. Bhattacharjee and A. Chatterjee. Transverse impact of a Hertzian body with an infinitely long Euler-Bernoulli beam. *Journal of Sound and Vibration*, 429:147–161, Sept. 2018.

[20] R. Boettcher, S. Eichmann, and P. Mueller. Influence of viscous damping and elastic waves on energy dissipation during impacts. *Chemical Engineering Science*, 199:571–587, May 2019.

[21] J. Boisson, F. Louf, J. Ojeda, X. Mininger, and M. Gabsi. Magnetic forces and vibrational behavior analysis for flux switching permanent magnet machines. In *2012 XXth International Conference on Electrical Machines*, pages 2988–2993, Marseille, France, Sept. 2012. IEEE.

[22] E. Boroson, S. Missoum, P.-O. Mattei, and C. Vergez. Optimization under uncertainty of parallel nonlinear energy sinks. *Journal of Sound and Vibration*, 394:451–464, Apr. 2017.

[23] H. Bouaziz, N. Peyret, M. S. Abbes, G. Chevallier, and M. Haddar. Vibration Reduction of an Assembly by Control of the Tightening Load. *International Journal of Applied Mechanics*, 08(06):1650081, Sept. 2016.

[24] P. Butaud, D. Renault, B. Verdin, M. Ouisse, and G. Chevallier. In-core heat distribution control for adaptive damping and stiffness tuning of composite structures. *Smart Materials and Structures*, 29(6):065002, June 2020.

[25] R. Chabrier, J. Roberjot, E. Sadoulet-Reboul, G. Chevallier, and E. Foltete. Dimensionnement d'un vibro-impacteur pour le contrôle vibratoire d'une maquette d'avion et validation expérimentale. In *CSMA 2022*, page 6, Giens, 2022.

[26] R. Chabrier, E. Sadoulet, G. Chevallier, E. Foltête, and T. Jeannin. Field measurement to understand the physics of vibroimpact for damping application. In *Proceedings of ISMA2020*, Leuven, Sept. 2020.

[27] R. Chabrier, E. Sadoulet-Reboul, G. Chevallier, E. Foltête, and T. Jeannin. Full-field measurements with Digital Image Correlation for vibro-impact characterisation. *Mechanical Systems and Signal Processing*, 156:107658, July 2021.

[28] G. Chevallier, S. Ghorbel, and A. Benjeddou. Piezoceramic shunted damping concept: testing, modelling and correlation. *Mécanique & Industries*, 10(5):397–411, Sept. 2009.

[29] K. Dai, J. Wang, R. Mao, Z. Lu, and S.-E. Chen. Experimental investigation on dynamic characterization and seismic control performance of a TLPD system: Experimental investigation of a TLPD system. *The Structural Design of Tall and Special Buildings*, 26(7):e1350, May 2017.

[30] S. Daouk, F. Louf, C. Cluzel, O. Dorival, L. Champaney, and S. Audebert. Study of the dynamic behavior of a bolted joint under heavy loadings. *Journal of Sound and Vibration*, 392:307–324, Mar. 2017.

[31] E. Dehghan-Niri, S. M. Zahrai, and A. F. Rod. Numerical studies of the conventional impact damper with discrete frequency optimization and uncertainty considerations. *Scientia Iranica*, 19(2):166–178, Apr. 2012.

[32] J.-L. Dion, S. Le Moyne, G. Chevallier, and H. Sebbah. Gear impacts and idle gear noise: Experimental study and non-linear dynamic model. *Mechanical Systems and Signal Processing*, 23(8):2608–2628, Nov. 2009.

[33] H. Dong and M. Moys. Measurement of impact behaviour between balls and walls in grinding mills. *Minerals Engineering*, 16(6):543–550, June 2003.

[34] H. Dong and M. Moys. Experimental study of oblique impacts with initial spin. *Powder Technology*, 161(1):22–31, Jan. 2006.

[35] M. Duncan, C. Wassgren, and C. Krousgrill. The damping performance of a single particle impact damper. *Journal of Sound and Vibration*, 286(1-2):123–144, Aug. 2005.

[36] P. Fan, B. Luo, Z. Zhu, and H. Chen. Modeling and parametric study on DE-based vibro-impact energy harvesters for performance improvement. *Energy Conversion and Management*, 242:114321, Aug. 2021.

[37] B. Fang, T. Theurich, M. Krack, L. A. Bergman, and A. F. Vakakis. Vibration suppression and modal energy transfers in a linear beam with attached vibro-impact nonlinear energy sinks. *Communications in Nonlinear Science and Numerical Simulation*, 91:105415, Dec. 2020.

[38] M. Feldman. Hilbert transform in vibration analysis. *Mechanical Systems and Signal Processing*, 25(3):735–802, Apr. 2011.

[39] L. Gagnon, M. Morandini, and G. L. Ghiringhelli. A review of particle damping modeling and testing. *Journal of Sound and Vibration*, 459:114865, Oct. 2019.

[40] F. Gehr, T. Theurich, C. Monjaraz-Tec, J. Gross, S. Schwarz, A. Hartung, and M. Krack. Computational and experimental analysis of the impact of a sphere on a beam and the resulting modal energy distribution. *Mechanical Systems and Signal Processing*, 180:109407, Nov. 2022.

[41] O. V. Gendelman and Y. Starosvetsky. Quasi-Periodic Response Regimes of Linear Oscillator Coupled to Nonlinear Energy Sink Under Periodic Forcing. *Journal of Applied Mechanics*, 74(2):325–331, Mar. 2007.

[42] X. Geng, H. Ding, K. Wei, and L. Chen. Suppression of multiple modal resonances of a cantilever beam by an impact damper. *Applied Mathematics and Mechanics*, 41(3):383–400, Mar. 2020.

[43] E. Gourc. *Etude du contrôle passif par pompage énergétique sous sollicitation harmonique : Analyses théoriques et expérimentales*. PhD thesis, INSA Toulouse, Toulouse, Oct. 2013.

[44] E. Gourc, G. Michon, S. Seguy, and A. Berlioz. Targeted Energy Transfer Under Harmonic Forcing With a Vibro-Impact Nonlinear Energy Sink: Analytical and Experimental Developments. *Journal of Vibration and Acoustics*, 137(3):031008, June 2015.

[45] E. Gourc, S. Seguy, G. Michon, A. Berlioz, and B. Mann. Quenching chatter instability in turning process with a vibro-impact nonlinear energy sink. *Journal of Sound and Vibration*, 355:392–406, Oct. 2015.

[46] E. Gourdon, N. Alexander, C. Taylor, C. Lamarque, and S. Pernot. Nonlinear energy pumping under transient forcing with strongly nonlinear coupling: Theoretical and experimental results. *Journal of Sound and Vibration*, 300(3-5):522–551, Mar. 2007.

[47] B. Guo, E. Ley, J. Tian, J. Zhang, Y. Liu, and S. Prasad. Experimental and numerical studies of intestinal frictions for propulsive force optimisation of a vibro-impact capsule system. *Nonlinear Dynamics*, 101(1):65–83, July 2020.

[48] M. Gzal, B. Fang, A. F. Vakakis, L. A. Bergman, and O. V. Gendelman. Rapid nonresonant intermodal targeted energy transfer (IMTET) caused by vibro-impact nonlinearity. *Nonlinear Dynamics*, 101(4):2087–2106, Sept. 2020.

[49] M. Gzal, A. F. Vakakis, L. A. Bergman, and O. V. Gendelman. Extreme intermodal energy transfers through vibro-impacts for highly effective and rapid blast mitigation.

Communications in Nonlinear Science and Numerical Simulation, 103:106012, Dec. 2021.

[50] A. Hartung, U. Retze, and H.-P. Hackenberg. Impulse Mistuning of Blades and Vanes. In *ASME Turbo Expo 2016*, page 10, Seoul, 2016.

[51] D. Hastie. Experimental measurement of the coefficient of restitution of irregular shaped particles impacting on horizontal surfaces. *Chemical Engineering Science*, 101:828–836, Sept. 2013.

[52] J. E. Higham, P. Shepley, and M. Shahnam. Measuring the coefficient of restitution for all six degrees of freedom. *Granular Matter*, 21(2):15, May 2019.

[53] F. Hild, A. Bouterf, and S. Roux. Measurement of kinematic fields via DIC for impact engineering applications. *International Journal of Impact Engineering*, 130:163–171, Aug. 2019.

[54] J. Horabik, M. Beczek, R. Mazur, P. Parafiniuk, M. Ryżak, and M. Molenda. Determination of the restitution coefficient of seeds and coefficients of visco-elastic Hertz contact models for DEM simulations. *Biosystems Engineering*, 161:106–119, Sept. 2017.

[55] K. Jaboviste. *Caractérisation expérimentale et modélisation de solutions amortissantes pour la réduction des transferts vibratoires et la stabilisation de systèmes embarqués*. PhD thesis, Université de Bourgogne Franche-Comté, Besançon, Dec. 2018.

[56] K. Jaboviste, E. Sadoulet-Reboul, N. Peyret, C. Arnould, E. Collard, and G. Chevallier. On the compromise between performance and robustness for viscoelastic damped structures. *Mechanical Systems and Signal Processing*, 119:65–80, Mar. 2019.

[57] Y. Kadmiri, E. Rigaud, J. Perret-Liaudet, and L. Vary. Experimental and numerical analysis of automotive gearbox rattle noise. *Journal of Sound and Vibration*, 331(13):3144–3157, June 2012.

[58] R. V. Kappagantu. Vibro-Impact Rotor Dampers For Brake Squeal Attenuation - Towards An Insulator Free Design To Quell Squeal. *SAE International Journal of Passenger Cars - Mechanical Systems*, 1(1):1188–1193, Oct. 2008.

[59] Y. Kawazoe and Y. Kanda. Analysis of Impact Phenomena in a Tennis Ball-Racket System : Effects of Frame Vibrations and Optimum Rocket Design. *JSME international journal. Ser. C, Dynamics, control, robotics, design and manufacturing*, 40(1):9–16, 1997.

[60] M. Kisa and J. Brandon. The effects of closure of cracks on the dynamics of a cracked cantilever beam. *Journal of Sound and Vibration*, 238(1):1–18, Nov. 2000.

[61] B. Koohbor, A. Kidane, M. A. Sutton, X. Zhao, and S. Mallon. Analysis of dynamic bending test using ultra high speed DIC and the virtual fields method. *International Journal of Impact Engineering*, 110:299–310, Dec. 2017.

[62] S. Krenk. Frequency Analysis of the Tuned Mass Damper. *Journal of Applied Mechanics*, 72(6):936–942, Nov. 2005.

[63] Y. S. Lee, F. Nucera, A. F. Vakakis, D. M. McFarland, and L. A. Bergman. Periodic orbits, damped transitions and targeted energy transfers in oscillators with vibro-impact attachments. *Physica D: Nonlinear Phenomena*, 238(18):1868–1896, Sept. 2009.

[64] Y. S. Lee, A. F. Vakakis, L. A. Bergman, D. M. McFarland, G. Kerschen, F. Nucera, S. Tsakirtzis, and P. N. Panagopoulos. Passive non-linear targeted energy transfer and its applications to vibration absorption: A review. *Proceedings of the Institution of Mechanical Engineers, Part K: Journal of Multi-body Dynamics*, 222(2):77–134, June 2008.

[65] H. Li. Potential of a vibro-impact nonlinear energy sink for energy harvesting. *Mechanical Systems and Signal Processing*, 159:107827, 2021.

[66] H. Li, M. Sécail-Géraud, A. Pelat, F. Gautier, and C. Touzé. Experimental evidence of energy transfer and vibration mitigation in a vibro-impact acoustic black hole. *Applied Acoustics*, 182:108168, Nov. 2021.

[67] H. Li, C. Touzé, A. Pelat, and F. Gautier. Combining nonlinear vibration absorbers and the Acoustic Black Hole for passive broadband flexural vibration mitigation. *International Journal of Non-Linear Mechanics*, 129:103558, Mar. 2021.

[68] H. Li, C. Touzé, A. Pelat, F. Gautier, and X. Kong. A vibro-impact acoustic black hole for passive damping of flexural beam vibrations. *Journal of Sound and Vibration*, 450:28–46, June 2019.

[69] H. Li, D. Wang, H. Zhang, X. Wang, Z. Qin, and Z. Guan. Optimal design of vibro-impact resistant fiber reinforced composite plates with polyurea coating. *Composite Structures*, 292:115680, July 2022.

[70] L. Li, L. Tan, L. Kong, D. Wang, and H. Yang. The influence of flywheel micro vibration on space camera and vibration suppression. *Mechanical Systems and Signal Processing*, 100:360–370, Feb. 2018.

[71] L. Li, S. H. Yang, C.-S. Hwang, and Y. S. Kim. Effects of string tension and impact location on tennis playing. *Journal of Mechanical Science and Technology*, 23(11):2990–2997, Nov. 2009.

[72] T. Li, S. Seguy, and A. Berlioz. Dynamics of Cubic and Vibro-Impact Nonlinear Energy Sink: Analytical, Numerical, and Experimental Analysis. *Journal of Vibration and Acoustics*, 138(3):031010, June 2016.

[73] T. Li, S. Seguy, and A. Berlioz. On the dynamics around targeted energy transfer for vibro-impact nonlinear energy sink. *Nonlinear Dynamics*, 87(3):1453–1466, Feb. 2017.

[74] T. Li, S. Seguy, and A. Berlioz. Optimization mechanism of targeted energy transfer with vibro-impact energy sink under periodic and transient excitation. *Nonlinear Dynamics*, 87(4):2415–2433, Mar. 2017.

[75] T. Li, S. Seguy, C. Lamarque, and A. Berlioz. Experiment-Based Motion Reconstruction and Restitution Coefficient Estimation of a Vibro-Impact System. *Journal of Vibration and Acoustics*, 141(2):021003, Apr. 2019.

[76] W. Li, N. E. Wierschem, X. Li, and T. Yang. On the energy transfer mechanism of the single-sided vibro-impact nonlinear energy sink. *Journal of Sound and Vibration*, 437:166–179, Dec. 2018.

[77] W. Li, N. E. Wierschem, X. Li, T. Yang, and M. J. Brennan. Numerical study of a symmetric single-sided vibro-impact nonlinear energy sink for rapid response reduction of a cantilever beam. *Nonlinear Dynamics*, 100(2):951–971, Apr. 2020.

[78] Y. Liu, E. Pavlovskaia, and M. Wiercigroch. Experimental verification of the vibro-impact capsule model. *Nonlinear Dynamics*, 83(1-2):1029–1041, Jan. 2016.

[79] S. Lo Feudo, S. Job, M. Cavallo, A. Fraddosio, M. Piccioni, and A. Tafuni. Finite contact duration modeling of a Vibro-Impact Nonlinear Energy Sink to protect a civil engineering frame structure against seismic events. *Engineering Structures*, 259:114137, May 2022.

[80] Z. Lu, X. Chen, and Y. Zhou. An equivalent method for optimization of particle tuned mass damper based on experimental parametric study. *Journal of Sound and Vibration*, 419:571–584, Apr. 2018.

[81] Z. Lu, X. Lu, H. Jiang, and S. F. Masri. Discrete element method simulation and experimental validation of particle damper system. *Engineering Computations*, 31(4):810–823, May 2014.

[82] Z. Lu, Z. Wang, S. F. Masri, and X. Lu. Particle impact dampers: Past, present, and future. *Structural Control and Health Monitoring*, 25(1):e2058, Jan. 2018.

[83] J. Luo, N. E. Wierschem, S. A. Hubbard, L. A. Fahnestock, D. Dane Quinn, D. Michael McFarland, B. F. Spencer, A. F. Vakakis, and L. A. Bergman. Large-scale experimental evaluation and numerical simulation of a system of nonlinear energy sinks for seismic mitigation. *Engineering Structures*, 77:34–48, Oct. 2014.

[84] V. Mahe, A. Renault, A. Grolet, O. Thomas, and H. Mahe. Dynamic stability of centrifugal pendulum vibration absorbers allowing a rotational mobility. *Journal of Sound and Vibration*, 517:116525, Jan. 2022.

[85] S. F. Masri. Analytical and Experimental Studies of Multiple-Unit Impact Dampers. *The Journal of the Acoustical Society of America*, 45(5):1111–1117, May 1969.

[86] S. F. Masri and J. P. Caffrey. Response of a multi-degree-of-freedom system with a pounding vibration neutralizer to harmonic and random excitation. *Journal of Sound and Vibration*, 481:115427, Sept. 2020.

[87] C. Monjaraz Tec, J. Gross, and M. Krack. A massless boundary component mode synthesis method for elastodynamic contact problems. *Computers & Structures*, 260:106698, Feb. 2022.

[88] C. Monjaraz-Tec, L. Kohlmann, S. Schwarz, A. Hartung, J. Gross, and M. Krack. Prediction and validation of the strongly modulated forced response of two beams undergoing frictional impacts. *Mechanical Systems and Signal Processing*, 180:109410, Nov. 2022.

[89] E. H. Moussi, S. Bellizzi, B. Cochelin, and I. Nistor. Nonlinear normal modes of a two degree of freedom oscillator with a bilateral elastic stop. In *VISHNO*, Clamart, 2012.

[90] S. Muthukumar and R. DesRoches. A Hertz contact model with non-linear damping for pounding simulation. *Earthquake Engineering & Structural Dynamics*, 35(7):811–828, June 2006.

[91] M. Nagurka and S. Huang. A mass-spring-damper model of a bouncing ball. In *Proceedings of the 2004 American Control Conference*, pages 499–504 vol.1, Boston, MA, USA, 2004. IEEE.

[92] Y. Nakamura and K. Watanabe. Effects of balanced impact damper in structures subjected to walking and vertical seismic excitations: Effects of Balanced Impact Damper in Structures. *Earthquake Engineering & Structural Dynamics*, 45(1):113–128, Jan. 2016.

[93] K.-T. Nguyen, N.-T. La, K.-T. Ho, Q.-H. Ngo, N.-H. Chu, and V.-D. Nguyen. The effect of friction on the vibro-impact locomotion system: modeling and dynamic response. *Meccanica*, 56(8):2121–2137, Aug. 2021.

[94] M. Nordin and P.-O. Gutman. Controlling mechanical systems with backlash—a survey. *Automatica*, 38(10):1633–1649, Oct. 2002.

[95] F. Nucera, F. Lo Iacono, D. McFarland, L. Bergman, and A. Vakakis. Application of broadband nonlinear targeted energy transfers for seismic mitigation of a shear frame: Experimental results. *Journal of Sound and Vibration*, 313(1-2):57–76, June 2008.

[96] F. Nucera, A. F. Vakakis, D. M. McFarland, L. A. Bergman, and G. Kerschen. Targeted energy transfers in vibro-impact oscillators for seismic mitigation. *Nonlinear Dynamics*, 50(3):651–677, Oct. 2007.

[97] P. Ray, G. Chahine, P. Smith, R. Kovacevic. Optimal Design of a Golf Club using Functionally Graded Porosity. In *International Solid Freeform Fabrication Symposium*, Austin, 2011.

[98] P. F. Pai, H. Peng, and S. Jiang. Acoustic metamaterial beams based on multifrequency vibration absorbers. *International Journal of Mechanical Sciences*, 79:195–205, Feb. 2014.

[99] M. Parseh, M. Dardel, and M. H. Ghasemi. Performance comparison of nonlinear energy sink and linear tuned mass damper in steady-state dynamics of a linear beam. *Nonlinear Dynamics*, 81(4):1981–2002, Sept. 2015.

[100] E. Pavlovskaia, D. C. Hendry, and M. Wiercigroch. Modelling of high frequency vibro-impact drilling. *International Journal of Mechanical Sciences*, 91:110–119, Feb. 2015.

[101] D. Pellecchia, S. Lo Feudo, N. Vaiana, J. Dion, and L. Rosati. A procedure to model and design elastomeric-based isolation systems for the seismic protection of rocking art objects. *Computer-Aided Civil and Infrastructure Engineering*, 37(10):1298–1315, Aug. 2022.

[102] C. Pozzolini, Y. Renard, and M. Salaun. Vibro-impact of a plate on rigid obstacles: existence theorem, convergence of a scheme and numerical simulations. *IMA Journal of Numerical Analysis*, 33(1):261–294, Jan. 2013.

[103] C. Pozzolini and M. Salaun. Some energy conservative schemes for vibro-impacts of a beam on rigid obstacles. *ESAIM: Mathematical Modelling and Numerical Analysis*, 45(6):1163–1192, 2011.

[104] A. Preumont, J.-P. Dufour, and C. Malekian. Active damping by a local force feedback with piezoelectric actuators. *Journal of Guidance, Control, and Dynamics*, 15(2):390–395, Mar. 1992.

[105] D. Qiu, S. Seguy, and M. Paredes. Design criteria for optimally tuned vibro-impact nonlinear energy sink. *Journal of Sound and Vibration*, 442:497–513, Mar. 2019.

[106] D. D. Quinn, S. Hubbard, N. Wierschem, M. A. Al-Shudeifat, R. J. Ott, J. Luo, B. F. Spencer, D. M. McFarland, A. F. Vakakis, and L. A. Bergman. Equivalent modal damping, stiffening and energy exchanges in multi-degree-of-freedom systems with strongly nonlinear attachments. *Proceedings of the Institution of Mechanical Engineers, Part K: Journal of Multi-body Dynamics*, 226(2):122–146, June 2012.

[107] P. L. Reu and T. J. Miller. The application of high-speed digital image correlation. *The Journal of Strain Analysis for Engineering Design*, 43(8):673–688, Aug. 2008.

[108] E. Rigaud and J. Perret-Liaudet. Investigation of gear rattle noise including visualization of vibro-impact regimes. *Journal of Sound and Vibration*, 467:115026, Feb. 2020.

[109] R. G. Rinaldi, L. Manin, C. Bonnard, A. Drillon, H. Lourenco, and N. Havard. Non Linearity of the Ball/Rubber Impact in Table Tennis: Experiments and Modeling. *Procedia Engineering*, 147:348–353, 2016.

[110] L. Rozas, R. L. Boroschek, A. Tamburrino, and M. Rojas. A bidirectional tuned liquid column damper for reducing the seismic response of buildings. *Structural Control and Health Monitoring*, 23(4):621–640, Apr. 2016.

[111] H. Ruan and T. Yu. The unexpectedly small coefficient of restitution of a two-degree-of-freedom mass-spring system and its implications. *International Journal of Impact Engineering*, 88:1–11, Feb. 2016.

[112] E. Sadoulet-Reboul, A. Le Bot, and J. Perret-Liaudet. A hybrid method for vibroacoustic coupling: Application to the noise radiated around an engine compartment. *European Journal of Computational Mechanics*, 17:689–699, June 2008.

[113] H. Safaeifar and A. Farshidianfar. Experimental and analytical investigation of impact dampers in free vibration reduction with coulomb friction. *Noise & Vibration Worldwide*, 53(3):91–103, Mar. 2022.

[114] D. Saletti, S. Pattofatto, and H. Zhao. Measurement of phase transformation properties under moderate impact tensile loading in a NiTi alloy. *Mechanics of Materials*, 65:1–11, Oct. 2013.

[115] R. Seifried, W. Schiehlen, and P. Eberhard. Numerical and experimental evaluation of the coefficient of restitution for repeated impacts. *International Journal of Impact Engineering*, 32(1-4):508–524, Dec. 2005.

[116] R. Seifried, W. Schiehlen, and P. Eberhard. The role of the coefficient of restitution on impact problems in multi-body dynamics. *Proceedings of the Institution of Mechanical Engineers, Part K: Journal of Multi-body Dynamics*, 224(3):279–306, Sept. 2010.

[117] L. Serdukova, R. Kuske, and D. Yurchenko. Stability and bifurcation analysis of the period-T motion of a vibroimpact energy harvester. *Nonlinear Dynamics*, 98(3):1807–1819, Nov. 2019.

[118] Z. A. Shami, C. Giraud-Audine, and O. Thomas. A nonlinear piezoelectric shunt absorber with 2:1 internal resonance: experimental proof of concept. *Smart Materials and Structures*, 31(3):035006, Mar. 2022.

[119] Y. Shul, S. Lim, S. Moon, and N.-C. Park. Localization of rattle noise sources in the vehicle underbody using acceleration signals. *Mechanical Systems and Signal Processing*, 166:108447, Mar. 2022.

[120] R. Singh, H. Xie, and R. Comparin. Analysis of automotive neutral grear rattle. *Journal of Sound and Vibration*, 131(2):177–196, June 1989.

[121] Y. Starosvetsky and O. Gendelman. Response regimes of linear oscillator coupled to nonlinear energy sink with harmonic forcing and frequency detuning. *Journal of Sound and Vibration*, 315(3):746–765, Aug. 2008.

[122] Y. Sun, J. Yuan, L. Pesaresi, E. Denimal, and L. Salles. Parametric Study and Uncertainty Quantification of the Nonlinear Modal Properties of Frictional Dampers. *Journal of Vibration and Acoustics*, 142(5):051102, Oct. 2020.

[123] G. Tao and P. V. Kokotovic. Adaptive control of systems with backlash. *Automatica*, 29(2):323–335, Mar. 1993.

[124] V. Tarigopula, O. Hopperstad, M. Langseth, A. Clausen, and F. Hild. A study of localisation in dual-phase high-strength steels under dynamic loading using digital image correlation and FE analysis. *International Journal of Solids and Structures*, 45(2):601–619, Jan. 2008.

[125] R. d. O. Teloli, P. Butaud, G. Chevallier, and S. da Silva. Good practices for designing and experimental testing of dynamically excited jointed structures: The Orion beam. *Mechanical Systems and Signal Processing*, 163:108172, Jan. 2022.

[126] T. Thenint, E. Balmès, and M. Corus. Stabilization effect of shock non-linearity on the dynamics of a steam generator tube. In *Proceedings of COMPDYN 2011*, page 15, France, 2011.

[127] T. Thenint, E. Balmès, and M. Corus. Definition of a linear equivalent model for a non-linear system with impacts. In *Proceedings of ISMA 2012*, page 15, Belgium, 2012.

[128] T. Theurich, J. Gross, and M. Krack. Effects of modal energy scattering and friction on the resonance mitigation with an impact absorber. *Journal of Sound and Vibration*, 442:71–89, Mar. 2019.

[129] T. Theurich, A. F. Vakakis, and M. Krack. Predictive design of impact absorbers for mitigating resonances of flexible structures using a semi-analytical approach. *Journal of Sound and Vibration*, 516:116527, Jan. 2022.

[130] V. Tiwari, M. A. Sutton, S. McNeill, S. Xu, X. Deng, W. L. Fourney, and D. Bretall. Application of 3D image correlation for full-field transient plate deformation measurements during blast loading. *International Journal of Impact Engineering*, 36(6):862–874, June 2009.

[131] M. Topenot, G. Chevallier, M. Ouisse, and D. Vaillant. Model Reduction of Electric Rotors Subjected to PWM Excitation for Structural Dynamics Design. In D. Di Maio and J. Baqersad, editors, *Proceedings of IMAC 2020*, pages 73–78, Houston, 2020.

[132] M. Trigui, E. Foltete, M. S. Abbes, T. Fakhfakh, N. Bouhaddi, and M. Haddar. An experimental study of a multi-particle impact damper. *Proceedings of the Institution of Mechanical Engineers, Part C: Journal of Mechanical Engineering Science*, 223(9):2029–2038, Sept. 2009.

[133] T. Vadcard, A. Batailly, and F. Thouverez. On Harmonic Balance Method-based Lagrangian contact formulations for vibro-impact problems. *Journal of Sound and Vibration*, 531:116950, Aug. 2022.

[134] B. Vaurigaud, A. Ture Savadkoohi, and C.-H. Lamarque. Targeted energy transfer with parallel nonlinear energy sinks. Part I: Design theory and numerical results. *Nonlinear Dynamics*, 66(4):763–780, Dec. 2011.

[135] R. Vinayaravi, D. Kumaresan, K. Jayaraj, A. Asraff, and R. Muthukumar. Experimental investigation and theoretical modelling of an impact damper. *Journal of Sound and Vibration*, 332(5):1324–1334, Mar. 2013.

[136] J. Wang, N. Wierschem, B. F. Spencer Jr., and X. Lu. Numerical and experimental study of the performance of a single-sided vibro-impact track nonlinear energy sink. *Earthquake Engineering & Structural Dynamics*, 45(4):635–652, 2016.

[137] L. Wang, B. Wu, Z. Wu, R. Li, and X. Feng. Experimental determination of the coefficient of restitution of particle-particle collision for frozen maize grains. *Powder Technology*, 338:263–273, Oct. 2018.

[138] W. Wang, X. Hua, X. Wang, Z. Chen, and G. Song. Optimum design of a novel pounding tuned mass damper under harmonic excitation. *Smart Materials and Structures*, 26(5):055024, May 2017.

[139] Y. Wang, B. Liu, A. Tian, D. Wei, and X. Jiang. Prediction methods for the damping effect of multi-unit particle dampers based on the cyclic iterations of a single-unit particle damper. *Journal of Sound and Vibration*, 443:341–361, Mar. 2019.

[140] L. Woiwode, F. Müller, J. Groß, M. Scheel, and M. Krack. How Intrusive Are Accelerometers for Measuring Nonlinear Vibrations? A Case Study on a Compressor Blade Subjected to Vibro-Impact Dynamics. *Journal of Vibration and Acoustics*, 144(4):041002, Aug. 2022.

[141] C. Wong, M. Daniel, and J. Rongong. Energy dissipation prediction of particle dampers. *Journal of Sound and Vibration*, 319(1-2):91–118, Jan. 2009.

[142] Z. Wu, Y. Sogabe, Y. Arimitsu, and T. Tamaogi. Numerical Examinations of Relation between Restitution Characteristic and Eigen Frequencies. *Procedia Engineering*, 10:3291–3296, 2011.

[143] W. Xiao, Y. Huang, H. Jiang, H. Lin, and J. Li. Energy dissipation mechanism and experiment of particle dampers for gear transmission under centrifugal loads. *Particuology*, 27:40–50, Aug. 2016.

[144] Y. Yan, B. Zhang, Y. Liu, and S. Prasad. Dynamics of a vibro-impact self-propelled capsule encountering a circular fold in the small intestine. *Meccanica*, May 2022.

[145] B. Youssef and R. I. Leine. A complete set of design rules for a vibro-impact NES based on a multiple scales approximation of a nonlinear mode. *Journal of Sound and Vibration*, 501:116043, June 2021.

[146] T. Yüzbasioglu, J. Aramendiz, and A. Fidlin. On the numerical simulations of amplitude-adaptive impact dampers. *Journal of Sound and Vibration*, 468:115023, Mar. 2020.

[147] C. L. Zhang, Z. H. Lai, G. Q. Zhang, and D. Yurchenko. Energy harvesting from a dynamic vibro-impact dielectric elastomer generator subjected to rotational excitations. *Nonlinear Dynamics*, 102(3):1271–1284, Nov. 2020.

[148] D. Zhao and Y. Liu. Improved Damping Constant of Hertz-Damp Model for Pounding between Structures. *Mathematical Problems in Engineering*, 2016:1–7, 2016.

Appendix A

Appendix chapter 2

A.1 Features of the experimental set-up

The diameter of the ball is 4,8 mm, its mass is $1,82.10^{-4}$ kg, and the mass of the entire structure of the VI absorber is $6,63.10^{-1}$ kg. The materials used for each part are summarized in Table A.1. The main dimensions are given in Fig. A.1. During all the tests presented in this paper, the distance between the upper disk and the lower disk was 16,6 mm.

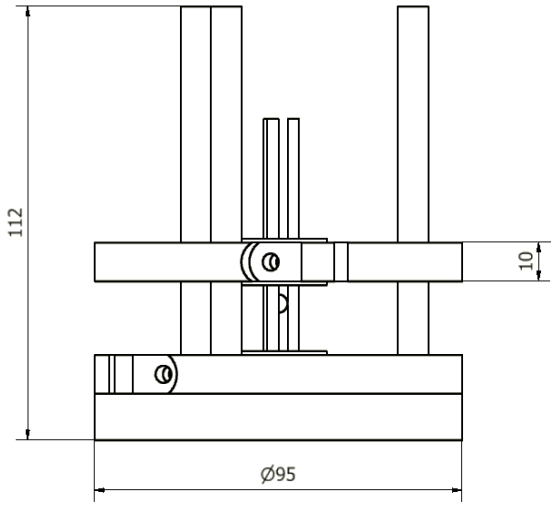

Figure A.1: Main dimensions (in mm) of the experimental set-up.

	material
ball	ceramic
plates	aluminium
guiding and holding rods	steel
disks	aluminium

Table A.1: Materials of the experimental set-up of the VI damper.

Appendix B

Appendix chapter 3

B.1 Analysis of the temporal response for the first mode

This appendix presents the temporal responses of both the ball and the beam for the different points from A to O of the FRFs of Fig. 3.6a

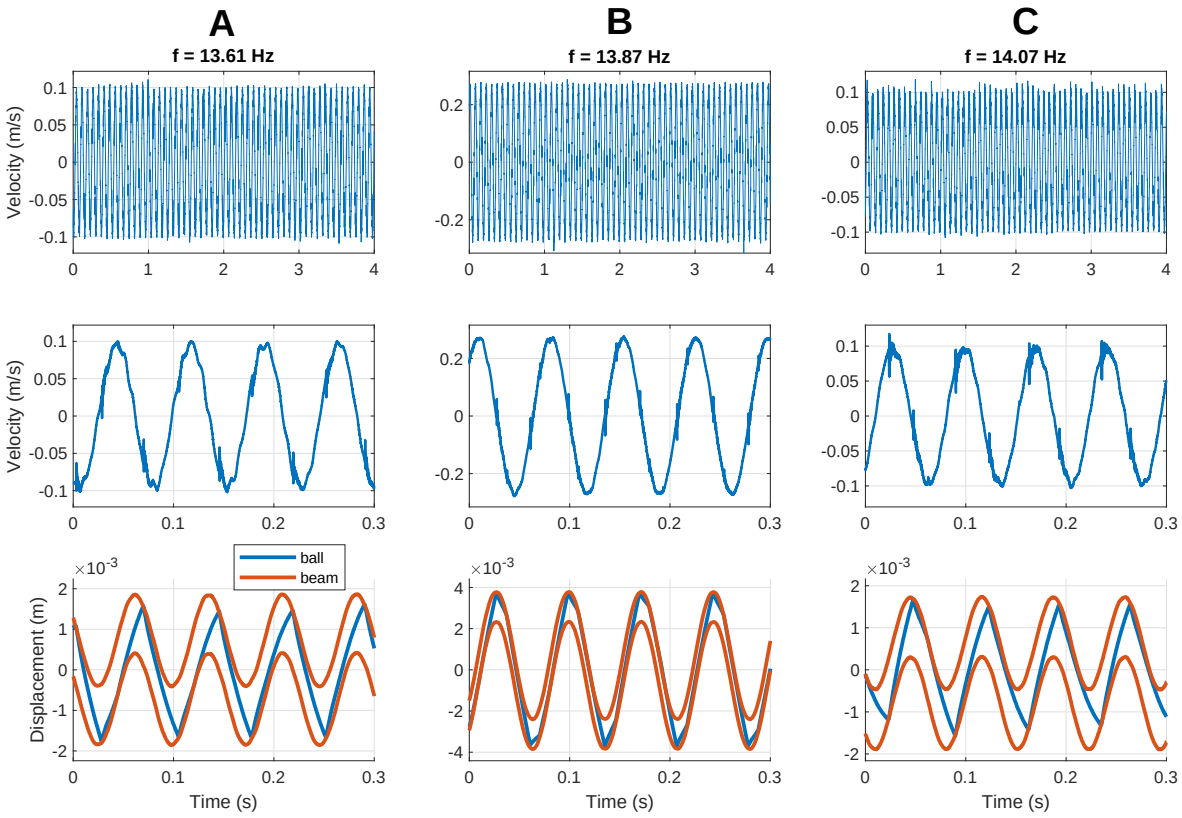

Figure B.1: Temporal responses for the gap = 1,53 mm. First line: Time velocity at the beam end on a 4 s duration. Second line: Zoom on the first line plot on a 0,3 s duration. Third line: Estimated displacement at the beam end (orange) and for the ball (blue).

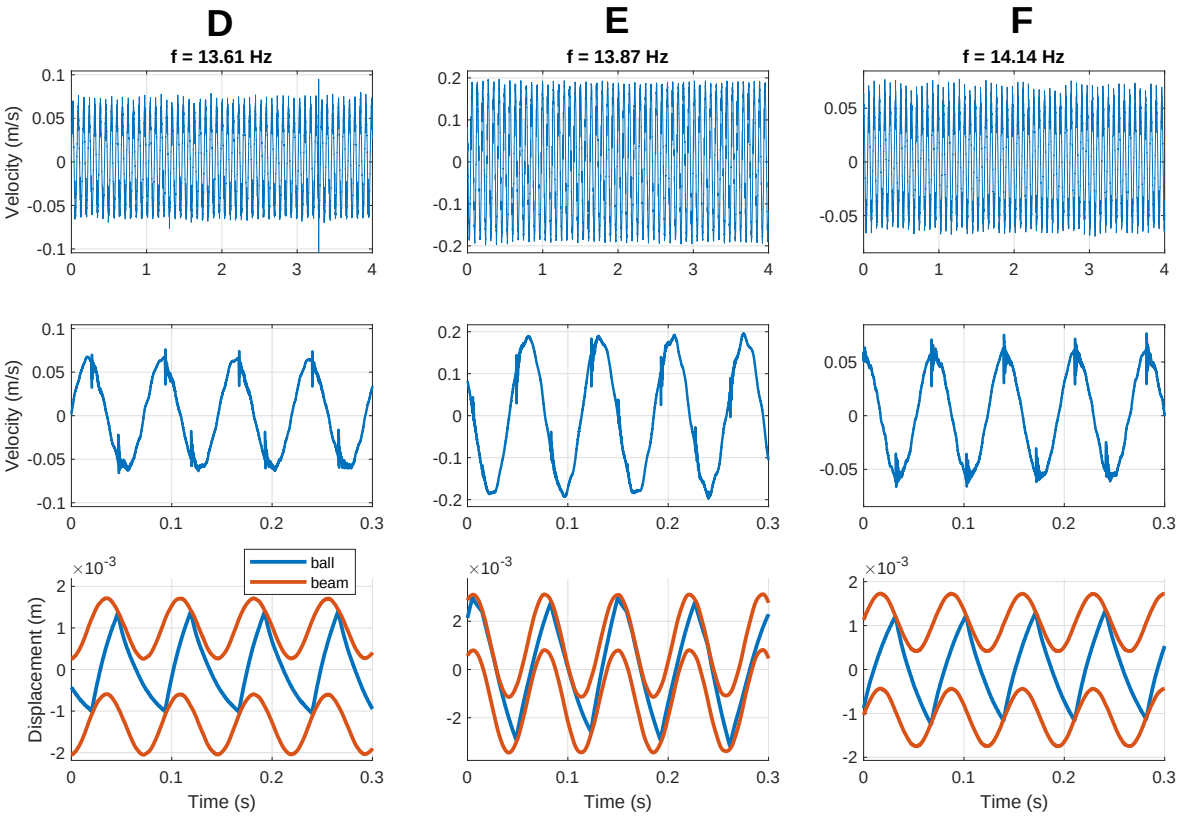

Figure B.2: Temporal responses for the gap = 2,29 mm.

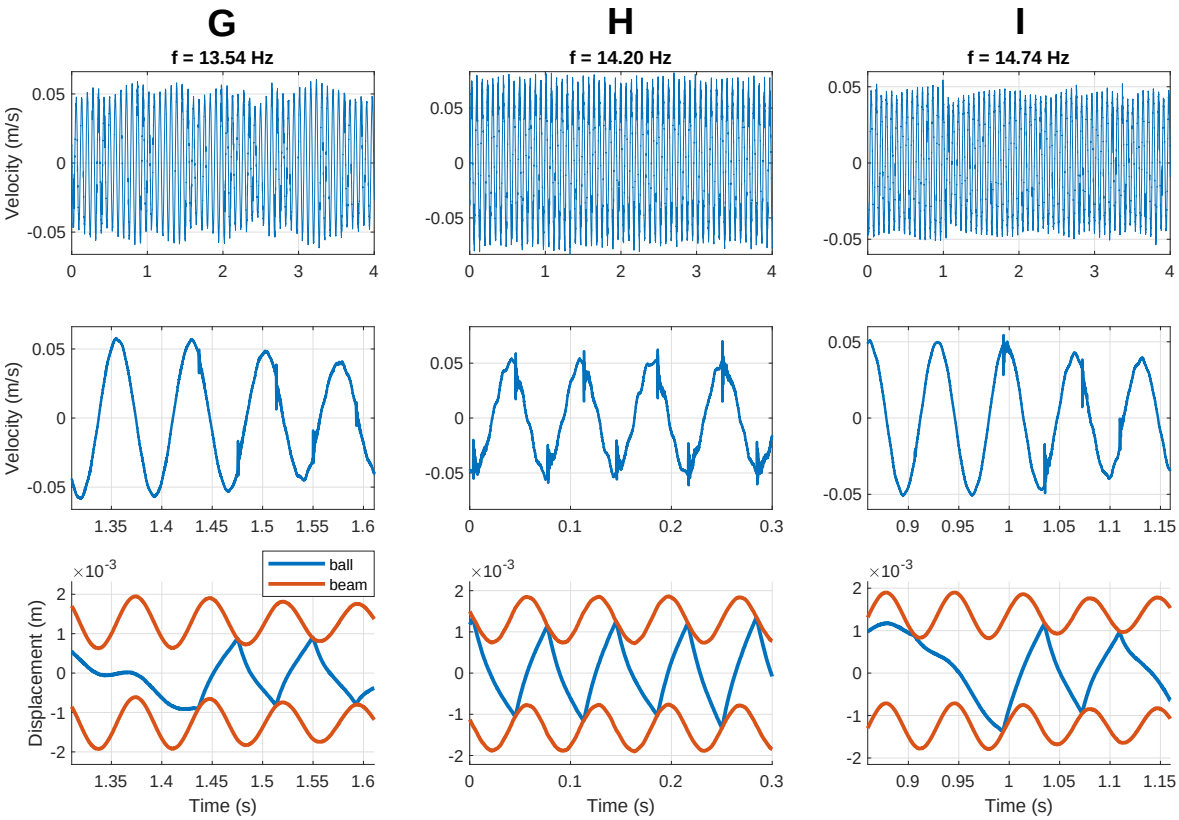

Figure B.3: Temporal responses for the gap = 2,67 mm.

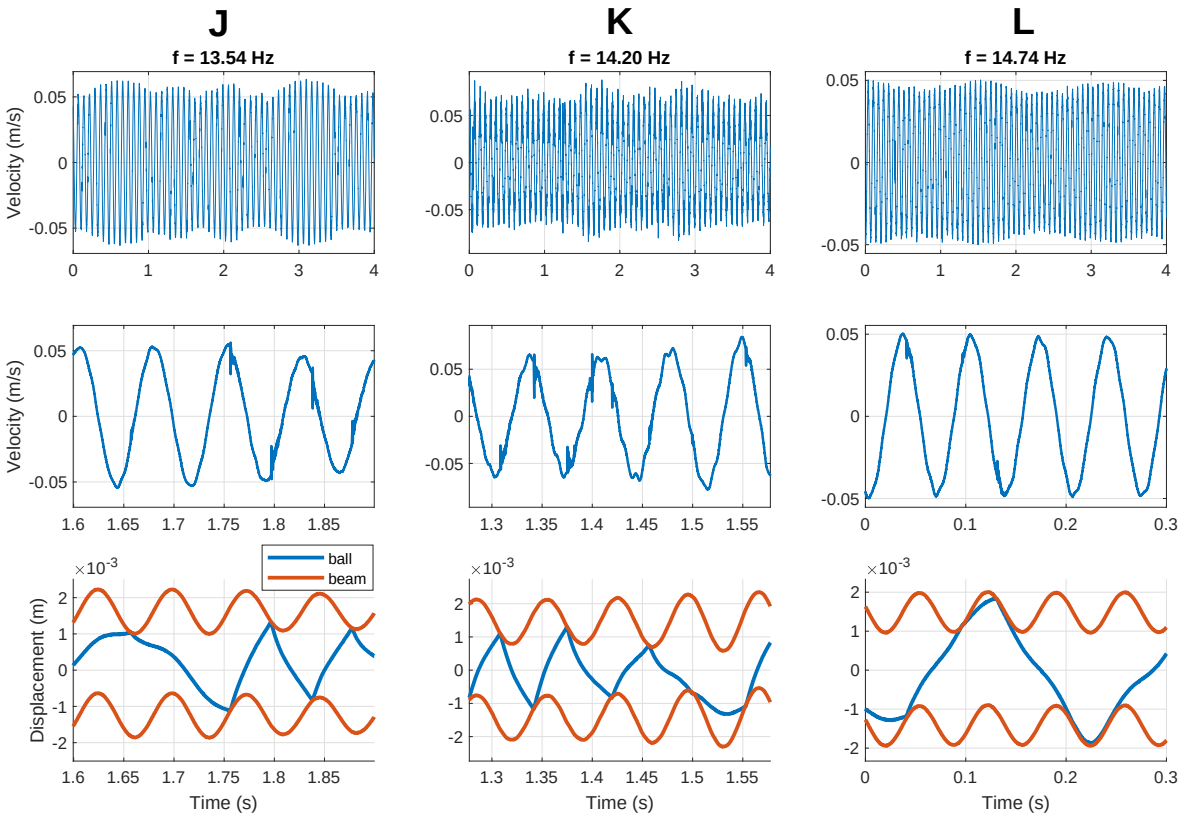

Figure B.4: Temporal responses for the gap = 2,99 mm.

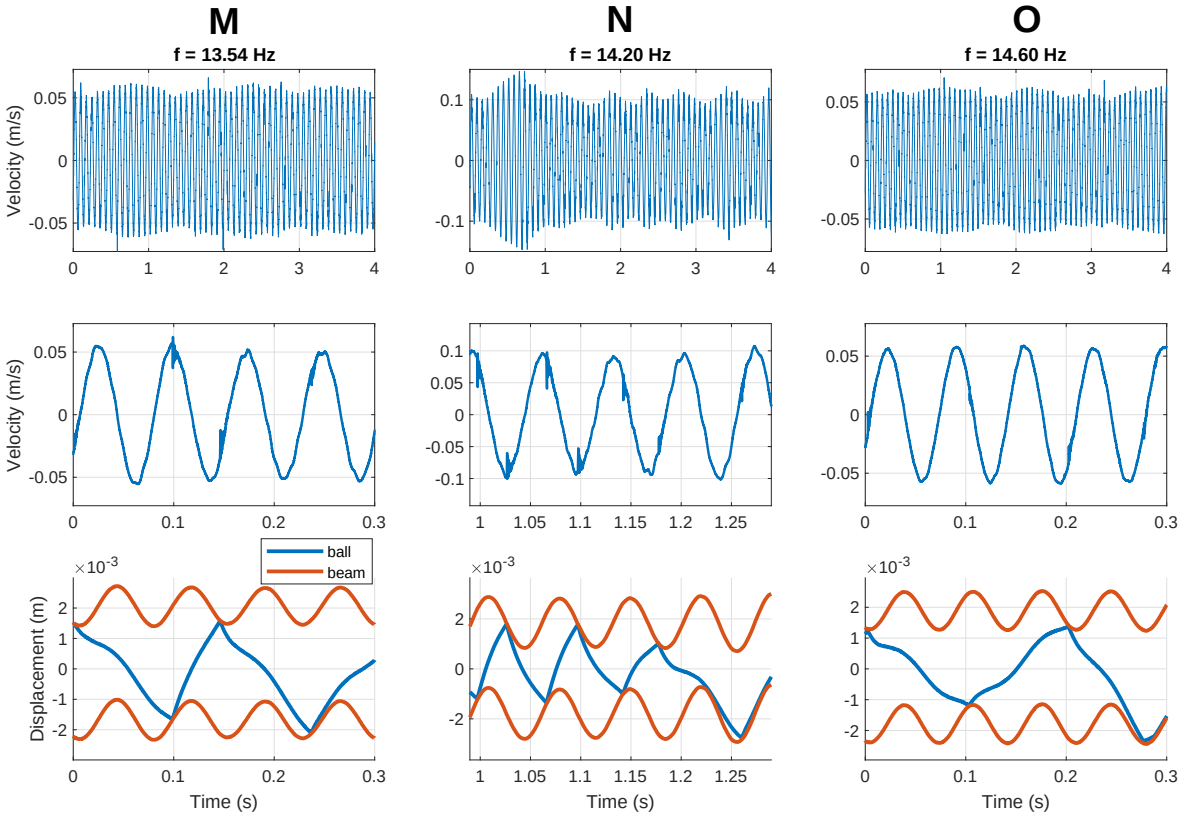

Figure B.5: Temporal responses for the gap = 3,77 mm.

B.2 Analysis of the temporal response for the second mode

This appendix presents the temporal responses of both the ball and the beam for the different points from A to O of the FRFs of Fig. B.6

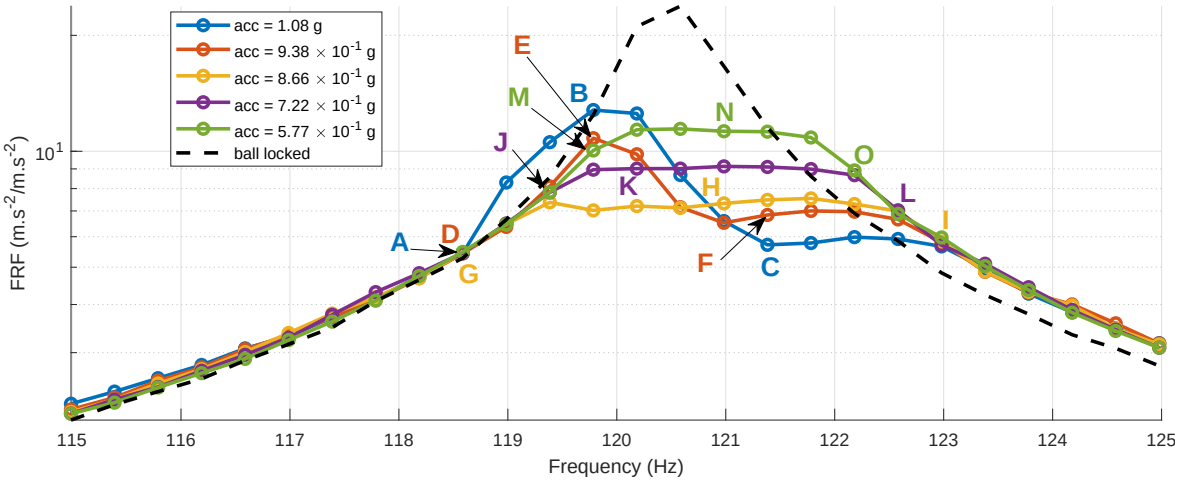

Figure B.6: FRF with the points for which the temporal response is analysed.

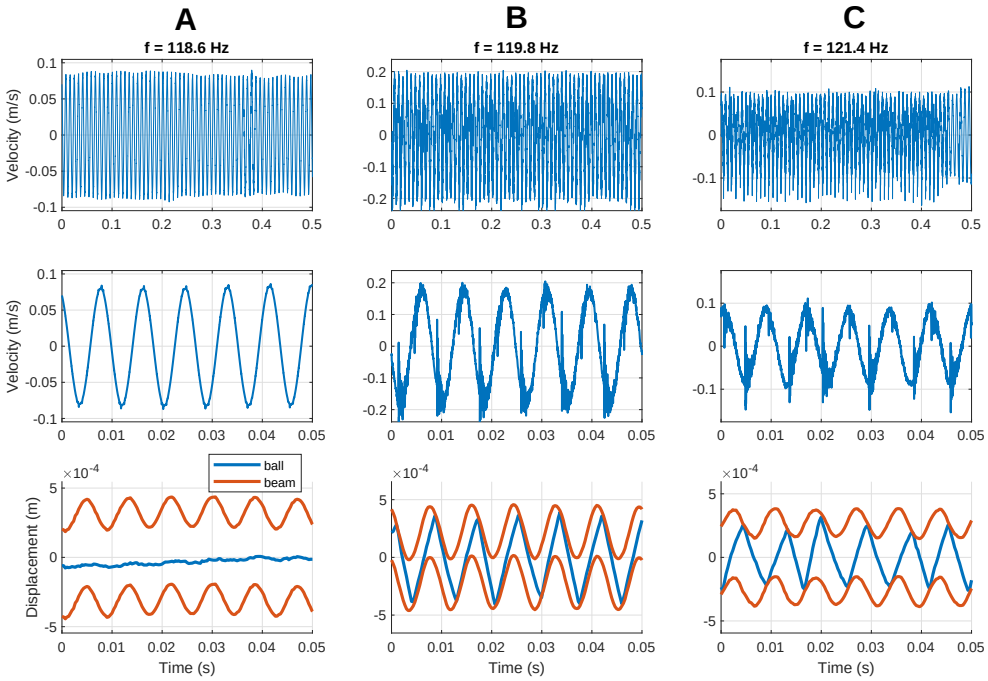

Figure B.7: Temporal responses for the acceleration = 1,08 g. First line: Time velocity at the beam end on a 4 s duration. Second line: Zoom on the first line plot on a 0,3 s duration. Third line: Estimated displacement at the beam end (orange) and for the ball (blue).

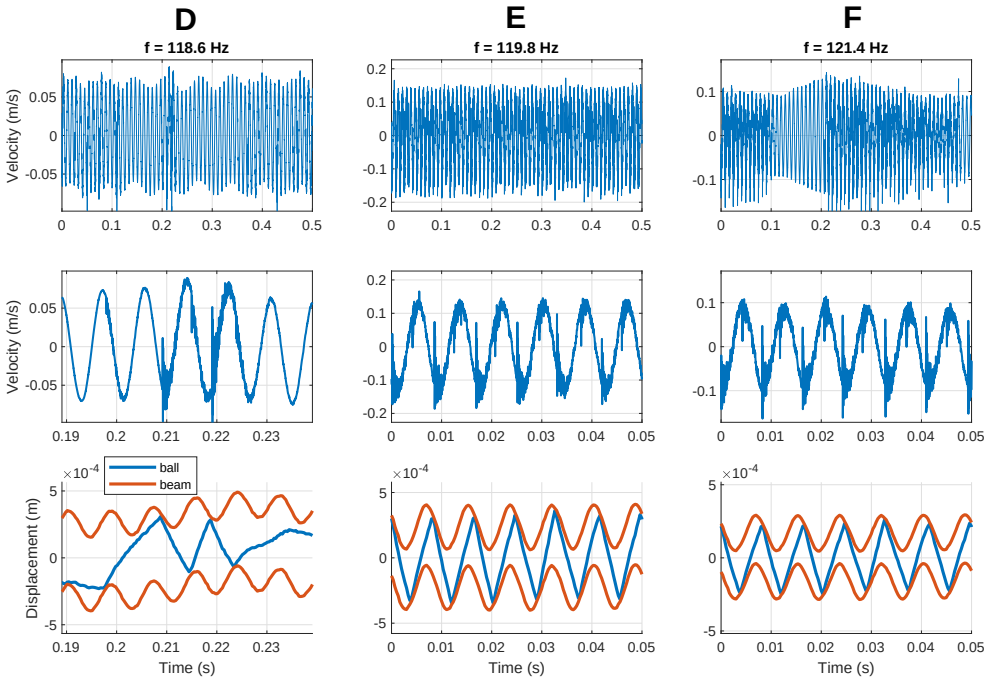

Figure B.8: Temporal responses for the acceleration = 0,938 g.

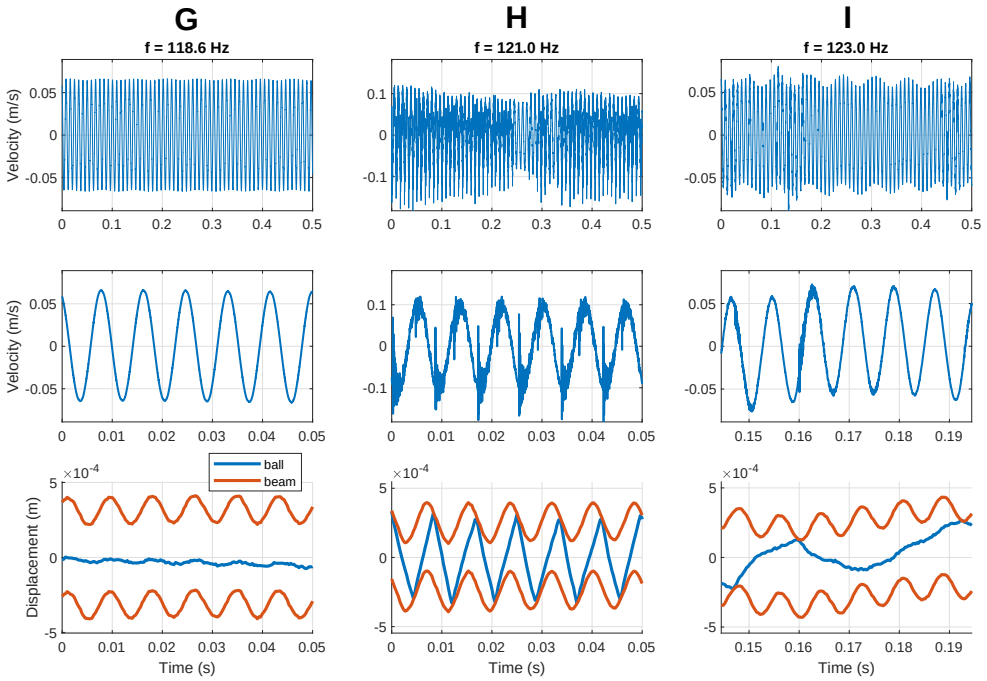

Figure B.9: Temporal responses for the acceleration = 0,866 g.

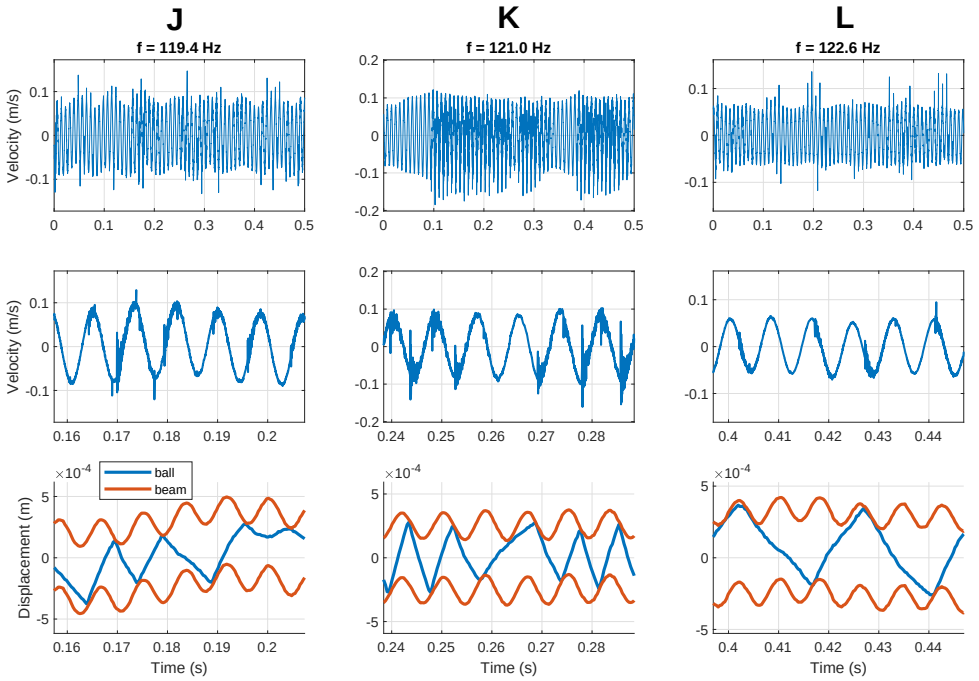

Figure B.10: Temporal responses for the acceleration = 0,722 g.

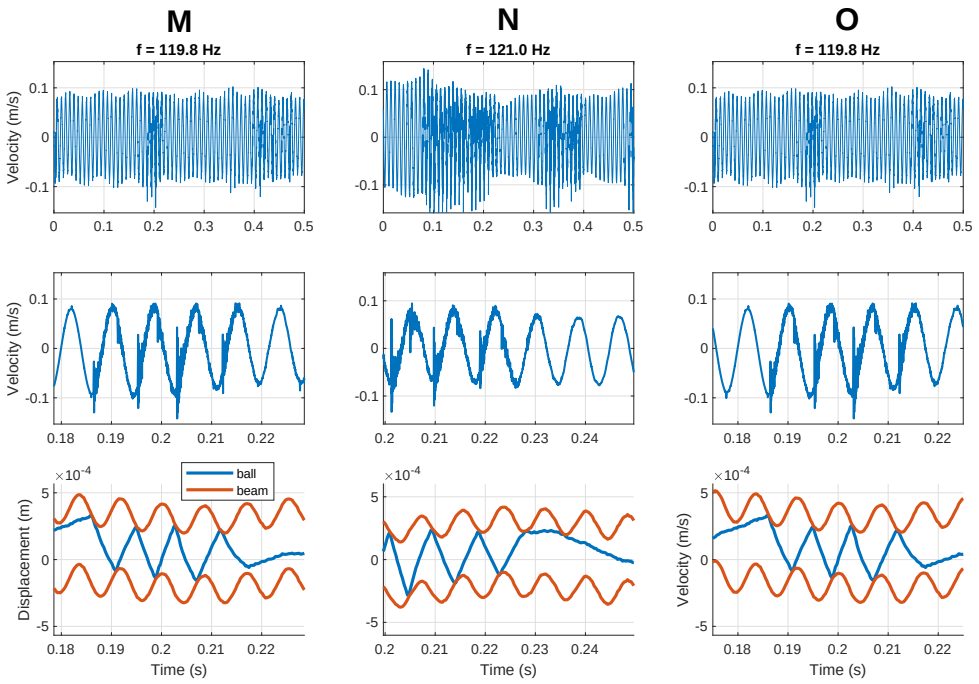

Figure B.11: Temporal responses for the acceleration = 0,577 g.

B.3 Masses, materials and drawings of the parts of the VI absorber

Part	Mass (g)	Material
Cavity	6,41	aluminium
Adjusting screw	7,54	steel
Counter nut	0,117	brass
Ball	2,71	steel
Beam	189,02	aluminium

Table B.1: Masses and materials of the components of the VI absorber.

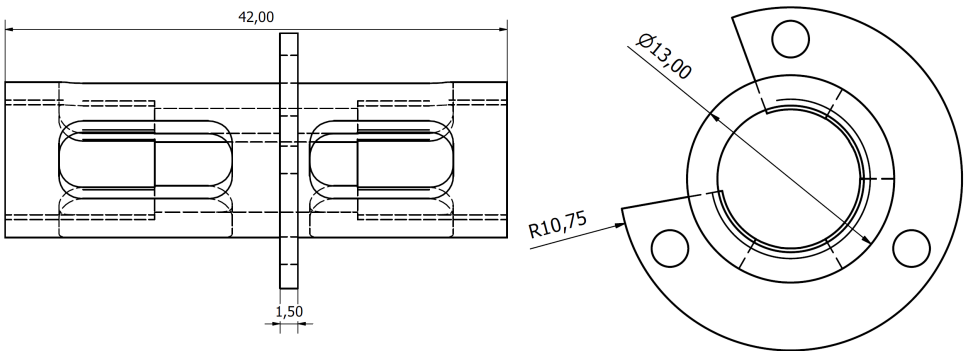

Figure B.12: Drawing and main dimensions of the cavity.

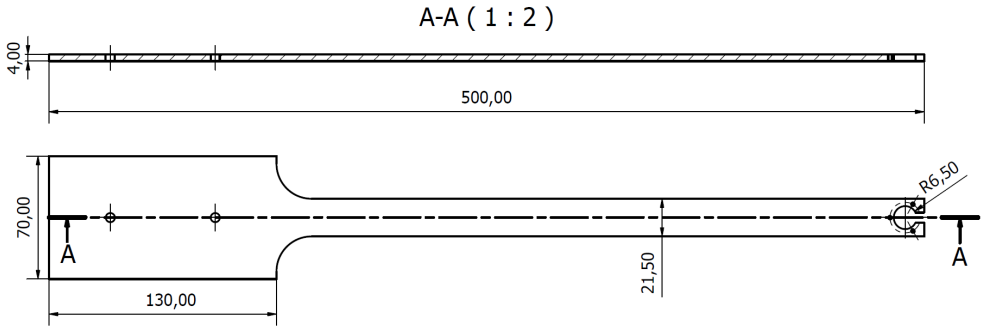

Figure B.13: Drawing and main dimensions of the beam.

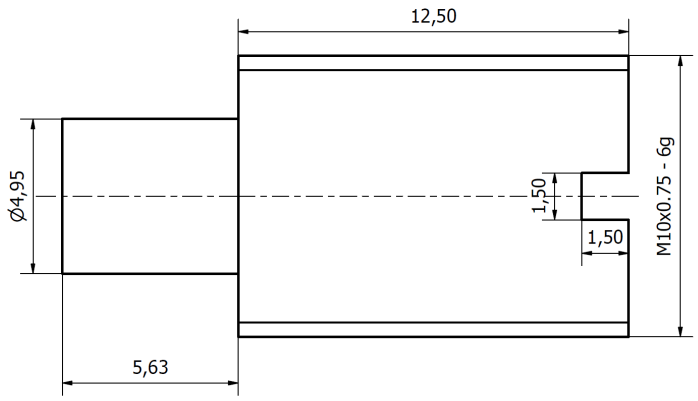

Figure B.14: Drawing and main dimensions of one adjusting screw.

Appendix C

Appendix chapter 4

C.1 Determination of the modal basis

The four boundary conditions of the beam are:

1. No displacement at $x = 0$: $w(0,t) = 0$ hence $\varphi(0) = 0$;
2. No rotation at $x = 0$: $-\frac{\partial w}{\partial x}(0,t)$ hence $\varphi'(0) = 0$;
3. No shearing force at $x = \mathrm{L}$: $-\mathrm{E.I}\frac{\partial^3 w_{rel}}{\partial x^3}(\mathrm{L},t) = 0$ hence $\varphi^{(3)}(\mathrm{L}) = 0$;
4. No bending moment at $x = \mathrm{L}$: $-\mathrm{E.I}\frac{\partial^2 w_{rel}}{\partial x^2}(\mathrm{L},t) = 0$ hence $\varphi^{(2)}(\mathrm{L}) = 0$.

And they lead to the following equation system:

$$\begin{cases} c+e &= 0; \\ d+h &= 0; \\ -c.\cos(k.\mathrm{L}) - d\sin(k.\mathrm{L}) + e.\cosh(k.\mathrm{L}) + h.\sinh(k.\mathrm{L}) &= 0; \\ c.\sin(k.\mathrm{L}) - d.\cos(k.\mathrm{L}) + e.\sinh(k.\mathrm{L}) + h.\cosh(k.\mathrm{L}) &= 0; \end{cases}$$

We choose to substitute e and h and to use only c and d:

$$\begin{cases} e = -c; \\ h = -d; \\ c.[\sin(k.\mathrm{L}) - \sinh(k.\mathrm{L})] - d.[\cos(k.\mathrm{L}) + \cosh(k.\mathrm{L})] = 0; \\ c.[\cos(k.\mathrm{L}) + \cosh(k.\mathrm{L})] + d.[\sin(k.\mathrm{L}) + \sinh(k.\mathrm{L})] = 0. \end{cases} \tag{C.1}$$

As said before, we are looking for non-trivial solutions. Hence, the two last equations must be dependant and the following determinant is null:

$$\det \begin{bmatrix} \sin(k.\mathrm{L}) - \sinh(k.\mathrm{L}) & -\cos(k.\mathrm{L}) - \cosh(k.\mathrm{L}) \\ \cos(k.\mathrm{L}) + \cosh(k.\mathrm{L}) & \sin(k.\mathrm{L}) + \sinh(k.\mathrm{L}) \end{bmatrix} = 0$$

$$\Leftrightarrow$$

$$[\sin(k.\mathrm{L}) - \sinh(k.\mathrm{L})].[\sin(k.\mathrm{L}) + \sinh(k.\mathrm{L})] + [\cos(k.\mathrm{L}) + \cosh(k.\mathrm{L})]^2 = 0$$

$$\Leftrightarrow$$

$$\cos(k.\mathrm{L}).\cosh(k.\mathrm{L}) = -1 \tag{C.2}$$

C.2 Analytical solutions during free flight phases

One can demonstrate that if the initial conditions $q_i(t_0)$ and $\dot{q}_i(t_0)$ are given and the second member of equation 4.19 is known, then:

$$\begin{cases} a_i &= \frac{\mathrm{A}_{13} - \mathrm{A}_{12}.b_i}{\mathrm{A}_{11}}; \\ b_i &= \frac{\mathrm{A}_{11}.\mathrm{A}_{23} - \mathrm{A}_{21}.\mathrm{A}_{13}}{\mathrm{A}_{11}.\mathrm{A}_{22} - \mathrm{A}_{21}.\mathrm{A}_{12}}; \\ d_i &= \frac{e_i}{c_i}.(m_i.\omega - \frac{k_i}{\omega}); \\ e_i &= \frac{\mathrm{F}_{exc}.\varphi_i(x_{\mathrm{VI}})}{-c_i.\omega + (\frac{m_i.\omega - \frac{k_i}{\omega}}{c_i}).(k_i - m_i.\omega^2)}. \end{cases}$$

With:

$$\begin{cases} \mathrm{A}_{11} &= e^{-\omega_i.\xi_i.t_0}.[-\omega_i.\xi_i.\cos(\Omega_i.t_0) - \Omega_i.\sin(\Omega_i.t_0)]; \\ \mathrm{A}_{12} &= e^{-\omega_i.\xi_i.t_0}.[-\omega_i.\xi_i.\sin(\Omega_i.t_0) + \Omega_i.\cos(\Omega_i.t_0)]; \\ \mathrm{A}_{21} &= e^{-\omega_i.\xi_i.t_0}.\cos(\Omega_i.t_0); \\ \mathrm{A}_{22} &= e^{-\omega_i.\xi_i.t_0}.\sin(\Omega_i.t_0); \\ \mathrm{A}_{13} &= \dot{q}_i(t_0) - \omega.[d_i.\cos(\omega.t_0) - e_i.\sin(\omega.t_0)]; \\ \mathrm{A}_{23} &= q_i(t_0) - d_i.\sin(\omega.t_0) - e_i.\cos(\omega.t_0). \end{cases}$$

C.3 Implementation of $q_i^h(t)$

The homogeneous solution $q_i^h(t)$ is:

$$q_i^h(t) = e^{-\omega_i.\xi_i.t}.[a_i.\cos(\Omega_i.t) + b_i.\sin(\Omega_i.t)].$$

In the perspective of an implementation in a computer program, one should notice that the term $e^{-\omega_i.\xi_i.t}$ is exponentially decreasing with respect to time. In order to satisfy the initial conditions described previously, it is necessary that a_i and b_i become larger at each impact to compensate the decay of the exponential term. Therefore, if the simulation is long enough, a_i and b_i may reach infinite values as $e^{-\omega_i.\xi_i.t}$ decays to zero. In order to get rid of this, one can redefine $q_i^h(t)$ this way:

$$q_i^h(t) = e^{-\omega_i.\xi_i.(t-t_0)}.[a_i.\cos(\Omega_i.t) + b_i.\sin(\Omega_i.t)]; \tag{C.3}$$

where t_0 is the impact instant. Doing this, the calculation of the terms A_{ij} is modified in the following manner:

$$\begin{cases} A_{11} = -\omega_i.\xi_i.\cos(\Omega_i.t_0) - \Omega_i.\sin(\Omega_i.t_0); \\ A_{12} = -\omega_i.\xi_i.\sin(\Omega_i.t_0) + \Omega_i.\cos(\Omega_i.t_0); \\ A_{21} = \cos(\Omega_i.t_0); \\ A_{22} = \sin(\Omega_i.t_0); \\ A_{13} = \dot{q}_i(t_0) - \omega.[d_i.\cos(\omega.t_0) - e_i.\sin(\omega.t_0)]; \\ A_{23} = q_i(t_0) - d_i.\sin(\omega.t_0) - e_i.\cos(\omega.t_0). \end{cases}$$

And a_i and b_i take values that remain reasonably low compared to the infinite value of the software used for the simulation.

C.4 Analytical evaluation of the energy terms

Among the terms of the energy balance defined in 4.3.2.1, the analytical calculation of E^i_{exc} and E^i_{diss} must be explained.

C.4.1 Energy of the excitation

Knowing that $F_{exc}(t) = F_{exc}.\sin(\omega.t)$, let's recall that:

$$E^i_{exc} = \int_0^t F_{exc}(t).\varphi_i(x_{exc}).\dot{q}_i(t).dt; \tag{C.4}$$

and from C.3, we have:

$$\begin{aligned} \dot{q}_i(t) =& e^{-\omega_i.\xi_i.(t-t_0)}.[-\omega_i.\xi_i.(a_i.\cos(\Omega_i.t) + b_i.\sin(\Omega_i.t)) - a_i.\Omega_i.\sin(\Omega_i.t) \\ &+ b_i.\Omega_i.\cos(\Omega_i.t)] + \omega.(d_i.\cos(\omega.t) - e_i.\sin(\omega.t)). \end{aligned} \tag{C.5}$$

The sine and cosine products that appears in $\sin(\omega.t).\dot{q}_i(t)$ can be linearized:

$$\sin(\omega.t).\cos(\Omega_i.t) = \frac{1}{2}.[\sin((\omega+\Omega_i).t) + \sin((\omega-\Omega_i).t)]; \tag{C.6}$$

$$\sin(\omega.t).\sin(\Omega_i.t) = \frac{1}{2}.[\cos((\omega-\Omega_i).t) - \cos((\omega+\Omega_i).t)]; \tag{C.7}$$

$$\sin(\omega.t).\cos(\omega.t) = \frac{1}{2}.\sin(2.\omega.t); \tag{C.8}$$

$$\sin^2(\omega.t) = \frac{1}{2}.[1 - 2.\cos(2.\omega.t)]. \tag{C.9}$$

Therefore, in order to derive the analytical expression of equation C.4, it is necessary to determine a primitive of $e^{a.(t-t_0)}.\cos(b.t+\varphi)$ where $t_0, a, b, \varphi \in \mathbb{R}$ and $b \neq 0$. The primitives of the other terms are well-known.

Realizing two successive integrations by parts, one can demonstrate that:

$$\int_0^t e^{a.(u-t_0)}.\cos(b.u+\varphi).du = \frac{e^{a.(t-t_0)}}{b.(1+(a/b)^2)}.[(\sin(b.t+\varphi) + (a/b).\cos(b.t+\varphi))] + \beta; \tag{C.10}$$

where β is a integration constant to determine. Practically, this term will be fixed indirectly ensuring the continuity of $E^i_{ext}(t)$ at the impact instants.

At the end, injecting the linearized expression C.6-C.9 in C.5 and C.4 and factorizing, we obtain:

$$E^i_{exc}(t) = F_{exc}.\varphi(x_{exc}).\frac{1}{2}.[(-\omega_i.\xi_i.a_i + b_i.\Omega_i).(\gamma_1+\gamma_2) - (\omega_i.\xi_i.b_i + a_i.\Omega_i).(\gamma_3-\gamma_4) + \frac{\omega}{2}.(d_i.\gamma_5 - e_i.\gamma_6)];$$

where:

$$\gamma_1 = \int_0^t e^{-\omega_i.\xi_i.(t-t_0)}.\sin((\Omega_i+\omega).t).dt; \tag{C.11}$$

$$\gamma_2 = \int_0^t e^{-\omega_i.\xi_i.(t-t_0)}.\sin((\omega-\Omega_i).t).dt; \tag{C.12}$$

$$\gamma_3 = \int_0^t e^{-\omega_i.\xi_i.(t-t_0)}.\cos((\omega-\Omega_i).t).dt; \tag{C.13}$$

$$\gamma_4 = \int_0^t e^{-\omega_i.\xi_i.(t-t_0)}.\cos((\omega+\Omega_i).t).dt; \tag{C.14}$$

$$\gamma_5 = \int_0^t \sin(2.\omega.t).dt = \frac{1}{2.\omega}.(1-\cos(2.\omega.t)); \tag{C.15}$$

$$\gamma_6 = \int_0^t [1-\cos(2.\omega.t)].dt = t - \frac{\sin(2.\omega.t)}{2.\omega}. \tag{C.16}$$

The terms C.11-C.14 can be calculated analytically using equation C.10 replacing a, b, and φ by the corresponding values and using that $\sin(\omega.t) = \cos(\omega.t-\pi/2)$.

C.4.2 Energy dissipated

Let's recall that:

$$E^i_{diss} = \int_0^t c_i.\dot{q}_i^2.dt. \tag{C.17}$$

Besides:

$$\dot{q}_i^2 = (\dot{q}_i^h)^2 + 2.\dot{q}_i^h.\dot{q}_i^p + (\dot{q}_i^p)^2. \tag{C.18}$$

Developing each term and linearizing the trigonometric terms lead to:

$$
\begin{aligned}
(\dot{q}_i^h)^2(t) =& e^{-2.\omega_i.\xi_i.(t-t_0)}.[(-a_i.\omega_i.\xi_i + b_i.\Omega_i)^2.\underbrace{\cos^2(\Omega_i.t)}_{\frac{1+\cos(2.\Omega_i.t)}{2}} \\
&+ (-b_i.\omega_i.\xi_i - a_i.\Omega_i)^2.\underbrace{\sin^2(\Omega_i.t)}_{\frac{1-\cos(2.\Omega_i.t)}{2}} \\
&+ 2.(-a_i.\omega_i.\xi_i + b_i.\Omega_i).(-b_i.\omega_i.\xi_i - a_i.\Omega_i).\underbrace{\cos(\Omega_i.t).\sin(\Omega_i.t)}_{\frac{1}{2}.\sin(2.\Omega_i.t)}].
\end{aligned} \tag{C.19}
$$

$$
(\dot{q}_i^p)^2(t) = \omega^2.[d_i^2.\underbrace{\cos^2(\omega.t)}_{\frac{1+\cos(2.\omega.t)}{2}} + e_i^2.\underbrace{\sin^2(\omega.t)}_{\frac{1-\cos(2.\omega.t)}{2}} - 2.d_i.e_i.\underbrace{\cos(\omega.t).\sin(\omega.t)}_{\frac{1}{2}.\sin(2.\omega.t)}]. \tag{C.20}
$$

$$
\begin{aligned}
\dot{q}_i^h(t).\dot{q}_i^p(t) =& \omega.e^{-\omega_i.\xi_i.(t-t_0)}.[d_i.(a_i.\omega_i.\xi_i + b_i.\Omega_i).\ \underbrace{\cos(\Omega_i.t).\cos(\omega.t)}_{\frac{1}{2}.[\cos((\Omega_i-\omega).t)+\cos((\Omega_i+\omega).t)]} \\
&+ d_i.(-b_i.\omega_i.\xi_i - a_i.\Omega_i).\ \underbrace{\sin(\Omega_i.t).\cos(\omega.t)}_{\frac{1}{2}.[\sin((\Omega_i+\omega).t)+\sin((\Omega_i-\omega).t)]}\ ].
\end{aligned} \tag{C.21}
$$

Injecting equations C.19, C.20, C.21 in equation C.18 and C.17, we can express $\mathrm{E}_{diss}^i(t)$ in a more compact expression, so that:

$$
\begin{aligned}
\mathrm{E}_{diss}^i =& c_i.[\frac{\Gamma_1}{2}.(\mu_i^2 + \eta_i^2) + \frac{\Gamma_2}{2}.(\mu_i^2 - \eta_i^2) + \Gamma_3.\mu_i.\eta_i \\
&+ \Gamma_4.\omega.(d_i.\mu_i - e_i.\eta_i) + \Gamma_5.\omega.(d_i.\mu_i + e_i.\eta_i) + \Gamma_6.\omega.(d_i.\eta_i - e_i.\mu_i) \\
&+ \Gamma_7.\omega.(d_i.\eta_i + e_i.\mu_i) + \frac{\omega^2}{2}.(\Gamma_8.d_i^2 + \Gamma_9.e_i^2 - 2.d_i.e_i.\Gamma_{10})].
\end{aligned} \tag{C.22}
$$

where the following terms have been defined:

$$
\mu_i = -a_i.\omega_i.\xi_i + b_i.\Omega_i; \tag{C.23}
$$

$$
\eta_i = -b_i.\omega_i.\xi_i - a_i.\Omega_i. \tag{C.24}
$$

And:

$$\Gamma_1 = \int_0^t e^{-2.\omega_i.\xi_i.(t-t_0)}.dt = -\frac{1}{2.\omega_i.\xi_i}.(e^{-2.\omega_i.\xi_i.(t-t_0)} - e^{2.\omega_i.\xi_i.t_0}); \tag{C.25}$$

$$\Gamma_2 = \int_0^t e^{-2.\omega_i.\xi_i.(t-t_0)}.\cos(2.\Omega_i.t).dt; \tag{C.26}$$

$$\Gamma_3 = \int_0^t e^{-2.\omega_i.\xi_i.(t-t_0)}.\sin(2.\Omega_i.t).dt; \tag{C.27}$$

$$\Gamma_4 = \int_0^t e^{-\omega_i.\xi_i.(t-t_0)}.\cos((\Omega_i-\omega).t).dt; \tag{C.28}$$

$$\Gamma_5 = \int_0^t e^{-\omega_i.\xi_i.(t-t_0)}.\cos((\Omega_i+\omega).t).dt; \tag{C.29}$$

$$\Gamma_6 = \int_0^t e^{-\omega_i.\xi_i.(t-t_0)}.\sin((\Omega_i+\omega).t).dt; \tag{C.30}$$

$$\Gamma_7 = \int_0^t e^{-\omega_i.\xi_i.(t-t_0)}.\sin((\Omega_i-\omega).t).dt; \tag{C.31}$$

$$\Gamma_8 = \int_0^t (1+\cos(2.\omega.t)).dt = t + \frac{1}{2.\omega}.\sin(2.\omega.t); \tag{C.32}$$

$$\Gamma_9 = \int_0^t (1-\cos(2.\omega.t)).dt = t - \frac{1}{2.\omega}.\sin(2.\omega.t); \tag{C.33}$$

$$\Gamma_{10} = \int_0^t \sin(2.\omega.t)).dt = -\frac{1}{2.\omega}.(\cos(2.\omega.t)-1). \tag{C.34}$$

The terms C.26-C.31 can be calculated analytically using equation C.10 replacing a, b, and φ by the corresponding values and using that $\sin(\omega.t) = \cos(\omega.t - \pi/2)$. Particular attention should be paid to equation C.25, as the term $e^{2.\omega_i.\xi_i.t_0}$ is expected to grow exponentially with the simulation duration. As explained before, it could lead to numerical discrepancies. Accordingly, this term can be chosen to zero at this point, and the question of the integration constant will be indirectly solved ensuring the continuity of $E^i_{diss}(t)$ at the impact instants.

C.5 Comparison with a Tuned Mass Damper

The figure C.1 compares the displacement response of the beam obtained in identical conditions as those described in section 4.3 in the following cases:

- No absorber attached to the beam ;
- Optimal VI absorber (based on the results depicted in figure 4.5) attached at the end of the beam ;
- Optimal Tuned Mass Damper attached at the end of the beam for various damping ratio ξ, and for a mass ratio equal to 1,8% similar to the case of the VI absorber.

Therefore, one can see that if ξ is greater or equal to 6,3%, these simulation results show that the TMD outperforms the VI absorber in terms of maximum vibration amplitude of the frequency range considered here. However, reaching such a damping ratio is particularly challenging. Damping ratios closer to 2% are more realistic. In this last case the VI

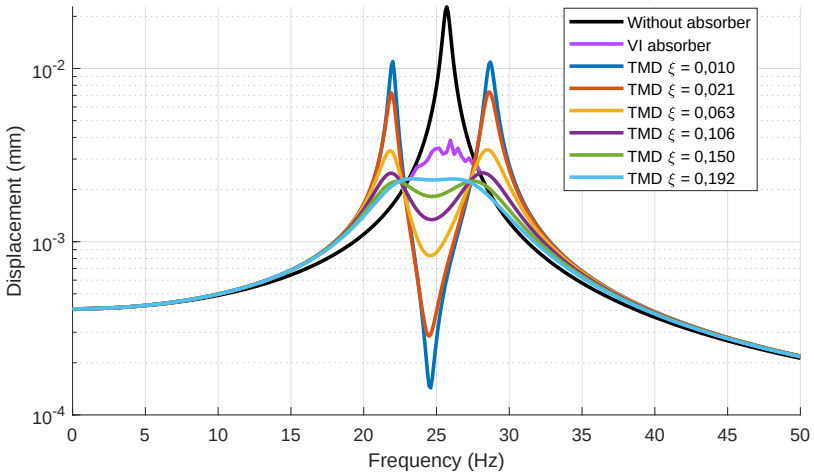

Figure C.1: Response of the beam equipped with the optimal VI absorber, or with a TMD.

absorber remains more effective. Moreover, we have seen at the end of chapter 4 that the VI absorber is particularly robust to eigenfrequencies variations, what is not the case for TMD.

C.6 Energy based approach with 6 modes

The present section aims to present the results obtained for the same simulations as in section 4.3 using only six modes in the modal basis instead of eight in order to see if the results are changed. The figure C.2, figure C.3 and figure C.4 present the FRF of the beam for an excitation in the vicinity of the first, second, and third mode. The figure C.5, figure C.6, and figure C.7 depicts the mechanical energy transferred to each mode for an excitation in the vicinity of the three first modes. At last, the figure C.8, figure C.9, figure C.10 shows the energy dissipated by each mode.

The conclusions previously established at the end of chapter 4 remains unchanged. In particular, the existence of an energy transfer towards the higher modes, and the negligible amount of energy transferred towards the lower modes is also demonstrated here.

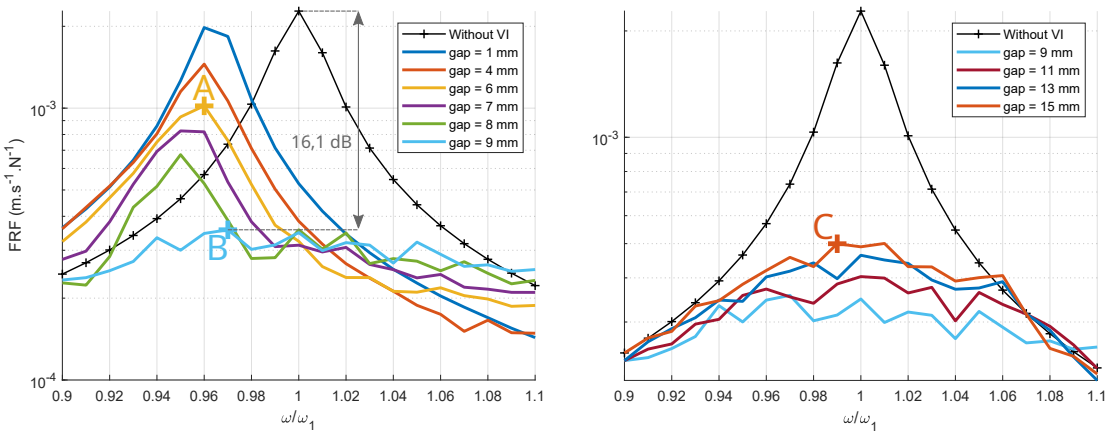

Figure C.2: FRFs of the beam excited on the first mode for several gap values.

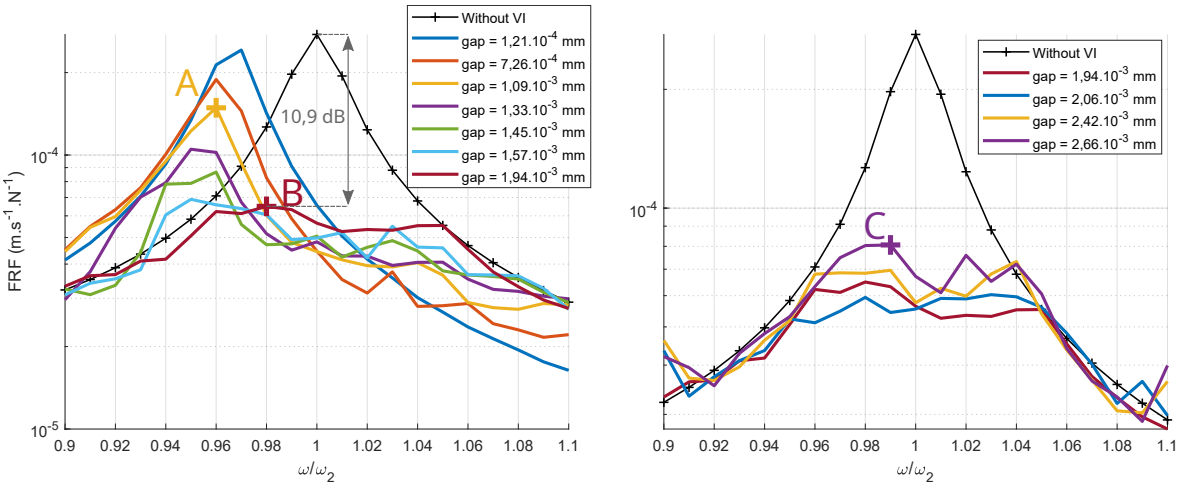

Figure C.3: FRFs of the beam excited on the second mode for several gap values.

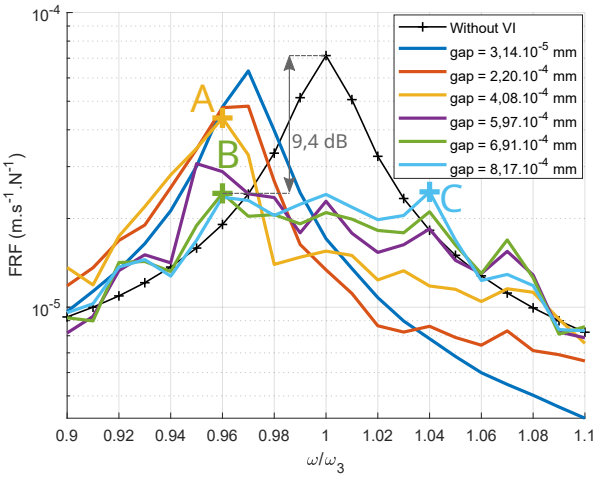

Figure C.4: FRFs of the beam excited on the third mode for several gap values.

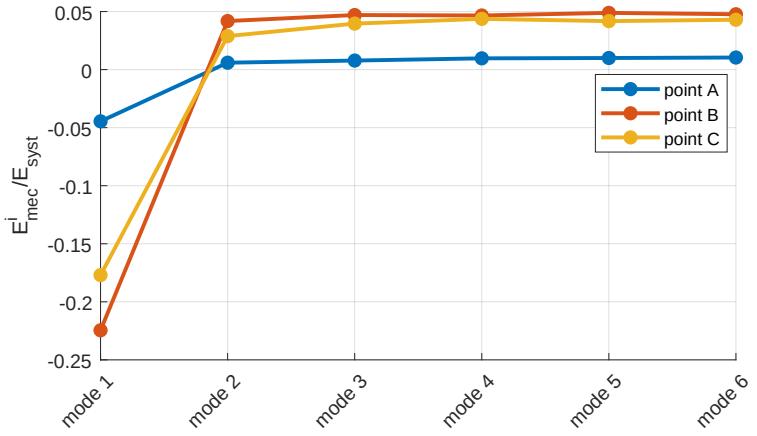

Figure C.5: Energy received by mode for an excitation on the first mode.

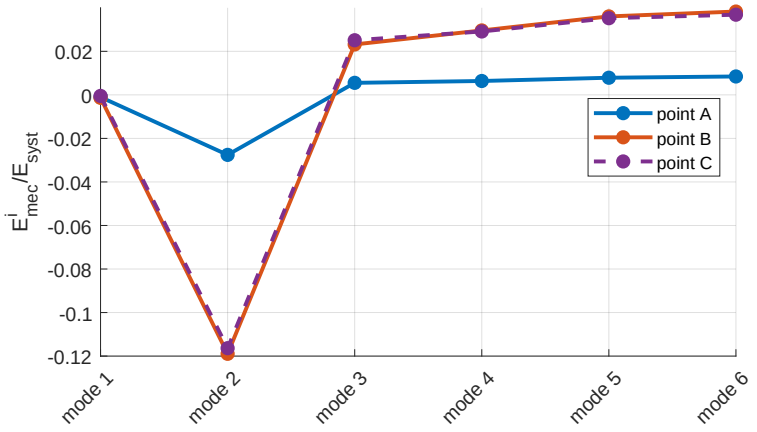

Figure C.6: Energy received by mode for an excitation on the second mode.

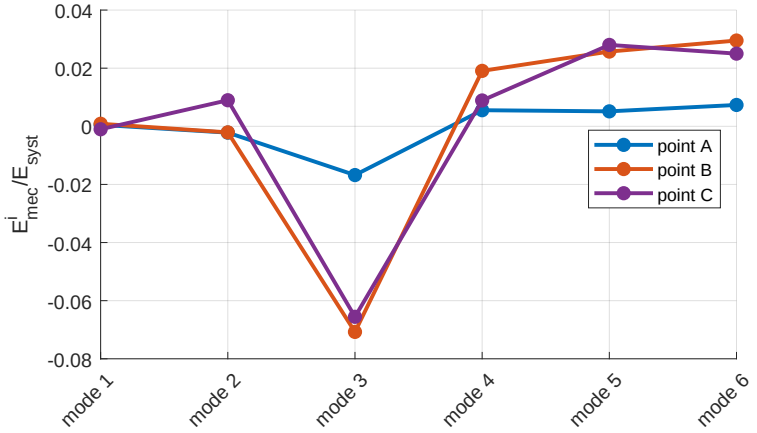

Figure C.7: Energy received by mode for an excitation on the third mode.

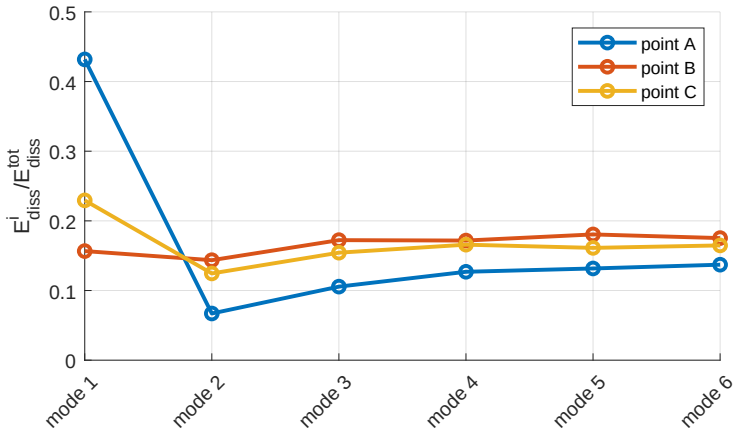

Figure C.8: Energy dissipated by mode for an excitation on the first mode.

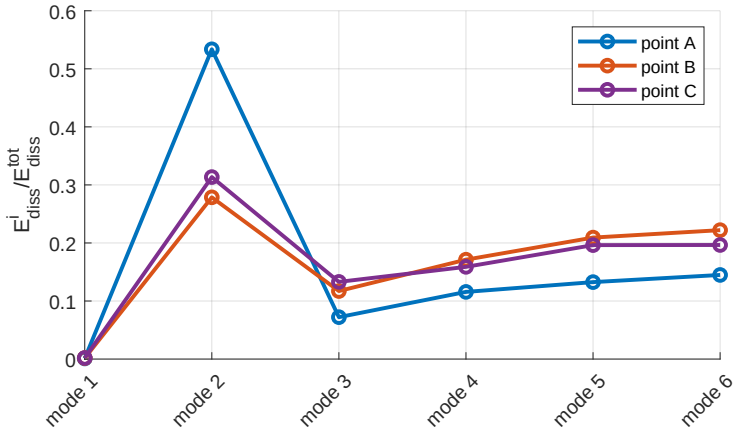

Figure C.9: Energy dissipated by mode for an excitation on the second mode.

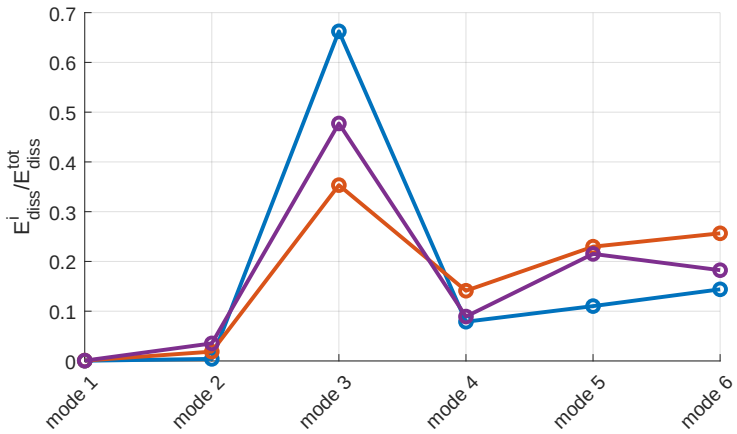

Figure C.10: Energy dissipated by mode for an excitation on the third mode.

Appendix D

Appendix chapter 5

D.1 Change of the FRFs due to added masses

The VI absorbers attached to the wing plane add small masses to the structure. This contributes to shift the eigenfrequency and to change slightly the mode shapes. In order to complement the section 5.4.2, the figure D.1 illustrates the change in the FRF when three VI absorbers with the balls locked are attached at the end of the wings. Because of the added masses, the resonance peaks are shifted towards lower frequencies. Moreover, their amplitudes are sometimes changed.

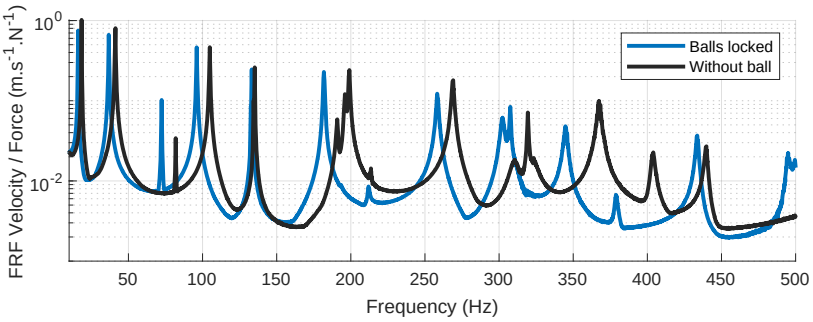

Figure D.1: Comparison of the FRFs to illustrate the effect of the added masses due to VI absorbers

D.2 Comparison of the displacements for flexural and torsional modes

This appendix specifies the amplitudes of the displacements measured on the plane wing in order to explain the efficiency observed in 5.4.3.1. The figure D.2 illustrates the difference of displacements that can be observed on the measuring points for flexural and torsional modes. This highlights very well that the point 1 undergoes larger displacements when the plane vibrates on the flexural modes, while points 5, 6, 7 and 8 has larger displacements when the plane vibrates on the torsional modes.

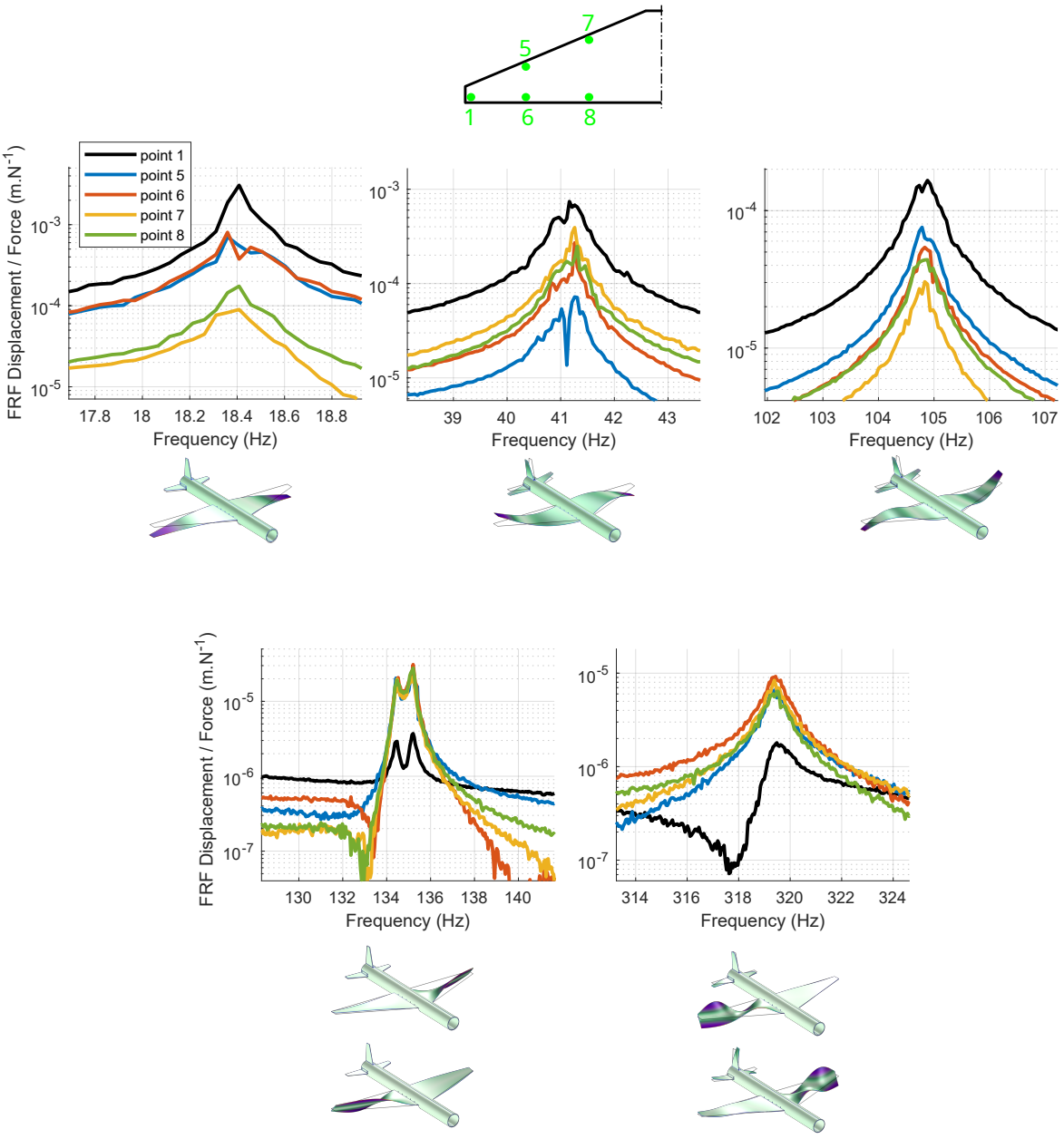

Figure D.2: Displacements of the measurement points depending on the mode shape.

D.3 Frequency Response Function in displacement of the model plane

This appendix comes as a developpement to explain the results presented in 5.4.3.2. As the efficiency of the absorbers are related to the gap and to the vibration amplitude of the plane, it is interesting to look at the displacement of the plane for the excitation frequency range. Consequently, the FRF displacement / force is depicted in figure D.3. This shows that the displacements decrease less rapidly with the frequency than in the case of the beam presented in chapter 3. Therefore, finding the gap values that enable to perform a multimodal attenuation may be easier in the case of the plane.

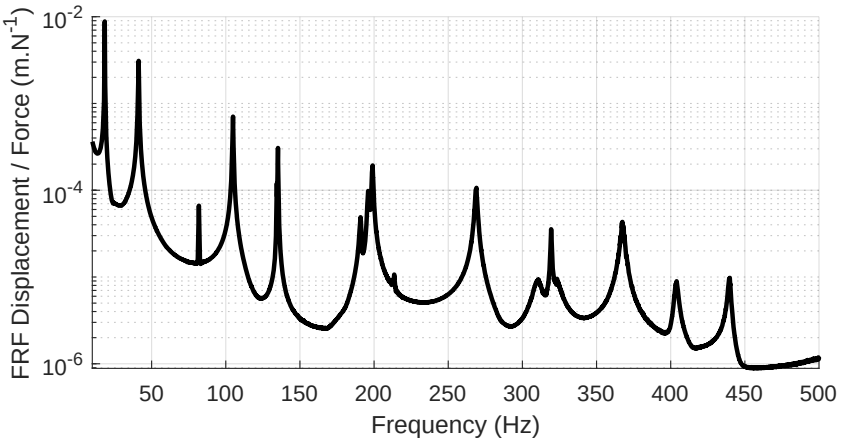

Figure D.3: FRF displacement / force of the plane without absorbers.

D.4 Repeatability with multiple VI absorbers

This appendix aims at assessing the repeatability of the tests realized on the model plane equipped with multiple absorbers. Even if the locations of the absorbers during these tests do not correspond to the tests realized in chapter 5, the conclusions can be extended to these tests.

D.4.1 Repeatability of the response

In the results presented below, two tests are realized. Before running the second test, the stinger of the shaker is removed and re-attached. The VI absorbers are also removed, the gap is set again, and the absorbers are re-arranged on the wings. The FRFs presented are calculated a single measurement point at the left end of the wing. The results demonstrate that no significant variations are observed.

D.4.2 Repeatability of the excitation force

The tests with multiple absorbers presented in chapter 5 are realized without controlling the excitation force. Nevertheless, the gain of the amplifier is set at the same level for each test, as is the voltage of the excitation signal. Since the force level is not monitored, it may

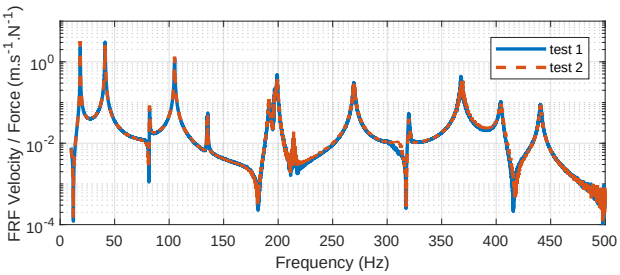

Figure D.4: Repeatability of the response without balls.

slightly vary in the tests. The objective of this appendix is to demonstrate that the variations of the excitation force remains at a reasonably low level, despite the absence of control. In the following results, the spectra of the excitation force are compared in figure D.6a for several different tests dealing with different gap values and different arrangements of the absorbers. The configuration of these tests are presented in figure D.6b. This last figure depicts the variation of the Root Mean Square level of the excitation force compared to the mean value.

Therefore, the variation through all the tests is not greater than 7 %, which seems to be reasonably acceptable in order to be able to compare the results of all the tests even if no force control is used.

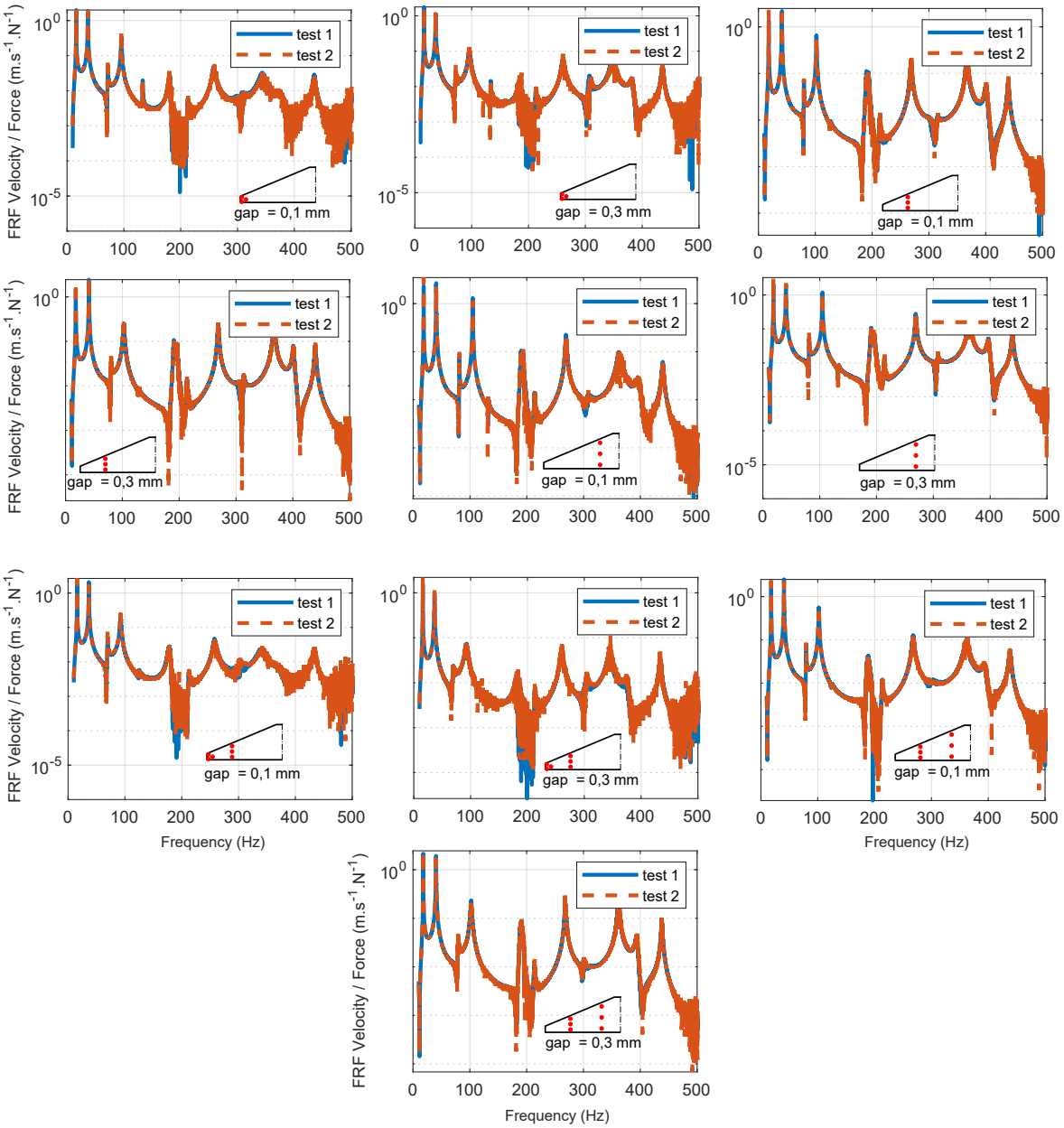

Figure D.5: Repeatability of the responses for several arrangement of the VI absorbers.

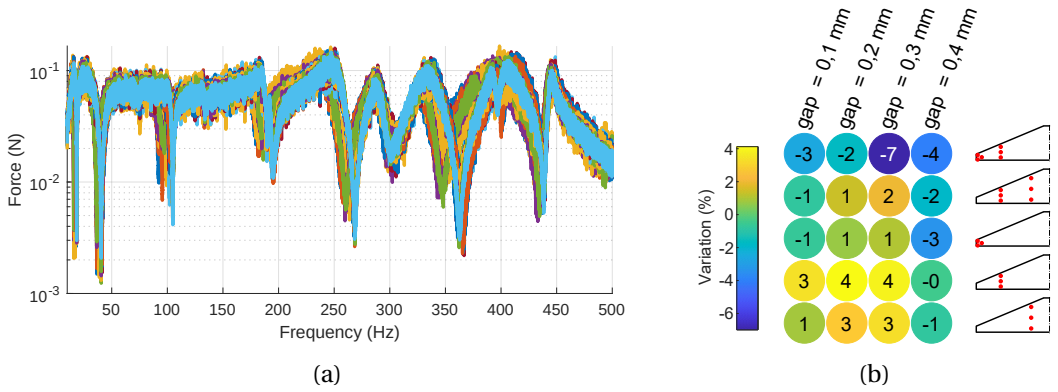

(a) (b)

Figure D.6: Repeatability of the excitation force.

Title: Contributions to the development of vibro-impact absorbers : from the characterization towards the design of multiple absorbers

Keywords: vibro-impact, vibration mitigation, non-linear dynamics, digital image correlation

Abstract : Structural vibrations take place in each systems because of their natural resonant behavior. In some cases though, these vibrations may become problematic since they lead to great amplitudes disturbing the systems, to noise, repeated stress and therefore fatigue, ending with failure of the structures. Accordingly, these vibrations should be controlled. Some well-known solutions exist, like Tuned Mass Dampers or the use of polymer materials that have very high dissipative capacity. However, the effectiveness of these solutions are reached if certain conditions are matched, such as a proper frequency tuning, or a specific range of temperature. Therefore, the solutions available to control the vibrations need a trade-off between the performance, the added mass, and the robustness of the device, among others.

Recently, devices involving non-linear phenomena have emerged for their interesting properties. For instance, such devices are expected to be efficient on a widest frequency range, requiring a low added mass. Vibro-impact based technologies are part of this approach. The usually take benefit of the impacts between a main vibrating structure to control and small oscillating and embedded masses. Because of the vibrations of the main structure, vibro-impacts are triggered, leading to energy transfers and vibration reduction. Consequently, the main objective of this PhD is to take advantage of vibro-impact phenomenon for vibration mitigation application.

The main contributions of this work concern new experimental approaches. To begin with, a method is proposed to measure and characterize vibro-impact phenomenon. Based on a high-speed camera and a Digital Image Correlation process, this new method allows to derive the Coefficient of Restitution and the friction forces acting on the ball in a vibro-impact system. Then, the effect of a vibro-impact absorber on a multi-modal structure is inquired. Experimentally, the cases of a beam and of a model plane are considered. On the beam, the performance of the absorber for various type of excitations is demonstrated. The results also highlights that the gap and the vibration amplitude plays analogous roles. Setting these two parameters fully determine the attenuation, and the occurrence of specific non-linear regime of vibration. Moreover, an energy-based approach is adopted numerically, demonstrating the important role of the modal energy transfers in vibro-impact problems. The case of the model plane aims to consider a more realistic structure before going towards industrial structures. A numerical approach based on the Finite Element method is developed to simulate the behavior of the plane equipped with a vibro-impact absorber. The simulation results are compared to experimental results, highlighting the limitations encountered with a single vibro-impact absorber. Finally, we took advantage of multiple vibro-impact absorbers to improve the vibration mitigation performance. More specifically, a multi-modal attenuation is achieved using a gap gradient and placing the vibro-impact absorbers at specific locations on the plane.

UBFC
UNIVERSITÉ
BOURGOGNE FRANCHE-COMTÉ

Université Bourgogne Franche-Comté
32, avenue de l' Observatoire
25000 Besançon

Titre: Contributions au développement d'absorbeurs à vibro-impacts : de la caractérisation à la conception d'absorbeurs multiples

Mots-clés: vibro-impact, réduction des vibrations, dynamique non-linéaire, corrélation d'images

Résumé: De par le caractère résonant des structures qui nous entourent, celles-ci se montrent plus ou moins sensibles aux vibrations auxquelles elles peuvent être soumises. Dans certaines conditions, ces vibrations peuvent devenir problématiques, notamment lorsqu'elles génèrent de grandes amplitudes de vibration qui perturbent le fonctionnement du système principal, du bruit, des contraintes répétées et donc de la fatigue pouvant conduire à la rupture. Des solutions existent, telles que les absorbeurs dynamiques (ou absorbeurs à masse accordée) ou encore l'utilisation de matériaux polymères qui possède une grande capacité de dissipation d'énergie. Cependant, des conditions particulières sont requises afin que ces solutions sont pleinement performantes. Il s'agit par exemple d'un bon accordage fréquentiel, ou d'une plage de température particulière. Par conséquent, les solutions de contrôle vibratoire sont nécessairement un compromis entre performance, masse ajoutée, et robustesse du dispositif notamment.

Récemment, l'exploitation de phénomènes non-linéaires dans les solutions de contrôle vibratoire a fait son apparition car des propriétés intéressantes ont été démontrées. Par exemple, de tels dispositifs sont supposés avoir une bande de fréquence d'efficacité plus importante, et nécessitent un faible ajout de masse. Les technologies basées sur le vibro-impact en sont un exemple. Il s'agit généralement de tirer profit des impacts entre une structure principale à contrôler et des masses libres en translation intégrées à la structure. Les vibrations de la structure principale déclenchent alors le phénomène de vibro-impact, conduisant à des transferts d'énergie et finalement une réduction du niveau vibratoire. Par conséquent, l'objectif de cette thèse est d'exploiter le phénomène de vibro-impact à des fins d'atténuation vibratoire.

Les principales contributions de ces travaux concernent des approches expérimentales nouvelles. Tout d'abord, une méthode de mesure et de caractérisation du vibro-impact est proposée. Basée sur une série d'image issue d'une caméra rapide et sur un calcul de corrélation d'images, cette nouvelle méthode permet d'obtenir le Coefficient de Restitution ainsi que les forces de frottement dans le système à vibro-impact. Puis l'effet d'un vibro-impacteur sur une structure multi-modale est investigué. Expérimentalement, les cas d'une poutre et d'un modèle d'avion sont étudiés. Sur la poutre, l'efficacité du vibro-impacteur pour plusieurs types d'excitation est démontrée. Par ailleurs, les résultats montrent que le gap et l'amplitude d'excitation jouent des rôles analogues. Ainsi, ces deux paramètres déterminent entièrement l'atténuation obtenue, ainsi que le régime de vibration non-linéaire du système. De plus, une étude énergétique numérique démontre l'importance du rôle des transferts d'énergie dans l'espace modal pour les problèmes de vibro-impact. Le cas du modèle d'avion vise quant à lui à considérer une structure plus réaliste avant de s'attaquer à des structures industrielles. Une méthode basée sur la méthode des éléments finis est développée pour simuler le comportement de l'avion équipé d'un vibro-impacteur. Les résultats de simulation obtenus sont comparés à des résultats expérimentaux, mettant bien en évidence les limitations rencontrées avec l'utilisation d'un unique vibro-impacteur. Finalement, des vibro-impacteurs multiples sont réalisés dans l'optique d'augmenter les performances vibratoires du dispositif. Il est ainsi possible d'obtenir une atténuation multi-modale en exploitant un gradient de gap et en choisissant judicieusement la localisation des vibro-impacteurs sur l'avion.

UNIVERSITÉ BOURGOGNE FRANCHE-COMTÉ

Université Bourgogne Franche-Comté
32, avenue de l' Observatoire
25000 Besançon